Andrea Infuso

Silicon photovoltaics: experimental testing and modelling of fracture across scales

Tesi per il conseguimento del titolo di Dottore di Ricerca
XXVIII Ciclo (2013 - 2014 - 2015)

Dottorato di Ricerca in Ingegneria delle Strutture
Politecnico di Torino

Marzo 2016

Dottorato di Ricerca in Ingegneria delle Strutture
Politecnico di Torino, Corso Duca degli Abruzzi 24, 10129 Torino, Italy

Tutore: Prof. Marco Paggi

Coordinatore: Prof. Vincenzo Ilario Carbone

The world breaks everyone, and afterward,
some are strong at the brocken places.

(Ernest Hemingway)

Acknowledgements

The research presented in this thesis was carried out at the Department of Structural and Geotechnical Engineering - Politecnico di Torino, under supervision of Prof. Marco Paggi and Prof. Mauro Corrado.

I would like to thank my tutor, Prof. Marco Paggi, who approached me to Fracture Mechanics allowing me also to fulfil engaging experiments and tests. I am also very grateful to Prof. Mauro Corrado for his essential support during laboratory tests and numerical simulations. Taking the example of their scientific dedication I have often found the motivation to persevere in my research.

A sincere gratitude also to Prof. Qi-Chang He and Prof. Quy Dong To for their hospitality and kindness during the period of my stay at the Laboratoire de Modéllisation et Simulation Multi Echelle - Universite Marne la Valée (UPEM). A long lasting memory of that period, places and experiences will be preserved. The research leading to the results presented in this thesis has received funding from the European Research Council under the European Union?s Seventh Framework Programme (FP/2007?2013)/ERC Grant Agreement No. 306622 (ERC Starting Grant Multi-field and Multiscale Computational Approach to Design and Durability of PhotoVoltaic Modules?CA2PVM) and from the Italian Ministry of Education, University and Research under the Project FIRB 2010 Future in Research Structural Mechanics Models for Renewable Energy Applications (RBFR107AKG). Special thanks are also due to the handful of people who had the patience to debate with me during gloomy days. I will always keep in mind with pleasure all the colleagues and staff who have spent day by day a kind gesture on me.

Summary

The study of the properties of materials can be addressed through a multi-scale approach, in order to have the possibility to grasp at each of the levels of analysis the peculiar aspects. Tracing a path inside the state-of-the-art in the available bibliography, historically in the field of mechanics s are found in which the material is studied through nonlocal theories based on continuous or discrete local approaches. More recently, with the advent of great computational power computers, analytical methodologies based on theories also very complex deriving from the field of chemistry and physics have been developed, capable to discretize at the atomic scale the material and study its behavior by applying energy approaches. Starting from the analysis of some of these theories at the nano- and micro-scales, it is possible to investigate the separation mechanisms at the molecular level, which may be considered as cracking processes within the material according to the adopted scale of analysis. The application of theories of this kind to large portions of material, in which there are up to some millions of particles involved is reasonably not an applicable solution, since it would require a huge effort in terms of computation time. To work around this problem and find a method suitable for the study of cracking mechanisms, a mixed method (MDFEM) was byconjugating pure molecular dynamics (MD) and the finite element method (FEM), in which the material is discretized by means of one-dimensional elements whose mechanical characteristics are derived from MD. This approach is based on the application of a nonlocal theory in which the contribution of a portion of material placed within a certain distance from the point of fracture is taken into account by means of a parameter of non-locality. Moreover, the study of the evolution of cracking is addressed at the meso-scale by the application of a cohesive non-linear model.

Towards the analysis of the macroscale, the theories put forward so far have been applied to the study of phenomena of breakage inside Silicon cells embedded into rigid or semi-flexible photovoltaic modules. By performing various laboratory tests, useful for the characterization of the material and for understating the evolution of cracking process due to multiple causes, a study on the main issues that may compromise the durability and maintenance of the expected service levels of photovoltaic panels has been conducted. Experimentally results have been interpreted by using appropriate macro-scopic continuum models. The research carried out had the purpose to provide an introduction to a correct design of these systems of energy production in order to increase their durability and resistance to cracking.

Sommario

Lo studio delle proprietà dei materiali può essere affrontato mediante un approccio multi-scala, al fine di cogliere per ciascun livello di analisi gli aspetti peculiari. Tracciando un percorso all'interno dello stato dell'arte presente mediante la bibliografia disponibile, si ritrovano storicamente nel campo della meccanica diversi metodi in cui il materiale è studiato mediante teorie nonlocali basate sul continuo o su approcci discreti locali. In tempi più recenti, con avvento dei calcolatori informatici di grande potenza computazionale, sono state sviluppate metodologie di analisi basate su teorie anche molto complesse derivanti dal campo della chimica e della fisica che discretizzano il materiale a livello atomico e ne studiano il comportamento mediante approcci energetici. Partendo dall'analisi di alcune di queste teorie alla nano- e micro-scala, é possibile indagare i meccanismi di separazione a livello molecolare, considerabili come processi di fessurazione all'interno del materiale relativamente alla scala di analisi a cui si fa riferimento. L'applicazione di teorie di questo genere su ampie porzioni di materiale, in cui sono presenti anche alcuni milioni di particelle non é ragionevolmente una soluzione applicabile, dal momento che richiederebbe un enorme sforzo computazionale il termini di potenza di tempo. Per ovviare al problema e individuare un metodo che risulti idoneo allo studio dei meccanismi di fessurazione, è preso in analisi un metodo misto (MDFEM) coniugando tra loro la pura dinamica molecolare (MD) e gli elementi finiti (FEM), in cui il materiale è discretizzato mediante elementi monodimensionali le cui caratteristiche meccaniche sono derivata dalla MD. Tale approccio è basato sull'applicazione di una teoria nonlocale che tenga in conto del contributo di una porzione di materiale collocato nei pressi della zona di fessurazione, mediante un parametro di non località . Inoltre, lo studio della evoluzione della fessurazione è affrontato alla meso-scala mediante l'applicazione di un modello coesivo non lineare.

Nel passaggio alla analisi alla macro-scala, le teorie fino ad ora formulate trovano applicazione nello studio dei fenomeni di frattura localizzati nelle celle di Silicio incapsulate nei moduli fotovoltaici rigidi o semi-flessibili. Mediante prove di laboratorio, utili per la caratterizzazione del materiale e per comprendere l'evoluzione della fessurazione e delle molteplici cause a cui č dovuta, è stato condotto uno studio relativo alle principali problematiche che inficiano la durabilità e il mantenimento delle prestazioni dei pannelli fotovoltaici. I risultati sperimentali sono stati interpretati mediante appropriati modelli continui alla macro-scala. La ricerca svolta ha avuto lo scopo di fornire una introduzione ad una corretta progettazione di questi sistemi di produzione energetica al fine di aumentarne la durabilità e la resistenza alla frattura.

Contents

Chapter 1

A brief geometrical and mechanical description of traditional and flexible PV modules

In this first chapter a brief overview on the operating principle of a photovoltaic (PV) module and then a description of the geometrical and mechanical properties of the different PV panels typologies nowadays available on the market are presented. The Photovoltaic effect allows to convert solar light into electrical power that can be used by a customer or be inserted in the electrical power network if the produced amount is great. More cells in a panel and more panels opportunely electrically connected together are used to produce electric energy. Related to the extension of the plant, it is possible to have a single panel, able to supply a low requesting charge user, up to a thousands modules plant used for factory production of electrical energy and sale to electric network managers.

The typical rigid PV module is a multilayer element composed by plies with different thickness and material, since each of them have to contribute with different tasks to the proper working condition of the system. The electrochemical process of solar light radiation conversion into electric charge is carried out by the thin film of silicon packed into the PV module and the so produced electric current is transmitted through metallic elements inside the module until the module connections. After that, a description of a semi-flexible PV module typology is provided, which is less common than rigid panels, suitable for with special applications in particular areas. This kind of modules differs from the previous one also for the constituent materials, which are to confer the possibility to be partially flexible.

One of the most relevant unknowns about photovoltaics is the estimation of the durability of those modules, identified as the time in which the panel is able to preserve a percentage high enough of the initial electrical production capacity. The functionality of the panel is directly dependent on the environmental condition in which it works and possible external agents acting on it, as damages due to weathering or to installation methods. For the accep-

tance of module performance, it is commonly establish a maximum loss of 10% in a time of 10 years and then less than 20% in the next 15 years. In such a way the estimated maximum time life of a PV module is 25 years. This is the guarantee that producers/installers of the plant have to guarantee for final customer satisfaction.

In order to establish which are the performance requirements of the different PV modules, there are several references in the literature to Standards and Technical rules (American and European) about the measurement of both new and aged modules, providing guidance for the optimal production chain as also for their correct installation. Classification criteria proposed in those documents are based on damage tests conduced on modules and measuring performance decay establishing backlinks which are the requested productive standards in order to build products with expected certified performances.

However the standards are still partially incomplete with some gaps in the criteria for classification, being silent about the damage mechanisms from the point of view of their evolution in time. The aim of this research is to propose a multi-physics and multi-scale model through which it is possible to study the genesis and the evolution of fractures in the silicon layer. Numerical results achieved at each of the analysed scale levels are then compared with experimental evidence emerged from laboratory tests performed to characterise the behaviour of PV panels subjected to different scenarios.

1.1 The photovoltaic effect: electrical energy from solar lightening. Electroluminescence: light emission from electrical energy

The so called solar photovoltaic effect is the ability of some materials to convert the solar energy into electricity. This is the basic working principle on which PV modules are based and particularly this role is normally carried out by the cells built with semiconductor material embedded into modules. The photovoltaic effect, that is the basic working principle of the PV modules, is a sub-category of the photoelectric effect which is the emission of electron made by a metallic surface when it is hit by electromagnetic radiation, namely by photons having a certain wavelength. The photovoltaic effect occurs when an electron lying in the valence band of a material, generally a semiconductor, passes into the conduction band due to the absorption of a photon of sufficient energy incident on the material.

The photovoltaic modules are realized by using the widely component utilised for electronic components, which is silicon. The silicon belongs to the group IV of the periodic table of the elements, has four valence electrons and is therefore called tetravalent element. These four electrons on the outermost orbital determine most of the chemical-physical characteristics of the element, sharing each atom its valence electron. This type of bond is called covalent. According with the lack of free electrons, it is not a so good conductive material and also offers a poor insulation. Only at higher temperatures some electrons in the covalent bonds may acquire enough energy to break the bond and in this case the released electron is free to move in the crystal, and can contribute to the current flow. The electrons near to the broken bond can move in the position left empty, leaving in their turn a gap and this process also contributes to the current flow. In order to obtain the photovoltaic effect it is necessary to

dope the structure, which means to enter foreign substances said impurities in a pure material in order to create some vacancies and facilitate the movement of electrons.

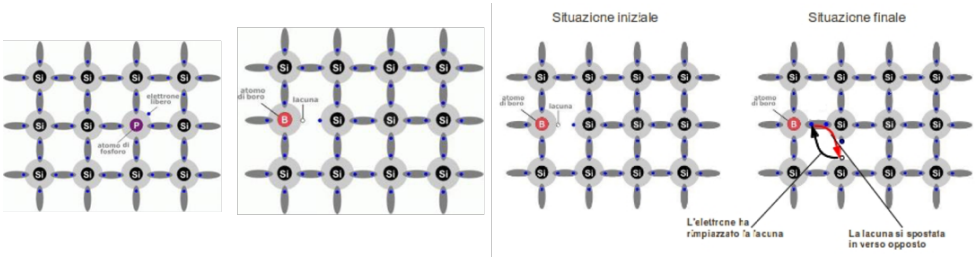

Figure 1.1: (a) Si doped with P (group V) (adapted from www.altervista.org); (b) Si doped with B (group III); (c) Si doped with B (group III).

Doping of material may be incorporated in the crystal structure in two ways: it can be infiltrated between the empty spaces that exist between the silicon atoms, taking the name of interstitial impurities, while in the second case it replaces some of the silicon atoms within the crystal lattice, named substitutional impurities. The elements of the III and the group V of materials act well as substitutional impurities for silicon. When an atom of an element of the group V, such as phosphorus, is used as dope, four of its valence electrons are used to form covalent bonds which were already formed by silicon, while the fifth electron remains bonded to the atom for electrostatic interaction, free from forming covalent bonds. Its own energy is much lower than that of covalent bonds, for which the electron remains free to move within the solid. According to this, as many phosphorus atoms are entered in the silicon crystal many more are free electrons. The effect of silicon doping with phosphorus atoms is to modify its conductivity in a controlled manner. In Fig. 1.1(a) it can be visualized the silicon crystal doped with a phosphorus atom from which it results in a free electron.

Similarly, when a silicon crystal is doped with an atom of group III, which has only three valence electrons, replacing the silicon, it is possible to restore only three of covalent bonds with neighbouring atoms. The lack of the fourth electron bond is called gap, which has a behaviour equivalent to that of a free charge. In Fig. 1.1(b) it is shown how the doping of silicon by means of a boron atom results in the formation of three covalent bonds with as many electrons of the silicon atoms adjacent and the formation of a gap. Even the gaps are free to move in the silicon crystal: in fact, thanks to the continuous movement of electrons, in a certain instant an electron which originates from a silicon-silicon bond can break free and suddenly it will be able to occupy the gap that had the boron-silicon bond. Later a new bond will break and freed electrons will take the place of the new gap. In Fig. 1.1(c) it is outlined with the red arrow moving gaps, the black arrow with the movement of the electrons and the direction of the two movements are one the opposite of the other. The gaps can be considered positive free charges. With the doping two superimposed layers are formed: the upper one directed towards the sunlight, doped with phosphorus atoms with an excess of electrons (negative charge), called *n-type*. At the bottom, the layer doped with

boron atoms which has an excess of holes and therefore of positive charge defined as *p-type*. The junction between the two layers is called a *p-n* junction [1]. In the p-n junction the electrons diffuse naturally by the high-density region (n) to a low density (p), creating an accumulation of negative charge in the region *p* and analogously occurs for the gaps, with accumulation (positive charges) in the region *n*. In other words, close to the junction area an electric field across the junction is established is established, which once reached the equilibrium situation is opposed to the further natural diffusion of charges. By applying a voltage from the outside, the junction allows the current to flow only in one direction, working as a diode. This situation is implemented by the photovoltaic effect in which light provides sufficient energy to electrons (photons) to pass from the valence band to the conduction. The electron, passing in the conduction band, determines a gap. The electric charges are set in motion by the potential difference present in the p-n junction. Connecting the junction with an external connector will result in a closed circuit in which the flow of electrons from the n-layer part with greater potential, towards the layer p at lower potential, takes place as long as the cell is exposed to light, see Fig. 1.2.

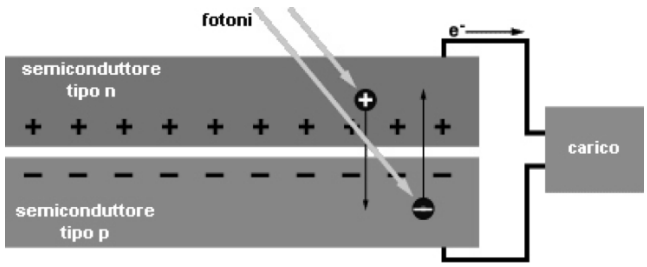

Figure 1.2: Scheme of p- and n-type semiconductors for electroluminescence production (adapted from www.itishertz.gov.it).

The outputs of PV modules can be measured by introducing some parameters able to express some characteristic data. First of all, the short-circuit current I_{sc} can be defined as the current passing through the solar cell when there is no voltage crossing it (i.e. a short-circuit condition in a solar cell) and it is ideally equal to the light-generated current I_L. Therefore, I_{sc} is the maximum current that could be obtained if materials behave optimally and there were no disturbances. It strictly depends by some factors as the area covered by the solar cell, the power of the incident light source that determines the number of photons reaching the solar cell upper surface, the spectrum of the incident light (standardised to the AM1.5 spectrum), the optical properties of absorption and reflection of the solar cell and the collection probability of the solar cell (that depends mainly on the surface passivation and the minority carrier lifetime in the base). In order to well understand the meaning of this value, it is possible to define a graph with the relationship between I and V (current intensity and voltage crossing the cell) and identify on it the position of the I_{sc} point as shown in Fig. 1.3.

In the same way, the open-circuit voltage V_{oc}, can be defined as the value of voltage occurring when the current in the solar panel is zero, representing the maximum voltage that can be obtained by a certain solar module. The V_{oc} value corresponds to the amount of

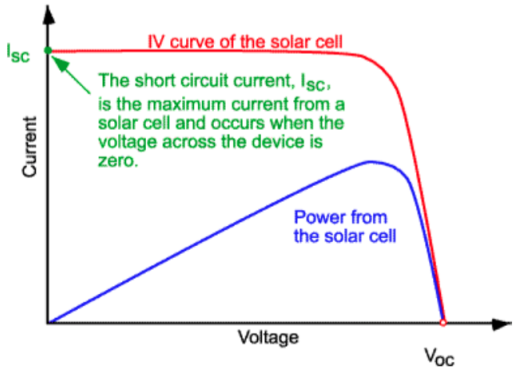

Figure 1.3: I_{sc} point on the I-V curve of a solar module (adopted from www.pveducation.org).

forward bias on the solar cell, related to the capacity to convert light into energy by the p-n junction belonging to the Si layer. The value of V_{oc} can be calculated through the canonical solar cell equation in Eq. (1.1), setting the net current equal to zero:

$$V_{oc} = \frac{nkT}{q} \log\left[\frac{I_L}{I_0} + 1\right] \tag{1.1}$$

In this equation k is the Boltzmann constant equal to $8.6173324(78) \cdot 10^{-5}[\mathrm{eVK}^{-1}]$, T is the temperature of the solar cell, n is the ideality factor (which is a measure of the junction quality and the type of recombination in solar cell; it is considered equal to 1 for typical simple recombination mechanisms), q is the electrical charge. As it can be seen in the equation, the open circuit voltage V_{oc} depends on the dark saturation current I_0 and the light generated current I_L. The value of I_0 in turn depends on recombination in the solar cell and it has a key effect on V_{oc}, which can be also considered as a measure of the amount of recombination in the device, while the short-circuit current I_{sc} has a typically small effect on this parameter. An alternative way to express the open-circuit voltage V_{oc} stems from the properties of the semiconductor material in the solar cell according to Eq. (1.2), which takes into consideration the dependence on I_0 density, can also be determined from the carrier concentration:

$$V_{oc} = \frac{kT}{q} \log\left[\frac{(N_A + \Delta n)\Delta n}{n_i^2}\right] \tag{1.2}$$

where $\frac{kT}{q}$ is the thermal voltage, N_A is the doping concentration, Δ_n is the excess carrier concentration and n_i is the intrinsic carrier concentration. The short-circuit current I_{sc} typically has a small effect on this parameter. As before for I_{sc}, it is possible to point out on the I-V curve in Fig. 1.4 the particular position of the V_{oc} point.

Commercial silicon solar cells made with multi-crystalline silicon are characterised by a typical open-circuit voltages around 600 mV measured under sun irradiation at standardised AM1.5 conditions, while PV panels consisting of high quality single-crystalline Si can have

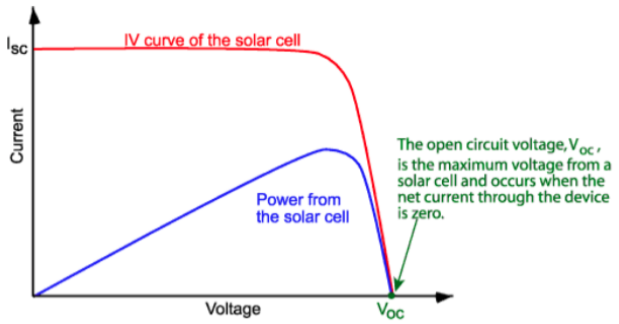

Figure 1.4: I-V curve of a solar panel, with V_{oc} point (http://pveducation.org/).

open-circuit voltages of up to 730 mV. The AM1.5 reference cited before is considered the universal standard to represent the overall yearly average air mass coefficient AM for mid-latitudes, with approximately 1.5 atmosphere thickness (corresponding to a solar zenith angle of Z = 48.2°). The AM defines the direct optical path length of solar radiation through the Earth's atmosphere, expressed as a ratio relative to the path length vertically upwards (i.e. at the zenith), and it can be used to help characterise the solar spectrum after solar radiation has traveled through the atmosphere. Finally, there is the fill factor FF, which determines the maximum power deliverable by a solar cell, in conjunction with V_{oc} and I_{sc}. It is defined indeed as the ratio of the maximum power (mp) from the solar cell to the product of V_{oc} and I_{sc}. Graphically, it is the measure of the "squareness" of the solar cell and is also the area of the largest rectangle, which will fit the I-V curve, as illustrated below in Fig. 1.5.

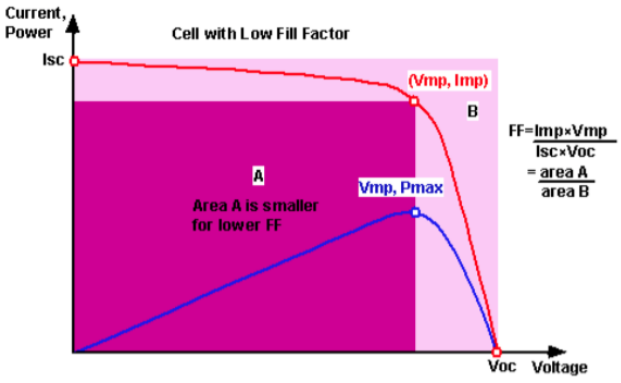

Figure 1.5: The graphical measure of the Fill Factor (FF) (http://pveducation.org/).

Therefore, the FF is commonly determined from measurement of the I-V curve and is

defined as the maximum power (subscript mp) divided by the product of V_{oc} and I_{sc}

$$FF = \frac{V_{\mathrm{mp}} I_{\mathrm{mp}}}{V_{\mathrm{oc}} I_{\mathrm{sc}}} \tag{1.3}$$

1.2 Geometrical, mechanical and functional description of PV modules

1.2.1 Crystalline Silicon Structures

The aspect that most affects the physical structure of a solid material is the configuration of constituent atoms or molecules together with the interatomic forces acting on them. If atoms and molecules are disposed repetitively in the three directions in the space, they give rise to a structure called crystalline solid or crystalline material. The arrangement of atoms in crystalline solids can be described by considering them as points of intersection of the lines of a three-dimensional mesh, called spatial lattice, that can be represented as an infinite sequence of points. In particular, silicon has the characteristic to solidify in the crystalline structure face centered cubic (CFC), which means that there is one atom in each corner of the cube and in the center of each face of the cube, as it can be seen in Fig. 1.6.

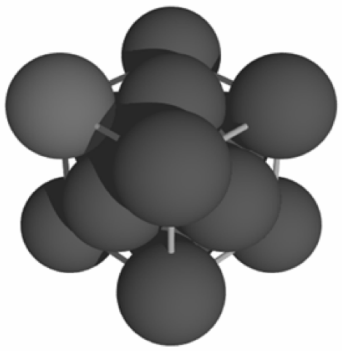

Figure 1.6: Silicon centered cubic (CFC) structure.

The crystallisation process of a metal takes place in several steps: at the beginning of the solidification there is the formation of stable nuclei (nucleation), while in a second time these nuclei grow giving rise to crystals. In each solidified crystal, atoms are arranged with regularity but can vary the orientation of each crystal with respect to the others. At the end of solidification crystals join together, although with different orientations, forming bonds between the grains (solidified crystals) limited to a certain number of atoms. The solidified metal that holds many crystals is said *polycrystalline* and surfaces between grains are called

grain boundaries. The number of nucleation sites influences the performance of metal materials: few sites give origin to a structure with large grains, many sites give rise to a fine grain structure. For this reason solidification of all metals and alloys of technologic interest are controlled and modified so that it is preferred to have a fine grain structure, since this type of structure determines the best properties of mechanical strength and uniformity of the finished products. Most of the crystalline materials are composed by many crystals (polycrystalline) but there are also materials in which there is a unique crystal (*monocrystalline*). In some cases, by acting on the manufacturing process it is possible, to obtain the same material both as mono and polycrystalline, such as silicon. In micro-electronic applications (i.e. chips of integrated electronic circuits) monocrystalline is needed because grain boundaries impede the flow of electrons in the formed devices. The photovoltaic cells, unlike the microcircuits, can tolerate within certain limits small structural imperfections, so that both mono and polycrystalline (less expensive to be produced) cells can be used.

1.2.2 Traditional rigid Silicon photovoltaic modules

It is possible to classify PV technologies into two main different classes according to the specific material employed as semiconductor in the production process and its own class of efficiency at turning solar light into electricity. The semiconductor materials of which photovoltaic cells can be made of are **wafer-based crystalline silicon** and **thin films**. The first one can in turn be further subdivided into two different sub-categories based on the morphology of silicon (Si): monocrystalline silicon, obtained slicing a single crystal of silicon (sc-SI) and polycrystalline silicon (mc-Si) from a block composed by several crystals of Si. In Fig. 1.7 it is presented the full productive chain of a mc-Si **wafer-based** PV system, starting from a raw piece of material that is cut in ingot and then rectified into square shape. Slicing these bricks with a high precision wafer machine, a thin wafer of mc-Si is then obtained; on them a potential junction is applied in order to build the PV cell, and an anti-reflective coating on the upper face is deposited, on which metal wire contacts are added. In order to link together cells of the same panel two main conductors are then placed, called busbars, orthogonally with respect to the direction of metal contacts. The task of these is to collect the electricity produced by cells and bring it to terminal clamps. The whole system is completed by a support structure on which the module is mounted on and some electronic equipments to regularise and to account produced electric current.

Starting with the analysis of the standard **rigid** PV modules, that is the most widely used in the PV dark, these are laminates composed of a 4 mm thick tempered front glass, a 0.166 mm thick layer of Si solar cells, encapsulated between two 0.5 mm layers of Ethylene Vinyl Acetate (EVA) polymer and a thin multilayered backsheet made of Tedlar/Aluminium/Tedlar 0.1 mm thick, as depicted in Fig. 1.8(b).

On their plane mono- or polycrystalline Si cells are separated by a thin amount of EVA in order to avoid mutual stresses due to thermic expansion/shrinkage imposed by external agents (i.e. heat radiated from the sun during cold season or sudden drop in temperature due to thunderstorm in the hot season). The efficiency of this kind of modules, that is the ratio of electric output over the incoming solar energy, stands usually between 15% and 20%. It is directly dependent on the quality of used materials and mainly on the accuracy achieved in manufacturing technology during the assembly, as well as on the temperature levels they

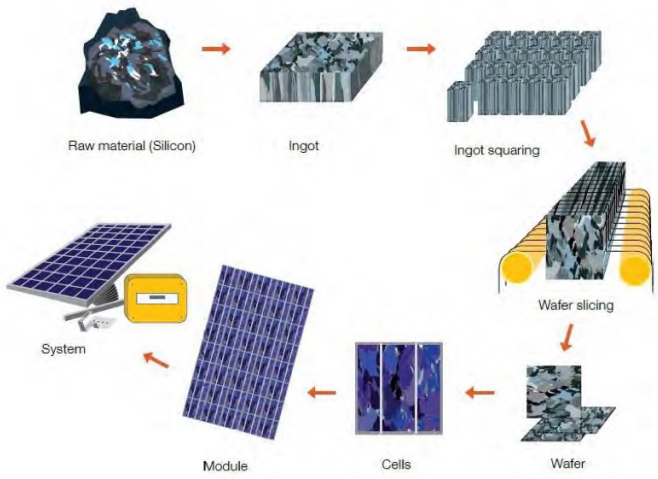

Figure 1.7: Production line of wafer-based crystalline Si systems.

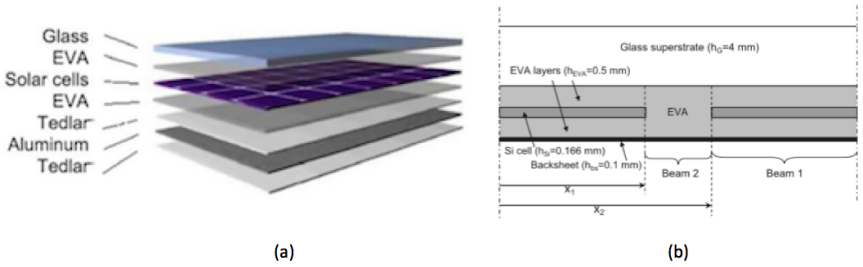

Figure 1.8: (a) and (b) the sketch of the composite stack of a standard PV module, made of crystalline silicon (Paggi et al. 2013).

reach under their working conditions [2]. These modules cover the largest part of the market (about 85%) with the warranty for a life-time between 25-30 years at maximum of the rated output, see. [3] for a comparison among various warranty specifics (Fig. 1.9).

The second constructive type of PV modules, the thin film, is realized by a extremely thin deposition of a semiconductor materials layer on a low-cost backing, such as glass, stainless steel or plastic having the sole role to provide support to the upper material, as it can be seen in Fig. 1.10.

Related to this production technology there are several sub-categories depending on the procedure applied for deposition and used materials for the semiconductors. As compared to the first typology, it requires lower production costs for the highly automation scheme that it is possible to use during manufacture processes, as shown in Fig. 1.11.

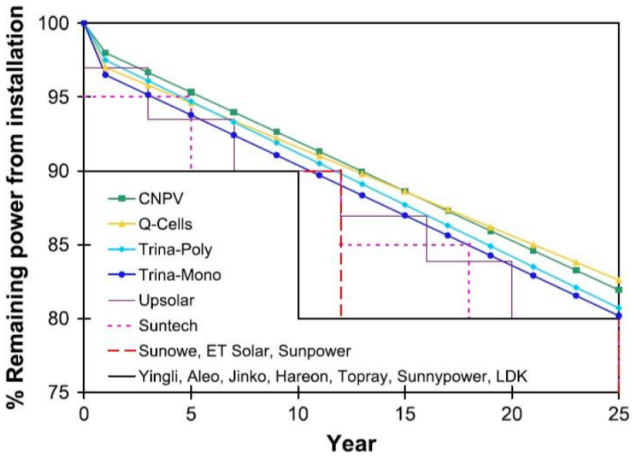

Figure 1.9: Comparison among warranty specifics declared by various producers of PV modules.

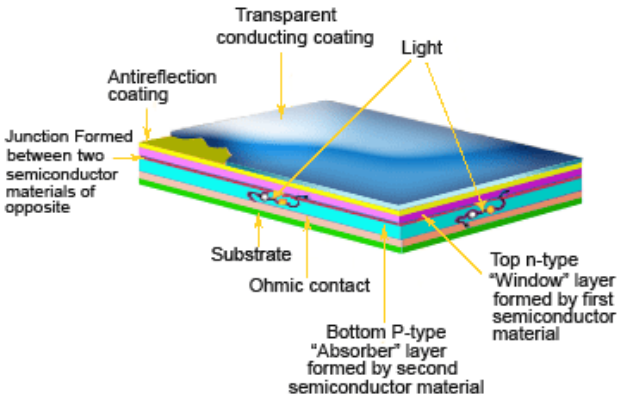

Figure 1.10: thin film PV module structure layout.

An additional feature is the possibility for thin films PV panels to be flexible and be installed in non-planar surfaces as are shelters and curved roofs. According with the great variety of sizes and possible colours they offer, thin films modules are easily integrated into building envelopes making less impactful their presence. The downside of this technology is the lower provided efficiency rates, no more than 13% in average, even though their efficiency does not

fluctuate so much with changes in temperature as for Si PV cells.

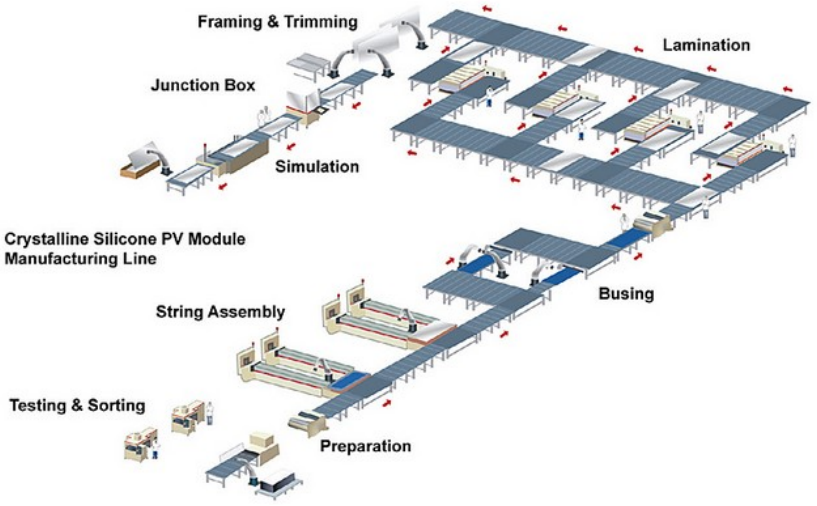

Figure 1.11: thin film solar module production line (courtesy of http://www.tsmc-solar.com/home).

1.2.3 Semi-flexible Silicon photovoltaic modules

A type of modules that lies in the middle between the two previously described types is the **semi-flexible** PV module. They have the same production process of the first one regarding sc-Si or mc-Si cells, but they can be partially flexible thanks to the lack of the glass front and Tedlar in the backsheet, both substituted in this case by thermoplastic polymeric thinner layers. The upper layer has the same functions as the glass, which are the capacity to let the light passing through and protect the lower EVA and Si layers from mechanical impacts, i.e. human-made damages and environmental agents. It is simple to understand that, in accordance with their own elastic modules, a polymeric layer can not offer the same resistance as glass. For this reason, cracking inside the Si layer, is now a concern. Semi-flexible PV modules are able to adapt their curvare in the main direction to the non-planarity of some surface: in particular can be placed on the curved deck of boats in the nautical field, lightly curved surfaces of cars' roofs in automotive field and also on irregular envelopes of some particular building as are mountain refugees (Fig. 1.12).

By analysing the layout of a semi-flexible panel, a typical stratigraphy is composed of a 0.265 mm PET (polyethylene therephthalate), 0.600 mm EVA, 0.166 mm Si mono- polycrystalline cell, 0.400 mm EVA and 0.345 mm PET or equivalent polymeric material to constitute the backsheet. This flexibility, allowed by the lack of rigid elements in the stratigraphy, lets the modules to be widely used for covering curved surfaces also being supported on the edges, without the need to be sustained over the whole area, but on the other hand under the point of

Figure 1.12: Applications of semi-flexible PV modules.

view of the resistance to mechanical impacts it produces a different behaviour as compared to traditional modules. In the latter in fact the upper glass layer represents the most rigid layer of the whole structure and the shock produced by an impact should damage this part and potentially the other layers could not be affected at all. In any case, it is not a complete defence for the optimal working condition preservation, since breaking of the glass and the consequent creation of a smeared cracking scenario could affect the transparency of the glass itself causing a decreasing functionality. In the worst case silicon cells could find themselves to be directly in contact with the external environment, giving rise to the possible generation of a hot spot which has the extreme consequence of firing the whole system. On the contrary, in a semi-flexible module, upper and lower layers made of a polymeric material are able to largely deform with respect to the Si one, so that the layer made with Si cells is the most brittle and subject to cracking, causing a rapid performance deterioration. When referring to shocks or damages, the field of analysis has not to be limited to the lifetime of panels under changing environmental conditions, but has to be analysed also the previous period regarding the stages of production and installation have to be analyzed, so that panels may present considerable damage also before their entry in service. Main damages during manufacturing may be due to poor precision in the manufacture and assembly of the different parts, in addition to using raw materials of poor quality, while defects during the installation phase are mainly due to carelessness (walkway above the panels) and awkward operations of transport and in the step of fix them to the support structure. In any case, the production process is not particularly difficult as can be understood from the following explanation of the assembly sequence. The thermoplastic material, which will become the matrix of the module, is at the beginning in the form of four different rolls of standard heights and desired thickness (Fig. 1.13).

By the use of a mechanic automatic cutter, from each roll a narrow element with an useful width for the realisation of the module is cut. At the end of the assembly procedure of the upper and lower part of the module, when different rolls become a unique structure after welding, it is necessary to procede to a precision trimming to remove exceeding parts. After this first operation a stratigraphy almost complete of the module is obtained . It is missing only the core part constituted by the photovoltaic cells, which by means of a second machine (or manually) are joined together by welding until you reach the desired size necessary to

Figure 1.13: Coupling of the different layer to compose the module.

realise an entire panel and to obtain the desired power in reached. A sketch of one machine used to weld each other the contacts of the silicon cells is shown Fig. 1.14.

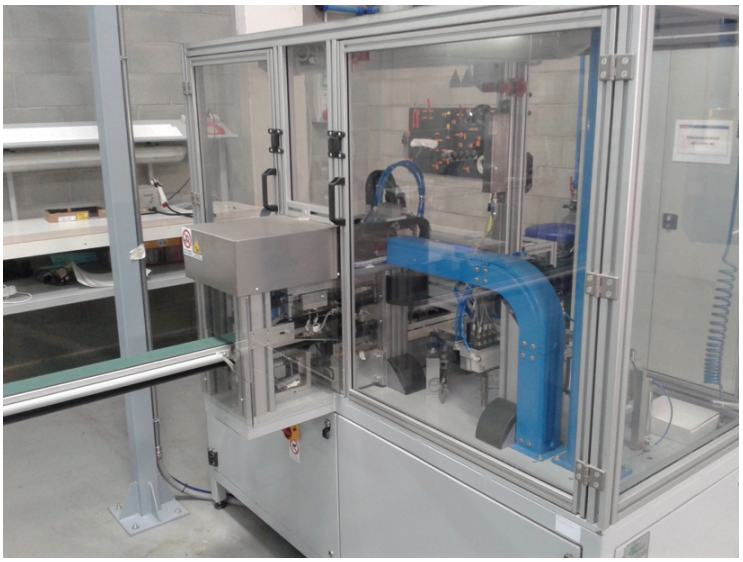

Figure 1.14: Automatic welding process for Si cells.

Once the welding of contacts on the Si cells is done, it is possible to proceed with the assembly of the whole panel, putting automatically or manually cells over backsheet and EVA and another layer of EVA over them, and the frontsheet. At this moment all the part needed to compose the whole panel are overlapped but not mutually fixed together. A press is used to create the pressure and bring the system to a certain temperature at which polymeric layers can partially merge and create a unique multilayer system that is then refined with a trimmer to remove the exceeding material. At the end of this procedure the panel is tested in a closed dark room where a special lamp is able to light the panel with an high intensity flash and through a voltmeter is measured the electricity produced by the panel, according to the request of the actual regulatory law.

1.3 The problem of durability and electric power losses

As it can be understood from the previous sections, it is necessary to constantly monitor a certain number of parameters in order to have a timely control the quality of production, intended as its capacity to produce an acceptable amount of energy from irradiation. It is normal to consider a certain natural decay in time due to degradation and problems of minor importance scattered among the various parts of the system, as presented in Fig. 1.9, but the core issue of our interest is to establish which could be the effect caused by external agents (mechanical actions mainly), in order to study a possible mathematic model to foresee a possible damaging process and control its evolution in time. The starting point in this field is to search for available Standards in order to ascertain what kind of specifics are given for the definition of performance rules for PV modules. According to achieved knowledge collected from them, strengths and weaknesses points are then analysed and possible improvements are proposed to make the criteria for classification performance more complete and reliable.

1.3.1 Existing standards and methods used to establish quality control for manufacturers and customers

In recent the years the use of photovoltaic technology by installing panels had a significant increase due to several factors. First among these, especially talking about Italy, is considered linked to the granting by the Government of an incentive for the installation of plants producing electricity from renewable sources like sun. In this way some people have decided to take advantage of this situation inserting photovoltaic panels particularly in the roofs of houses at the time of rebuilding of these same. The second reason, also partially linked with the first one, lies in the growing awareness among the population about environmental issues related to energy saving, choosing environmentally friendly solutions and limited environmental impact both visually and with regard to the production of waste. In fact, PV modules do not produce any kind of pollution or solid waste following their production cycle, unless the disposal of the panels themselves at the end of their life time. This last topic is nowadays one of the most nontrivial problems related to photovoltaics, so there are several options for recovery of materials composing the panel and several techniques to do so, but it is not the subject of this specification. According with the need to place the rules relating to the use of PV, the legislature sought to establish a set of parameters that can indicate clearly what

the rules have to be respected in the field. All requested standard are the result of laboratory tests and not on real-conditions in the field, developed under controlled conditions without the possibility that it may be varied the configuration. Ultimately, this type of information are prescriptive reason why is difficult to apply in non-standard conditions. In particular much of their attention has been paid in the classification of characteristics relating to materials and performance that PV modules must ensure in order to be sold. In this way, rules have been written related to production methods or tests to be conducted to certify their product and be authorised to place on the market of selling a certain own product. Nowadays, according to their typology, PV modules are certified by following qualification procedures presented both for Europe and North America by the International Electrotechnical Commission (IEC), the world's leading organisation for the preparation and publication of International Standards for all electrical, electronic and related technologies [4]. In particular IEC 61215 is for crystalline Silicon modules, while IEC 61646 contains all the standard parameters for thin film modules.

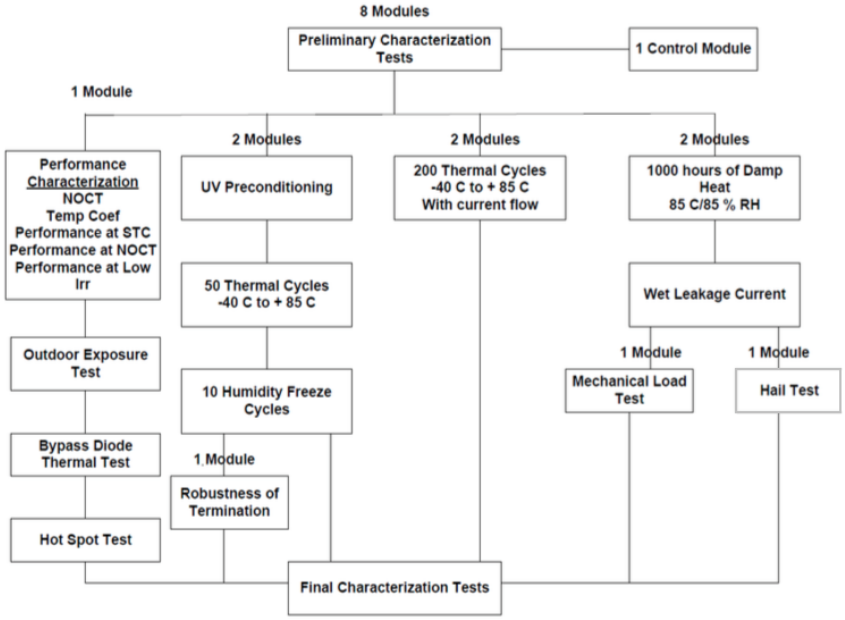

Figure 1.15: IEC 61215 available tests for modules certification.

For each specific item that has to be certified, the producer should test 8 samples, that will be subjected to several tests, according to the diagram in Fig. 1.15 [5]. Once the item passes all the different tests, it is certified and, according with the Standards, it means that it is well designed and it has an acceptable probability to survive in field conditions.

1.3.2 Weak points of the existing standards, possible improvement with an advanced analytical model

It is easy to understand, reading the previous section, that the regulatory framework loses sight of a large part of the aspects that would be useful to define to take also into account all aspects related to the durability of the modules in the real fields conditions. There is no Standards which considers the study of the crack inside the panel (in particular in the Si layer). For example, a micro-crack due to an impact could evolve in time due to cyclic phenomena of freezing and heating of the panel. Likewise, how the same micro-crack present in a semi-flexible module may grow as a result of wave movements due to a hypothetical action of wind or snow above the faces of the module is not investigated. As proposed by Wohlgemuth in [6], it is possible to find some limitation of those qualification tests, and consequently in the IEC 61215. In particular, at first thing, wear-out mechanisms are not identified and quantified, so that parameters to establish supposed lifetime concerned to mechanical performances are not given. Then, failure mechanisms for all climates and systems configurations are not addressed and difference between long and short lifetimes items are not established. It is possible to summarise what has been said and concluded that it is not of a settlement performance, not giving the possibility to adapt the methods for testing for search also on the long-term. In order to bypass the gaps left by the regulatory framework, the development of a mechanical model able to take into account peculiarities of the problem and provide a faithful description of its evolution it is crucial.

1.4 Formulation of a multiphysics model able describe the degradation phenomena in photovoltaic modules

The study of damage phenomena due to various causes taking place in time can be carried out by means of laboratory tests that reproduce in a short time scenarios in which the panel operates. This allows to obtain, with the necessary precautions, a projection of what would be on the module during its cycle of use, in a few hours obtaining a result equivalent to that after 25 years (useful average life of the panel). At the same time, the problem of damage needs to be addressed by virtual tests by preparing a numerical model that simulates the degradation process. This calculation procedure has to adapt to the peculiarities of the problem: first of all taking into account the multilayer material, concentrating to what could be the contribution of the individual layers as a function of their geometric and mechanical characteristics, as well as their mutual influence, bearing in mind that the attention will be particularly focused on the study of the behaviour of the silicon layer, the core center of the operation of the PV module. Then multi-physics aspects of the problem have to be taken into consideration, as is the presence of three different fields of forces acting on the model (mechanical, electrical and thermal), creating synergistic effects between them. Last, the opportunity to study the problem analysing mechanisms at different scales, from micro- to macro-scale, by applying different techniques depending on the level of detail under investigation.

1.4.1 Main novelties of the model: coupling of the effects deriving from different fields

The model proposed has the aim of studying the impact of cracking in the entire silicon cells, with the prerogative to discriminate impact of cracking on electric power degradation. The starting point is the coupling between elastic, electric and thermal fields by suitable mathematical relations able to describe impact of the the stress state on the electric response o the solar cell. Interactions and mutual influences between the elastic, thermal and electric fields are graphically expressed with the sketch in Fig. 1.16.

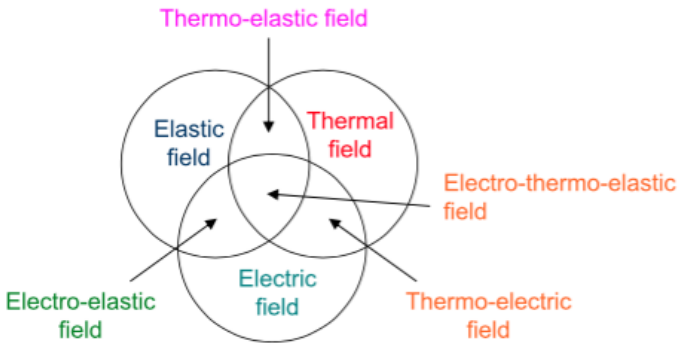

Figure 1.16: Interplay among the elastic, the thermal and the electric fields in PV modules.

The coupling between the elastic and the thermal fields can be described using the classic equations of the thermo-elasticity, accounting or the localized thermal resistance of cracks. Relations between electrical and thermal fields can be taken into account through a rigorous approach considering the coupling between electric and magnetic fields of the semiconductor by means of partial differential equations, according to the physics of the photovoltaic effect. As proposed in [7], it is also possible to address this issue in a simplified manner by considering an equivalent electric circuit representing both the cell and the whole module (see Fig. 1.17) which results of particular interest for industrial applications since it can be implemented in commercial software for mathematical problem solution (i.e. MatLab/Simulink) or implemented as a user defined routine in the finite element software.

In the circuit, the photovoltaic effect, due to the movement of electrons and holes in Silicon as a result of the so-called p-n junction, is considered as the source of a photonic current I_{ph}. The effect of the p-n junction is then modelled with a single diode, even if it is possible to use also a two diodes scheme [8]. The circuit is then completed with series and parallel resistances, where particular importance assumes the series resistance, which takes into account the bulk resistance of the semiconductor, contacts and interconnectors. The parallel resistance, also called shunt resistance, takes into account defects and the effect of impurities of the p-n junction with respect to an ideal one. As a result, the equation describing the current-voltage response of a PV module with Si cells connected in series can

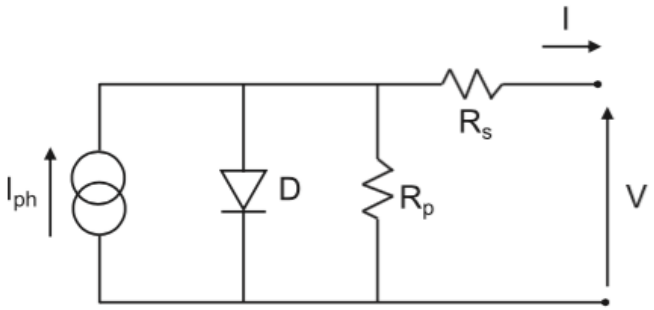

Figure 1.17: Single diode equivalent circuit model.

be expressed [7] according to Eq. (1.4):

$$I = I_{ph} - I_s \left\{ \exp\left[\frac{e(V/n + IR_s)}{a\kappa T} \right] - 1 \right\} - \frac{V/n + IR_s}{R_p} \tag{1.4}$$

where n is the number of cells, I_{ph} [A] is the photonic current, I_s [A] is the saturation current, V [V] is the module terminal voltage, I [A] is the module terminal current, R_s [Ω] is the parallel resistance, $e = 1.6 \cdot 10^{-19}$ [C] is the electronic charge, $a \cong 2$ is the diode quality factor for polycrystalline Silicon, $\kappa = 1.38 \times 10^{-23}$ [J/K] is the Boltzmann's constant, and T [K] is the ambient temperature. The main quantities in Eq. (1.4) depends upon the cell temperature T [7]:

$$I_{ph} = I_{ph}^{T=300}[1 + k_0(T - 300)] \tag{1.5a}$$

$$I_s = k_1 T^3 \exp\left(-\frac{eV_g}{\kappa T} \right) \tag{1.5b}$$

$$R_s = R_s^{T=300}[1 - k_2(T - 300)] \tag{1.5c}$$

$$R_p = R_p^{T=300} \exp\left(-k_3 T\right) \tag{1.5d}$$

where V_g [V] is the band gap voltage and the coefficients k_i are determined from experiments [7]. Under a mathematical point of of view, the proposed Eq. (1.4) is implicit and non linear, so that a solution for each voltage V has to be obtained by using a numerical solution method. In this case it is appropriate to use a Newton-Raphson iterative scheme to achieve quadratic convergence. After an appropriate manipulation Eq. (1.4) becomes:

$$f(I) = I - I_{ph} - I_s \left\{ \exp\left[\frac{e(V/n + IR_s)}{a\kappa T} \right] - 1 \right\} - \frac{V/n + IR_s}{R_p} = 0 \tag{1.6}$$

where the solution at the generic iteration $i + 1$ is attempted from the approximation at the

previous step i:

$$I_{i+1} = I_i - \left[\frac{\mathrm{df}}{\mathrm{dI}}\right]^{-1}_{I_i} \tag{1.7}$$

where the derivative df/dI is:

$$\frac{\mathrm{df}}{\mathrm{dI}} = 1 + I_s \exp\left[\frac{e(V/n + IR_s)}{a\kappa T}\right]\frac{eR_s}{a\kappa T} + \frac{R_s}{R_p} \tag{1.8}$$

The Equation (1.8) is iterated until convergence (i.e. $|I_{(i+1)} - I_i| < \mathrm{tol}$ with tol = 0.001) choosing $I_0 = I_{sc}$ as the starting point for the iteration procedure. As obtained in [9], the saturation current I_s is linearly dependent on the electrically inactive cell area. If the electric charge produced in a certain area cannot reach the two main conductors between cells (called busbars) this portion of the cell is called electrically inactive. In order to take into account this wffect, a damage variable expressed as the ratio between inactive area and total cell area is introduced for each cell:

$$D = \frac{A_{inactive}}{A_{total}} \tag{1.9}$$

By applying the same concept to an ensemble of cells (i.e. a PV module), the damage variable is the maximum of the damage variables of the various cells due to series connections. Taking into consideration this form of damage, the saturation and photonic currents undergo the following change:

$$I_s = I_s^{D=0}(1 - D) \tag{1.10a}$$

$$I_{ph} = I_{ph}^{D=0}(1 - D) \tag{1.10b}$$

Considering again the concepts previously expressed at in Section 1.1, and particularly Fig. 1.5 and the relation with the fill factor (FF), it is possible to evaluate the power-loss of a panel simply comparing its FF of the intact module and of the damaged one.

Moreover, after the analysis of the interplay between the elastic and the electric fields, it is of primary importance to study the coupling between the electric and the thermal fields, since the results of mutual effects are not negligible. Generally, the current intensity-voltage (I-V) curves move towards lower voltages by increasing the cell temperature. A temperature increase of 60°C arriving to a final temperature of 70°C reduces the open circuit voltage of about 20%. The study of the coupling between the elastic and the thermal fields is also important but is quite challenging to be modelled. From experiments in [10, 11], it was noticed with an infrared (IR) thermal camera that in a micro-cracked cell there is a local increase of operating temperature near cracks. At continuum level, this evidence can be modelled by considering an additional thermal resistance of micro-cracks with respect to the situation of perfect bonding. The relation between the thermal flux q normal to the interface and the temperature jump g_T across the crack faces can be implemented with an interface constitutive law:

$$q = -k_{int} \cdot g_T \tag{1.11}$$

where k_{int} represents the constant conductivity of the interface according to the Kapitza model, derived from nanoscale applications [12].

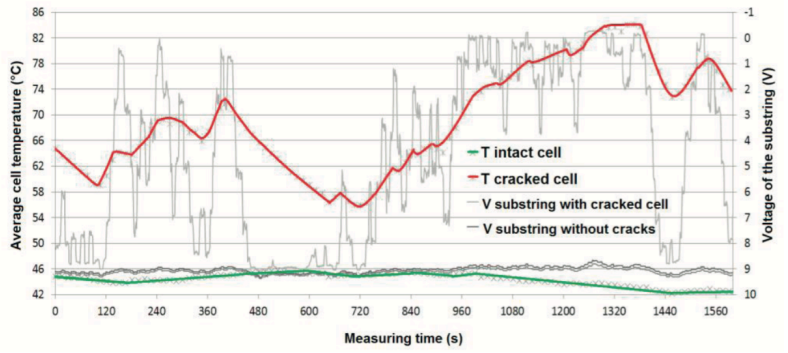

Figure 1.18: Cell temperature and voltage of a substring with a micro-cracked cell vs. measuring time, showing a highly oscillating response adapted from [13].

From monitoring of a micro-cracked cell with a relevant area potentially electrically inactive, the average cell temperature is not constant during the monitoring time (see Fig. 1.18 from [13]). In a comparison with the intact cell, the temperature is higher and strongly oscillating, while the output voltage of the string oscillates from 1V to 9V. The underlined behaviour is the confirmation that the presence of a micro-crack does not produce a complete the electrical insulation across its faces, but it is sill able to partially conduct heat flux and electricity. A possible hypothesis is that recovery of electrical response (self-healing) is the result of contact closure of the crack faces due to thermo-elastic effects. Hence, it is necessary to formulate a thermo-mechanical model to simulate how environmental conditions can promote power-loss due to the combined action of heat conduction and transfer of mechanical tractions. In [14, 15] an approach based on a cohesive zone model (CZM, whose general outline [16] will be detailed in Chapter 4). This apporach can establish a correlation between normal (Mode I) and tangential (Mode II) cohesive tractions and the relative opening and sliding displacements measured at the crack faces. According to atomic potentials principle, it is possible to select several shapes for the CZM depending on the failure criterion of materials. For a Mode I problem, CZM are characterised by the peak cohesive traction, $\sigma_{\max}$, and the corresponding fracture energy, G_{IC}, which is the area under the CZM curve. The last notable point is g_{nc}, a critical separation value corresponding to the creation of a stress-free crack. Some typical shapes of CZM models are shown in Fig. 1.19, in which linear or bilinear softening are usually selected for brittle materials, whereas trapezoidal or bell-shape CZM are used for more ductile fracture.

As proposed in [17, 18], the CZM formulation for mechanical tractions can be extended by taking into account also thermo-elastic contributions (thermo-mechanical CZMs), by including an equation relating the thermal flux across the crack faces to the temperature jump of the type (1.11). A different approach to formulate a thermo-mechanical CZM is based on contact mechanics principles as in [14, 15], where the temperature jump at the interface

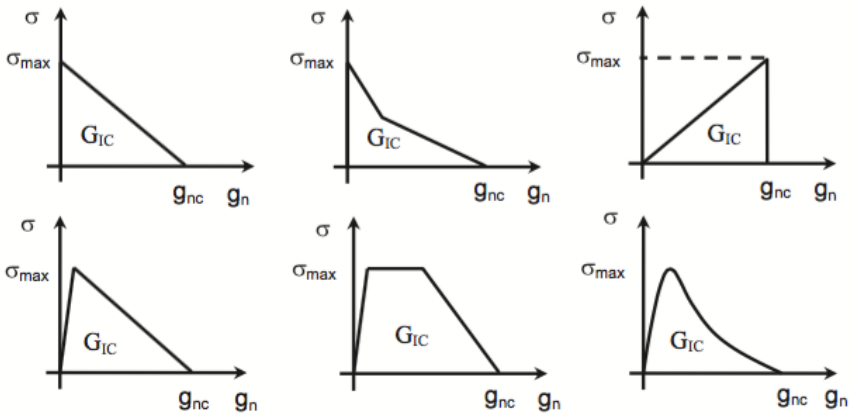

Figure 1.19: Comparison of different CZMs trends available in the literature for brittle and ductile fracture.

between two materials takes place due to rough cracks boundaries and imperfect contact. The contact conductance due to roughness is proportional to the contact stiffness, as asserted in the fundamental theorem by Barber [19]. In this way, it is possible to estimate the interface contact conductance directly from the solution of the normal contact problem, with the need to formulate a special constitutive relation for the thermal contribution. Considering that contact stiffness as dependent on the pressure at the interface, a a separation-dependent interface contact conductance is obtaining [20]. Following the sketch in Fig. 1.20 (from right to left), a compressive contact pressure p (taken as negative value) is applied to the rough surface, ranging from zero at the first point of contact, to the full contact pressure p_{FC}, with a reverse process in case of fracture, where the full contact regime corresponds to an intact interface. On the opposite with respect to contact mechanics, to separate the two bodies and create a stress free crack, a tensile pressure (now considered as positive) with a module value equal to p_{FC} has to be applied. At the end of the cracking process, the produced rough surface tends to become the microscopically rough stress-free crack (from left to right in Fig. 1.20) Consequently, the Mode I cohesive traction σ which, by definition, is the traction opposed to crack opening, considered as the opposite of the applied contact pressure p corresponding to the same separation, can be evaluated for any mean plane separation g_n from the solution of the contact problem.

The most suitable pressure-separation relation for this case is the exponential model proposed by Greenwood and Williamson [21], with an exponential distribution of asperity heights whose root mean square is 'rms' and considering an exponential decay of the cohesive tractions for $g_n > l_0$.

A separation with a g_{nc} value means that a stress-free crack is formed, so that a cut-off to the cohesive tractions corresponding to the formation of a stress-free crack is introduced for values higher than g_{nc}. Moreover, also a tangential gap g_t has to be taken into account to model the weakening effect of Mixed-Mode deformation. The resulting expression for the

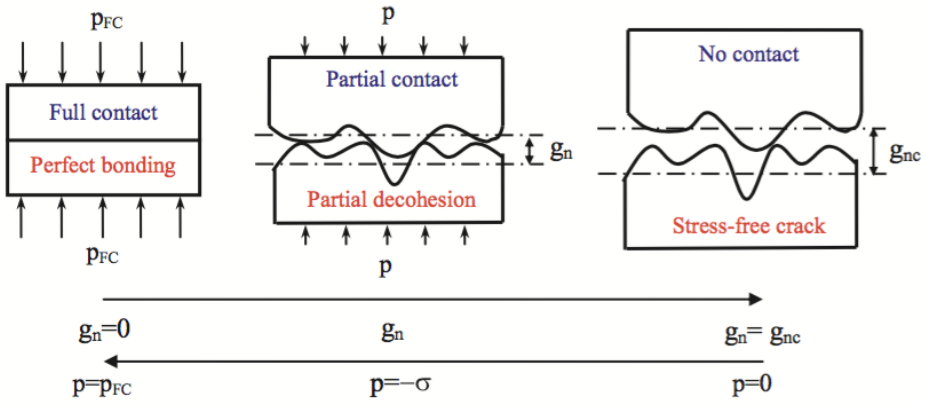

Figure 1.20: Analogy between contact mechanics and fracture mechanics for stress-free crack production.

normal cohesive traction is the following:

$$\sigma = \begin{cases} \sigma_{max} \exp\left(\dfrac{-l_0 - g_t}{rms}\right)\dfrac{g_n}{l_0} & \text{if } 0 \le \dfrac{g_n}{rms} < \dfrac{l_0}{rms} \\ \sigma_{max} \exp\left(\dfrac{-g_n - g_t}{rms}\right) & \text{if } \dfrac{l_0}{rms} \le \dfrac{g_n}{rms} < \dfrac{g_{nc}}{rms} \\ 0 & \text{if } \dfrac{g_n}{rms} \ge \dfrac{g_{nc}}{rms} \end{cases} \tag{1.12}$$

with a similar relation for the Mode II tangential cohesive tractions

$$\tau = \begin{cases} \tau_{max} \exp\left(\dfrac{-l_0 - g_n}{rms}\right)\dfrac{g_t}{l_0} & \text{if } 0 \le \dfrac{g_t}{rms} < \dfrac{l_0}{rms} \\ \tau_{max} \exp\left(\dfrac{-g_t - g_n}{rms}\right) & \text{if } \dfrac{l_0}{rms} \le \dfrac{g_t}{rms} < \dfrac{g_{tc}}{rms} \\ 0 & \text{if } \dfrac{g_t}{rms} \ge \dfrac{g_{tc}}{rms} \end{cases} \tag{1.13}$$

while for the thermal conductance:

$$k_{int} = \begin{cases} \dfrac{1}{\rho_{int}} & \text{if } 0 \leq \dfrac{g_n}{rms} < \dfrac{l_0}{rms} \\ \dfrac{2\sigma}{\rho_{int} E_{int} rms} & \text{if } \dfrac{l_0}{rms} \leq \dfrac{g_n}{rms} < \dfrac{g_{nc}}{rms} \\ 0 & \text{if } \dfrac{g_n}{rms} \geq \dfrac{g_{nc}}{rms} \end{cases} \tag{1.14}$$

where the resistivity ρ_{int} and the Young's modulus E_{int} of the interface can be evaluated as $\rho_{int} = \rho_1 + \rho_2$ and $E_{int} = \left[\frac{(1-\nu_1^2)}{E_1} + \frac{(1-\nu_2^2)}{E_2}\right]^{-1}$, the the subscripts refer to the two materials separated by the interface and ρ is the Poisson's ratio.

1.4.2 Development of the mechanical part of the model: A multi-scale approach

The final goal of this study is the formulation of a model able to study the cracking process occurring inside PV modules starting from the analysis of the main causes which occur in the formation and propagation of the damaged scenario. The mathematical formulation of the problem is supported by several laboratory tests conducted on PV modules both with mono- and poly-crystalline silica, useful to compare results obtained numerically with real cases of crack propagation, for benchmark for further research. The approach chosen here to investigate the behaviour of the Si layer, is a multi-scale approach where the same problem is studied through the application of theories for different scales, starting with the theories usually adapted at the continuum level up to the atomic scale with Molecular Dynamics Theories. In each of those models, some features are taken into consideration, in an equilibrium formulation of force for energies involved at each scale, while others are neglected because not significative at that level of analysis. Some of the developed methods are then implemented in a software for Finite Element Analyses to study specific scenarios in which one of the main causes of degradation in the Si layer are investigated.

Chapter 2

State-of-the-art: continuum approaches to fracture

The starting point for the study of fracture phenomena in Silocon cells is to provide a historical and conceptual background of the different methods available, in order to describe the techniques used in this study. In this chapter a comparison between several computational methods based on continuum models is proposed. Approaches are divided in linear and nonlinear models, depending on the type of material, that is directly related to its constitutive law. Brittle and quasi-brittle materials are characterised mainly by brittle structure, while fracture in materials able to perform a plastic deformation is often approached through nonlinear models, most of them based on a nonlocal study of cracking.

2.1 Computational methods for fracture in quasi-brittle materials

In materials science, brittleness is associated to those materials, subject to stress, which break without significant strain, absorbing generally a small amount of energy before cracking, even those of high strength. Brittleness of a material may also depend on temperatures, so that it is possible the same material should be ductile at high or room temperature and brittle for low temperatures (i.e. glass or steel). From the solids mechanics point of view, a material can be defined brittle if it fails when there is little or no evidence of plastic deformation before failure. One possible test is to match the broken halves, which should fit exactly due to the lack of plastic deformation.
First of all, there are three different ways to apply a force and enable the propagation of the crack: in the Mode I (also called opening mode) a tensile stress normal to the plane of a crack is applied, while in the Mode II (also called shearing mode) a shear stress acts parallel to the plane of the crack and perpendicular to the crack front. Lastly, in the Mode III (also called tearing mode), a shear stress exerts its action parallel to the plane of the crack and parallel to the crack front. In many applications materials fail for a combined action, named Mixed Mode.

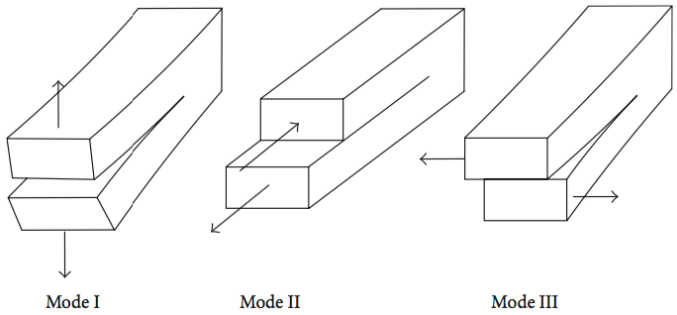

Figure 2.1: Different fracture modes.

Fracture in brittle materials can be modelled by Linear Elastic Fracture Mechanics (LEFM). Brittle materials are characterised by linear elastic material behaviour in the bulk and a small fracture process zone. However, LEFM cannot be used when the failure process zone is of the same size order of the specimen, so it follows that the relative size of the fracture process zone (l) with respect to the smallest critical dimension of the structure (D) is important for the choice of the fracture model [22, 23]. A valid application of LEFM is for $D/l>100$, while for $5<D/l<100$ a nonlinear quasi-brittle approach should be invoked [23]. The size of the fracture process zone is of the order of the characteristic length:

$$L_{ch} = \frac{EG_f}{f - t^2} \quad \text{or} \quad L_{ch} = \frac{EG_f}{(1-\nu^2)f - t^2} \tag{2.1}$$

where E is the modulus of elasticity, ν is the Poisson's ratio, G_f is the fracture energy and f_t denotes the tensile strength of the material. Carpinteri [24] introduced a nondimensional brittleness number $s_E = g_f/(f_t b)$ where b is a characteristic geometry length scale of the specimen. The distance between the notch and the upper boundary of the beam is b. If the process zone is small compared to b, the failure is brittle and LEFM can be applicable, otherwise in the absence of plasticity we may call failure as quasi-brittle.The stress-strain curve for quasi-brittle materials is characterised by a drop of the stress after the peak stress is overcome.

The use of strain-softening material models leads to an ill-posed boundary value problem (BVP), creating material instabilities. In order to solve the issue, some regularisation techniques such as higher order continuum models, gradient based models, Cosserat continuum, nonlocal models, viscous models or cohesive zone models can be invoked. All these regularisation methods introduce a characteristic length scale into the model. Namely, the local character of the deformation is lost, and fracture is "smeared" over a certain domain involving several elements, so that a very fine mesh has to be used in orde to resolve the crack. In addition, the different length scales (of the structure and the characteristic length) may significantly increase the computation cost.

2.1.1 Linear elastic fracture mechanics

For linear fracture mechanics, the **Griffith's** energy criterion for crack propagation will be provided, along with, the definition of the stress intensity factor, the Irwins criterion and the relations between these methods. Crack propagation phenomena in brittle materials can be studied both with energy (global) terms through the Griffith's theory and in tensional (local) form using Irwin's theory. The approach proposed by Griffith dates back to 1920, providing the answer to the problem of brittle material strength evaluation, that was always lower than the theoretically supposed one. Griffith was able to demonstrate that this mismatch was due to stress concentration at the crack tips within the material. Considering a sheet of perfectly brittle material loaded uniformly under tension, and introducing a hole in the middle of it, flow lines are forced to avoid the hole so that a concentration of stress at the end of the hole occurs, becoming mores severe the more the shape of the hole tends to a crack. Far away enough from the hole, the stress distribution seems not to be perturbed by the defect. Analytical solution for the determination of stresses at the crack tip were proposed by Inglis as the limit case of the elliptic hole solution. Starting from this point, Griffith deduced that classical resistance criterion could not be applied for cracked brittle materials, because at the end of the notch the stress tends to infinity regardless of the applied load. Moreover, he observed that for the crack nucleation or propagation, it is necessary to provide a certain energy per unit area, so as to overcome the resistance of cohesion between the molecules on the two sides of the crack. At this stage, this energy is treated as a constant property of the material while in general it may depend on the evolution of cracking process. Considering a plate where b is its thick and a is the length of the crack under a certain fixed load, the energy needed for the propagation of the crack of a infinitesimal quantity da is:

$$\mathrm{d}W^F = G_f \, \mathrm{d}a \times b \tag{2.2}$$

where G_f is the specific energy release. The general Griffith's criterion can be summarised as follows:

$$\begin{array}{llll} G < G_f & \mathrm{d}a = 0 & \mathrm{dK} = 0 \longrightarrow & \text{No propagation (stable)} \\ G = G_f & \mathrm{d}a > 0 & \mathrm{dK} = 0 \longrightarrow & \text{Quasi-static propagation} \\ G > G_f & \mathrm{d}a > 0 & \mathrm{dK} > 0 \longrightarrow & \text{Dynamic propagation (unstable)} \end{array} \tag{2.3}$$

As it can be noticed, if the available energy is less than what is needed for crack propagation the structure stays stable, while if the available energy is equal to the needed one, the crack can statically propagate (negligible inertial forces). Finally if the available energy overcomes the needed one, the structure becomes unstable and the crack can propagate dynamically. The core problem is to determine the amount of available energy dW^R for crack propagation. Griffith applied the energetic criterion for the evaluation of propagation of a crack in a infinite plate under uniform stretch engraved from a crack of length 2a (Fig. 2.2). He demonstrated that specific energy released in a plate with unit thickness under uniform tensile stress σ, due to a crack length 2a, is:

$$G = \pi a^2 \frac{\sigma^2}{E^*} \tag{2.4}$$

where E^* is equal to Young's module E in a plane stress case while it is equal to $E/(1-\nu^2)$ in a plane strain case.

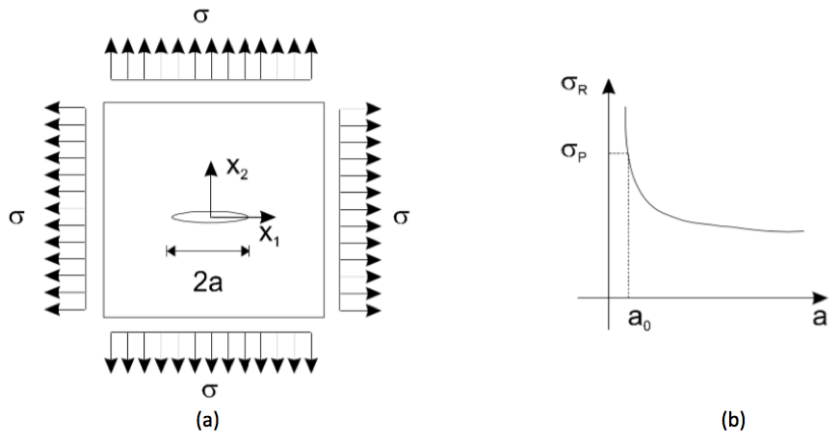

Figure 2.2: (a) Plate subject at infinite to a uniform tensile stress; (b) rupture stress as function o the crack length obtained with Griffith's principle.

From Eqs. (2.3) that expresses the quasi-static propagation condition and from Eq. (2.4) it is possible to achieve the formulation of the cracking criterion and the trend between the rupture stress and the semi-length of the crack a:

$$\sigma_R = \sqrt{\frac{E^* G_f}{\pi a}} \tag{2.5}$$

From the inversion of Eq. (2.5) the critical semi-length a_R of the crack in correspondence of which there is propagation for a determined applied stress σ can be determined. From Fig. 2.2 it can be noticed that, when the extension of a tends to zero the material resistance tends to infinity, while on the contrary when the value of a tends to infinity, the corresponding criterion stress vanishes. If an intrinsic resistance σ_p of the material is supposed to exist, then can be a semi-length a_0 equal to:

$$a_0 = \frac{1}{\pi} \frac{g_f E^*}{\sigma_p^2} \tag{2.6}$$

corresponds to the value of a characteristic defect such that the yield strength in tension precedes the propagation of the defect.

Thirty years later, the LEFM theory was rephrased by **Irwin** (1957) in terms of tensile stress at the crack tip, showing up the correspondence between his approach and the one proposed by Griffith and based on global energy. Irwin established that a crack is able with its presence to modify the stress field of a body only in the zone near to the crack tip. Moreover, Irwin concluded that dimensions, shape and boundary conditions have no influence on the

direction of the stresses but only on their intensity. To calculate the stress concentration that occurs at the tip of a crack in an elastic body, it is necessary to mathematically solve the corresponding partial differential equations with the presence of a crack. The problem solution is not trivial and the exact solution in closed form can be achieved only for simple geometries, as two-dimensional infinite solids subject to Mode I, II or III. For-example, solutions related to the Mode I are provided below. A two-dimensional solid under a plane stress or strain condition is considered, as in Fig. 2.3 in which $x_1 - x_2$ is an orthogonal reference system with x_1 coinciding with the crack axis, so that the stress field at the tip of the crack can be defined as follows:

$$\sigma_{11} = \frac{K_I}{(2\pi r)^{1/2}} \cos\frac{\theta}{2}\left(1 - \sin\frac{\theta}{2}\sin\frac{3\theta}{2}\right) \tag{2.7}$$

$$\sigma_{22} = \frac{K_I}{(2\pi r)^{1/2}} \cos\frac{\theta}{2}\left(1 + \sin\frac{\theta}{2}\sin\frac{3\theta}{2}\right) \tag{2.8}$$

$$\tau_{12} = \frac{K_I}{(2\pi r)^{1/2}} \cos\frac{\theta}{2}\left(\sin\frac{\theta}{2}\cos\frac{3\theta}{2}\right) \tag{2.9}$$

where r and θ are the local polar coordinates with origin in the tip $x_1 = \pm a$ of the crack and K_I is the stress intensity factor related to Mode I. Under the hypothesis of plane strain, σ_{33} can be evaluated as:

$$\sigma_{33} = \nu(\sigma_{11} + \sigma_{22}) \tag{2.10}$$

It is appropriate to clarify that the stress field components predicted in such a way are accurate only near the crack tip, i.e. in case of a r/a ratio tending to zero such that stresses are characterised by an asymptotic trend with singularity $r^{-1/2}$. The power $-1/2$ and the functions of polar variable θ are independent of the conditions at infinity but only on the boundary conditions on the two sides of the crack. The stress field is univocally determined by the stress intensity factor K_I in turn function of the crack length and, for finite size plates, also of boundary conditions. Physical dimensions of K_I are $[\mathrm{F} \cdot \mathrm{L}]^{-3/2}$. For the case examined above, K_I is given by the expression:

$$K_I = \sigma\sqrt{\pi a} \tag{2.11}$$

In general, the stress path is asymptotic in all cracked bodies, independently from their geometry, while the stress intensity factor depends on the geometric configuration, by the boundary conditions and by a characteristic dimension of the body. The displacement u_2 in the direction x_2 of the points along the face of the crack ($\theta = \pi$) is characterised by a parabolic curve having a tangent parallel to the axis x_2 and it is given by the following formula:

$$u_2(\theta = \pi) = \frac{2}{E^*}\sqrt{\frac{r}{\pi}}K_I \tag{2.12}$$

Substituting the expression of K_I, given by Eq. (2.11) into (2.12), the opening of the crack, COD (crack opening displacement) is obtained as the sum of the displacement of the top face and bottom face of the crack, i.e.:

$$w = u_2^+ - u_2^- = \frac{4\sigma}{E^*} r \tag{2.13}$$

and at the center of the crack ($r = a$) the maximum opening of the crack is obtained:

$$w = \frac{4\sigma}{E^*} a \tag{2.14}$$

For a body subject to different loading that generate different ways of fracture, the stress field at the crack tip can be determined using the superposition principle applied to the displacement and stress fields induced by each mode of fracture.

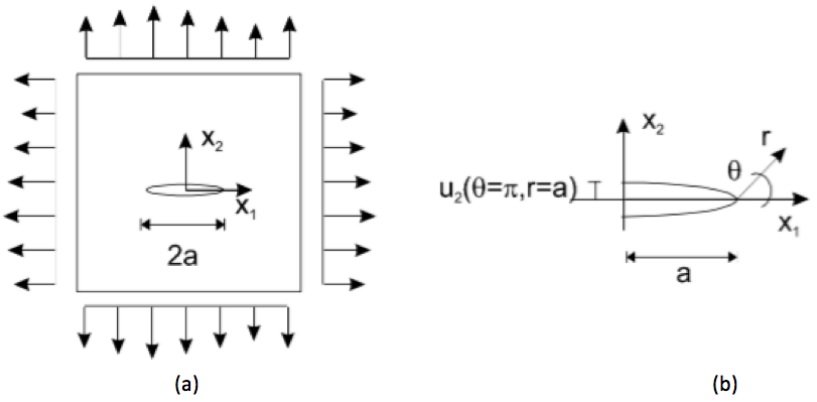

Figure 2.3: (a) Plate with uniform deformation to infinity ; (b) detail of the crack tip.

The Irwin's criterion for fracture of brittle materials can be now introduced. According to this criterion, the crack propagates when the stress intensity factor K_I that defines the stress field reaches a critical value K_{Ic}. The critical stress intensity factor K_{Ic}, also called "fracture resistance" (fracture toughness), is a material constant. In Mode I, the criterion is expressed by the following formulas:

$$\begin{aligned} K_I < K_{Ic} &\longrightarrow \text{No propagation (stable)} \\ K_I = K_{Ic} &\longrightarrow \text{Quasi-static propagation} \\ K_I > K_{Ic} &\longrightarrow \text{Dynamic propagation (unstable)} \end{aligned} \tag{2.15}$$

In 1957 Irwin demonstrated the perfect equivalence between the global energy and the local stress based formulations for the study of crack propagation into brittle materials. He establish a correlation between the G release energy, equal to the total potential energy variation of the system corresponding to a unit increase in the crack length and stress intensity factor $K_{I,II,III}$ which defines the stress field at the crack tip. Irwin took under consideration

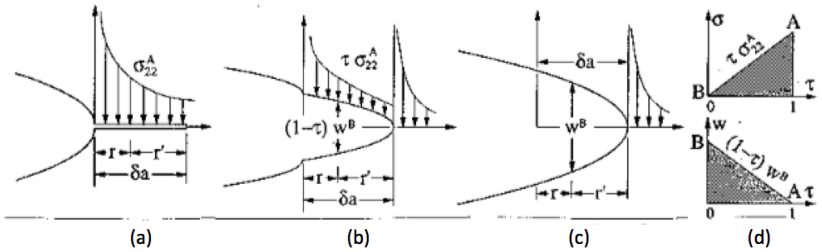

Figure 2.4: Proportional reduction of reclosure tensions.

the particular case of an infinite plate with an initial notch of length $2a$ and displacements imposed on the boundary, with a perfectly brittle material, in a plane stress of strain condition. Considering the fracture Mode I let the crack proceed of an infinitesimal quantity da in the direction of the x_1 axis. The initial (a) and final (c) conditions are represented in Fig. 2.4. The state (a) is obtained introducing a notch with length da at the tip of the existing crack, that is maintained closed by an external reclosure stress σ^A_{22} equal to σ_{22} effectively present in the state (a). The system at the end can reach the state (c) where the previous notch with length da is completely opened by a crack where displacements are equal to u^B_2. Since da is an infinitesimal quantity, it can be assumed that for $x_1 \in [a,\, a + \mathrm{d}a]$ the stress field σ^A_{22} and the displacement field u^B_2 can be given by Eq. (2.8) and Eq. (2.12), valid only in the vicinity of the crack tip. Intermediate states as the one represented in Fig. 2.4(b) are characterised by reduced reclosure stress equal to $\tau\sigma^A_{22}$ where τ is a scalar parameter equal to 1 in the state (a) and equal to 0 in the final one (c). At the same time, the crack opening should vary linearly from a null value to the final displacement distribution u^B_2 so that in a intermediate stage the displacement field is equal to $(1-\tau)u^B_2$. The energy release G can be calculated as the variation of the total potential energy associated to the crack size increase of length da. The elementary work done per unit area at a given point by the reclosing stress σ_{22} when the crack opening is du_2 is given by -$\sigma_{22} \cdot \mathrm{d}u_2$ where the negative sign is due to the opposite orientation between stress and displacement. The elementary work per unit area of an intermediate stage where the parameter τ has a dτ variation is given by the expression:

$$\mathrm{d}\left(\frac{dW}{b\,dr}\right) = -\left(\tau\sigma^A_{22}\right)\mathrm{d}\left[(1-\tau)\,u^B_2\right] = -\tau\sigma^A_{22}\left(-\mathrm{d}\tau u^B_2\right) \tag{2.16}$$

where b is the thickness of the body. Integrating (2.16) with respect to τ, the total work per unit area passing from state (a) to state (c) is obtained:

$$\frac{\mathrm{d}W_{A-B}}{\mathrm{b\ dr}} = \sigma^A_{22}u^B_2\int_1^0 \tau\mathrm{d}\tau = -\frac{1}{2}\sigma^A_{22}u^B_2 \tag{2.17}$$

so that an integration of the Eq. (2.17) with respect to r gives:

$$U_B - U_A = W_{A-B} = -\frac{1}{2}b\int_1^{\delta a}\sigma^A_{22}u^B_2\mathrm{d}r \tag{2.18}$$

From Eq. (2.8), setting $\theta = 0$, the stress field σ_{22}^A is:

$$\sigma_{22}^A = \frac{K_I^A}{\sqrt{2\pi r}} \tag{2.19}$$

where r has its origin in the crack tip in the state A, while the displacement field u_2^B can be obtained by Eq. (2.12):

$$u_2^B = \frac{2}{E^*}\sqrt{\frac{r^*}{\pi}}K_I^B \tag{2.20}$$

where $r^* = \mathrm{d}a - r$ in Eq. (2.20); introducing Eqs. (2.19) (2.20) in Eq. (2.18), we obtain:

$$\mathrm{d}U = -b\frac{2K_I^A K_I^B}{\pi E'}\int_0^{\mathrm{d}a}\sqrt{\frac{\mathrm{d}a - r}{r}}\mathrm{d}r = -b\frac{K_I^A K_I^B}{\pi E'}\mathrm{d}a \tag{2.21}$$

Keeping into consideration that for fixed boundary conditions the relations $G\ \mathrm{d}a \cdot b = -\mathrm{d}U$ and $K_I^B \to K_I^A$ for $\mathrm{d}a \to 0$ can be obtained the relation between energy release and the Irwin'a stress intensity factor can be derived:

$$G = \frac{K_I^2}{E^*} \tag{2.22}$$

and in the same way for Mode II and Mode III. The relation between critical fracture energy G_f and the critical stress intensity factor K_{Ic}, for Mode I can be also be defined in a similar way:

$$G_f = \frac{K_{Ic}^2}{E^*} \tag{2.23}$$

This equation expresses the equivalence between the criterion of crack propagation based on the local field stress proposed by Irwin and the global energy criterion proposed by Griffith [25].

2.1.2 Nonlinear Fracture mechanics

A brief description of the most common approaches for the study of nonlinear fracture is outlined in this section. In contrast to LEFM, a non perfectly brittle beahavior of the material under fracture is assumed, so that a coexistence between cracking evolution process and increasing of stress field near the crack tip can exist, so that propagation of damage is conditioned by both these phenomena. While LEFM supposes that cracking process is localized at the tip of the crack, in NLFM (Non Linear Fracture Mechanics), a process zone near the crack tip, with nonlinear traction-separation relations is supposed to exist. Hence, propagation of the crack is ruled by the stress level into the bulk. Even in the field of NLFM, cracking process can be studied both through a tensional approach (local), and in a global way applying energy approaches as is the "R-curves" theory.
In the LEFM theory, cracking process is concentered at the tip of the crack. In the real case, there is a zone all around the crack tip where there is a diffused cracked scenario and the

material is characterised by closing tractions due to imperfections, material aggregates and inclusions that are opposing to the propagation of the macro-crack. In that zone, called *process zone*, microscopical non linear and dissipative phenomena take place. In case the process zone is small as compared to real crack size, all LEFM concepts are completely valid and can be applied. On the contrary if the dimensions of the process zone are comparable with the specimen size, then this has to be carefully modelled. The process zone can be simulated by imposing a distribution of cohesive tractions behind the crack tip. This scheme was firstly introduced by Dungdale [26], Baremblatt [27] and more recently with some modifications by many researchers as Hillerborg [28] with the name of Fictitious or Cohesive Crack Model.
The cohesive fracture model for Mode I, where the whole process of cracking is localized in the process zone and the material is characterized by a stress-strain softening law is now described. According to Fig. 2.5 the point separating the real crack from the fictitious one is called "real crack tip" while the point which separates the process zone from the intact material is called "fictitious crack tip". The hypothesis of the cohesive model are the following:

- The process zone begins growing when the maximum principal stress reaches the tensile strength of the material, f_t, and it propagates in the orthogonal direction with respect to the principal stress.
- The material in the process zone is partially damaged but it is still able to transfer stress thanks to microscopic processes such as friction, adhesion of fibres and so on.
- The behaviour of the material is linear-elastic out of the process zone.
- The model is well posed if there are no points out of the process zone for which the principal stress reaches the maximum traction strength of the material.

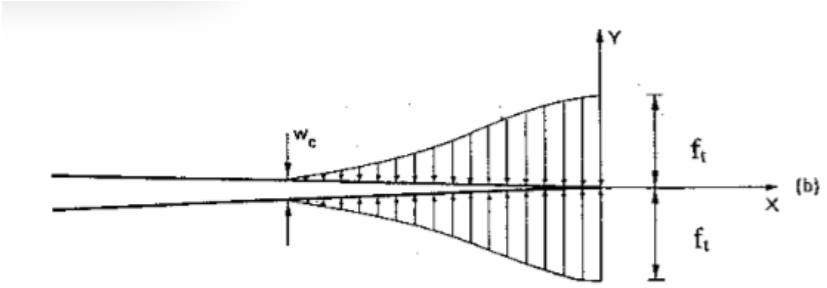

Figure 2.5: Cohesive tractions in the process zone.

Cohesive tractions acting in the process zone are defined as decreasing functions of the distance w between the two sides of the crack. Assumptions usually adopted in models are the following:

- The softening law linking cohesive tractions σ and displacements w is linear, bilinear (typical for concrete) or exponential;

- There is a critical value for displacement (w_c) for which larger displacements make the material not able to transfer stress any longer.

- The area over the curve σ - w is equal to the fracture energy G_f.

Another important issue is the determination of the process zone size: it is possible to obtain an estimation through the method proposed by Irwin (1958) for ductile materials. Irwin considered that the σ_{22} distribution for the fracture Mode I at the tip of the crack along the direction of propagation can be given by Eq. (2.8) with $\theta = 0$. In Fig. 2.6 the trend of σ_{22}, given by $\sigma_{22}=\dfrac{K_I}{\sqrt{2\pi r}}$ obtained by Eq. (2.8), where x is substituted by r is shown. The relation proposed is valid only for small values of x with respect to the dimensions of the structure. A first try of the length R of the process zone, admissible tractions are bonded to the yield stress σ_y, that is for $x = R$, $\sigma_{22} = \sigma_y$ leads:

$$R = \frac{1}{2\pi}\left(\frac{K_I}{\sigma_y}\right)^2 \tag{2.24}$$

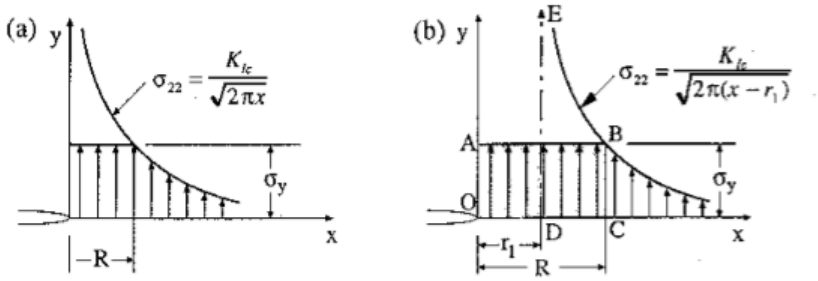

Figure 2.6: Irwin estimation of the process zone extension.

In fact the inelastic zone must be larger because the result of the tractions in this area must be equal to the stress $\sigma_{22} = \dfrac{K_I}{\sqrt{2\pi\, x}}$ provided by the elastic solution, so that, for the Saint Venant principle, the stress field to a certain distance from the process zone remains unchanged. For this reason, the real crack tip is shifted by an unknown quantity r_1, obtaining an equivalent elastic slit, as represented in Fig. 2.6. Graphically, the area below the elastic stress distribution equal to BCDE must be equal to the area below the distribution of plastic stress OABCO:

$$\int_{r_1}^{R} K_I[2\pi(x - r_1)]^{-1/2}dx = R\sigma_y \tag{2.25}$$

From the condition $\sigma_{22} = \sigma_y$ for $x = R$, considering also $\sigma_{22} = \dfrac{K_I}{\sqrt{2\pi(x-r)}}$:

$$R - r_1 = \frac{1}{2\pi}\left(\frac{K_I}{\sigma_y}\right)^2 \tag{2.26}$$

from Eq. (2.25) and (2.26), R is:

$$R = \frac{1}{\pi}\left(\frac{K_I}{\sigma_y}\right)^2 \tag{2.27}$$

It can be noticed in Eq. (2.27) that the size of the process zone is proportional to the square of the ratio between the intensity factor and the strength of the material and the proportionality parameter depends on the type of problem examined and in particular by the material and specific loading conditions. The maximum process zone size, when $K_I = K_{Ic}$ is:

$$Rc = \frac{1}{\pi}\left(\frac{K_{Ic}}{\sigma_y}\right)^2 \tag{2.28}$$

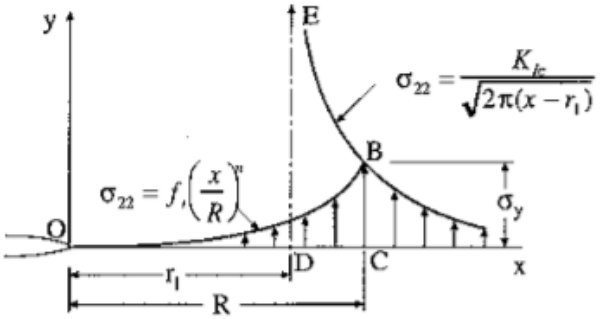

Figure 2.7: Process zone length estimation for a material with softening behaviour.

It is possible to extend the evaluation of the area of the process zone to quasi-brittle materials. Considering the critical situation, when $K_I = K_{Ic}$, the softening process at the crack tip is complete and $\sigma_{22} = 0$, while other points in the process zone are in an intermediate situation of fracture. Along the process zone it a stress distribution σ_{22} as depicted in Fig. 2.7 is assumed, i.e.:

$$\sigma_{22} = f_t\left(\frac{x}{R_c}\right)^n \tag{2.29}$$

where f_t is the tensile strength of the material; for $n = 1$ is obtained a linear distribution represented in Fig. 2.8 is obtained. Following the Irwin's procedure the resultant of the

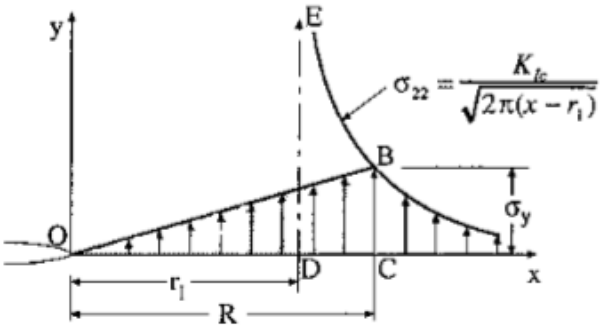

Figure 2.8: Process zone length estimation for a material with linear softening behaviour.

elastic stress distribution (DEBCD area) is equaled to the resultant tension in the process zone (OBCDO area):

$$\int_{r_1}^{R_c} K_{Ic}[2\pi x - r_1]^{-1/2}\mathrm{d}x = \int_0^{R_c} f_t\left(\frac{x}{R_c}\right)^n \mathrm{d}x = \frac{1}{n+1}R_c f_t \tag{2.30}$$

Eq. (2.30), together with Eq. (2.26), leads to:

$$R_c - r_1 = \frac{1}{2\pi}\left(\frac{K_I c}{f_t}\right)^2 \tag{2.31}$$

providing the value of R_c:

$$R_c = \frac{n+1}{\pi}\left(\frac{K_I c}{f_t}\right)^2 = \eta\frac{E^* G_f}{f_t^2} \tag{2.32}$$

where the expression provided by Irwin in Eq. (2.23) has been used. As in the previous case of a ductile material, Eq. (2.32) can provide only an approximate estimation of the process zone size. If R_c is small enough as compared to the dimensions of the structure, LEFM can be applied, otherwise all non-linear processes that occur in the zone near to the crack tip have to be analysed and taken into consideration. Referring to the previous cohesive fracture model, other researchers such as **Hillerborg** and **Petersson** (1976) proposed a characteristic length l_{ch} equal to:

$$l_{ch} = \frac{E^* G_f}{f_t^2} \tag{2.33}$$

which depends on the resistance and fracture energy of the material [29]. In particular, the model proposed by Hillerborg et al. [28] was extended to the study of concrete with the name of fictitious crack model [30, 31, 25]. The main difference between the fictitious crack model of Hillerborg and the CZM by Dugdale [26] and Barenblatt [27] is that crack initiation and propagation is not restricted along a predetermined path but cracks can initiate anywhere in

the structure. Meanwhile, many models developed later are able to handle also mixed mode (instead of Mode I only) and other complex phenomena including permanent deformations, stress triaxiality, and rate dependence. Some CZMs include fine scale effects obtained from micro-mechanical models or atomistic simulations [32, 33, 34]. The analysis of CZMs with their application in some specific cases will be further discussed in Chapter 4.

More complex models proposed in order to achieve an even more precise analysis, are smeared crack models, with the idea to spread the energy release along the width of the localization band usually within a single finite element. This is achieved by calibrating the width of the band such that the dissipated energy is the correct one. This introduces a characteristic length into the discretization that depends on the size of the elements. A milestone in smeared crack models is the crack band model by Bazant and Oh [35]. It is based on the observation that the process zone localizes in a single element, the so-called crack band. Therefore, Bazant and Oh modified the constitutive model after localization so that the correct energy is dissipated. Since the width of the numerically resolved fracture process zone depends on the element size and tends to zero if the mesh is refined, the crack band model cannot be considered as a real localization limit. It only partially regularizes the problem in the sense that the global characteristics do not exhibit spurious mesh dependence. When the element size exceeds the size of the process zone, the stress-strain curve has to be adjusted horizontally as shown in Fig. 2.9(b) [25]. This makes the stress-strain curve in the post-localization region steeper, and the appropriate scaling ratio achieves the dissipation energy remains the same. The crack band model was successfully used for Mode-I fracture.

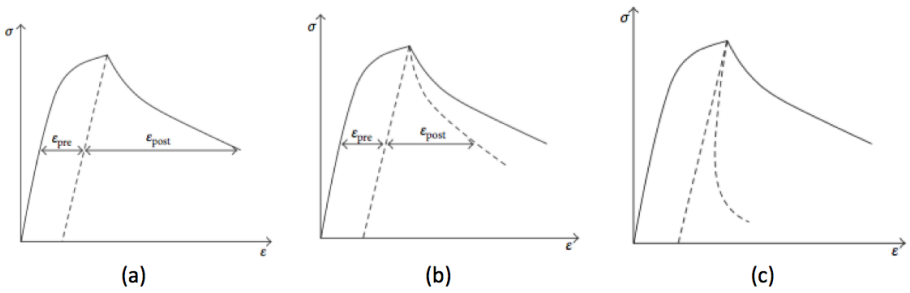

Figure 2.9: Adjustment of the stress-strain curve in the crack band model, (a) master curve and decomposition of the strains into prelocalizaton and post-localization parts, (b) horizontal scaling for an element larger than the physical process zone, and (c) snap back for too large elements (reproduced from Bazant and Jirasek [36]).

When the elements are too large (larger than the physical process zone), the post-localization diagram will develop a snap back, see Fig. 2.9(c). In turn, when the elements are much smaller than the process zone, the adjusted post-localization diagram becomes less steep, and the band of cracking elements converges to a set of measure zero. Thus, the limit corresponds to the solution of a cohesive crack model. The smeared crack models can be further classified into *rotating* and *fixed* crack models. In the *fixed* crack model, the orientation of the crack is not allowed to change. Fixed crack models can be again classified into *single*

fixed crack models and *multiple fixed* crack models. In the latter case, more than one crack initiates in an element. Often, a second crack is only allowed to be initiated perpendicular to the first crack (this should avoid the initiation of too many cracks).

2.2 Application of fracture model based on continuum

Models for the study of fracture mechanisms inside materials proposed before are based on a continuum theory so that material is considered as a periodic medium where properties are the same in each point, except for particular condition that might be present at the edges. Taking into account the different approaches from local or non-local considerations, the theories explained above can be efficiently applied at the macro-scale, through the study of the problem expecially with an energetic approach based on the application of the Virtual Work Principle. This is a fundamental part of the study of the behaviour of materials, but cannot provide a satisfactory answer about which mechanisms apply to smaller scales, thus being not suitable for the study of the behavior of materials at the atomic or molecular scales. For this reason, some methods that can be applied for the discretization of the material and the contextual study of its physical and mechanical properties for the identification of the mechanisms that regulate the resistance when subjected to stresses is proposed. Starting with the analysis of discretization methods that can be applied to the macro-scale, as is the continuum based approach, some techniques commonly used for the study of materials at the meso- and the micro-scale are then proposed. Particularly, the goal is to study phenomena that occurs at the micro-scale and evaluate how they can be influence the behavior at the macro-scale. According to that, it is necessary to explore theories belonging to different research fields as chemistry and physics, able to analyse the material with a deeper view, as will be presented in the next Chapter with an overview on different methods available, see Chapters 4 and 5.

Chapter 3

Discrete multi-scale modeling techniques for the study of mechanical properties of materials

The motivation for the need of studying the properties of materials at different scales of observation is herein discussed. The proposed methods are based on different scales of analysis, each of them concurring to model and understand different properties peculiar at the different scales and leading to macroscopical emergent behaviours. At nano- and micro-scales, chemical and physical features can be properly analyzed through the use of molecular dynamics, while mesco-scale investigations require the application of homogeneization techniques for continuum mechanics material model formulations that can be solved using the finite element method. In this Chapter, a brief overview on modeling techniques commonly used for the prediction of mechanical behavior of materials is presented with special focus on Computational Chemistry and Computational Mechanics modeling techniques.

3.1 Discrete Models

3.1.1 Generalized Born Model

Originally, the Born model was adopted in chemistry field to study diffusion of atoms and molecules with a liquid medium [37]. The generalization of the approach can be applied also to the probabilistic study of crack growth inside a solid material [38, 39]. In order to model the solvent in which molecules are dispersed, an implicit solvent framework is introduced , in which the real fluid is replaced with an environment consisting of discrete molecules by an infinite continuum with the same dielectric properties of the fluid. The approach is based on the Poisson-Boltzmann (PB) model, in which the Poisson equation (PE) of classical electrostatics provides an exact formalism for computing the electrostatic potential $\phi(r)$ produced by an arbitrary charge distribution $\rho(r)$, while the Boltzmann distribution for the density of mobile ions inside the potential field $\phi(r)$ is used to represent the total charge density, giving

rise to a full non-linear Poisson-Boltzmann equation.

$$\nabla \left[\varepsilon(r) \nabla \phi(\vec{r})\right] = -4\pi\rho(r) \tag{3.1}$$

The analytical GB method is an approximate version of the PB model, to compute the electrostatic part of the solvation free energy, ΔG_{el}:

$$G(r_i, r_j) = \frac{1}{\varepsilon|r_i - r_j|} + F(r_i, r_j) \tag{3.2}$$

where $F(r_i, r_j)$ corresponds to the reaction field due to polarization charges induced at the boundary; $F(r_i, r_j)$ is not vanishing at the boundaries. Of course, computing $F(r_i, r_j)$ for an arbitrary charge distribution inside an arbitrary molecular boundary is as hard as solving the original Poisson equation, so that further approximations are needed. The choice of the boundary shape is limited to a sphere, for which an exact solution of the PE equation exists, and according with [40] it is possible to separate the self-contribution, $F(r_i, r_j)$, from the interaction part, $F(r_i, r_j)$:

$$F(r_i, r_i)^{sphere} = -\left(\frac{1}{\varepsilon_{in}} - \frac{1}{\varepsilon_{out}}\right)\frac{1}{A}\sum_{l=0}^{\infty}\frac{t_{ii}^{l}}{1 + \frac{l}{l+1}\beta} \tag{3.3a}$$

$$F(r_j, r_j)^{sphere} = -\left(\frac{1}{\varepsilon_{in}} - \frac{1}{\varepsilon_{out}}\right)\frac{1}{A}\sum_{l=0}^{\infty}\frac{t_{ij}^{l} P_l(\cos\theta)}{1 + \frac{l}{l+1}\beta} \tag{3.3b}$$

where $t_{ij} = r_i r_j / A^2$, r_i is the atom's position relative to the center of the sphere, A is the molecule's radius, θ is the angle between r_i and r_j, and $\beta = \varepsilon_{in}/\varepsilon_{out}$ (see Fig. 3.1).

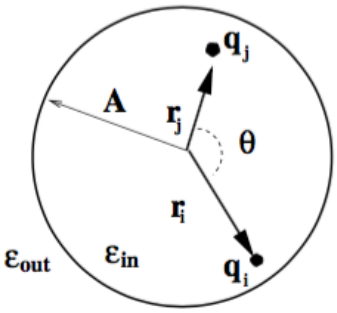

Figure 3.1: Illustration for Eqs. (3.3): a sphere of dielectric ε_{in} and radius A with two charges, q_i and q_j at positions r_i and r_j relative to the center of the spheres. The sphere is surrounded by infinite medium of uniform dielectric ε_{out}

The solution of Eqs. (3.3) is one of the cornerstones of the GB theory, considering that both the cross-term $F(r_i, r_j)$ and the self-term $F(r_i, r_i)$ of the Green function depend only on

$(A - r_i^2/A)$, quantity that will be called the effective Born radius R_i of atom i. Consequently, to perform practical computations one needs the effective Born radii R_i for every atom. In practice, the effective radius for each atom i can be calculated by approximately evaluating the electrostatic part of the solvation free energy ΔG_{el} via a proper volume integral. Two main challenges have to be overcome on the way to develop accurate and easy to use methods for computing the effective radii: (i) finding a computationally simple, physically justified integral representation for ΔG_{el}; and (ii) developing numerical routines to perform the integration over specific volume/surface corresponding to a physically realistic dielectric boundary between the solute and the solvent. The generalized Born (GB) model provides a simple analytical formula for molecular electrostatic energy in the presence of an implicit solvent. In the hierarchy of approximations that lead to model, the GB lies below the more fundamental model based on the Poisson equation (PE) of continuum electrostatics. In fact, apart from a heuristic correction term, the general mathematical form of the GB corresponds to the exact PE result for the electrostatic part of solvation free energy for a hypothetical perfectly spherical molecule surrounded by uniform dielectric medium in the conductor limit (infinitely high dielectric property). The accuracy of the GB model depends critically on the accuracy of the so-called effective Born radii that characterize positions of each partial atomic charge relative to the molecular surface of the structure.

3.1.2 Lattice Boltzmann model

This approach was widely used for simulating fracture in heterogeneous materials such as concrete and rock, for which the typical failure mechanism, crack face bridging, can be simulated by use of a lattice model. The model can be used at a small scale, where the particles in the grain structure are generated and aggregate, matrix and bond properties are assigned to the lattice elements. In an homogeneous material, cracks generally propagate in a direction which is perpendicular to the maximum tensile stress, see Chapter 2. In heterogeneous materials (i.e. concrete) cracks also follow the weakest links in the material, so that crack patterns will be never be straight and continuous. Due to the heterogeneity of the material, cracks are tortuous and there are overlaps or so-called crack face bridges. Definitely, crack propagation in structures can be properly simulated with the finite element methods (FEM) based on continuum theories only if homogeneous materials are concerned or if the degree of disorder is low. For studying fracture of materials in the cases where disorder is important, lattice models are often preferred. In lattice models, the medium is discretized such that all sites are equivalent, that means that the grid is not made finer in regions of higher stress as often done for FEM, and each site has the same number of neighbours so that the lattice is regular. The material is schematized as a lattice of brittle-breaking beam elements and commonly a triangular lattice is chosen as shown in Fig. 3.2. This type of lattice gives the least chance for preferential crack directions, that is the essential for the model, which is based on a linear elastic finite element code.

The nonlinearities are introduced into the discretized material through the fracture criterion, which means that a bar element is removed from the mesh as soon as a combination of acting forces (i.e. normal force and bending moment) caused by either an external load on the lattice or by boundary displacements is exceeded. The relation can be expressed in

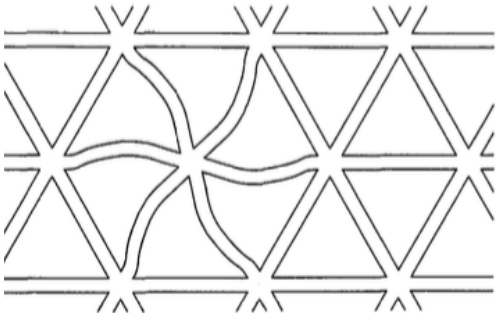

Figure 3.2: Triangular lattice of beams

Eq. (3.4):

$$\sigma_t < \frac{F}{A} + \alpha \frac{(|M_i|, |M_j|)_{\max}}{W} \tag{3.4}$$

where F is the normal force in the beam element, M_i and M_j are the bending moments in nodes i and j of the bar element, respectively, $A = bh$ is the cross-sectional area of the beams, and $W = bh^2/6$ is the section modulus.The coefficient α is introduced in order to select a failure mode where bending plays either a dominant or a restricted role. After removal of a beam element the linear analysis is repeated. The external load P that can be carried by the lattice is simply determined by the beam element with the highest $\frac{\sigma}{\sigma_t}$ ratio, where σ is the beam stress caused by a test-load P_{test} applied to the lattice:

$$P = P_{test}(\sigma/\sigma_t) \tag{3.5}$$

The computational efforts depend on the number of lattice elements. The first approach used for introducing the heterogeneity of the concrete is generating the grain structure of concrete, where an assumption has to be made for the distribution of the diameters of the intersection circles in a cross-section of a concrete body (for the sake of simplicity, aggregate particles are assumed to be spherical). For the distribution of the aggregate particles in the concrete mix, a Fuller curve has been chosen in [41]. Using this function for a given concrete mix, the distribution of circle diameters in a certain cross-section can be generated. The circles are randomly positioned in the area, starting with the largest circles (Fig. 3.3). The minimum distance between the centres of two circles A and B is taken as $1.1(D_A + D_B)/2$ according to Hsu [42], van Mier et al. [41, 43, 44], Rots et al. [45].

The triangular lattice is projected on top of the generated grain structure, and different strengths and stiffnesses are assigned to the respective beam elements, as in Fig. 3.4(a) and 3.4(b). In Fig. 3.4(a), the projection on the grain structure of the lattice of a single-edge notched (SEN) tensile specimen (which will also be discussed later) is shown. When an element is situated inside an aggregate particle, the stiffness and the failure strength of the aggregate will be assigned to this element; an element located on the boundary between aggregate and matrix will possess a strength and a stiffness somehow lower than the matrix

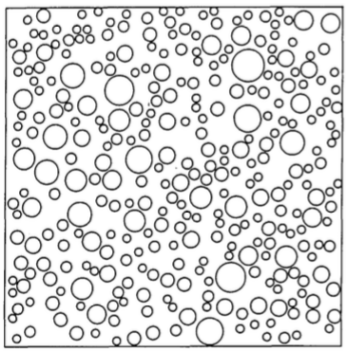

Figure 3.3: Generated grain structure

stiffness when fracturing of normal concrete is to be simulated. Matrix properties will be assigned to those beam elements projected on the cement matrix in the generated two-phase material.

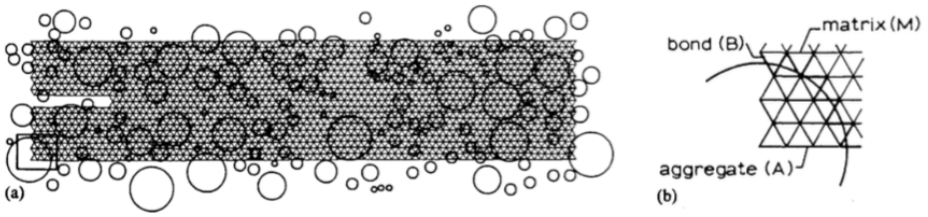

Figure 3.4: (a) Triangular lattice projected on the grain skeleton; (b) definition of aggregate, bond and matrix beam elements

From the simulations conduced in [41] on uniaxial tensile tests, it can be concluded that lattice models are a sufficient tool for studying micromechanisms of fracture. The typical failure type of crack face bridging in heterogeneous materials could be simulated quite well when the disorder was introduced through the generation of a heterogeneous structure. It should be possible to simulate fracture processes in different materials and at different scales through the generation of granular structures. The input parameters for the beam elements representing aggregates, matrix and bond proved to be important in the approach with the grain structure. The exact value of these input parameters should be determined from a parametic study or identified by comparing predictions with experimental measurements. For the prediction of crack patterns in larger structures such as plates or beams, the procedure of assigning randomly chosen material properties to the lattice elements gives good results. A relation between the size of the bar elements in the lattice and the random distribution of the material properties is required. Finally, the model seems to predict fracture mechanisms quite accurately.

3.2 Scale-based different methods developed to determine material strength and toughness

In the last 20 years, many research centres have noticed the need for a more systematic approach to new materials development through a multi-scale modeling approach. This approach was one that would combine interdisciplinary research, new advances in computational modeling and simulation, and critical laboratory experiments to rapidly reduce the time from the concept to the end product. The general consensus is that this new paradigm will govern the design of all future materials and it has suggested to use the term "Computational Materials". It is recognized that, within the scope of materials and structures research, the breadth of length and time scales may range over more than 12 orders of magnitude, and different scientific and engineering disciplines are involved at each scale. To help address this wide-ranging interdisciplinary research, Computational Materials programs have been formulated with the specific goal of exploiting the physical and mechanical properties of materials by understanding their properties at atomic, molecular, and supramolecular levels. Mechanical properties of materials can be studied by a set of defined computational methods. These modeling methods span a wide range of length and time scales: Computational Chemistry is primarily used to predict atomic structure using first-principles theory. On the other side, for largest time scales and length scales Computational Mechanics is invoked to predict the mechanical behavior of materials and engineering structures. Both Computational Chemistry and Computational Mechanics modeling methods are based on several principles developed in science and engineering. For intermediate length and time scales, general modeling methods are not yet fully developed. Multiscale modeling techniques give an help and can be employed taking advantage both by Computational Chemistry and Computational Mechanics methods simultaneously for the prediction of the structure and properties of materials.

Computational Materials programs have developed schemes for spanning both the length and time scales associated with analyses that describe material behavior. Schematically, this approach is illustrated in Fig. 3.5. The starting point is a Quantum mechanical and Nanomechanical modeling approach based on the assumption of the presence of a discrete atomic or molecular structure of matter; this is carried forward to an atomistic scale for initial model development. Models at this scale are based on Molecular Mechanics or Molecular Dynamics. At the next scale, the models can incorporate micro-scale features and simplified constitutive relationships. Further upscaling progress leads to the meso- or in-between levels that rely on combinations of micromechanics and well-established theories such as elasticity. The last step towards engineering-level performance is to move from Mechanics of Materials to Structural Mechanics, in which the presence of a continuous material structure, by using methods that rely on empirical data, constitutive models, and fundamental mechanics is assumed.

3.3 Overview of the methods

The logical scheme usually adopted in scientific research is shown in In Fig. 3.6 and in particular it depicts the whole procedure conducted to come from experimental data to the formulation of a theory and to use it producing numerical simulation for the validation of initial

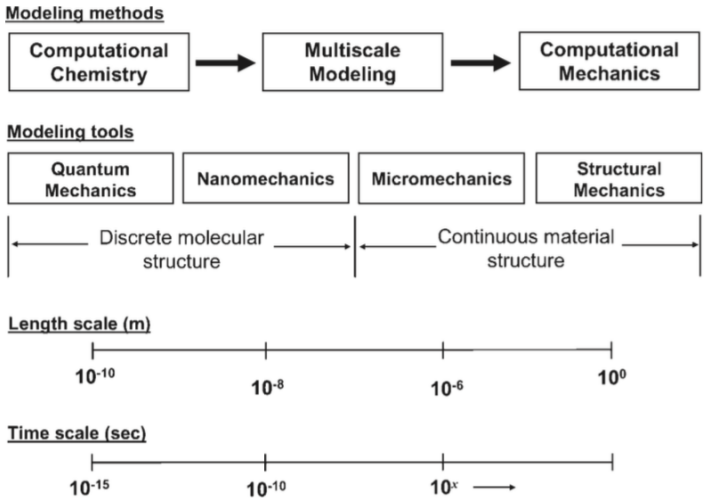

Figure 3.5: Various length and time scales used in determining mechanical properties of materials.

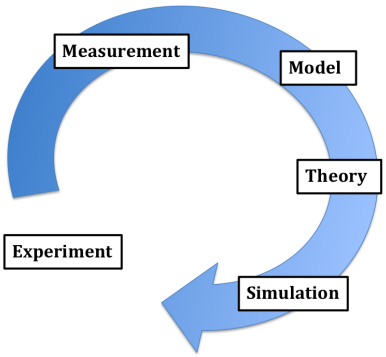

Figure 3.6: Scheme of the procedure of formulation theory and the validation of experimental data (adapted from [46]).

experiments. The engine of the whole procedure is modeling for understanding of the behavior of matter. The fist step in the prediction of material properties and material behavior is usually to start an observation from experiments. Careful measurements of observed data are subsequently used for the development of trial models that provide a prediction of the observed experimental behavior under the corresponding conditions. At their own, models are necessary to develop the theory. The theory is then used to compare predicted behavior to experiments via simulation. This comparison serves to either validate the theory, or to

provide a feedback loop to improve the theory using modeling data. Therefore, the development of a realistic theory of describing the structure and characteristics of materials is highly dependent on accurate modeling and simulation techniques.

The whole schematic scenario of specific modeling techniques in Computational Mechanics and Computational Chemistry is represented in Fig. 3.7 in order better understand their interdependence. The continuum-based methods primarily include techniques such as the Finite Element Method (FEM), the Boundary Element Method (BEM), and micromechanics approaches developed for composite materials. Specific Micromechanical homogeneization techniques include Eshelby approach, Mori-Tanaka method, Halpin-Tsai method [47, 48]. The molecular modeling tools include Molecular Dynamics (MC), Monte Carlo, and Ab-initio techniques. Each of these continuum and molecular-based modeling methods are described in the following Chapters.

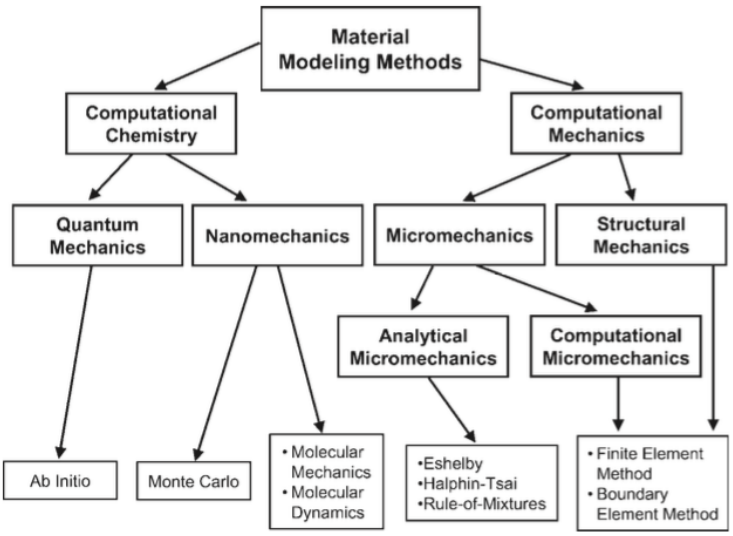

Figure 3.7: Diagram of material modeling techniques

Chapter 4

Nano(Molecular)- to Micro-scale Models

From a "bottom-up" perspective, the multi-scale approach should consider the intrinsic attributes of the constituent materials of the system. The multi-scale approach formulated within a Computational Materials software is a formulation of a set of integrated predictive models that bridge the time and length scales associated with material behavior from the nano to the meso-scale. At the atomistic or molecular level, the focus is on molecular mechanics, molecular dynamics, and coarse-grained simulations [49]. Molecular models encompassing thousands and perhaps millions of atoms can be solved by these methods and used to predict fundamental, molecular level material behavior. The methods are both for static or dynamics. For example, molecular mechanics can establish the minimum-energy structure statically and molecular dynamics can resolve the nanosecond-scale evolution of a molecule or of a molecular assembly. These approaches can model both bonded and nonbonded forces (e.g., van der Waals and electrostatic), but are not parameterized for bond cleavage. In recent years molecular modeling has emerged as an important tool in the prediction of physical material properties such as elastic response, atomic structure, vibrational frequencies, heat of reaction, electric permitivity, and binding energies. Molecular modeling assumes a noncontinuous composition of the material, which makes it a powerful tool for studying atomic interactions at the nanometer length scale. Due to the discrete nature of these techniques, they are often limited by the length and time scales that can be achieved in the simulations. Three widely used molecular modeling techniques for the prediction of mechanical properties of nanostructured materials are molecular dynamics (MD), Monte Carlo (MC), and ab initio simulation. A review of classical nano- to micro-scale approaches developed are herein reviewed, and then themodel proposed by Paggi and Infuso [50] for the study of the stretch in a nanoscale material under external tensile loading is reported. This approach has been tested on a mono-dimensional and two-dimensional structures in order to study the effect of non-locality considering single mass entities linked not only to neighbours but also to further masses.

4.1 Ab initio simulations

Ab initio electronic structure methods have the advantage that they can be made to converge to the exact solution, when all approximations are sufficiently small in magnitude and when the finite set of basis functions tends toward the limit of a complete set. In this case, configuration interaction, where all possible configurations are included (called Full CI), tends to the exact non-relativistic solution of the electronic Schrödinger equation (in the Born-Oppenheimer approximation). The convergence, however, is usually not monotonic, and sometimes the smallest calculation gives the best result for some properties. Understanding the strength of materials from microscopic scale is essential for materials mechanics. Multi-scale modeling for this issue has revealed that the behavior of materials in atomistic and/or at the electronic scale can play an important role for the mechanical properties [51, 52]. Unlike most material simulation methods that are based on classical potentials, the main advantages of ab initio methods, which is based on first-principles density functional theory (without any adjustable parameters), are the generality, reliability, and accuracy. The simplest type of ab initio electronic structure calculation is the Hartree-Fock (HF) scheme, in which the instantaneous Coulombic electron-electron repulsion is not specifically taken into account. Only its average effect (mean field) is included in the calculation. This is a variational procedure; therefore, the obtained approximate energies, expressed in terms of the system's wave function, are always equal to or greater than the exact energy, and tend to a limiting value called the Hartree-Fock limit as the size of the basis is increased. Most commonly used solution strategies are VASP (Vienna Ab-initio Simulation Package) for the first-principles calculations, which is a DFT Density Functional Theory simulation package, using a plane-wave basis set with ultrasoft pseudopotentials [53]. They involve the solution of Schrödinger's equation for each electron, under the action of a self-consistent potential created by the other electrons and the nuclei.
Ab initio methods can be applied to a wide range of systems and properties. However, ab initio molecular dynamics is extremely time-consuming, and in the end the response of very small aggregates of atoms can be solved using the largest available computers. It will be obvious that ab-initio analyses include all the structural conditions of the atoms directly, which remains rather problematic in any hierarchical (multi-scale) approach. There are three different widely-used procedures in ab initio simulations. These procedures are single point calculations, geometry optimization, and frequency calculation. Single point calculations involve the determination of energy and wave functions for a given geometry. This is often used as a preliminary step in a more detailed simulation. Geometry calculations are used to determine energy and wave functions for an initial geometry, and subsequent geometries with lower energy levels. A number of procedures exist for establishing geometries at each calculation step. Frequency calculations are used to predict Infrared and Raman intensities of a molecular system. Ab initio simulations are restricted to small numbers of atoms because of the intense computational resources required.

4.2 Molecular Dynamics models

Molecular dynamics (MD) was first introduced by Alder and Wainwright in the late 1950s to study the interactions of hard spheres [54]. Many important insights concerning the behavior of simple liquids emerged from their studies. The next major advance was in 1964, when Rahman carried out the first simulation by using a realistic potential for liquid Argon [55]. MD is a computer simulation technique that allows one to predict the time evolution of a system of interacting particles (e.g., atoms, molecules, granules, etc.) and estimate the relevant physical properties. Specifically, it provides quantitative information on atomic positions, velocities and forces from which the macroscopic properties (e.g., pressure, energy, heat capacities) can be derived by means of statistical mechanics. The simulation results could be average quantities at a thermodynamic state point or the development of a structure-based property in time. In a non-equilibrium simulation, where the system is subjected to a temporary perturbation, the response of the material can be analyzed. The connections to measurable quantities are made through thermodynamics and statistical mechanics. MD simulation usually consists of three constituents:

(I) A set of initial conditions (e.g., initial positions and velocities of all particles in the system);

(II) The interaction potentials to represent the forces among all the particles;

(III) The evolution of the system in time by solving a set of classical Newtonian equations of motion for all particles in the system.

Molecular dynamics simulations generate information at the nano-level, including atomic positions and velocities. The conversion of this information to macroscopic observable quantities such as pressure, energy, heat capacities, etc., requires statistical mechanics. The equations of motion are given by Newton's second law, and are expressed in Eq. (4.1):

$$\vec{F}_i(t) = m_i \frac{d^2 \vec{r}_i}{dt^2} \tag{4.1}$$

where $\vec{F}_i$ is the force acting on the i-th atom or particle at time t which is obtained as the negative gradient of the interaction potential U, m_i is the atomic mass and $\vec{r}_i$ the atomic position. MD is a statistical mechanics method. A set of configurations is distributed according to a statistical ensemble or statistical distribution function. The trajectories of the motion of the atoms are calculated under the influence of interaction forces exerted by the atoms. A physical simulation involves the proper selection of interaction potentials, numerical integration, periodic boundary conditions, and the controls of pressure and temperature to mimic physically meaningful thermodynamic ensembles. The trajectory is calculated in a phase space with 6N dimensions; three position and three momentum components for each atom. Calculation of physical quantities by MD simulation is obtained by arithmetic averages of instantaneous energy values from individual simulation steps. MD simulations, if run for a sufficiently long time, can completely sample the phase space. However, in practice, simulation times are limited. Physical quantities are sampled after the molecular system reaches a thermodynamic equilibrium.

The interaction potentials together with their parameters, i.e., the so-called force field, describe in detail how the particles in a system interact with each other, i.e., how the potential energy of a system depends on the particle coordinates. Such a force field may be obtained by quantum method (e.g., the previously proposed ab initio approach), empirical method (e.g., Lennard-Jones, Mores, Born-Mayer) or quantum-empirical method (e.g., embedded atom model, glue model, bond-order potential). A great amount of interaction potentials derives from the chemical nano- micro-scale analysis of drug diffusion into blood or generally inside liquid solvent. Some of these will be briefly analyzed in Section 4.2.3. The criteria for selecting a force field include the accuracy, transferability and computational speed. A typical interaction potential U may consist of a number of bonded and non-bonded interaction terms:

$$\begin{aligned}\vec{U}(\vec{r_1},\vec{r_2},...,\vec{r_N}) = &\sum_{i_{bond}}^{N_{bond}} U_{bond}(i_{bond},\vec{r_a},\vec{r_b}) \\ &+ \sum_{i_{angle}}^{N_{angle}} U_{angle}(i_{angle},\vec{r_a},\vec{r_b},\vec{r_c}) \\ &+ \sum_{i_{torsion}}^{N_{torsion}} U_{torsion}(i_{torsion},\vec{r_a},\vec{r_b},\vec{r_c},\vec{r_d}) \\ &+ \sum_{i_{inversion}}^{N_{inversion}} U_{inversion}(i_{inversion},\vec{r_a},\vec{r_b},\vec{r_c},\vec{r_d}) \\ &+ \sum_{i=1}^{N-1}\sum_{j>1}^{N} U_{vdw}(i,j,\vec{r_a},\vec{r_b}) \\ &+ \sum_{i=1}^{N-1}\sum_{j>1}^{N} U_{electrostatic}(i,j,\vec{r_a},\vec{r_b})\end{aligned} \tag{4.2}$$

The first four terms in Eq. (4.2) represent bonded interaction potential emergies, i.e., bond stretching U_{bond}, bond-angle bend U_{angle}, dihedral angle torsion $U_{torsion}$, and inversion interaction $U_{inversion}$, while the last two terms are non-bonded interactions, i.e., van der Waals energy U_{vdw} and electrostatic energy $U_{electrostatic}$. Termes $\vec{r_a}$,$\vec{r_b}$,$\vec{r_c}$ and $\vec{r_d}$ are the positions of the atoms or particles specifically involved in a given interaction; N_{bond}, N_{angle}, $N_{torsion}$ and $N_{inversion}$ stand for the total numbers of these respective interactions in the simulated system; i_{bond}, i_{angle}, $i_{torsion}$ and $i_{inversion}$ uniquely specify an individual interaction of each type; i and j in the van der Waals and electrostatic terms indicate the atoms involved in the interaction. There are many algorithms for integrating the equation of motion using finite difference methods. The algorithms of Verlet, velocity Verlet, leap-frog and Beeman, are commonly used in MD simulations [56]. All algorithms assume that the atomic position $\vec{r}$, velocities $\vec{v}$ and accelerations $\vec{a}$ can be approximated by a Taylor series expansion:

$$\vec{r}(t+\delta t) = \vec{r}(t) + \vec{v}\delta t + \frac{1}{2}\vec{a}(t)\delta t^2 + ..., \tag{4.3}$$

$$\vec{v}(t+\delta t) = \vec{v}(t) + \vec{a}\delta t + \frac{1}{2}b(t)\delta t^2 + ..., \tag{4.4}$$

$$\vec{a}(t+\delta t) = \vec{a}(t) + b\delta t + ..., \tag{4.5}$$

It should also be easy to implement and computationally efficient, and permit a relatively long time-step. The Verlet algorithm is probably the most widely used method. It uses the positions $\vec{r}(t)$ and accelerations $r\vec{a}(t)$ at time t, and the positions $\vec{r}(t-\delta t)$ from the previous step $t-\delta t$ to calculate the new positions $\vec{r}(t+\delta t)$ at $t+\delta t$. According to Taylor series expansion of Eq. (4.6), we have:

$$\vec{r}(t+\delta t) = \vec{r}(t) + \vec{v}\delta t + \frac{1}{2}\vec{a}(t)\delta t^2 + ..., \tag{4.6}$$

$$\vec{r}(t-\delta t) = \vec{r}(t) + \vec{v}\delta t + \frac{1}{2}\vec{a}(t)\delta t^2 - ..., \tag{4.7}$$

Merging together Eqs. (4.6) and (4.7) gives

$$\vec{r}(t+\delta t) = 2\vec{r}(t) - \vec{r}(t-\delta t) + \vec{a}(t)\delta t^2. \tag{4.8}$$

The velocities at time t and $t + \frac{1}{2}\delta t$ can be respectively estimated as:

$$\vec{v}(t) = [2\vec{r}(t+\delta t) - \vec{r}(t-\delta t)]/2\delta t, \tag{4.9}$$

$$\vec{v}\left(t + \frac{1}{2}\delta t\right) = [\vec{r}(t+\delta t) - \vec{r}(t)]/\delta t \tag{4.10}$$

MD simulations can be performed in many different ensembles, such as grand canonical (mVT), microcanonical (NVE), canonical (NVT) and isothermal-isobaric (NPT) systems. The constant temperature and pressure can be controlled by adding an appropriate thermostat (e.g., Berendsen, Nose, Nose-Hoover and Nose-Poincare) and barostat (e.g., Andersen, Hoover and Berendsen), respectively. The most time consuming part of a molecular dynamics simulation is the calculation of the nonbonded terms in the potential energy function, e.g., the electrostatic and van der Waals forces. In principle, the non-bonded energy terms between every pair of atoms should be evaluated. This requirement would imply that the number of computations increases as the square of the number of atoms for a pair-wise model. To speed up the computation, the interactions between two atoms separated by a distance greater than a predefined distance, the cutoff distance, are ignored.

4.2.1 LAMMPS: a software for MD simulation

LAMMPS stands for Large-scale Atomic/Molecular Massively Parallel Simulator. A detailed description of LAMMPS features can be found directly at lammps.sandia.gov. LAMMPS [57] is a classical molecular dynamics simulation code designed to run efficiently on parallel computers. It was developed at the Sandia National Laboratories, a US Department of Energy facility, with funding from the Dept. of Energy. It is an open-source code, distributed freely

under the terms of the GNU Public License (GPL), which means that can be downloaded and used by everyone could be interested in molecular simulations. LAMMPS can model an ensemble of particles in a liquid, solid, or gaseous states. It can model atomic, polymeric, biological, metallic, granular, and coarse-grained systems using a variety of force fields and boundary conditions. LAMMPS can model systems with only a few particles up to millions or billions. LAMMPS runs efficiently on single-processor desktop or laptop machines, but is designed for parallel computers. It will run on any parallel machine that compiles C++ and supports the MPI (Multi-Processor Instructions) message-passing library. This includes distributed- or shared-memory parallel machines and Beowulf-style clusters. In the most general sense, LAMMPS integrates Newton's equations of motion for collections of atoms, molecules, or macroscopic particles that interact via short- or long-range forces with a variety of initial and/or boundary conditions. For computational efficiency, LAMMPS uses neighbour lists to keep track of nearby particles. The lists are optimized for systems with particles that are repulsive at short distances, so that the local density of particles never becomes too large. On parallel machines, LAMMPS uses spatial-decomposition techniques to partition the simulation domain into small 3d sub-domains, one of which is assigned to each processor. LAMMPS requires as input a list of initial atom coordinates and types, molecular topology information, and force-field coefficients assigned to all atoms and bonds. LAMMPS will not build molecular systems and assign force-field parameters by itself. For atomic systems, LAMMPS provides a create atoms command which places atoms on solid-state lattices (fcc, bcc, user-defined, etc) that can be useful for modeling small amount of atoms. At the same, the assigning small numbers of force field coefficients can be done via the pair coeff, bond coeff, angle coeff, commands. A feasible solution to simulate a periodic atoms path of structured molecules may simply be the writing of a procedure routine in a computer programming language as are fortran or better C++ able to compile an input file directly importable in LAMMPS. On the contrary, when the amount of entities becomes larger, as are molecular systems or more complicated simulation geometries, it is convenient to rely on an another external code builder and convert its output to LAMMPS input format, or write an own code to generate atom coordinate and molecular topology for LAMMPS to read in, as the same proposed before. As an example, for complicated molecular systems (e.g. organic molecules as proteins), a multitude of topology information and hundreds of force-field coefficients must typically be specified. After having successfully conducted the simulation at the end, one is faced with a situation similar to the previous one, since LAMMPS creates output files in a simple format, and it is required by the user to post-process them or import in visualization packages. One of the weak point of this kind of analysis in that complicated computations can slow down the molecular dynamics timestepping, particularly if the computations are not parallel.

A LAMMPS input script typically has 4 parts:

1. **INITIALISATION**: Set parameters that need to be defined before atoms are created or read-in from a file. Most important are:

    1.1. Unit of measure for mass, distance, time, energy, velocity, force, temperature, pressure, etc. If no commands related to this input are given at the beginning of the script, default units will be adopted for the analysis.

1.2. Dimension: set the dimensionality of the simulation. By default LAMMPS runs 3d simulations. To run a 2d simulation, this command should be used prior to setting up a simulation box.

1.3. Boundary: set the style of boundaries for the global simulation box in each dimension. The style p means the box is periodic, so that particles interact across the boundary, and they can exit one end of the box and re-enter the other end. A periodic dimension can change in size due to constant pressure boundary conditions or box deformation. The styles f, s, and m mean the box is non-periodic, so that particles do not interact across the boundary and do not move from one side of the box to the other. For style f, the position of the face is fixed. If an atom moves outside the face it will be deleted on the next tilmestep that re-neighboring occurs. For style s, the position of the face is set so as to encompass the atoms in that dimension (shrink-wrapping), no matter how far they move.

2. **ATOM DEFINITION**: there are mainly 2 ways to define atoms in LAMMPS. The most common is to create an external input file through a specific modelling software, or a self-made script and then insert into LAMMPS routine a command to let it read the external file (read data command). Otherwise, for most simple cases, it is possible to create set of particles directly into LAMMPS (lattice, create atoms commands).

3. **SETTINGS**: once atoms and molecular topology are defined, a variety of settings can be specified: force field coefficients, simulation parameters, output options, etc. Force field coefficients can be set using some specific commands as are:

   3.1. Pair coeff: specify the pairwise force field coefficients for one or more pairs of atom types. The number and meaning of the coefficients depends on the pair style. Pair coefficients can also be set in the data file read by the read data command or in a restart file.

   3.2. Bond coeff : specify the bond force field coefficients for one or more bond types. The number and meaning of the coefficients depends on the bond style. Bond coefficients can also be set in the data file read by the read data command or in a restart file.

   3.3. Fix: fixes impose a variety of boundary conditions, time integration, and diagnostic options. Are used to impose strict conditions to the system, as are control or initial parameters.

   3.4. Compute: define a computation that will be performed on a group of atoms. Quantities calculated by a compute are instantaneous values, meaning they are calculated from information about atoms on the current timestep or iteration, though a compute may internally store some information about a previous state of the system. Defining a compute does not perform a computation. Generally these options produces a numerical data set that can be also exported to an external file.

   3.5. Dump: produce a snapshot of atom quantities to one or more files every N timesteps in one of possible styles. The image and movie styles are the exception: the image style renders a picture file of the atom configuration every N timesteps while the movie style combines and compresses them into a movie file.

4. **RUN A SIMULATION**: a molecular dynamics simulation is run using the run command. Energy minimization (molecular statics) is performed using the minimize command.

   4.1. Run: start or continue a simulation for a certain number of steps.

   4.2. Minimize: perform an energy minimization of the system, by iteratively adjusting atom coordinates. Iterations are terminated when one of the stopping criteria is satisfied. At that point the configuration will hopefully be in local potential energy minimum.

4.2.2 Different force fields: AMBER, CHARMM, DREIDING, REBO and AIREBO

Depending on the different type of molecules one wants to simulate using LAMMPS solution software, an appropriate force field to represent the whole interaction ensemble involved in the system has to be chosen. Most of the proposed force fields have been studied, discovered and applied to organic molecules (i.e. proteins, nucleic acids) in particular the AMBER and the CHARMM potentials, while the REBO and its modification AIREBO were firstly employed for the study of hydrocarbon properties. The most general potential is DREIDING, which can be adopted for a wide field of analysis.

AMBER (an acronym for Assisted Model Building with Energy Refinement) is a family of force fields for molecular dynamics of biomolecules originally developed by Peter Kollman's group at the University of California, San Francisco. AMBER is also the name for the molecular dynamics software package that simulates these force fields se ambermd.org. The reader is referred to [58] for a full description of the method, where the complete expression of the adopted force field is:

$$\begin{aligned} V(r^N) = &\sum_{bonds} k_b(l-l_0)^2 + \sum_{angles} k_a(\theta-\theta_0)^2 + \sum_{torsion}\sum_{n}\frac{1}{2}V_n[1+\cos(n\omega-\gamma)] \\ &+ \sum_{j=1}^{N-1}\sum_{i=j+1} N f_{ij}\left\{\varepsilon_{ij}\left[\left(\frac{r_{0ij}}{r_{ij}}\right)^{12} - 2\left(\frac{r_{0ij}}{r_{ij}}\right)^{6}\right] + \frac{q_i q_j}{4\pi\varepsilon_0 r_{ij}}\right\} \end{aligned} \tag{4.11}$$

which formally, despite the term force field, defines the potential energy of the system; the force is the derivative of this potential with respect to position. The meanings of right hand side terms are:

- First term (summing over bonds): represents the energy between covalently bonded atoms. This harmonic (ideal spring) force is a good approximation near the equilibrium bond length, but becomes increasingly poor as atoms separate.

- Second term (summing over angles): represents the energy due to the geometry of electron orbitals involved in covalent bonding, as the first term represented by a simple

diagonal harmonic expression.

- Third term (summing over torsions): represents the energy for twisting a bond due to bond order (e.g. double bonds) and neighboring bonds or lone pairs of electrons. Note that a single bond may have more than one of these terms, such that the total torsional energy is expressed as a Fourier series.

- Fourth term (double summation over i and j): represents the non-bonded energy between all atom pairs, which can be decomposed into van der Waals 6-12 potential (first term of summation) and electrostatic (second term of summation) energies, modeled by a Coulombic interaction of atom-centered point charges.

The form of the van der Waals energy is calculated using the equilibrium distance r_{0ij} and well depth ε. The factor of 2 ensures that the equilibrium distance is r_{0ij}. The energy is sometimes reformulated in terms of σ, where $r_{0ij} = 2^{1/6}(\sigma)$, as used e.g. in the implementation of the softcore potentials. The form of the electrostatic energy used here assumes that the charges due to the protons and electrons in an atom can be represented by a single point charge (or in the case of parameter sets that employ lone pairs, a small number of point charges). Electrostatic and van der Waals interactions are only calculated between atoms in different molecules or for atoms in the same molecule separated by at least three bonds. Those non-bonded interactions separated by exactly three bonds ('1-4 interactions') are reduced by the application of a scale factor.

CHARMM (Chemistry at Harvard Macromolecular Mechanics) is the name of a widely used set of force fields for molecular dynamics as well as the name for the molecular dynamics simulation and analysis package associated with them. The CHARMM Development Project involves a network of developers throughout the world working with Martin Karplus [59] and his group at Harvard. (see charm.org) CHARMM is one of the first programs for molecular dynamics: its program allows generation and analysis of a wide range of molecular simulations. The most basic kinds of simulation are minimization of a given structure and production runs of a molecular dynamics trajectory. More advanced features include free energy perturbation (FEP), quasi-harmonic entropy estimation, correlation analysis and combined quantum, and molecular mechanics (QM/MM) methods. The parameter evaluation was based on a self-consistent approach designed to achieve a balance between the internal (bonding) and interaction (nonbonding) terms of the force field and among the solvent-solvent, solvent-solute, and solute-solute interactions. The interaction parameters, particularly the atomic charges, were determined by fitting ab initio interaction energies and geometries of complexes between water and model compounds that represented the back bone and the various side chains. The form of the potential energy function for CHARMM is an empirical expression that contains terms for both internal and external interactions, given

by the following equation [60]:

$$
\begin{aligned}
U(\vec{R}) = & \sum_{bonds} K_b(b-b_0)^2 + \sum_{UB}(S-S_0)^2 \\
& + \sum_{angle} K_\theta(\theta-\theta_0)^2 + \sum_{dihedrals} K_\chi(1+\cos(n\chi-\delta)) \\
& + \sum_{impropers} K_{imp}(\varphi-\varphi_0)^2 \\
& + \frac{1}{2}V_n[1+\cos(n\omega-\gamma)] \\
& + \sum_{nonbond} \varepsilon\left[\left(\frac{R_{min_{ij}}}{r_{ij}}\right)^{12} - 2\left(\frac{R_{min_{ij}}}{r_{ij}}\right)^{6}\right] + \frac{q_i q_j}{\varepsilon_1 r_{ij}}
\end{aligned}
\tag{4.12}
$$

where K_b, K_{UB}, K_θ, K_χ and K_{imp} are the bond, Urey-Bradley, angle, dihedral angle, and improper dihedral angle force constants, respectively; b, S, θ, χ and φ are the bond length, Urey-Bradley 1,3-distance, bond angle, dihedral angle, and improper torsion angle, respectively, with the subscript zero representing the equilibrium values for the individual terms. Coulomb and Lennard-Jones 6-12 terms contribute to the external or nonbonded interactions; ε is the Lennard-Jones well depth and R_{min} is the distance at the Lennard-Jones minimum, q_i is the partial atomic charge, ε_l is the effective dielectric constant, and r_{ij} is the distance between atoms i and j. The Lennard-Jones parameters between pairs of different atoms are obtained from the Lorentz-Berthelodt combination rules, in which ε_{ij} values are based on the geometric mean of ε_i and ε_j and $R_{min_{ij}}$ values are based on the arithmetic mean between R_{min_i} and R_{min_j}. Because of the role of electrostatic contributions in determining intramolecular, as well as intermolecular, energetics (as described below), the effective dielectric constant ε_1 must be set equal to unity in this potential energy function since otherwise an unbalanced parametrization will be obtained.

Given $\vec{R}$, the vector of the coordinates of the atoms, the various distances and angles required to evaluate U($\vec{R}$) in Eq.(4.12) are readily determined. Typically, initial values of the intermolecular parameters (Coulomb and Lennard- Jones) were chosen from previous CHARMM parameter sets or based on the reproduction of ab initio interaction calculations on rigid monomers. With the improved interaction parameters, the structures, vibrational spectra, and energy surfaces of the model compounds were re-optimized by adjusting the internal parameters. This iterative process was repeated until convergence of the parameters was achieved. Once satisfactory geometries were obtained, the force constants associated with the bond length, bond angle, dihedral angle, and improper torsion terms were adjusted by fitting vibrational data for the model systems.

DREIDING is a generic force field developed by the Goddard group and is useful for predicting structures and dynamics of organic, biological and main-group inorganic molecules. The philosophy of DREIDING is to use general force constants and geometry parameters based on simple hybridization considerations, rather than individual force constants and geometric parameters that depend on the particular combinations of atoms involved in the bond,

angle, or torsion terms. DREIDING has an explicit hydrogen bond term to describe interactions involving a hydrogen atom on strong electronegative atoms. Mayo et al [61] in their reference paper for the explanation of DREIDING force field asserts that it is a good choice for predicting structures and dynamics of organic, biological, and main-group inorganic molecules. The core assumption in DREIDING is to use general force constants and geometry parameters based on simple hybridization considerations rather than individual force constants and geometric parameters that depend on the particular combination of atoms involved in the bond, angle, or torsion terms as in methods proposed before. Thus all bond distances are derived from atomic radii, and there is only one force constant each for bonds, angles, and inversions and only six different values for torsional barriers. Parameters are defined for all possible combinations of atoms and new atoms can be added to the force field rather simply.

In the AMBER force field and the CHARMM force field, there are often subtle distinctions in force constants and geometric parameters for similar atoms in slightly different environments, and it is often not clear how to generalize for new atoms or new bond types. In order to facilitate prediction of structures for molecules where there are little or no experimental data, has been developed a generic approach to force fields called DREIDING using parameters that are deliberately restricted to very simple rules. This may lead to lower accuracy for a specialized subset of molecules but has the virtue of allowing reasonably accurate predictions to be made for novel combinations of elements. The elements of the DREIDING force field are the atom types. Atoms with the same atom type are treated identically in the molecular mechanics force field. Each atom type uses a five-character identificative label where the first two characters correspond to the chemical symbol (letter plus underscore for single letter elements) and others characters are related to geometry and chemical properties. The potential energy for an arbitrary geometry of a molecule is expressed as a superposition of valence (or bonded) interactions (E_{val})that depend on the specific connections (bonds) of the structure and nonbonded interactions (E_{nb}) that depend only on the distance between the atoms

$$E = E_{val} + E_{nb} \tag{4.13}$$

In DREIDING the valence interactions consist of bond stretch (E_B, two-body), bond-angle bend (E_A, three-body), dihedral angle torsion (E_T, four-body), and inversion terms (E_I, four-body).

$$E_{val} = E_B + E_A + E_T + E_I \tag{4.14}$$

while the nonbonded interactions consist of van der Waals or dispersion (E_{vdw}), electrostatic (E_Q), and explicit hydrogen bonds (E_{hb}) terms

$$E_{nb} = E_{vdw} + E_Q + E_{hb} \tag{4.15}$$

Passing to the analysis of each single term of the equivalence, DREIDING describes the bond stretch interaction either as a simple harmonic oscillator

$$E_B = \frac{1}{2} k_e (R - R_e)^2 \tag{4.16}$$

otherwise with the Morse function

$$E_B = D_e[e^{(-\alpha nR - R_e)} - 1]^2 \tag{4.17}$$

Writing the force constant as

$$k_e = \left(\frac{\delta^2 \cdot E}{\delta \cdot R^2}\right)_{R=R_e} \tag{4.18}$$

where $\alpha = \left[\frac{k_e}{2D_e}\right]^{1/2}$

Even if the Morse function is a more accurate description, in many applications the starting geometry for new structures may be very approximate so that can be justified to use the simple harmonic oscillator because it is essential that the force field quickly adjust to the optimum geometry.

To predict the equilibrium bond distance R^0_{IJ} for bond IJ, additivity of bond radii can be postulated

$$R^0_{IJ} = R^0_I + R^0_J - \delta \tag{4.19}$$

where the bond radii $\mathbf{R^0_J}$ are based on structural data of standard reference molecules and $\delta = 0.01$ [Å]

For two bonds IJ and JK sharing a common atom, the three-body angle bend terms are all taken of the harmonic cosine form

$$E_{IJK} = \frac{1}{2}C_{IJK}[cos\theta_{IJK} - cos\theta^0_J]^2 \tag{4.20}$$

where θ is the angle between bonds IJ and JK. The equilibrium angles θ^0_J are assumed independent of I and K, and were obtained from standard reference structures of the parent hydrides. Where the structural data were unavailable, the θ^0_J were extrapolated from nearby elements in the same column of the periodic table. The harmonic angle form

$$E_{IJK} = \frac{1}{2}K_{IJK}[\theta_{IJK} - \theta^0_J]^2 \tag{4.21}$$

is in common use but should be preferred Eq. (4.20) because Eq. (4.21) does not generally leads to zero slope as θ approaches 180°. The C_{IJK} term in Eq. (4.20) is related to the force constant K_{IJK} by

$$C_{IJK} = \frac{K_{IJK}}{(sin\theta^0_J)^2} \tag{4.22}$$

For molecules with linear equilibrium geometries ($\theta^0_J = 180°$), the Eq. (4.20) can be replaced with

$$E_{IJK} = K_{IJK}[1 + cos\theta_{IJK}] \tag{4.23}$$

where the force constants for all angle bend interactions K_{IJK} is independent of I, J, K. The torsion interaction for two bonds IJ and KL connected via a common bond JK is taken of the form

$$E_{IJKL} = \frac{1}{2} V_{JK} \left\{ 1 - cos[n_{JK}(\phi - \phi^0_{JK})] \right\} \tag{4.24}$$

where ϕ is the dihedral angle (angle between the IJK and JKL planes), n_{JK} is the periodicity (an integer), V_{JK} is the barrier to rotation (always positive), and ϕ^0_{JK} is the equilibrium angle. The form of Eq. (4.24) is chosen so that the torsion energy has a zero value at the equilibrium angle and never negative. Because of symmetry (zero slope at 0° and 180°), the torsion potential must be a maximum or minimum at 0° and 180° and there are only discrete choices for ϕ^0_{JK} (multiple of $180°/n_{JK}$).The parameters V_{JK}, n_{JK} and ϕ^0_{JK} are taken as independent of I and L. In DRElDlNG the torsional parameters arc based on hybridization and are independent of the particular atoms involved. For an atom I bonded to exactly three other atoms, J, K,L, it is often necessary to include an energy term describing how difficult it is to force all three bonds into the same plane (inversion) or how favourable it is to keep the bonds in the same plane. Thus for planar molecules such as ethylene, the use of bond angle terms will not in general lead to the proper restoring force toward the planar configuration, and it is necessary to add an explicit four-body inversion term. Similarly for a nonplanar molecule, the constants used for bond angle terms may not lead to the correct inversion barrier, requiring an explicit four-body term to correctly describe the inversion energy. Denoting the angle between the IL bond and the JIK plane as ψ, has often be used the form

$$E^S_{inv}(\psi) = \frac{1}{2} K_{inv}(\psi - \psi^0)^2 \tag{4.25}$$

ψ_0 where is defined so that it is zero for a normal planar molecule (where the projection of the IL bond onto the JIK plane points away from the bisector of the IJ and IL bonds). In the literature on biological simulations, it has been more common to use expressions in which the inversion is treated as if it were an (improper) torsion (i.e. CHARMM and AMBER formulations) Although the improper torsion formulations are easier to program, it is to prefer the inversion of the general expression in Eq. (4.25) because of its close correspondence to chemical concepts. However, in order that the energy have zero slope for planar configurations ($\psi^0 \rightarrow 180°, 0°$) in Eq. (4.25) can be replaced by the form

$$E^d_{IJKL} = \frac{1}{2_I} (\cos\psi - \cos\psi^0_I)^2 \tag{4.26}$$

where

$$C_I = K_I/(\sin\psi^0_I)^2 \tag{4.27}$$

and K_I is the force constant.

The most common expressions for describing van der Waals nonbonded interactions is the Lennard-Jones 12-6 type expression (denoted LJ)

$$E^{LJ}_{vdw} = AR^{-12} - BR^{-6} \tag{4.28}$$

that can be written in a general form

$$E^{LJ} = D_0[\rho^{-12} - 2\rho^{-6}] \tag{4.29}$$

Even if there are different expressions able to describe short-range interactions, the LJ form is simpler and faster to compute. Nonbond interactions are not calculated between atoms bonded to each other (1,2 interactions) or atoms involved in angle interactions (1,3 interactions), since it is assumed that these interactions are included in the bond angle energy terms, while nonbond interactions between 1,4 neighbors can be included, excluded, or opportunely scaled according to specific material molecule properties.

Electrostatic Interactions can be calculated using the expression

$$E_Q = \beta \frac{Q_i Q_j}{\varepsilon R_{ij}} \tag{4.30}$$

where Q_i and Q_j, are charges in electron units, R is the distance in Angstrom [Å], ε is the dielectric constant (usually $\varepsilon = 1$). and β is the conversion for E_Q to kcal/mol. Interactions are not calculated between atoms bonded to each other (1,2 interactions) or involved in angle terms (1,3 interactions) since these are assumed to be contained in the bond and angle interactions. A serious difficulty is how to predict the charges. so that a method for predicting accurate charges of large molecules is still needed. Within the constraint that charges and van der Waals interactions must be centered on nuclei, it is difficult to obtain a force field that correctly predicts the structure and bond energy. As a result, DREIDING uses a special hydrogen bond term to describe the interactions involving a hydrogen atom on the very electronegative atoms associated with hydrogen bonds. In conclusion, the DREIDING force field can be considered to be the simplest generic force field capable of providing accurate geometries for organic, biological, and main-group inorganic systems. Thus, all geometric parameters arise from either addition of bond radii or angles of the simplest hydrides and only a single force constant each is used for bonds, angles, and in- versions, and only six values for torsional barriers are used. DREIDING is conceived as a hierarchy of force fields where the simple versions (neglecting more accurate analysis and some minor components of the force fields) allow rapid considerations of new structures and compositions while the more complex versions are tuned to accurately predict properties specific for particular systems. The current uncertainties in predicting the distribution of charges in molecules and in estimating the van der Waals interactions are limitations that we believe are as serious as the restricted set of parameters used in DREIDING.

The last force field here analyzed is the **Reactive Empirical Bond-Order (REBO)**, used as function for calculating the potential energy of covalent bonds and the interatomic force. In this model, the total potential energy of system is assumed equal to the sum of nearest-neighbour pair interactions which depend not only on the distance between atoms but also on their local atomic environment. A parametrized bond order function was used to describe chemical pair bonded interactions. The early formulation and parametrization of REBO was at the origins pointed out for carbon systems thanks to the effort by Tersoff in 1988 [62, 63] based on previous works of Abell (1985) [64]. The model proposed by Tersoff

could describe single, double and triple bond energies in carbon structures such as in hydrocarbons and diamonds. A significant step forward was taken by Brenner [65] introducing an extension of the potential function found by Tersoff to with the addition of two additional terms into the bond order function, in order to make applicable this approach also to further carbon configurations. Compared to classical first-principle and semi-empirical approaches, the REBO model is less time-consuming, since only the 1st- and 2nd-nearest-neighbour interactions were considered. This advantage of computational efficiency is especially helpful for large-scale atomic simulations. Despite numerous successful applications of the first-generation REBO potential function, several drawbacks have been reported (e.g. its form is too restrictive to simultaneously fit equilibrium distances, energies, and force constants for all types of covalent bonds,...). To overcome these problems, an extension of the potential by Brenner was proposed by Stuart et al. (2000) [66]. It is called the adaptive intermolecular reactive bond order (**AIREBO**) potential, in which both the repulsive and attractive pair interaction functions in REBO function are modified to fit bond properties, and the long-range atomic interactions and single bond torsional interactions are included. The general analytic form used for the intramolecular potential energy was originally derived by Abell from chemical pseudopotential theory [64]. Beginning with a local basis of unperturbed atomic orbitals, Abell showed that chemical binding energy E_b can be simply written as a sum over nearest neighbours in the form

$$E_b = \sum_i \sum_{j>i} [V^R(r_{ij}) - b_{ij} A(r_{ij})] \tag{4.31}$$

The functions $V^R(r)$ and $V^A(r)$ are pair-additive interactions that represent all interatomic repulsions (core-core, etc) and attraction from valence electrons, respectively. The quantity r_{ij} is the distance between pairs of nearest-neighbour atoms i and j, and b_{ij} is a bond order between atoms i and j. Abell argued that local coordination N is the primary quantity controlling the value of the bond order, and using a Bethe lattice derived the expression for regular structures linking the bond order with the local coordination

$$b \propto (N)^{-1/2} \tag{4.32}$$

Furthermore, the form predicts an increase in bond length and a decrease in individual bond energies as coordination increases. This is consistent with well- established chemical trends. Tersoff introduced analytic parametrized forms for the bond order that were the value of it was assumed to depend both on the local coordination and on bond angles. The general Abell-Tersoff form Eq. (4.31) is used for the total potential energy. Following the earlier hydrocarbon bonding expression, the empirical bond order function used here is written as a sum of terms [67]:

$$\overline{b}_{ij} = \frac{1}{2}[b_{ij}^{\sigma-\pi} + b_{ji}^{\sigma-\pi}] + b_{ij}^{\pi} \tag{4.33}$$

Values for the functions $b_{ij}^{\sigma-\pi}$ and $b_{jj}^{\sigma-\pi}$ depend on the local coordination and bond angles for atoms i and j, respectively. The funtcion b_{ij}^{π} is further written as a sum of two terms:

$$b_{ij}^{\pi} = \Pi_{ij}^{RC} + b_{ji}^{DH} \tag{4.34}$$

The value of the first term Π_{ij}^{RC} depends on whether a bond between atoms i and j has radical character and is part of a conjugated system. The value of the second term b_{ij}^{DH} depends on the dihedral angle for carbon-carbon double bonds. This expression combined with Eq. (4.31) is used to define the binding energy due to covalent bonding of any collection of hydrogen and carbon atoms. Atomic bonding is determined strictly from local bonding neighbours and non-local conjugation as defined below. The specific analytic forms for the pair terms and bond order function given below are somewhat complicated, and the number of parameters needed is large to accurately model bonding for the wide range of atomic models considered. To simplify the fitting procedure, a two-step process was developed. In the first step, functional forms and parameters for the pair terms in Eq. (4.31) and discrete values of the empirical bond order function were obtained. In the second step of the fitting procedure, parameters in the bond order function are fitted to the discrete values of the bond order determined in the first step, as well as additional properties such as vacancy formation energies and barriers for rotation about double bonds. In the latter step, direct correlations between individual parameters and physical properties are attempted within physically motivated choices for the functional forms. Regarding the original formulation proposed by Abell, as anticipated, it was determined that this form is too restrictive to simultaneously fit equilibrium distances, energies, and force constants for covalent bonds. This form has the further disadvantage that both terms go to finite values as the distance between atoms decreases, limiting the possibility of modelling processes involving energetic atomic adjacency. In the second-generation potential, developed principally by Brenner et al. [65] the forms

$$V^R(r) = f^c(r)(1 + Q/r)Ae^{-\alpha r} \tag{4.35}$$

and

$$V^A(r) = f^c(r) \sum_{n=1,3} B_n e^{-\beta_n r} \tag{4.36}$$

are used for the pair terms. The subscript n refers to the sum in Eq. (4.36), and r is the scalar distance between atoms. The Coulomb function used for the repulsive pair interaction in Eq. (4.35) goes to infinity as interatomic distances approach zero, and the attractive term in Eq. (4.36) has sufficient flexibility to simultaneously fit the bond properties that could not be fitted with the Morse-type terms used previously. The function $f^c(r)$ limits the range of the covalent interactions, ensuring that the interactions include nearest neighbours only. In conclusion, changes in the functional forms assumed for the potential together with an expanded fitting database produce a more reliable function for simultaneously predicting bond lengths, energies, and force constants than an earlier version of this potential.

4.3 Ginzburg-Landau method

For completeness, a latest model which addresses issues relating to systems at the microscale is the Ginzburg-Landau method, though its use appears much more complex than the previous over. The **Time-dependent Ginzburg-Landau method** (TDGL) is a microscale method for simulating the structural evolution of phase-separation principally in polymer blends and block copolymers [68]. It is based on the Cahn-Hilliard-Cook (CHC) nonlinear

diffusion equation for a binary blend and can be included into the general phase-field and reaction-diffusion models. In the TDGL method, a free-energy function is minimized to simulate a temperature variation moving the particles of the system, thus the resulting time-dependent structural evolution can be investigated by solving the TDGL/CHC equation for the time dependence of the local material concentration. Further details on this method can be found in Ginzburg et al. literary production, as is [68].

4.4 Brownian dynamics

Brownian Dynamics (BD) simulation is similar to MD simulations [69]. However, it introduces a few new approximations that allow one to perform simulations on the microsecond timescale whereas MD simulation is known up to a few nanoseconds. In BD the explicit description of solvent molecules used in MD is replaced with an implicit continuum solvent description. Besides, the internal motions of molecules are typically ignored, allowing a much larger time-step than that of MD. Therefore, BD is particularly useful for systems where there is a large gap of time scale governing the motion of different components. For example, in systems where a short time-step is required to resolve the fast motion of the solvent molecules, whereas the evolution of the slower modes of the system requires a larger time-step. However, if the detailed motion of the solvent molecules is concerned, they may be removed from the simulation and their effects on the polymer are represented by dissipative ($-\gamma p$) and random ($\sigma\zeta(t)$) force terms. Thus, the forces in the governing is expressed by a Langevin equation:

$$F_i(t) = \sum_{j \neq i} F_{ij}^C - \gamma p_i + \sigma\zeta_i(t) \tag{4.37}$$

where F_{ij}^C is the conservative force of particle j acting on particle i, γ and σ are constants depending on the system, p_i the momentum of particle i, and $\zeta(t)$ a Gaussian random noise term. One consequence of this approximation of the fast degrees of freedom by fluctuating forces is that the energy and momentum are no longer conserved, which implies that the macroscopic behavior of the system will not be hydrodynamic. In addition, the effect of one solute molecule on another through the flow of solvent molecules is neglected. Thus, BD can only reproduce the diffusion properties but not the hydrodynamic flow properties since the simulation does not obey the Navier-Stokes equations.

4.5 Infuso-Paggi stretch model

This model has been developed by Infuso and Paggi in 2014 with the aim of studying the behaviour of a discretized material taking into account the existence of non-local phenomena (binding forces) which affect the material's ability to tolerate defects or deficiencies at the atomic level within it. Even if the present method is located in this section related to molecular models, there is no relation with chemical or quantic- or nano-physical theories as for previous methods, but it is a simple choice to underline, as can be intended in the following, that the proposed approach can have an absolutely generalized valence and it is herein

adopted at the molecular scale to provide an interpretation of experimental evidence about flaw-tolerance.

4.5.1 General description

The method is based on a theory related for the most on mechanical interpretation of the discrete material and is governed by simple laws, as in elasticity by linking together stress and displacements of a discrete system of particles via a constitutive relation. The only concept in common with the methods presented above is related to the adoption also in this case of a force field governing the behaviour of the particles, which is reduced to a canonical equation of the Lennard-Jones potential. The material is represented as a discrete system, composed by particles disposed as a network of nodes (particles, molecules, or atoms) linked together by nonlinear springs for large displacements governed by a constitutive law derived from van der Waals forces. These systems are purely local if only "1-interaction" is considered, namely only neighbour nodes are directly linked together. It is possible to introduce nonlocal interactions by considering the existence of links connecting non-adjacent nodes. Apparently this kind of links are not physical bonds for the system, but can be intended as non-bonded interaction forces, in line with the terms contained within the equation of the L-J potential. For the topological characterization of the above mentioned links, a nonlocality index (NLI) inspired by network theory is proposed. After explaning the analytical content of the model and its development procedure, the mechanical response of 1D and 2D nonlocal discrete example systems is predicted according to finite element (FE) simulations based on a nonlinear spring element for large displacements implemented in the FE programme FEAP. In this way the role of nonlocal links inside the system and how these can affect the network system characteristics is investigated. Uniaxial force-displacement responses of intact and defective systems (with links or nodes removed) are numerically simulated. Strain localization phenomena, size-scale effects and the ability to tolerate defects are investigated by varying the degree of nonlocality. In the following, the tensile and compressive responses of 1D and 2D discrete sample systems of molecules with or without flaws are numerically simulated, by varying the range of the nonlocality index NLI. The distribution of the internal forces at different load levels is analyzed in relation to the topological properties of the underlying network, in order to understand the force redistribution mechanisms in the presence of defects.
The literature shows how the effect of long-range interactions into materials has been studied in mechanics through the application of different theories based on a nonlocal continuum approach. Some of them are gradient models [70, 71, 72], integral formulations [73] or also fractional calculus [74, 30], while on the other hand in the physics community were developing theories in this chapter up to here analyzed. Generally, they are based on a discrete representation of the material as a system composed of particles and molecules to analyze the behaviour of materials at the nano or micro scales. Theories from which the here proposed method draws inspirations are two presented in the previous Chapter 3. The first one, named Lattice Boltzmann model [75], even if it suffers from mesh dependency due to the consideration of links having only local valence, it has been extensively used to simulate the meso-scale behavior of concrete. The other is the three-dimensional Born model [38, 76] able to take into account nonlocal effects, which has been proposed to study the distribution of broken bonds within a homogeneous discrete mechanical system. With the increasing de-

velopment in computer science and engineering, producing increasingly powerful computers and advanced computational systems, big tridimensional discrete systems can nowadays be modelled by molecular dynamics (MD), accounting for complex nonlinear interatomic potential laws and strongly nonlocal interactions among the discrete molecules. At the mean time, in the modeling context, attempts to couple MD with FEM have been explored in [14], with the intent to mix together different analysis strategies with the goal to exploit information from them and connect discrete systems to continuum finite elements performing a scalable analyses.

4.5.2 Adopted constitutive law

The discrete system is composed by punctual entities, each of them representing a certain quantity of material, under a nonlinear interactions field represented by springs. The behaviour of these links is schematized by a generalized Lennard-Jones potential, described below and their ranging between one point to another can be expressed referring to graph theory, in which an element of the distribution is linked to a group composed by other elements only if a certain criterion is met. The here adopted strategy for the numerical solution of the problem derives from the technique developed by Paggi et al. [16], fully explained in Chapter 5, based on a CZM approach for the study of stress-separation law. For the mathematical formulation each link is implemented as a finite element defined by to points whose coordinates in the initial global undeformed reference system can be expressed as:

$$X = (X_1, Y_1, X_2, Y_2)^T \tag{4.38}$$

and each i-th node so defined in case of 2D problem has two translational degrees of freedom u_i and v_i collected in the element displacement vector u:

$$u = (u_1, v_1, u_2, v_2)^T \tag{4.39}$$

so that the nodal coordinates vector in the uploaded configuration can be written as:

$$x = X + u \tag{4.40}$$

Relative opening and sliding displacement of each single element defined by two nodes are collected in a gap vector, were the g_n value is the stretching component.

The constitutive law used here stems from a generalization of the Lennard-Jones (L-J) potentials:

$$P_{LJ} = 4\varepsilon \left[\left(\frac{r_0}{g_n} \right)^{\alpha} - \left(\frac{r_0}{g_n} \right)^{\beta} \right] \tag{4.41}$$

where ε is the depth of the potential well, r_0 is the distance at which the potential between two neighbouring atoms is equal to zero (cut-off distance), α and β are the parameters defining the shape of the L-J potential. In the classical formula of the L-J potential derived from molecular scale models, α is equal to 12 while β is equal to 6. Keeping the exponents α and β as free parameters is suggested in [77, 78, 79] to bypass the rapid decay of the law after the equilibrium point and being able compute non-bonded interactions between nodes also at

longer distances, or also for coarse-grained representations. The corresponding displacement-force relation can be obtained by differentiating the L-J potential with respect to the normal opening displacement g_n:

$$F_{IJ}(g_n) = -\frac{d}{d(g_n)} P_{LJ}(g_n) = -\nabla P_{LJ}(g_n) = -4\varepsilon \left[\alpha \left(\frac{r_0^{\alpha}}{g_n^{\alpha+1}} \right) - \beta \left(\frac{r_0^{\beta}}{g_n^{\beta+1}} \right) \right] \tag{4.42}$$

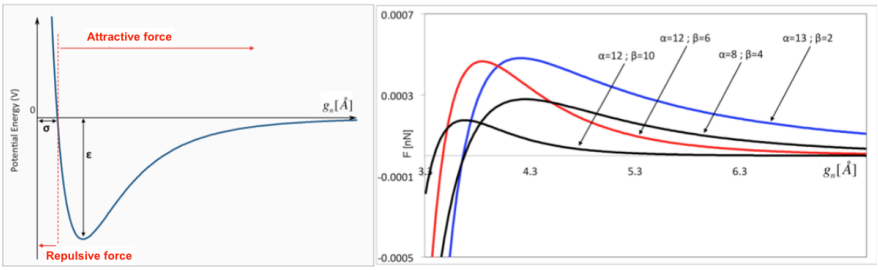

(a) (b)

Figure 4.1: (a) Lennard-Jones potential law: attractive and repulsive branches. (b) Different force-displacement forces by varying and : the $\alpha = 12\,\beta = 6$ curve refers to L-J potential in Fig. 4.1(a). The $\alpha = 13\,\beta = 2$ curve is the modified law used in this study.

As can be noticed in the proposed formula, whose trend is depicted in Fig. 4.1(a), the generalized L-J potential is composed by the sum of two terms. The first one in brackets represents the repulsive force contribution between atoms (Pauli repulsion), where the value is greater the more the particles are to approach each other, up to a theoretical asymptotic value to infinity in case of contact. The second one describe the long-range attractive force (van der Waals force), which tends to assume null value when the particles are located at a distance as not to be affected by the mutual effect. Different force-displacement curves are shown in Fig. 4.1(b) by varying the parameters of the model: specifically α and β coefficients in order to obtain a curve with the same pick value of the canonical one (12-6 coefficients) but with a smooth decay in the last part of attractive term. In the numerical simulations discussed in the next sections, the selected parameters are 13 and 2 .

4.5.3 Introduction of non-locality parameter

First of all it is necessary to understand the nonlinear behaviour of a L-J nonlocal system of atoms for different degrees of non-locality. The simplest way is considering a 1D set of nodes representing atoms equally spaced by a length l_0 along a straight line. A local system (1-interaction) would be represented by the case where only local interactions take place between each node and its nearest neighbours, as represented in Fig. 4.2(a). This is classified just as a mechanical system of nonlinear springs in series, where the removal of a link (due

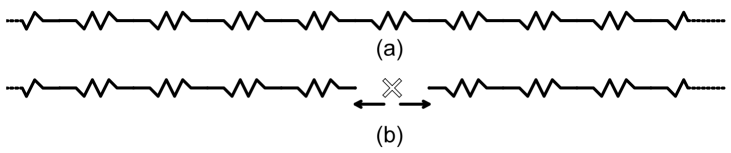

Figure 4.2: (a) System with only local links. (b) Collapse of the system due to failure of just one link.

to failure or lack of one spring) leads to the failure of the entire chain, as can be seen in Fig. 4.2(b) where the broken chain leads to the crash of the system.

Long range interactions can be modelled by introducing additional links between a generic node and the nodes located at further distances $2l_0$, $3l_0$, ... and so forth. Various systems with different degree of non-locality can be generated by changing the cut-off distance for nonlocal interactions, namely establish a maximum distance beyond which it is considered that an atom can not influence the other. For comparison purposes between possible different geometrical configuration, it is useful to introduce a dimensionless number NLI [80] (called NonLocality Index) synthesizing the topological properties of the set of links:

$$NLI = \frac{\max(l_i)}{l_0} \tag{4.43}$$

where l_i is the length of the i-th link between two connected nodes and l_0 is the length of the local link between two adjacent nodes. Therefore, NLI=1 corresponds to a local system, whereas NLI>1 refers to nonlocal systems where long range interactions between atoms are taken into consideration with a decreasing power according with the curve in Fig. 4.1.

For the sake of explanation, a first example composed by 5 nodes and and NLI=2 (so that $\max(l_i) = 2 \cdot l_0$) subjected to the uniaxial tension test it is considered, whose representation is in Fig. 4.3(a). Four local links are present and three additional links due to the consideration of long-range interactions are introduced. For a preliminary qualitative analysis of the system, it is convenient to consider a linearized version consisting in springs with different stiffnesses k_i, depending on the distance between the connected nodes. As further simplification due to the symmetry of the problem, only half model can be analyzed (Fig. 4.3(b)).

Given a certain set of stiffnesses of the links, it is possible to determine analytically the relation between the displacement Δ of the whole system and the specific displacement Δ_i of each single spring, satisfying the equilibrium and the congruence relations:

$$\begin{cases} \Delta_1 = \dfrac{k_2 + 2 \cdot k_4}{k_1 + k_2 + 2 \cdot k_4} \cdot \Delta \\ \Delta_2 = \dfrac{k_1}{k_1 + k_2 + 2 \cdot k_4} \cdot \Delta \\ \Delta_3 = \Delta \end{cases} \tag{4.44}$$

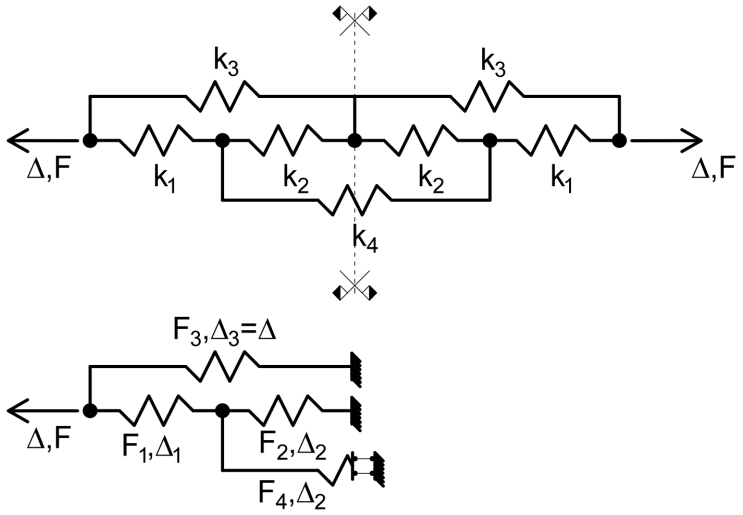

Figure 4.3: (a) Complete 5 nodes NLI=2 system. (b) Simplified configuration due to the symmetry

The relations between the spring forces and the total imposed displacement Δ are:

$$\begin{cases} F_1 = k_1 \cdot \Delta_1 = k_1 \cdot \dfrac{k_2 + 2 \cdot k_4}{k_1 + k_2 + 2 \cdot k_4} \cdot \Delta \\ F_2 = k_2 \cdot \Delta_2 = \dfrac{k_2}{k_1 + k_2 + 2 \cdot k_4} \cdot \Delta \\ F_3 = k_3 \cdot \Delta_3 \\ F_4 = k_4 \cdot 2 \cdot \Delta_2 = k_4 \cdot \dfrac{2 \cdot k_1}{k_1 + k - 2 + 2 \cdot k_4} \cdot \Delta \end{cases} \tag{4.45}$$

These analytical results provide some qualitative information on the solution of the fully nonlinear system. In general, comparing Δ_1 and Δ_2 in Eq. (4.44), we expect $\Delta_1 > \Delta_2$, which is a main difference with respect to a purely local system where all the local springs experience the same elongation. A second important strength of a nonlocal system can be understood considering that if a spring is removed, then the system has still an equilibrium configuration guaranteed by the presence of nonlocal links, whereas a purely local system would fail, due to the snatch between one node and the next one. The solution of the fully nonlinear problem is discussed in the next subsections.

4.5.4 Implementation in FEAP

In order to conduce a numerical analysis on the effect of non-locality provided by links and the effect of the lack of one of them, it is necessary to implement the method in a Finite Element software, which is here FEAP (Finite Element Analysis Program) [81].

Once defined the vector of initial nodal coordinate in the global system, as in the previous Eq. (4.38) and the vector of translational degrees of freedom as in Eq. (4.39) leading to the expression of the nodal coordinates vector in the uploaded configuration (Eq. (4.40), a local reference system is now introduced, since the constitutive relation is usually defined in this frame.

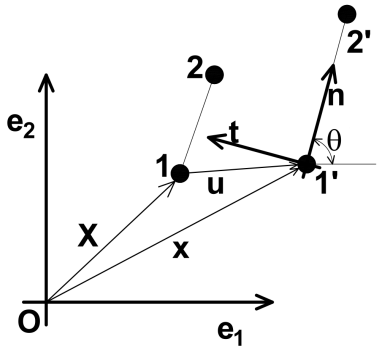

Figure 4.4: Reference coordinate systems for the large displacements analysis

Hence, the normal vector n pointing from node $1'$ to node $2'$ and the vector t perpendicular to the link are introduced, see Fig. 4.4. The origin of the local reference system is in the node $1'$. Such a frame is rotated by an angle with respect to the axis of the global reference system. The following rotation matrix R can be introduced:

$$R = \begin{bmatrix} \cos\theta & \sin\theta \\ -\sin\theta & \cos\theta \end{bmatrix} \tag{4.46}$$

The relative opening and sliding displacements between the nodes $1'$ and $2'$ are collected in the gap vector $\mathbf{g}$, given by the product between a matrix operator $\mathbf{L}$ and the position vector $\mathbf{x}$ containing the coordinates of the element nodes in the updated configuration:

$$\mathbf{g} = \mathbf{L} \cdot \mathbf{x} \tag{4.47}$$

where the $\mathbf{L}$ matrix operator has the form:

$$\mathbf{L} = \begin{bmatrix} -1 & 0 & 1 & 0 \\ 0 & -1 & 0 & 1 \end{bmatrix} \tag{4.48}$$

LOOP	until the convergence of the Newton-Raphson scheme
CALL	to the element subroutine
INPUT:	**X**initial nodal coordinates, **u** nodal displacements
COMPUTE:	updated coordinates $\mathbf{x} = \mathbf{X} + \mathbf{U}$
	rotation matrix **R** and gap vector **g** (Eq. (4.48)
	gap vector in the local frame $\mathbf{g_{loc}}$ (Eq. (4.49))
	local force vector $\mathbf{F_{loc}}$ and the tangent operator **C** (Eq. (4.51))
OUTPUT	residual vector **p** and tangent matrix **K** (Eq. (4.50))
END LOOP	

Table 4.1: Sequence of operations for each interface element

so that the gap vector between the nodes in the local reference system is obtained by the product between the previously defined rotation matrix **R** and the gap vector **g**:

$$\mathbf{g_{loc}} = \mathbf{R} \cdot \mathbf{g} \tag{4.49}$$

The acting force according to the L-J potential, as defined in Eq. 4.42 directed along the normal vector **n** is collected in the local force vector, $\mathbf{F} = (F_{LJ}, 0)^T$.

Through the application of the Principle of Virtual Work, where each element contribution is related to the scalar product between the force vector and the gap vector as for a classical interface element [16,82], its virtual variation and fully consistent linearization have to be performed in order to derive the residual vector **p** and the stiffness matrix **K** for the application of the Newton-Raphson iterative procedure. After a lengthy calculation can be obtained:

$$\begin{cases} \mathbf{p} = (\mathbf{RL} + \frac{\partial \mathbf{R}}{\partial \mathbf{u}}\mathbf{Lu})^{\mathbf{T}}\mathbf{F_{loc}} \\ \\ \mathbf{K} = \mathbf{K_{mat}} + \mathbf{K_{geom}} \\ \\ \mathbf{K_{mat}} = \mathbf{L^T R^T C R L} \\ \\ \mathbf{K_{geom}} = \mathbf{u^T L^T} \frac{\partial R^T}{\partial u} C \frac{\partial R}{\partial u} Lu + \left(L^T R^T C \frac{\partial R}{\partial u} Lu + u^T L^T \frac{\partial R^T}{\partial u} CRL \right) \end{cases} \tag{4.50}$$

where **C** is the tangent operator stemming from the consistent linearization of the local force vector $\mathbf{F_{loc}}$ with respect to the local gap vector $\mathbf{g_{loc}}$

$$\mathbf{C} = \begin{bmatrix} \frac{\partial F_{IJ}}{\partial g_n} & 0 \\ 0 & 0 \end{bmatrix} \tag{4.51}$$

whereas the term $\partial R/\partial u$ related to the differentiation of the rotation matrix with respect to the displacements vector is a third order tensor. This mathematical formulation has been implemented in the Finite Element Analysis Program FEAP. A flow-chart of the operative procedure followed by FEAP for the calculation is reported in Tab. 4.1.

Results provided from the software, containing numerical values of force and displacement at each simulation steps are collected into output files and post-processed with MATLAB in order to gain to a graphical representation of results.

4.5.5 Example: flaw-tolerance and stress distribution

The first case-study regards the mono-dimensional discrete system depicted in Fig. 4.5 with different values of NLI equal to 1, 2 or 3. In the local system characterized by springs in series (Fig. 4.5(a)), the forces and the elongations are the same for all the springs. Each spring presents an increasing branch until the achievement of the maximum force and then a softening, according to the L-J constitutive equation Eq. (4.42), with the critical point of a possible rupture causing collapse of the system. In case of NLI=2, the situation is much more complex. Due to the symmetry, it is sufficient to comment on the behaviour of the springs 1, 2, 5 and 6. The forces in such springs vs. the total imposed displacement Δ are shown in Fig. 4.6(a). The positions of the nodes of each spring vs. Δ are illustrated in Fig. 4.6(b). From these diagrams we note that springs 1 and 5 have elongations monotonically increasing during the simulation. The force level of the local spring 1 is much higher than that of the nonlocal spring 5. This is due to the fact the spring 5 is connecting nodes that are at an initial distance twice larger than that of the spring 1. Springs 2 and 6, after an initial positive relative displacement between their connected nodes, then experience a progressive reduction of their elongations with a consequent elastic unloading.

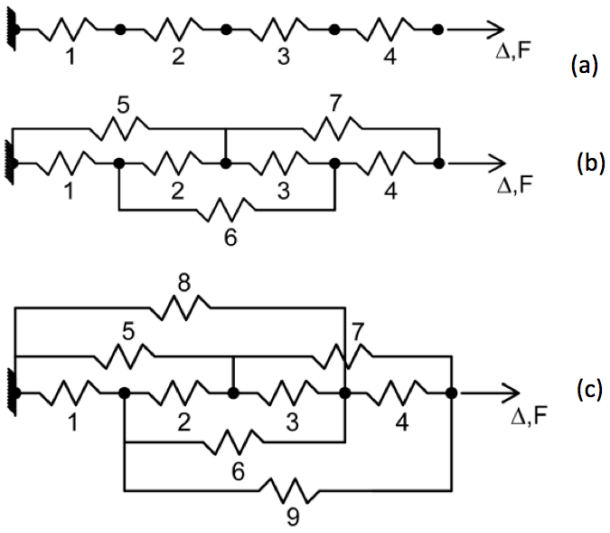

Figure 4.5: Sketch of the discrete system with 5 nodes by varying NLI. (a) NLI=1; (b) NLI=2; (c) NLI=3

A similar response takes place for the system with NLI=3. Springs 1, 5 and 6 have an

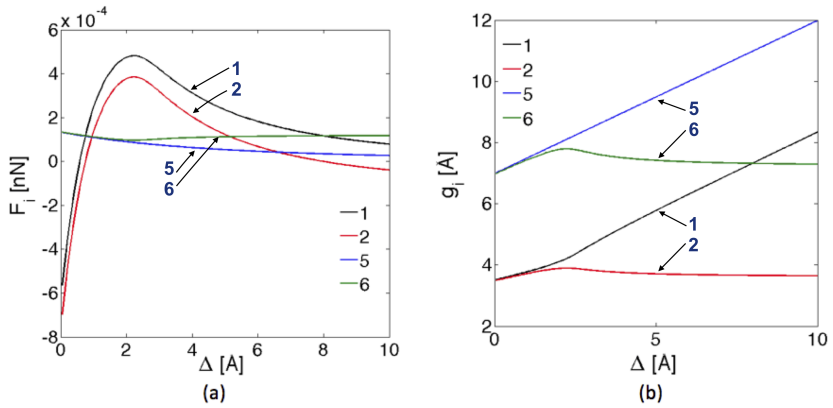

Figure 4.6: System with 5 nodes and NLI=2. (a) Spring forces vs. imposed displacement. (b) Spring nodal positions vs. imposed displacement

elongation monotonically increasing with time, whereas springs 2 and 6 experience an elastic unloading after an initial increased separation, as shown in Fig. 4.7(a) and (b).

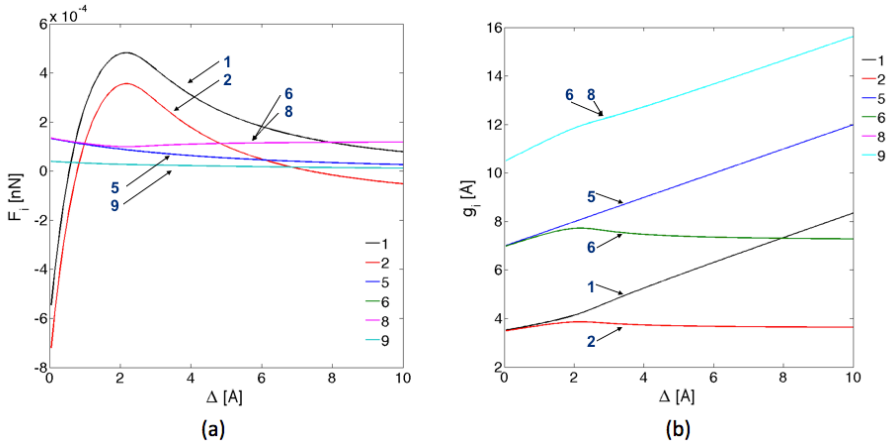

Figure 4.7: System with 5 nodes and NLI=3. (a) Spring forces vs. imposed displacement. (b) Spring nodal positions vs. imposed displacement

A comparison between the force-displacement curves of the various systems depending on NLI is shown in Fig. 4.8(a). The nonlocality increase the peak force observed in case of NLI=1. Moreover, a gain in the capacity of tolerating defects takes place, as we will quantify in the next subsection. The difference between the responses of the systems with NLI=2 and NLI=3 is quite small, in line with the observation that nonlocal interactions are rapidly

decaying by increasing the nodal distance, see Fig. 4.8(b). For a given degree of nonlocality, e.g., NLI=2, the effect of the size of the system can be explored by increasing the number of nodes at a distance l0 for each pair (see Fig. 4.8(b)). As a trend, the peak force does not change, whereas the post-peak response becomes more and more brittle by increasing h.

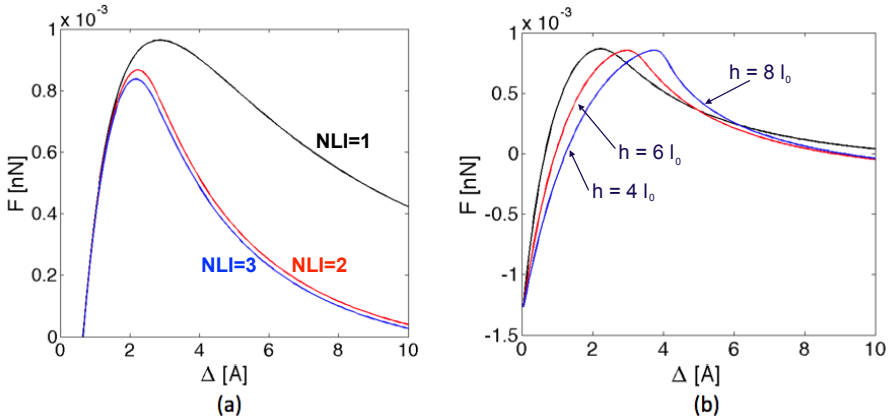

Figure 4.8: Global force vs. global displacement curves. (a) The effect of NLI for a system with a size $h = 4 \cdot l_0$. (b) The effect of the size h of the system with NLI=2

Let now to take into consideration a system similar to the previous one, again composed by 5 nodes ($h = 4 \cdot l_0$), disposed as shown in Fig. 4.9(a), where one of the local link is broken or missing. This can be the case in nanoscopic systems when there is an atomic vacancy or a weakened interatomic potential due to dislocations. The problem is solved numerically again through the algorithm proposed before, under displacement control. During the simulation a very complex behaviour of the various springs is observed, directly dependent by the presence of the lack of a link inside the system. In order to express some comments about that, it is useful to analyze the force-nodal distance curve of each spring as report in Fig. 4.9(b). All the "1-interaction" springs in series (named 1, 3, 4) are initially in the initial branch of the van der Waals forces and all of them experience an elastic unloading (see the direction of the arrows in Fig. 4.9(b)). Springs 5, 6 and 7 used to model long-range interactions ("2-interaction") are all in the softening branch of the van der Waals force diagram. The spring 7 experiences an increasing in the corresponding load level due to the shortening of springs 3 and 4. On the other hand, 5 and 6 increase their elongation monotonically in time. The global response of the system, shown in Fig. 4.10(a) presents a global softening curve, due to the heavy damage induced by the removal of a local link. However, the defect can be tolerated thanks to the nonlocality and the load-carrying capacity of the system is an increasing function of NLI (higher NLI leads to higher loads), see Fig. 4.10(a). On the oder hand, by increasing the system size and removing only the second local spring in all the cases, the force is an increasing function of h as shown in Fig. 4.10(b), as the same was observed in case of a defect-free system.

Further application of the same model can be found across a two-dimensional model,

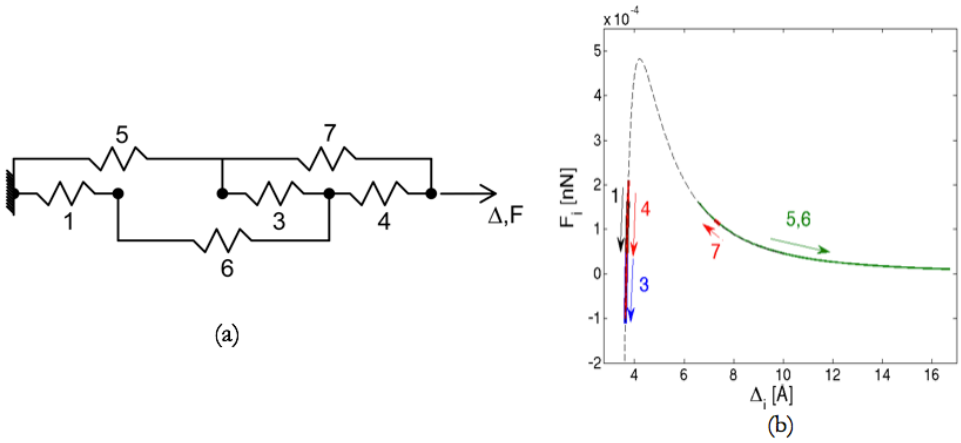

Figure 4.9: (a) Geometry of the 5 nodes system without the link no. 2. (b) Force-displacement diagram of the springs

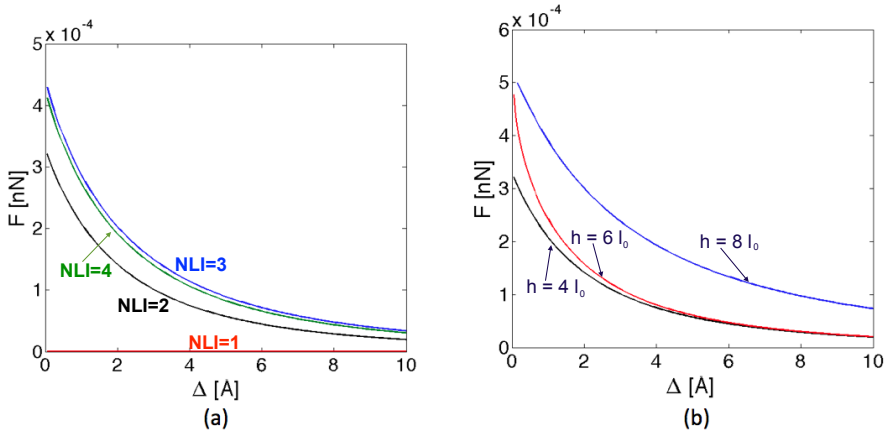

Figure 4.10: Global force-displacement response. (a) The effect of NLI ($h = 4 \cdot l_0$). (b) The effect of the system size (NLI=2)

intended as a collection of nodes and links forming a geometrical grid in the plane. In sake of praticity, has been chosen an hexagonal disposition of nodes is adopted, so that resulting shape is similar to an honeycomb geometry, that is the typical molecular configuration of a graphene sheet. The NLI definition is the same also for this case, which can be identified as the maximum cut-off radius for long range interactions and the length of the link for pure local connections. The numerical construction of the finite element meshes for numerical

simulations in a bit more complex than one-dimensional case and requires the definition of the list of nodes and the element connectivity matrix. For the latter need, a pre-processor written in MatLab has been developed where, centering in the i-th node of the grid, all the other nodes within the cut-off radius defined by the product $NLI \cdot l_0$ are identified and spring elements are inserted. Clearly, by increasing NLI and the size of the system, the computational complexity drastically increases with a more than proportional law, so that the numerical simulation on personal computer ca not be completed for big systems or high NLI, needing a parallel computation strategy to reduce requested calculation time. As an illustrative example, let us consider square grids with l_0 = 3.5Å and with lateral size 14x14Å, 31x31Å, and 70x70Å, respectively. For each grid, the NLI can range from 1 up to a maximum value NLI_{max} given by the longest distance between two nodes belonging to the system. For the three system sizes considered, we have NLI_{max} = 6,12 and 29. The maximum number of links in case of NLI_{max} is equal to 600 for the smallest system, 4,851 for the intermediate system, and 126,756 for the largest one.

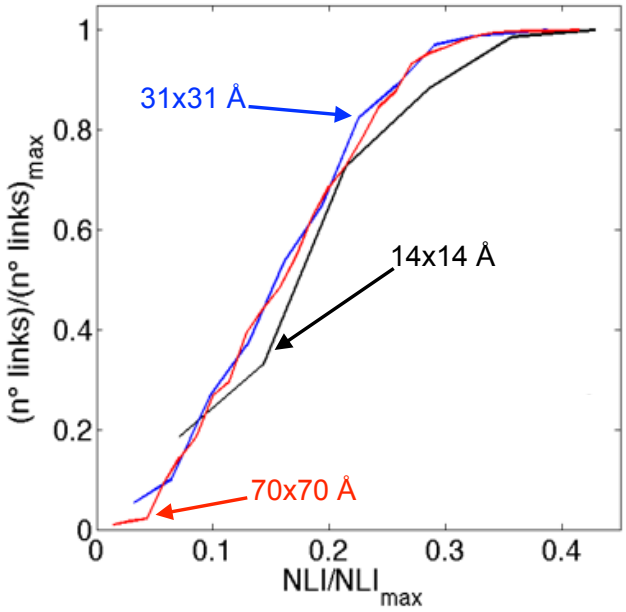

Figure 4.11: Number of links vs. NLI in dimensionless form, for 3 systems with different sizes

In dimensionless form, as reported in Fig. 4.11, the ratio between the number of links and the maximum value has a nonlinear dependency with the ratio between NLI and NLI_{max}. The deviation from linearity observed for all the cases when NLI is approaching NLI_{max} is due to the finite size of the system. As far as the numerical simulations are concerned, the increase of NLI leads to a transition from a sparse connectivity matrix to a very dense one, see Fig. 4.12 where systems with NLI=1, 2 and 3 are compared.

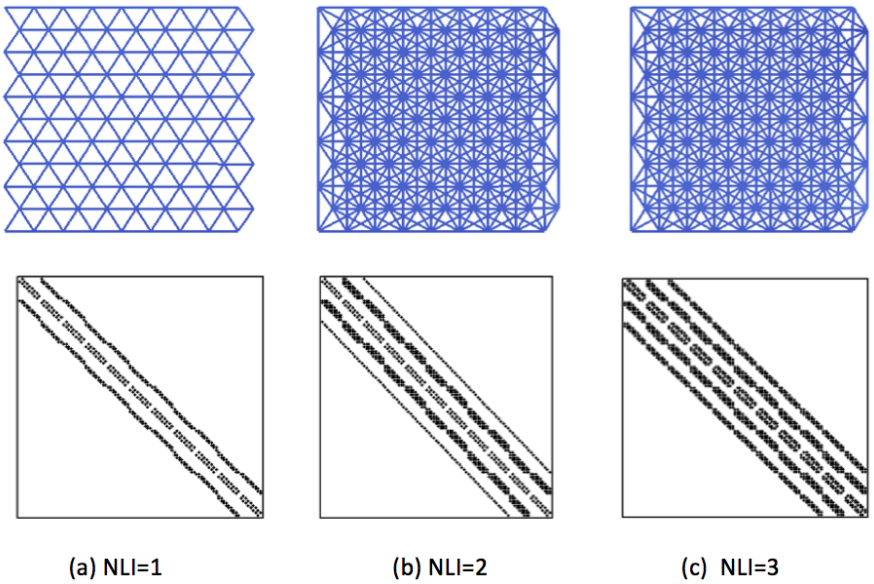

Figure 4.12: (a) Representation of the two-dimensional hexagonal geometric network by varying NLI. (b) Connectivity matrices for the same NLI

The next step is the study of the behaviour of the hexagonal net bi-dimensional system previously proposed, subjected to uniaxial tension in the vertical direction, simulating a simple tensile test under displacement control. In the same way as done for one-dimensional case are here compared one case where all the links are present with other three cases presenting defects: (1) removal of a single node in the centre of the specimen; (2) removal of 2 not adjacent nodes; (3) removal of 2 adjacent nodes. Three different values of NLI are considered for each system: NLI=1 (local system), NLI=2, NLI=3. In Fig. 4.13 it is presented a sketch of the three configurations with defects, choosing the case with NLI=1 for greater graphic clearness for the benefit of the reader.

The global force vs. displacement curves for all the examined configurations are grouped in Fig. 4.14. For a given value of NLI, can be noticed that Case 3 leads to the higher load and stiffness reduction, meaning that removal of two neighbour nodes is more impactful on the structure than two nodes not near one another. Case 1 is the less critical one, whereas Case 2 provides an intermediate response. This trend is in line with the fact that the removal of two adjacent nodes is particularly critical and induces a significant number of removed links, higher than other cases of removal. The effect of NLI is particularly important. The system with NLI=1 is initially compressed, due to the choice to position the nodes initially at a distance slightly smaller than the equilibrium one given by the L-J potential. By increasing NLI, further links in a tension state are introduced and reduce this initial compressive stress state. Although the nodes removal has a higher impact on the systems characterized by higher nonlocality indices since a larger number of links is removed, the force is an increasing

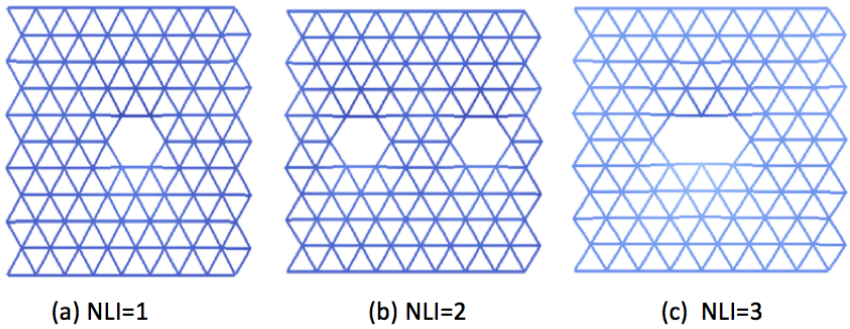

Figure 4.13: Representation of the two-dimensional hexagonal network with different types of flaws (NLI=1)

function of NLI, thus showing that nonlocality has a very important role for flaw-tolerance.

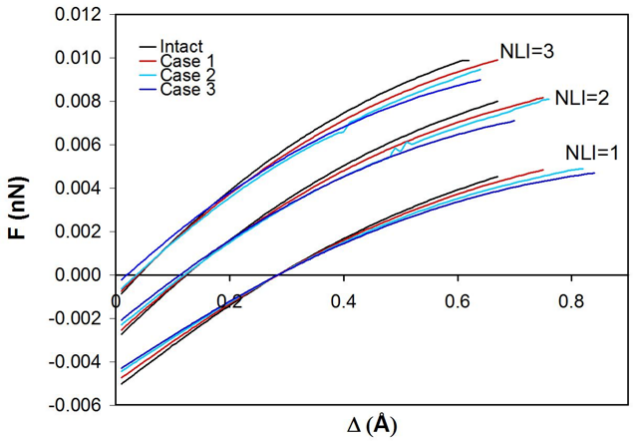

Figure 4.14: Comparison of the force-displacement curves varying NLI, depending on the type of defect

In conclusion, taking into consideration nonbonded interactions between nodes according to the L-J generalized potential, the influence of non-locality on the mechanical response of discrete systems has been investigated. In the one-dimensional case, has been observed a complex behaviour of the links correlated to the considered non-locality index NLI. In the case of a link absent or removed, a phenomenon analogous to strain localization observed in continuum systems has been evidenced. Results on two-dimensional systems have also shown the important role exerted by the non-locality on the load carrying capacity of the system and its ability to tolerate defects or vacancies. It is possible to affirm that the proposed

approach and its further extension to 3D can be applied to predict strength and stiffness of discrete systems as, e.g., 2D graphene layers of carbon-carbon bonds, or nanotubes, represented by a 3D network of carbon atoms. Moreover, a constitutive law based on L-J potential is definitely useful to study problems where interactions between two different materials are governed by nonbonded interacrions. This is for example the case of an interphase boundary interaction between collagen and graphene. Future developments regarding the implementation of bonded interactions, including not only stretching energy, but also bending and torsion energy contributions to describe physical links between atoms or molecules, are envisaged.

4.6 MD-FEM MODEL

One of the weakness of micro-scale analysis methods proposed before is the high computational cost required for a simulation of the atomic interactions, so that classical molecular dynamics (MD) is restricted to structures containing a low number of atoms such as carbon nanotubes. In order to bypass the problem and extend the analysis also to wider range of molecules and to slightly different problems, it is necessary to study the possible integration of pure MD models into Finite Element Method (FEM) [83], which is commonly used for the analysis at upper scales. To gain the result, it is necessary to introduce a new type of finite element in order to operate into force fields that include multi-body potentials. These elements have to take into account not only bond stretch but also bending, torsion and inversion without using rotational degrees of freedom. Since natural lengths and angles are implemented as intrinsic material parameters, the developed Molecular Dynamic Finite Element Method (MDFEM) starts with a conformational analysis.

4.6.1 Attempts to couple MD and FEM

Since MD technique do not belong to standard applications of FEM codes, the user has to make needed adjustments to have a correct formulation of the problem and a suitable method to solve it. Up to now, mainly standard elements such as beam or shell elements have been used to calculate nano-structured materials, see e.g. [84]. However, an atom, as a point object, cannot have rotational degrees of freedom which complicates the application of these standard elements. For instance, the bending of a beam leads to improper constraints in adjacent molecular parts. To overcome this disadvantage, in the following a new 4-node element is introduced, which has only translational degrees of freedom and thus is capable of properly representing the different nonlinear force field potentials.

4.6.2 Nasdala-Kempe-Rolfe 4-nodes element method

One of the most well-posed models, is the approach proposed by Nasdala and Ernst [85], where force field method utilizes nonlinear spring elements for the reproduction of both chemical and physical bonds. The stiffness of each individual spring element does not only depend on the nearest neighboring atoms (nonlocal model), but also crucially on the subsequent atoms or rather parts of molecules. Therefore, in each particular case has to be checked whether the selected force field approach contains all the needed information for

the molecules of interest. Among the most well-known approaches (see point 4.2 of this same work for the description of those MD force fields), in this case has been chosen the DREIDING force field. The potential energy is expressed as:

$$E = E_{val} + E_{nb} \tag{4.52}$$

as the sum of two contribution: energy of the valence (or bonded) interactions, E_{val}, and energy of non-bonded interactions, E_{nb}. By its own, the valence bond (chemical) energy is given as

$$E_{val} = E_B + E_A + E_T + E_I \tag{4.53}$$

where E_B, E_A, E_T and E_I are bond stretch, angle bend, torsion and inversion energy, respectively. The energy of non-bonded interactions (physical bonds)

$$E_{nb} = E_{vdW} + E_Q + E_h b \tag{4.54}$$

and it consists of energy of van der Waals forces, E_{vdW}, electrostatic forces, E_Q, and hydrogen bonds, E_{hb}. Most of these interactions can be computed using common normal springs. For the computation of the angle bend energy E_A and the torsion energy E_T, the interactions between 3 or rather 4 atoms has to be computed so that standard springs or other standard elements are not suitable for this purpose, reason that imply the adoption of a special 4-node-element, as shown in the following sections. The inversion energy also takes into account the interactions between 4 atoms. It arises when an atom moves out of the plane defined by the three adjacent atoms, as can be read in [61] in the general DREIDING analysis. In order to understand the first component of the force field, related to the bond stretch of neighbour atoms, it necessary to define the equilibrium distance, as reported in Fig. 4.15:

$$R_e = R^0_{IJ} = R^0_I + R^0_J - \delta \tag{4.55}$$

between two atoms I and J does not only depend on the two involved atoms, but in particular also on the conformation of subsequent parts of the molecule, taking into account the specific chemical element bonding and the geometry of the same molecule. Namely, a carbon atom may have a certain equilibrium distance from an other different in case it is part of an hexagonal net (graphene), or involved in a hydrocarbon chain (being in both cases linked with another Carbon atom). The value of atomic radius for each specific chemical element can be found in databases available in bibliography and nowadays also on the internet. A slightly change of the distance R between two atoms I and J leads to a change of the bond stretch energy E_B.

For small displacements it is possible to use a linearized approach:

$$E^{lin}_B = \frac{1}{2} k_e (R - R_e)^2 \tag{4.56}$$

and the derivative of the harmonic potential energy E_B with respect to the geometric distance R gives the spring force

$$F^{lin}_B = \frac{\mathrm{d}E_B}{\mathrm{d}R} = k_e (R - R_e) \tag{4.57}$$

and the second derivative gives the spring stiffness

$$c_B^{lin} = \frac{\mathrm{d}F_B}{\mathrm{d}R} = k_e \tag{4.58}$$

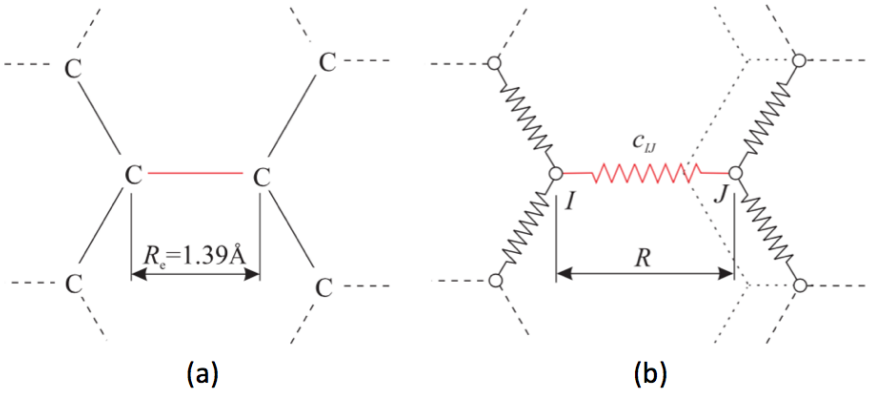

Figure 4.15: Modelling of bond stretch with normal spring elements: (a) zero-energy state of carbon atoms and (b) increase of potential energy E_B as a result of bond stretch.

Large deformations lead to nonlinear bonding forces. Therefore, often the Morse function is applied

$$E_B = D_e[\exp(-\alpha n(R - R_e)) - 1]^2 \tag{4.59}$$

The first derivative gives the corresponding spring force

$$F_B = -2\alpha n D_e[\exp(-2\alpha n(R - R_e) - \exp(-\alpha n(R - R_e))] \tag{4.60}$$

while the second derivative gives the nonlinear spring stiffness

$$c_B = c_{IJ} = (-2\alpha n)^2 D_e[\exp(-2\alpha n(R - R_e)) - 0.5\exp(-\alpha n(R - R_e))] \tag{4.61}$$

The parameter n indicates the bond order between the two atoms I and J. This parameter, as well as the corresponding stiffness, are provided in [61] for a range of molecules. The parameter α results

$$\alpha = \frac{1}{n}\sqrt{\frac{k_e}{2D_e}} \tag{4.62}$$

where k_e is the stiffness of a simple harmonic oscillator and D_e represents the finite energy for breaking the bonding according to the Morse function. The nonlinear problem can be linearized ($R \to R_e$) for small deformations. The next step is the definition of the energy to take into account the angle variation between two consecutive couples of atoms (i.e. IJ and

JK). A bending energy E_A is different from zero if the angle Θ_{IJK} between the bonds IJ and JK changes from an initial equilibrium angle. For example, if the rotation a of bond JK and the rotation b of bond IJ are given, we would obtain an angle of $\Theta_{IJK} = \Theta_J^0 + \beta - \alpha$ for the equilibrium state shown in Fig. 4.16(a). It should be noticed, that the bonds next to IJ rotate by the angle β as well and that the bonds next to JK rotate by the angle α. The third angle is $\gamma = \dfrac{\alpha + \beta}{2}$.

The expression for small rotations $\Theta IJK \rightarrow \Theta_J^0$ can be obtained from a linearization of the general approach related to large displacement by replacing the coefficient $C_{IJK} = \dfrac{K_{IJK}}{\sin^2 \Theta_J^0}$ In the general formulation leading to the following bending energy

$$E_A = \frac{1}{2} C_{IJK} [\cos \Theta_{IJK} - \cos \Theta_J^0]^2 \tag{4.63}$$

several energy-free equilibrium angles might exist. The corresponding moment and nonlinear rotational spring stiffness read

$$M_A = -C_{IJK} [\cos \Theta_{IJK} - \cos \Theta_J^0] \sin \Theta_{IJK} \tag{4.64}$$

and

$$c_A = C_{IJK} [\cos \Theta_{IJK} \cos \Theta_J^0 - \cos(2\Theta_{IJK})] \tag{4.65}$$

While the bond stretch energy E_A can be modelled with normal spring elements, since it involves only an axial stiffness, it is quite complicated to consider the bending energy E_B. A model using beam elements leads to wrong results, i.e. wrong angles for the adjacent bonds, as illustrated in Fig. 4.16(b). This behavior can be explained by the fact that atoms have no rotational degrees of freedom, in contrast to the nodes of beam elements. Beam elements transfer these rotations to other bonds. Fig. 4.16(c) shows an approach with beam elements which are connected by joints to eliminate all rotational degrees of freedom. In order to avoid under-determined systems, constraints have to be introduced. For example, the rotation of the beam element which represents the bond JK is set to $\frac{\beta+\gamma}{2}$ at node J. On the one hand, this approach has the advantage that, in contrast to the pure beam approach (3 translational + 3 rotational = 6 dof per node in 3D) given in Fig. 4.16(b), only half the number of degrees of freedom (3 translational + 0 rotational = 3 dof per node in 3D) has to be used. On the other hand, however, the adjacent parts of molecules are still rotated by an incorrect angle. An overlay technique is presented in Fig. 4.16(d) to overcome these limitations. This approach uses 3-node bending elements consisting of two beam subelements with the ends being rigidly fixed to each other. The rotational degrees of freedom of this 3-node bending element (in Fig. 4.16(d) connecting nodes I, J and K) are eliminated by joints. Please note, that each node has to be connected to all pairs of neighboring atoms by means of these 3-node bending elements.

Consequently, node J, for example, is part of nine 3-node bending elements: 3 times as a emiddle node and 6 times as an end node. The superposition of elements has no influence on the number of degrees of freedom since the same number of nodes are used. In fact, the total number of degrees of freedom is even lower than with the pure beam approach because

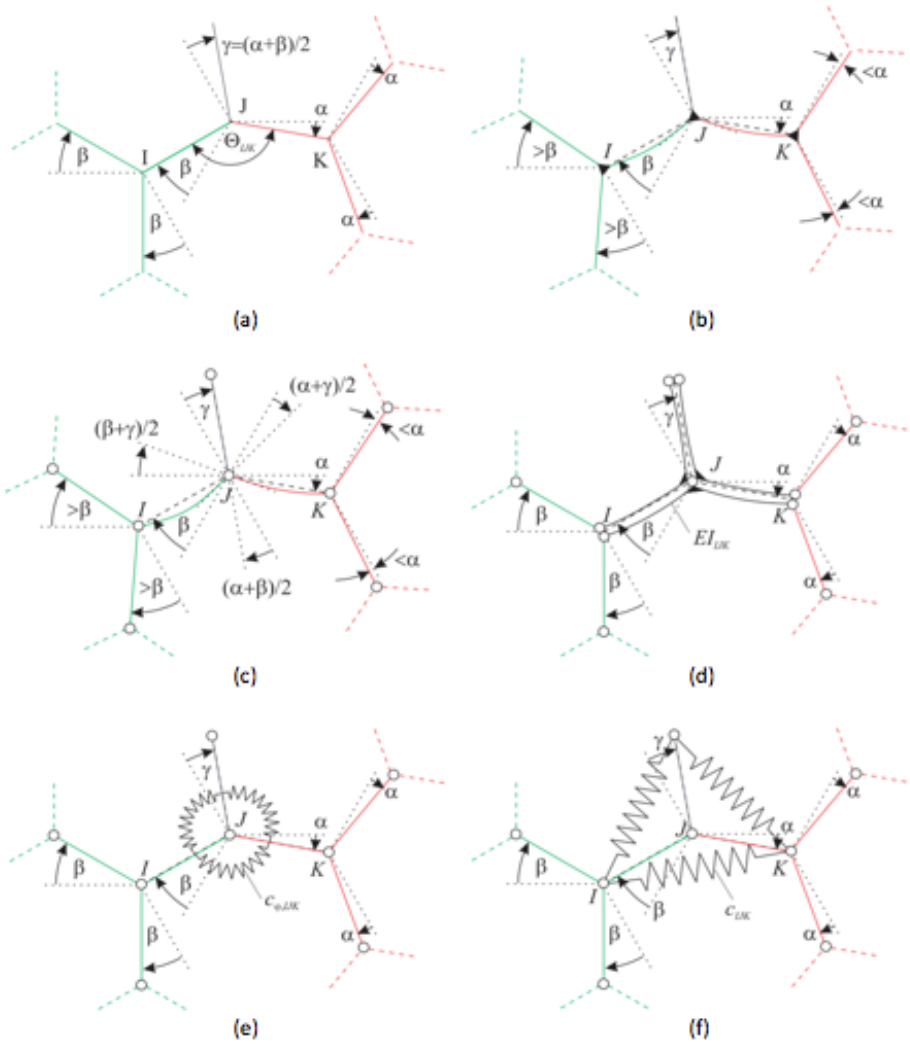

Figure 4.16: Modelling of angle bend: (a) increase of potential energy E_A as a result of angle bend H_{IJK}, (b) beam elements, (c) constraints, (d) superposition technique, (e) rotational spring elements and (f) normal spring elements

only translational degrees of freedom are needed. Two further approaches that are equivalent to the overlay technique and, thus, are also capable of representing the atomic interactions are shown in Figs. 4.16(e) and 4.16(f). Instead of four beam elements, a truss element can be placed between two neighboring atoms I and J and the bond angle energy is represented by rotational or rather normal springs. The use of normal springs has the advantage that

no rotations are introduced in the model. On the other hand, there is the disadvantage that the bending potential given in Eq. (4.63) can only be calculated by means of too complex geometrical relationships for large deformation. Therefore, the use of rotational springs is preferred for sake of simplicity. Since the nodes do not have rotational degrees of freedom, the angle θ_{IJK} of Eq. (4.65) has to be determined from the translational degrees of freedom of the nodes I, J and K. The last component of deformation that has to be analyzed is the twisting, defining, according to the DREIDING approach, the twisting energy with the expression

$$E_T = E_{IJKL} = \frac{1}{2} V_{JK}[1 - \cos[n_{JK}(\phi - \phi^0_{JK})]] \tag{4.66}$$

that is a function of the dihedral angle $\phi = \phi_{IJKL}$ which is defined by the two planes IJK and JKL. From this, we get the corresponding twisting moment as:

$$M_T = \frac{\mathrm{d}E_T}{\mathrm{d}\phi} = \frac{1}{2} V_{JK} n_{JK} \sin[n_{JK}(\phi - \phi^0_{JK})] \tag{4.67}$$

and the nonlinear spring coefficient is:

$$c_T = \frac{dM_T}{d\phi} = \frac{1}{2} V_{JK} n^2_{JK} \cos[n_{JK}(\phi - \phi^0_{JK})] \tag{4.68}$$

where the equilibrium angle ϕ^0_{JK} depends on the interacting atoms involved in the element as well as the stiffness V_{JK} that is a parameter provided by experiments.

In case of small deformations, Eq. (4.66), (4.67), (4.68) can be linearized ($\phi > \phi^0_{JK}$), yielding the twisting energy

$$E^{lin}_T = \frac{1}{4} V_{JK} n^2_{JK} (\phi - \phi^0_{JK})^2 \tag{4.69}$$

the linear twisting moment

$$M^{lin}_T = \frac{1}{2} V_{JK} n^2_{JK} (\phi - \phi^0_{JK}) \tag{4.70}$$

and the spring constant

$$c^{lin}_T = \frac{1}{2} V_{JK} n^2_{JK} \tag{4.71}$$

The example of the 180° - element (equilibrium point) is shown in Fig. 4.17 illustrating how the twisting energy E_{IJKL} can be represented correctly using the overlay technique in combination with beams and torsional springs. Based on the approach illustrated in of Fig. 4.16(d), two beam elements are connected together. The rotational degrees of freedom of the rigid joints can be eliminated at the element level, so that only translational degrees of freedom have to be considered. In order to calculate the twisting energy correctly, the beam elements may deform only within their planes IJK or rather JKL. In the direction perpendicular to the planes, they must remain rigid. In order to fulfil this requirement, the in-plane flexural stiffness EI_ζ (see Fig. 4.18(a)) is selected according to the stiffness given in for angle bend and the out-of-plane flexural stiffness EI_η is set to infinity. The twisting loading given in Fig. 4.17(d) leads to the deformation shown in Fig. 4.17(a)and 4.17(c). The resulting bending and twisting moments can be taken from Fig. 4.17(e) and 4.17(f).

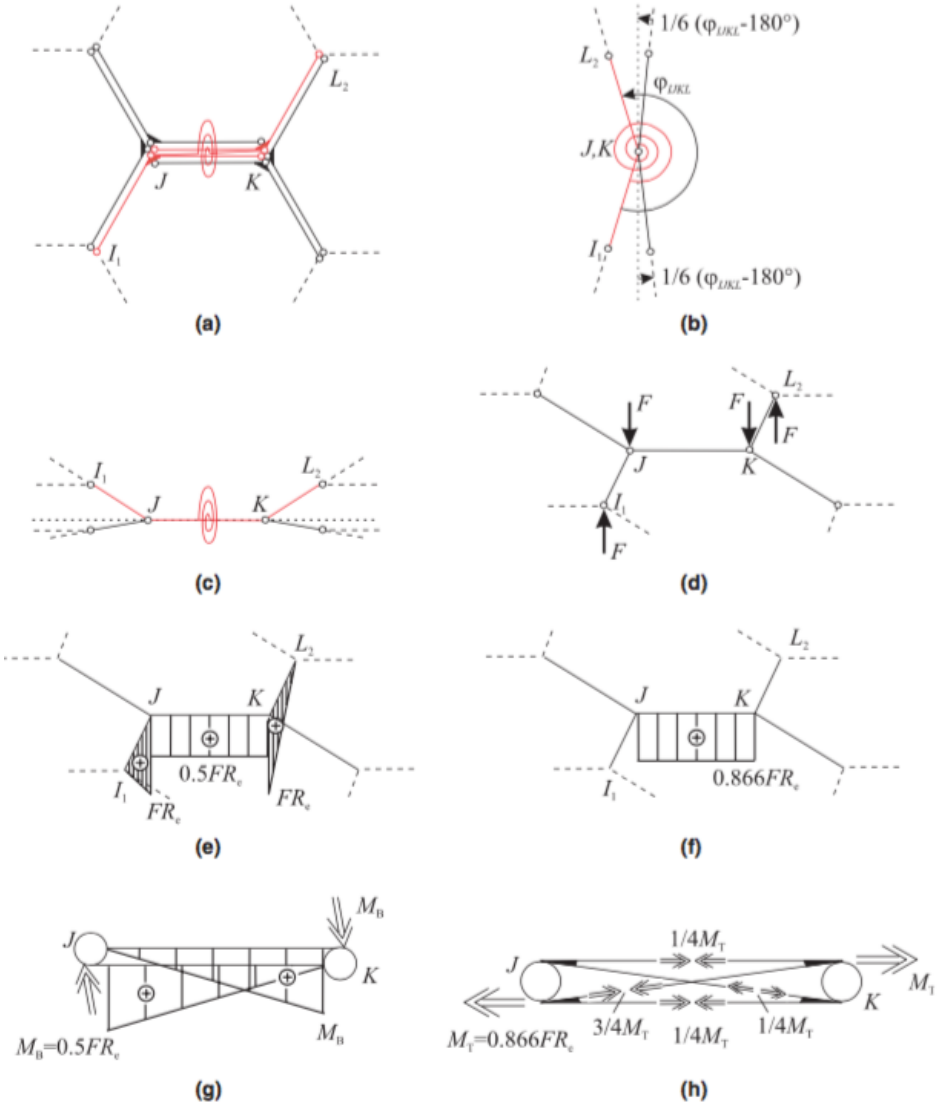

Figure 4.17: Modelling of torsion with 4-node element: (a) top view, (b) side view, (c) front view, (d) 3D view, (e) bending moment M_B, (f) torsional moment M_T, (g) superposition of all bending moments and (h) superposition of all torsional moments

The stored energy goes to zero due to the infinite flexural stiffness, so that the twisting energy E_T is produced exclusively by the torsional springs. For demonstration purposes, we

assume small deformation. Then,

$$\begin{aligned} E_T^{lin} &= \lim_{EI_\eta \to \infty} \int -\frac{1}{2} M_B w'' \, \mathrm{d}\zeta + \int_{\zeta_J}^{\zeta_K} \frac{1}{2} M_T \phi' \, \mathrm{d}\zeta \\ &= \lim_{EI_\eta \to \infty} \int \frac{1}{2} \frac{M_B^2}{EI_\eta} \, \mathrm{d}\zeta + \int_{\zeta_J}^{\zeta_K} \frac{1}{2} \frac{M_T}{GI_T} \, \mathrm{d}\zeta \\ &= 0 + \int_0^{R_e} \frac{1}{2} \frac{M_T^2}{c_T^{lin} R_e} \, \mathrm{d}\zeta \end{aligned} \tag{4.72}$$

The overall bending and twisting moments M_B and M_T are given in Fig. 4.17(e) and 4.17(f). As shown in Fig. 4.17(g) and 4.17(h), several elements contribute to the bending and torsional moments between the nodes J and K.The contributions to the bending moment stem from the two bending subelements I_1JKL_2, see Fig. 4.17(a). For the twisting moment, however, all four user elements are involved:

$$M_T = \frac{1}{4} M_{T,I_1JKL_1} + \frac{3}{4} M_{T,I_1JKL_2} - \frac{1}{4} M_{T,I_2JKL_1} + \frac{1}{4} M_{T,I_2JKL_2} \tag{4.73}$$

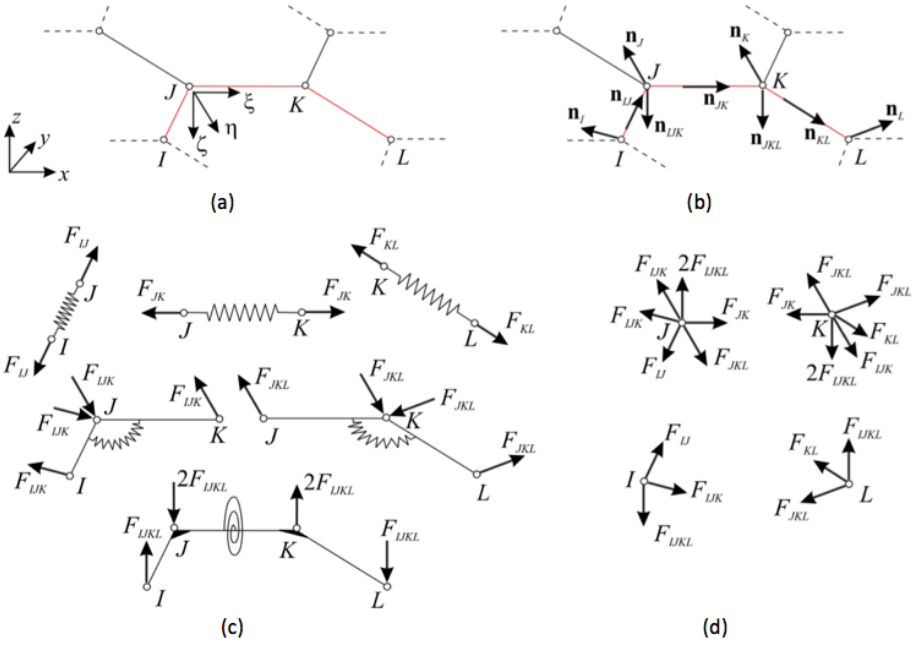

Figure 4.18: The developed 4-node element: (a) coordinate systems, (b) unit vectors, (c) all six components and (d) nodal forces

4.6.3 FEAP implementation

The general mathematical method described before needs an implicit procedure to be solved at each time step due to the underlying nonlinearity. In particular, the so-called right hand side vector, which results from the residual forces, as well as the corresponding tangent stiffness matrix are needed. For a better understanding of all six individual parts of the developed 4-node-element introduced before, see the exploded view in Fig. 4.18(c). To compose the whole acting force three normal springs for the bond stretch, two bending elements and one twisting element are needed. In reason of that, each 4-node user element has to take into account all the contributions given by the different element composed respectively by two, three and four nodes and then combinate appropriately these six subelements. In this way, the mesh generation costs, i.e. the number of required finite elements, can be reduced. Otherwise, instead of one 4-node element, the six base elements would be required to describe the interactions between four atoms I,J,K and L. Starting from formulation proposed in [85], Infuso and Paggi have fully developed in analytical way all the algebraic vectorial combination to obtain the terms of the residual force vector and the terms of the stiffness matrix, needed to perform the calculation using FEAP [81]. Since the finite element here adopted is taylor made for the specific use, according with the FEAP architecture, it was necessary to compile user element with the required equations, combining together different contributions provided by 2 to 4 nodes finite elements. With the goal to describe the more general solution procedure possible large displacements theory has been taken into account. Without any loss of generality, the same equilibrium distance R_e between all atoms has been set. For different molecules, these values must be chosen in accordance with the geometric dimensions. First of all, a coordinate reference system as shown in Fig. 4.18(a) has been introduced. The x, y, z coordinates are the global system, while the coordinates η, ν and ζ define a local right-handed cartesian coordinate system where the η ν plane is given by the nodes I, J and K. For greater clarity for the reader, a few rules of vector algebra are provided here. Defining $\mathbf{u} = (u_1\mathbf{i}, u_2\mathbf{j}, u_3\mathbf{k})$ and $\mathbf{v} = (v_1\mathbf{i}, v_2\mathbf{j}, v_3\mathbf{k})$ as vectors we introduce the following operator:

- **Cross product**

$$\begin{aligned}
&\mathbf{u} \times \mathbf{v} = \\
&= (u_1\mathbf{i}, u_2\mathbf{j}, u_3\mathbf{k}) \times (v_1\mathbf{i}, v_2\mathbf{j}, v_3\mathbf{k}) \\
&= u_1v_1(\mathbf{i} \times \mathbf{i}) + u_1v_2(\mathbf{i}) \times \mathbf{j} + u_1v_3(\mathbf{i} \times \mathbf{k}) \\
&+u_2v_1(\mathbf{j} \times \mathbf{i}) + u_2v_2(\mathbf{j}) \times \mathbf{j} + u_2v_3(\mathbf{j} \times \mathbf{k}) \\
&+u_3v_1(\mathbf{k} \times \mathbf{i}) + u_3v_2(\mathbf{k}) \times \mathbf{j} + u_3v_3(\mathbf{k} \times \mathbf{k})
\end{aligned}$$

- **Dyadic product**

$$\begin{aligned}
&\mathbf{u} \otimes \mathbf{v} = \\
&u_1 \cdot v_1\mathbf{ii} + u_1 \cdot v_2\mathbf{ij} + u_1 \cdot v_3\mathbf{ik} \\
&+u_2 \cdot v_1\mathbf{ji} + u_2 \cdot v_2\mathbf{jj} + u_2 \cdot v_3\mathbf{jk} \\
&+u_3 \cdot v_1\mathbf{ki} + u_3 \cdot v_2\mathbf{kj} + u_3 \cdot v_3\mathbf{kk}
\end{aligned}$$

Applying the cross product to the unit vectors between two atoms:

$$\mathbf{n_{ij}} = \frac{\mathbf{x_j} - \mathbf{x_i}}{|\mathbf{x_j} - \mathbf{x_i}|} \quad \text{with i=I,J,K; j=J,K,L} \tag{4.74}$$

can determined the two normal vectors

$$\mathbf{n_{ijk}} = \frac{\mathbf{n_{ij}} \times \mathbf{n_{jk}}}{|\mathbf{n_{ij}} \times \mathbf{n_{jk}}|} \quad \text{with i=I,J; j=J,K; k=K,L} \tag{4.75}$$

with regard to the planes IJK and JKL. Another application of the cross product yields the in-plane unit vectors

$$\begin{aligned} \mathbf{n_I} &= \mathbf{n_{IJ}} \times \mathbf{n_{IJK}} \\ \mathbf{n_J} &= \mathbf{n_{JK}} \times \mathbf{n_{JKL}} \\ \mathbf{n_K} &= \mathbf{n_{JK}} \times \mathbf{n_{IJK}} \\ \mathbf{n_L} &= \mathbf{n_{KL}} \times \mathbf{n_{JKL}} \end{aligned} \tag{4.76}$$

which are normal to the unit vectors given in Eq. (4.74).

According to the DREIDING approach presented in the previous section, the forces which correspond to these unit vectors are

$$F_{ij} = -2\alpha n \frac{D_e}{12} \left[\exp(-2\alpha n(|x_j - x_i| - R_e)) - \exp(-\alpha n(|x_j - x_i| - R_e)) \right] \quad \text{with i=I,J,K; j=J,K,L} \tag{4.77}$$

for bond stretch,

$$F_{ijk} = -\frac{C_{ijk}}{4R_e} [\cos\Theta_{ijk} - \cos\Theta_j^0] \sin\Theta_{ijk} \quad \text{with i=I,J; j=J,K; k=K,L} \tag{4.78}$$

for angle bend with $C_{IJK} = C_{JKL}$, $\Theta_K^0 = \Theta_J^0$ and the bond angle

$$\Theta_{ijk} = 180^\circ - \arcsin|n_{ij} \times n_{jk}| = \arccos(-n_{ij} \cdot n_{jk}) \quad \text{with i=I,J; j=J,K; k=K,L} \tag{4.79}$$

and

$$F_{IJKL} = \frac{V_{JK}}{4\sqrt{3}R_e} \sin[n_{JK}(\varphi_{IJKL} - \varphi_{JK}^0)] \tag{4.80}$$

for twisting with the twisting angle

$$\varphi_{IJKL} = \begin{cases} \arcsin[(n_{IJK} \times n_{JKL}) \cdot n_{JK}] & \text{if } (n_{IJK} \cdot n_{JKL}) \geq 0 \\ 180^\circ - \arcsin[(n_{IJK} \times n_{JKL}) \cdot n_{JK}] & \text{if } (n_{IJK} \cdot n_{JKL}) < 0 \end{cases} \tag{4.81}$$

For example, in graphite, one carbon atom J is neighbored by three atoms that are I_1, I_2 and K. Atom K is neighbored by the three atoms J, L_1 and L_2, and so on. Thus, when superposing all 4-node elements, this results in 12 normal spring subelements being placed between the atoms J and K, 4 bending subelements between three atoms I, J

and K and 4 torsional spring subelements between two atoms J and K. For this reason, Eqs. (4.60), (4.64) and (4.70) are premultiplied by the factors $\frac{1}{12}$, $\frac{1}{4}$ and $\frac{1}{4}$, respectively, which leads to Eqs. (4.77), (4.78) and (4.80). From the force equilibrium at the nodes, shown in Fig. 4.18(d), one defines the residual forces:

$$\begin{aligned}
\mathbf{R_I} &= +F_{IJ}\mathbf{n_{IJ}} - F_{IJK}\mathbf{n_I} + F_{IJKL}\mathbf{n_{IJK}} \\
\mathbf{R_J} &= +F_{IJ}\mathbf{n_{IJ}} - F_{JK}\mathbf{n_{JK}} + F_{IJK}\mathbf{n_I} + F_{IJK}\mathbf{n_K} - F_{JKL}\mathbf{n_J} - \frac{3}{2}F_{IJKL}\mathbf{n_{IJK}} - \frac{1}{2}F_{IJKL}\mathbf{n_{JKL}} \\
\mathbf{R_K} &= -F_{JK}\mathbf{n_{JK}} + F_{KL}\mathbf{n_{KL}} - F_{IJK}\mathbf{n_K} + F_{JKL}\mathbf{n_J} + F_{JKL}\mathbf{n_L} + \frac{1}{2}F_{IJKL}\mathbf{n_{IJK}} - \frac{3}{2}F_{IJKL}\mathbf{n_{JKL}} \\
\mathbf{R_L} &= -F_{KL}\mathbf{n_{KL}} - F_{JKL}\mathbf{n_L} - F_{IJKL}\mathbf{n_{JKL}}
\end{aligned} \tag{4.82}$$

In order to be able to consider large rotations, the forces at nodes J and K originating from the torsion element must be divided into $\frac{1}{2}F_{IJKL}$ and $\frac{3}{2}F_{IJKL}$. Thus, Fig. (4.18)(c) only represents the special case of small rotations, because there the nodal forces must not be split into components normal to the planes IJK and JKL. The global residual vector is set to zero at convergence:

$$\mathbf{R}(\mathbf{x}) = \mathbf{0} \tag{4.83}$$

The corresponding stiffness matrix $\mathbf{K}$, given in the **Appendix A**, has to be determined by linearizing $\mathbf{R}$. This gives the possibility to apply the incremental-iterative Newton-Raphson sceme. The solution of this system of equations gives:

$$\mathbf{K}(\mathbf{x_k}) \cdot \mathbf{\Delta u} = -\mathbf{R}(\mathbf{x_k}) \tag{4.84}$$

which provides the increment Δu to the previous solution. The procedure is iterated by updating $\mathbf{K}$ until the norm of the residual becomes less than a prescribed tolerance. The consistent update of the tangent stiffness matrix assumes quadratic convergence.

Chapter 5

Meso-scale Models

According to the description presented in the previous Chapter about nano- and micro-scales computational methods, it is easy to understand how much they can be computationally expensive to solve a whole structure composed by million of molecules. For this reason, it is at the moment not so common the study fracture and damage inside material with a pure atomistic scale method based on force fields. A partial solution to the problem has been found in the development of a mixed theory (MDFEM) in with the molecular dynamics peculiar approach based on potential energy and its derivatives has been adapted in order to allow its application to simple elements (i.e. beam or truss) and to be implemented in a FEM procedure, as described previously for the 4 nodes element.
A more reliable strategy for the analysis of materials behaviour and fracture can rely on in the meso-scale analysis where, despite the importance of understanding the molecular, its behavior can be suitably homogenized to move to a continuum model. Typically, the observed macroscopic behavior is usually investigated by neglecting the discrete atomic and molecular structure zooming out from the previous models, that were taking into account the laws governing interactions between different atoms and molecules.

In the meso-scale analysis, it is assumed that the material is continuously distributed throughout its volume, considering uniform characteristic inside the smallest unit of volume that can be modeled. The continuum material is thus assumed to have an average density and can be subjected to body forces such as gravity and surface forces as can be the contact between two bodies. Generally speaking, the defined meso-scale methods (also called continuum methods hereafter) obey the fundamental laws of:

- continuity, derived from the conservation of mass;
- equilibrium, derived from momentum considerations and Newton's second law;
- the moment of momentum principle, based on the model that the time rate of change of angular momentum with respect to an arbitrary point is equal to the resultant moment;
- conservation of energy, based on the first law of thermodynamics;
- conservation of entropy, based on the second law of thermodynamics.

These laws provide the basis for the construction of the continuum model and must be coupled with the appropriate constitutive equations and the equations of state to provide all the equations necessary for solving a continuum problem. The state of the continuum system is described by several thermodynamic and kinematic state variables. The equations of state provide the relationships between the non-independent state variables. The continuum method relates the deformation of a continuous medium to the external forces acting on the medium and the resulting internal stress and strain field. Computational approaches range from simple closed-form analytical expressions to micromechanics and complex structural mechanics calculations. In this section two continuum methods are briefly introduced, namely micromechanics models and finite element analysis, although others approaches are in any case possible. The continuum-mechanics methods rely on describing the geometry, (i.e., a physical model), and must be supplied with a constitutive relationship to achieve a solution [86].

For a displacement-based continuum formulation, the principle of virtual work is assumed to hold. In general, this is given as

$$\begin{aligned} \delta W &= \oiint\oiint\oiint_V \sigma_{ij}\delta\varepsilon_{ij}\mathrm{dV} \\ &= \oiint\oiint\oiint_V P_j\delta u_j\mathrm{dV} + \oiint\oiint\oiint_S T_j\delta u_j\mathrm{dS} + F_j\delta u_j \end{aligned} \tag{5.1}$$

where W is the virtual work which is the work done by virtual displacements, ε is the strain, σ is the stress, P is the body force, u is the virtual displacement, T is the traction and F is the point force. The symbol δ is the variational operator designating the virtual quantity. For a continuum system, a necessary and sufficient condition for equilibrium is that the virtual work done by the sum of the external forces and internal forces vanish for any virtual displacement. Since the assumption of uniformity in continuum mechanics may not hold at the microscale level, micromechanics methods are used to express the continuum quantities associated with an infinitesimal material element in terms of structure and properties of the microconstituents. Thus, a central theme of micromechanics models is the development of a representative volume element (RVE) to statistically represent the local continuum properties. The RVE is constructed to ensure that the length scale is consistent with the smallest constituent that has a first-order effect on the macroscopic behavior. The RVE is then used in a repeating or periodic nature in the full-scale model. The micro-mechanics method can account for interfaces between constituents, discontinuities, and coupled mechanical and non-mechanical properties. The volume average of a typical, spatially variable, integrable quantity $T(x)$ is

$$\langle T\rangle \equiv \frac{1}{V}\int_V T(x)dV \tag{5.2}$$

where V is the volume of the RVE. The unweighted volume average stress and strain are given by

$$\bar{\sigma} \equiv \langle\sigma\rangle \quad \text{and} \quad \bar{\varepsilon} \equiv \langle\varepsilon\rangle \tag{5.3}$$

respectively. The Finite Element Method is a general purpose numerical method for obtaining approximate solutions in space to initial-value and boundary-value problems including time-dependent processes. It employs preprocessed mesh generation, which enables the model to fully capture the spatial discontinuities of highly inhomogeneous materials. It also allows complex, nonlinear relationships to be incorporated into the analysis. Thus, it has been widely used in mechanical, biological and geological systems. In FEM, the entire domain of interest is spatially discretized into an assembly of simply shaped subdomains (e.g., hexahedra or tetrahedral in three dimensions, and rectangles or triangles in two dimensions) without gaps and without overlaps. The subdomains are interconnected at nodes. The FEM goal is to provide a numerical, approximate solution to initial-value and boundary value problems including time-dependent processes. The method uses a variational technique for solving the differential equations where the continuous problem described by the differential equation is recast into the equivalent variational form and the solution is found to be a linear combination of approximation functions. In the FEM, the physical shape of the domain of interest is partitioned into simple subdomains (elements) that are interconnected and fill the entire domain with- out overlaps. A displacement-based form of the FEM starts with the principle of virtual work for a continuum described above. The following steps outline the FEM approach:

1. Replace the continuum domain with an assemblage of subdomains.
2. Select the appropriate constitutive laws.
3. Select the interpolation functions necessary to map the element topology.
4. Describe the problem by using the variational principle and divide the system level integral into subintegrals over the elements.
5. Replace continuum state variables by interpolated values.
6. Assemble element equations.
7. Solve global system of equations, taking into account the prescribed boundary conditions.
8. Calculate the state equation values from state variables.

5.1 Cohesive zone model for intergranular fracture

Here the a method developed in [16] based on a mesoscale analysis of the material able to correctly describe what could happen in a finite thickness interface according with a Cohesive Zone Model formulation is described. The same method will be applied to a practical sample where a polycrystalline Silicon sample is subjected to a tensile test, with the aim to describe the cracking process starting from a preexisting notch. The nonlocal cohesive zone models are derived taking into account the properties of finite thickness interfaces and are able to describe materials that exhibit a strain-softening behaviour. The fundamental point on which they are based on, is the fictitious crack (namely *process zone*) as an extension of the real crack. In this portion, cracking is incipient and the material, albeit damaged, is

still able to transfer stresses. Following the constitutive law curve, the crack is assumed to propagate when the stress at the crack tip reaches a value equal to the tensile strength. When the crack opens, the stress is not assumed to fall to zero at once as in linear elastic fracture mechanics, but to decrease gently with increasing crack width, until a critical displacement is reached and the interaction vanishes (a cut-off value on the crack opening). In order to characterize both the undamaged and the cracked situations, this modelling requires the use of a pair of constitutive equations: a stress-strain relationship for the undamaged material, and a softening stress-displacement discontinuity curve for the damaged one. Dugdale [26] for the first time postulated the existence of uniform tractions equal to the yield stress transmitted through a narrow yield zone in front of a crack tip in elastic-perfectly plastic materials. In the same time indipendently, Barenblatt [27] introduced the study of cohesive forces to take into consideration the effect of interatomic forces into polycrystal modeling. Subsequently, Hillerborg et al. [28] for the study of nonlinear mechanical behaviour of concrete, proposed the Fictitious Crack Model for the study of the nonlinear mechanical behaviour of concrete. As said before, this CZM introduces a stress-separation curve with a linear or bilinear shape for the study of the cracked field. More recently, the Cohesive Crack Model terminology was introduced by Carpinteri [87, 31] when snap-back branches may be captured. Nowadays, important applications refer to interface fracture mechanics, where different shapes of the CZM are proposed, namely the linear softening shape [86], the trapezoidal shape [88], as well as bell-shapes or exponential forms suggested by a qualitative fit to atomistic calculations. Even if the progress achieved in models for nonlinear fracture mechanics is high, it is convenient to choose the shape of the CZM and its input parameters are as simple as possible for numerical reasons, rather than being physical meaningful. The reason of that has to be found in the difficult to quantify properly the mechanisms that control those parameters. To overcome such a drawback, which inevitably leads to a big uncertainty and to a problem of reliability of the numerical predictions, inverse methods have recently been proposed. Once the displacement field is measured, an inverse calculation is performed in order to find the parameters of the CZM leading to such displacements [89].

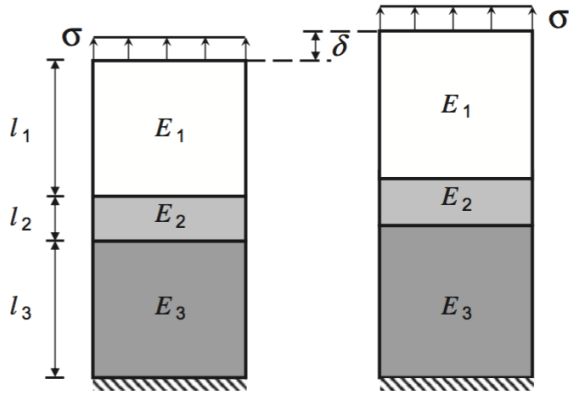

Figure 5.1: A trimaterial system subjected to uniaxial tension (adapted from [16].

5.1.1 Mathematical formulation

In order to analyze peculiarities and define the operational procedure to formulate a nonlocal CZM, it is proposed an example regarding the study of mechanisms occurring along a finite thickness interface, considering simple bimaterial mechanical systems subjected to either Mode I or Mode II loading. The property degradation in the interface region is modelled according to a continuum damage mechanics formulation. The anelastic stress-displacement response of the system can be interpreted as a new CZM, whose shape comes directly from the damage evolution law, so that the input parameters can be related to the failure phenomena occurring at lower length scales. In reason of this, the new CZM establishes a proper link between MD simulations and continuum damage mechanics. It is here considered the Mode I deformation for a system composed by three layered material system: one layer with Young's modulus E_2 embedded between two layers with Young's modulus E_1 and E_3 (see Fig. 5.1). Both the interfaces are assumed to be perfectly bonded and the specimen is subjected to uniaxial tension in vertical direction. During the loading process, three different stages can be identified. In the first one the materials behave linear elastically so that deformations are proportional to the induced load and the total axial displacement δ of the system is the sum of the elastic displacements of the material regions 1-3:

$$\delta = \delta_1 + \delta_2 + \delta_3 = \left(\frac{l_1}{E_1} + \frac{l_2}{E_2} + \frac{l_3}{E_3} \right) \sigma \tag{5.4}$$

This relation it is assumed valid until the axial deformation of layer 2 reaches a certain threshold value, say δ_e. After that, progressive damage in the material 2 occurs as a result of complex dissipative mechanisms, for the most related to micro-scale analysis, such as dislocation motion, breaking of interatomic bonds, formation of free surfaces and microvoids. This form of nonlinearity can be globally taken into account by introducing a damage variable, D, ranging from zero (no damage, $\delta_2 = \delta_e$) to unity (fully developed damage or appearance of a macroscopic crack according with classical continuum mechanics, $\delta_2 = \delta_c$). The distributed defects not only lead to crack initiation and final fracture, but also induce progressive material deterioration and degradation of the elastic properties. Hence, the damaged Young's modulus of material 2 can be expressed taking into consideration che previously defined parameter D, so that $E_2^D = E_2(1 - D)$ and the global stress-displacement relationship (Eq. (5.4)) becomes:

$$\delta = \left[\frac{l_1}{E_1} + \frac{l_2}{E_2(1 - D)} + \frac{l_3}{E_3} \right] \sigma \tag{5.5}$$

It is convenient to recast Eq. (5.4) introducing the increment of axial displacement g_N, with respect to the undamaged case:

$$\delta = \left(\frac{l_1}{E_1} + \frac{l_2}{E_2} + \frac{l_3}{E_3} \right) \sigma + g_N \tag{5.6}$$

where

$$g_N = \left[\frac{l_2}{E_2(1 - D)} - \frac{l_2}{E_2} \right] \sigma = \frac{l_2 D}{E_2(1 - D)} \sigma \tag{5.7}$$

In order to satisfy energy requirements, the mechanical dissipation must be non-negative, condition satisfied by considering a monotonically increasing damage with time, which implies that the degradation is irreversible. The damage variable D is set equal to the ratio between the increment of deformation from the undamaged case, $w = (\delta_2 - \delta_e)$, and its critical value corresponding to crack formation, $w_c = (\delta_c - \delta_e)$, raised to a power α:

$$D = \left(\frac{w}{w_c}\right)^{\alpha} \tag{5.8}$$

The variables δ_e, δ_c and α, depend on damage mechanisms taking place at the lower scales as better explained in the following. Inserting Eq. (5.8) into Eq. (5.7) can be obtained:

$$g_N = \frac{l_2 \left(\frac{w}{w_c}\right)^{\alpha}}{E_2 \left[1 - \left(\frac{w}{w_c}\right)^{\alpha}\right]}\sigma = \frac{\delta_e \left(\frac{w}{w_c}\right)^{\alpha}}{\sigma_e \left[1 - \left(\frac{w}{w_c}\right)^{\alpha}\right]}\sigma \tag{5.9}$$

where w/w_c ranges between 0 and 1 and $\sigma_e = E_2\delta_e/l_2$ is the stress corresponding to the onset of damage. This equation can be rewritten in order to determine the relationship $\sigma = f(g_N)$ between stress and anelastic displacement of the mechanical system:

$$\sigma = \frac{E_2}{l_2}\frac{1 - \left(\frac{w}{w_c}\right)^{\alpha}}{\left(\frac{w}{w_c}\right)^{\alpha}} g_N = \sigma_e \frac{1 - \left(\frac{w}{w_c}\right)^{\alpha}}{\left(\frac{w}{w_c}\right)^{\alpha}} k_N \frac{g_N}{\delta_c} \tag{5.10}$$

that in dimensionless form becomes:

$$\frac{\sigma}{\sigma_e} = \frac{1 - \left(\frac{w}{w_c}\right)^{\alpha}}{\left(\frac{w}{w_c}\right)^{\alpha}} k_N \frac{g_N}{\delta_c} \tag{5.11}$$

where $\delta_c = k_N\delta_e$. The relationship between σ and g_N is actually nonlinear and implicit, since w depends on g_N in its turn ($w = g_N - \delta_e + \sigma l_2/E_2$). In the last case, for $\sigma_2 \geq \delta_c$, a macroscopic crack is fully developed and the specimen is no longer able to sustain external loading ($\sigma = 0$). The second interesting aspect of the analysis is related to the comparison between the mechanical behaviour obtained from continuum damage mechanics with that of a system ruled by a CZM with a zero-thickness bimaterial interface, as can be seen in Fig. 5.2.

Also in this case it is possible to be in front of three different stages, as for the trimaterial system previously examined. The first linear elastic stage is characterized by the following displacement-stress relationship:

$$\delta = \left(\frac{h_1}{E_1} + \frac{h_3}{E_3}\right)\sigma \tag{5.12}$$

that becomes equal to Eq. (5.4) if the equation below is satisfied:

$$\frac{E_1}{h_1} + \frac{E_3}{h_3} = \frac{E_1}{l_1} + \frac{E_2}{l_2} + \frac{E_3}{l_3}$$

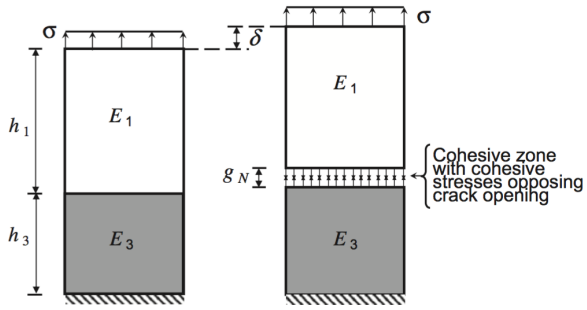

Figure 5.2: A bimaterial system subjected to uniaxial tensile loading with the formation of one cohesive crack (adapted from [16]).

and combining it with $h_1 + h_3 = l_1 + l_2 + l_3$ because it is suitable to have the same total size of the system, h_1 and h_3 can be obtained:

$$h_1 = l_1 + \frac{E_1}{E_2}\left(\frac{E_2 - E_3}{E_1 - E_3}\right) l_2 \tag{5.13a}$$

$$h_3 = l_3 + \frac{E_3}{E_2}\left(\frac{E_1 - E_2}{E_1 - E_3}\right) l_2 \tag{5.13b}$$

For $\delta_e < \delta < \delta_c$, a cohesive crack develops along the bimaterial interface and the total displacement follows as the sum of two contributions: the elastic one and the localized displacement g_N in the process zone. The latter depends on the shape of the CZM being considered, say $g_N = f^{-1}(\sigma)$:

$$\delta = \left(\frac{h_1}{E_1} + h_3 E_3\right)\sigma + g_N \tag{5.14}$$

and the previous Eq. (5.14) matches Eq. (5.6) if:

$$g_N = f^{-1}(\sigma) = \frac{l_2 D}{E_2(1 - D)}\sigma \tag{5.15}$$

Finally, when $\delta > \delta_c$, a crack is fully developed and the stress is zero. Therefore, under such conditions, it is possible to state that the bimaterial linear elastic system in Fig. 5.2, whose failure is modelled according to a zero-thickness interface CZM with the stress-separation law in Eq. (5.11), has a complete physical similarity with the trimaterial system with damage shown in Fig. 5.1. Moreover, the stress-displacement relation $\sigma = f(g_N)$, obtained according to damage mechanics, can now be reinterpreted as a new cohesive stress-separation law whose shape is no longer assumed a priori.

It is now considered the same trimaterial system, but subjected to shear so that G_1, G_2 and G_3 denote the tangential elastic moduli of materials1, 2, and 3, respectively as reported in Fig. 5.3.

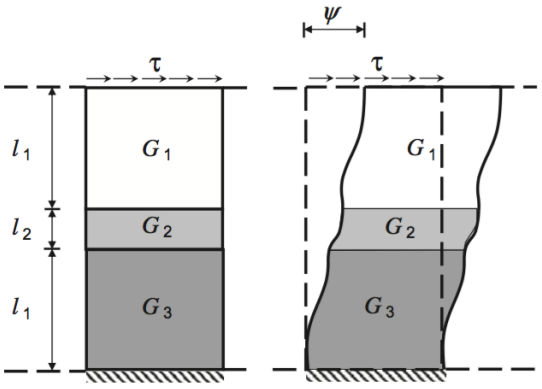

Figure 5.3: A trimaterial system subjected to shear.

As is for the Mode I problem, three different stages can be considered: the first one is the linear elastic stage, until the horizontal displacement of layer 2 is less than a threshold value ($|\psi_2| < \psi_e$). Then, a damaged stage for the material 2 takes place ($\psi_e < |\psi_2| < \psi_c$). Finally, shear failure occurs for $|\psi_2| = \psi_c$. Regarding the relationship between the horizontal displacement of the system, ψ, and the applied shear traction, τ, it is still possible to apply Eqs. (5.4) to (5.8), replacing the corresponding quantities for Mode I with Mode II variales:

$$\psi = \psi_1 + \psi_2 + \psi_3 = \left(\frac{l_1}{G_1} + \frac{l_2}{G_2} + \frac{l_3}{G_3}\right)\tau \tag{5.16}$$

$$\psi = \left(\frac{l_1}{G_1} + \frac{l_2}{G_2(1-D)} + \frac{l_3}{G_3}\right)\tau \tag{5.17}$$

$$\psi = \left(\frac{l_1}{G_1} + \frac{l_2}{G_2} + \frac{l_3}{g_3}\right)\tau + g_T \tag{5.18}$$

where

$$g_T = \left[\frac{l_2}{G_2(1-D)} - \frac{l_2}{G_2}\right]\tau = \frac{l_2 D}{G_2(1-D)}\tau \tag{5.19}$$

Again, an assumption on the damage evolution equation has to be made. It is defined in close analogy to Eq. (5.8), as:

$$D = \left(\frac{u}{u_c}\right)^{\alpha} \tag{5.20}$$

where $u = |\psi_2| - \psi_e$ and $u_c = (\psi_c - \psi_e)$. After some algebra, the relation between tangential traction and anelastic displacement, $\tau = f(g_T)$, can be determined:

$$\frac{\tau}{\tau_e} = 1 - \left(\frac{u}{u_c}\right)^{\alpha} k_T \frac{g_T}{\psi_c} \tag{5.21}$$

where $\psi_c = k_T \psi_e$ and $\tau_e = G_2 \psi_e / l2$. Since this functional expression is formally the same as for Mode I, the effects of the stiffness ratio do not need be further investigated. The analogy with a zero-thickness CZM yields the relations

$$h_1 = l_1 + \frac{G_1}{G_2}\left(\frac{G_2 - G_3}{G_1 - G_3}\right) l_2 \tag{5.22a}$$

$$h_3 = l_3 + \frac{G_3}{G_2}\left(\frac{G_1 - G_2}{G_1 - G_3}\right) l_2 \tag{5.22b}$$

In case of Mode Mixity, different approaches can be considered. The simplest way is to introduce an effective dimensionless displacement λ in the form

$$\lambda = \sqrt{\left(\frac{w}{w_c}\right)^2 + \left(\frac{u}{u_c}\right)^2} \qquad \text{with } \lambda \leq 1 \tag{5.23}$$

Damage will be equal to $D = \lambda^\alpha$ and the traction is given by:

$$\frac{\sigma}{\sigma_e} = \frac{1 - \lambda^\alpha}{\lambda^\alpha} k_N \frac{g_N}{\delta_c} \tag{5.24}$$

$$\frac{\tau}{\tau_e} = \frac{1 - \lambda^\alpha}{\lambda^\alpha} k_T \frac{g_T}{\psi_c} \tag{5.25}$$

At the end of the formulation, it is possible to analyze the principal strengths of the proposed method, on account of what has emerged from some practical applications of the same, as reported in [16]. The main idea is to establish if it is possible to define the present approach able to bridge the gap between damage mechanics and nonlinear fracture mechanics, combining together features of both molecular dynamics analysis and FEM, with a possible application to continua approaches. The advantages of the proposed mathematical formulation are:

1. The origin of the terms involved in the nonlocal cohesive stress-separation law in Eq. (5.11) has to be found in a process of damage accumulation taking place at smaller scales. Therefore, the model parameters α, δ_e and δ_c can be tuned according to MD simulations of the nonlinear behaviour of material 2.

2. The shape of the cohesive stress-separation law is the main feature of the damage model. This is the core part of the analysis, since the shape of the CZM is usually assumed a priori in structural computations, rather than based on real damage mechanisms. It is important to note that, depending on the parameter α, Eq. (5.11) is able to lead to several shapes of CZMs proposed so far in the literature. For instance, the linear and the bilinear curves are typically used to characterize the post-peak behaviour of quasi-brittle materials, with special regard to concrete [24, 25, 28, 90]. Linear softening cohesive laws are also used for the characterization of zero-thickness bimaterial interfaces [91], although very often bell-shapes are assumed, as the one obtained from Eq. (5.11) for large α [92, 93].

3. The proposed CZM can be suitable for correctly represent finite thickness interfaces, solving common problem in engineering applications where different materials joined together are involved in the investigation. Since the existence of an sharp transition from one material to another is often a pure mathematical artefact, more than a verifiable physical reality. In many cases, there is the growth of a transition layer that can not be correctly modeled with the zero-thickness interface CZMs available in the literature, not able to take into account the finite thickness properties of the interface.

4. The established analogy between the mechanical systems in Figs. 5.1 and 5.2 allows to make a simplification in the representation of complex bimaterial systems taking a great advantage from the computational point of view. This is for instance the case of composite material where an hard granular matrix is embedded into thin binder. In spite of its vanishingly small thickness, the binder is the main source of damage and the preferred path for crack propagation [94]. According to the proposed analogy, a new geometry of the material microstructure can be considered, where the size of the grains is suitably augmented. Then, a zero-thickness interface can be placed around the augmented grains with the nonlocal CZM given by Eq. (5.11) that takes into account the properties of the finite thickness interface. Further examples will be provided in the next part of the analysis.

5. The proposed method can be extended also to 3D problems. Then, instead of two relative displacement components, g_N and g_T, three components g_N, g_{T1} and g_{T2} have to be considered, where 1 and 2 will denote, respectively, the direction of the in-plane and of the out-of-plane relative tangential displacements. Again, each finite thickness interface region can be simplified by suitably augmenting the size of the 3D grains.

The nonlocal CZM proposed before can be applied to fracture mechanics problems characterized by interfaces with finite thicknesses. A notable example is represented by polycrystalline materials, where stiff polycrystalline grains are embedded into a softer matrix. An appropriate example is the polycrystalline structure composing PV solar cells. Experimental results at the microscale suggest a relation between interface thickness and grain diameter of the following type:

$$l_2 = kd^{\beta} \tag{5.26}$$

where the parameters k and β depend on the material and δ and l_2 are measured in micrometers. Even if can be considered that the thickness of the interface is generally one order of magnitude less than the grain size diameter, as suggested by the correlation in Eq. (5.26), the interface region has to be considered one of the main sources of nonlinearity for polycrystalline materials. The reason has to be attributed to the fact that shear stresses grown at the interface are about 2-3 times higher than those in a homogeneous/uniform material. In reason of that, it is therefore quite logical to expect that the initiation of plastic flow is localized in the grain boundary regions. Moreover, this phenomenon is enhanced by the fact that grain boundaries may be possible sources of dislocations that build up at interfaces, and that grain boundaries segregate impurities with mechanical properties different from the grain interiors. One of the first attempts to model finite interface region in the computations included as a

continuum was made by Benson et al. [95] who modelled it with a perfectly plastic constitutive law.
A more appropriate formulation from the computational point of view, is to adopt a standard cohesive zone model (CZM) to depict the phenomenon of progressive separation of the grains, neglecting the finite thickness of the interfaces [96, 97, 98]. In addition, such modelling would lead to model interfaces considering the same fracture mechanics parameters, which is not correspondent with the reality. Hence, a step forward in modelling requires the use of random interface fracture energies, according to predefined statistical distributions. In brittle polycrystalline materials, as, e.g., in ceramics, a Weibull probabilistic distribution can be adopted to provide a good approximation to the actual distribution of fracture energies, whereas the Gaussian distribution is preferred for ductile polycrystals [94]. Although this methodology leads in general to a better match between numerical predictions and experimental results, the assignment of the fracture properties to each interface is somehow arbitrary and not related to the real damage mechanisms taking place at the lower scales in the interface regions. Although the simulated global response may be closer to the experimental one, local aspects, such as the crack patterns, may be substantially different. As said previously, the main advantage of the proposed nonlocal CZM is the chance to take into account the damage phenomena occurring at lower length scales inside the region near to the interface. The adopted shape of the CZM can be selected according to MD simulation evidences and it is found to be directly related to the interface thickness. Therefore, a stochastic distribution of CZM properties (shape, peak traction, fracture energy) derives from the spatial variation of the interface thicknesses in the material microstructure, without the need of making ad hoc statistical hypotheses. Furthermore the grain-size effects on the tensile strength are also direct consequences of the variation of the interface thicknesses, that depend on the grain diameter according with the manufacturing process.
Due to the nonlocality, normal and shear deformations of the original interface region defined by its finite thickness must be summed to the normal and tangential relative displacements (called gaps in the sequel) computed at each iteration step in order to obtain the actual value of the cohesive tractions at the Gauss points. Here, a nested Newton-Raphson loop is used in close analogy with elasto-plasticity. Since this computation has to be repeated at each iteration and for all Gauss points of the interface elements, the fast convergence of the algorithms is essential. To reach this objective, a series expansion of the stress-separation laws is derived to obtain approximate values for the normal and tangential cohesive tractions to be used in the first iteration of the Newton-Raphson loop. In the next section, numerical applications to polycrystalline materials are presented. The examples focus on to the capability of the proposed nonlocal CZM to generate statistical distributions of fracture parameters.

Cohesive zone models (CZM) are commonly implemented by the use of interface elements, suitably inserted between the boundaries of the solid elements of the continuum discretization. Several applications ranging from structural mechanics to materials science can be found in [91, 92, 93, 94, 99, 100, 101, 102, 103]. The fundamental element that is here employed is a 4-noded bi-dimensional interface element as sketched in Fig. 5.4, where each node i has two translational degrees of freedom, u_i and v_i, that can be collected in the element displacement vector $\mathbf{u}$:

$$\mathbf{u} = (u_1, v_1.u_2, v_2, u_3, v_3, u_4, v_4)^T \tag{5.27}$$

where the displacement components in the global reference system are ordered in the sequence u_i and v_i for each node. Then, it is introduced the middle line $1'2'$ of the element and a local reference system is defined by the tangential vector t and the normal vector n to this middle line as reported in Fig. 5.4. The origin O of the local reference system is placed in the center of the middle line, which is in general rotated with respect to the global x-axis by an angle Θ. Therefore, nodal displacements of the i-th node in the local coordinate system, u_i^* and v_i^* , can be computed as $\mathbf{u_i^*} = \mathbf{ru_i}$

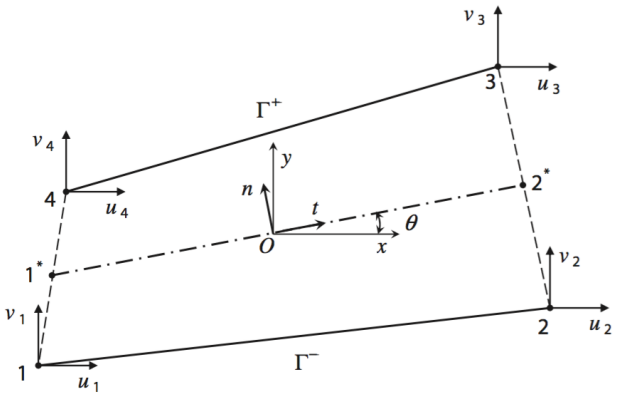

Figure 5.4: 2D interface element.

$$\begin{Bmatrix} u_i^* \\ v_i^* \end{Bmatrix} = \begin{bmatrix} \cos\theta & \sin\theta \\ -\sin\theta & \cos\theta \end{bmatrix} \begin{Bmatrix} u_i \\ v_i \end{Bmatrix} \tag{5.28}$$

so that the element displacement vector in the local reference system
$\mathbf{u}^* = (u_1^*, v_1^*, u_2^*, v_2^*, u_3^*, v_3^*, u_4^*, v_4^*)^T$ can be related to the vector of displacements $\mathbf{u}$ in global coordinates with the relation

$$\mathbf{u}^* = \mathbf{Ru} \tag{5.29}$$

where $\mathbf{R}$ is obtained by the collection of the individual rotation matrices $\mathbf{r}$:

$$\mathbf{R} = \begin{bmatrix} \mathbf{r} & 0 & 0 & 0 \\ 0 & \mathbf{r} & 0 & 0 \\ 0 & 0 & \mathbf{r} & 0 \\ 0 & 0 & 0 & \mathbf{r} \end{bmatrix} \tag{5.30}$$

The relative displacement vector $\mathbf{\Delta u}^* = (u_4^* - u_1^*, v_4^* - v_1^*, u_3^* - u_2^*, v_3^* - v_2^*)$ is defined as $\mathbf{\Delta u}^* = \mathbf{Lu}^*$,where the operator matrix $\mathbf{L}$ relates the displacement field components to the

relative displacements between the upper and the lower sides of the interface, Γ^+ and Γ^- :

$$\mathbf{L} = \begin{bmatrix} -1 & 0 & 0 & 0 & 0 & 0 & +1 & 0 \\ 0 & -1 & 0 & 0 & 0 & 0 & 0 & +1 \\ 0 & 0 & -1 & 0 & +1 & 0 & 0 & 0 \\ 0 & 0 & 0 & -1 & 0 & +1 & 0 & 0 \end{bmatrix} \tag{5.31}$$

The vector of the tangential and normal gaps at a generic point of the middle line, $g = (g_T, g_N)^T$, can be determined from $\mathbf{\Delta u}^*$ using standard interpolation functions, $\mathbf{g} = \mathbf{N\Delta u}^*$, where N is given by

$$\mathbf{n} = \begin{bmatrix} N_1 & 0 & N_2 & 0 \\ 0 & N_1 & 0 & N_2 \end{bmatrix} \tag{5.32}$$

In the present case it is chosen to adopt linear shape functions for the nodes 1^* and 2^*, so that $N_1 = (1 - s)/2$ and $N_2 = (1 + s)/2$. The s parametric coordinate ranges between 1 and +1 values , as for a standard 2-nodes isoparametric finite element. The vector $\mathbf{g}$ can therefore be related to the nodal displacement vector as follows:

$$\mathbf{g} = \mathbf{NLRu} = \mathbf{BRu} \tag{5.33}$$

where the operator $\mathbf{B} = \mathbf{NL}$ has a simple form:

$$\mathbf{B} = \begin{bmatrix} -N_1 & 0 & -N_2 & 0 & +N_2 & 0 & +N_1 & 0 \\ 0 & -N_1 & 0 & -N_2 & 0 & +N_2 & 0 & +N_1 \end{bmatrix} \tag{5.34}$$

It is now considered the weak form of the interface element formulation:

$$G_{int} = \int_S \delta \mathbf{g}^\mathbf{T} \mathbf{t} dS = \delta \mathbf{u}^\mathbf{T} \mathbf{R}^\mathbf{T} \int_S \mathbf{B}^\mathbf{T} \mathbf{t} dS \tag{5.35}$$

where $\mathbf{t} = (\tau, \sigma)^T$ is the traction vector which is a nonlinear function of the normal and tangential relative displacements according to the specified CZM. Linearization of Eq. (5.35) is therefore necessary to achieve quadratic convergence in the global Newton-Raphson scheme used to solve the nonlinear boundary value problem. This yields, since $\mathbf{B}$ is independent of $\mathbf{u}$:

$$G_{int} = \delta \mathbf{u}^\mathbf{T} \mathbf{R}^\mathbf{T} \int_S \mathbf{B}^\mathbf{T} \mathbf{C} \mathbf{B} dS \, \mathbf{Ru} \tag{5.36}$$

where the traction vector is related to the nodal relative displacement vector

$$\mathbf{t} = \mathbf{Cg} = \mathbf{CBRu} \tag{5.37}$$

through the constitutive matrix $\mathbf{C}$

$$\mathbf{C} = \begin{bmatrix} \dfrac{\partial \tau}{\partial g_T} & \dfrac{\partial \tau}{\partial g_N} \\ \dfrac{\partial \sigma}{\partial g_T} & \dfrac{\partial \sigma}{\partial g_N} \end{bmatrix} \tag{5.38}$$

Since **C** is nonsymmetric, the element stiffness matrix is in general not symmetric, as can be noticed in Eq. (5.38). The integrals in Eq. (5.36) will be computed using a 2-point Gaussian quadrature scheme with respect to the undeformed middle line of the element. This choice is able to give a stable traction profiles for the here considered nonlocal CZM. Hence, the residual and tangent matrix for the Newton-Raphson algorithm are:

$$\mathbf{F} = \mathbf{R}^{\mathbf{T}} \sum_{ip=1}^{2} \mathbf{B}_{\mathbf{ip}}^{\mathbf{T}} \mathbf{t}_{\mathbf{ip}} l/2 \tag{5.39a}$$

$$\mathbf{K} = \mathbf{R}^{\mathbf{T}} \left(\sum_{ip=1}^{2} \mathbf{B}_{\mathbf{ip}}^{\mathbf{T}} \mathbf{C}_{\mathbf{ip}} \mathbf{B}_{\mathbf{ip}} l/2 \right) \mathbf{R} \tag{5.39b}$$

where l is the length of the middle line of the interface element. A flow chart of these elementary operations for each interface element is shown in Tab. 5.1.

INPUT	from the main subroutine: nodal coordinates **x** and nodal displacements **u** Compute rotation matrix **R** and element length l Compute displacements $\mathbf{u}^*$ in the local reference system, Eq. (5.29)
LOOP	over Gauss Points of the interface element Compute tangent constitutive matrix **C** Eq. (5.38), and traction vector **t**, Eq. (5.37) Compute residual vector **F**, Eq. (5.39)(a) Compute tangent stiffness matrix **K**, Eq. (5.39)(b)
END LOOP	

Table 5.1: Sequence of operations for each interface element.

Considering now the most general case of Mode Mixity, the relative normal and tangential tractions σ and τ given by the proposed nonlocal CZM are functions of the damage variable, D:

$$\tau = \tau_e \frac{1-D}{D} \frac{g_T}{\psi_E} \tag{5.40a}$$

$$\sigma = \sigma_e \frac{1-D}{D} \frac{g_N}{\delta_E} \tag{5.40b}$$

where δ_e and ψ_e can be considered as internal characteristic materia lengths for the beginning of the damage. It is necessary to introduce an effective separation parameter λ at Gauss points, which is a function o the global axial and shear displacements w and u at the boundary of the real finite thickness interface:

$$\lambda = \sqrt{\left(\frac{w}{w_c}\right)^2 + \left(\frac{u}{u_c}\right)^2}, \quad 0 \leq \lambda \leq 1 \tag{5.41}$$

Here, the variables w_c and u_c are parameters referred to the material, with the same meaning of the critical opening and sliding relative displacements l_{Nc} and l_{Tc} used in local CZMs. The normal and tangential displacements w and u are given by:

$$w = g_N - \delta_e + \sigma \frac{l_2}{E_2} u = g_T - \psi_e + \tau \frac{l_2}{G_2} \tag{5.42a}$$

where l_2 is the thickness of the interface and E_2 and G_2 denote, respectively, the elastic axial and shear moduli of the interface material. Moreover, it is now introduced the relation between the damage variable and the effective dimensionless separation λ:

$$D = \lambda^\alpha \tag{5.43}$$

so that Eqs. (5.40) can be rewritten as

$$\tau = \tau_e \frac{1 - \lambda^\alpha}{\lambda^\alpha} \frac{g_T}{\psi_E} \tag{5.44a}$$

$$\sigma = \sigma_e \frac{1 - \lambda^\alpha}{\lambda^\alpha} \frac{g_N}{\delta_E} \tag{5.44b}$$

where α is the free-parameter of the model. Eqs. (5.44) constitutes a set of implicit equations for the unknown cohesive tractions σ and τ because, for given gaps in the normal and tangential directions, g_N and g_T, the displacements w and u needed to compute k are also functions of the unknowns σ and τ. A closed form solution is not available, so that σ and τ are computed via an iterative NewtonRaphson method, as it is done for elasto-plastic constitutive laws. Fixing the variables g_N and g_T, at the iteration index i, the nonlinear system of Eqs. (5.40) can be written as follows:

$$\mathbf{R^i} = \mathbb{I}\mathbf{t^i} - \mathbf{r^i}(\mathbf{t^i}) = \mathbf{0} \tag{5.45}$$

where $\mathbb{I}$ is a 2 x2 identity matrix and the components of $\mathbf{r^i}$ are:

$$r_1^i = \tau_e \frac{1 - D^i}{D^i} \frac{g_T}{\psi_e} r_2^i = \sigma_e \frac{1 - D^i}{D^i} \frac{g_N}{\delta_e} \tag{5.46a}$$

The proposed before application of the Newton-Raphson method gives rise to the following algorithm:

$$\mathbf{A^i} \Delta \mathbf{t^{i+1}} = -\mathbf{R^i t^{i+1}} = \mathbf{t^i} + \Delta \mathbf{t^{i+1}} \tag{5.47a}$$

where the matrix $\mathbf{A^i}$ follows from the linearization of the residual defined in Eq. (5.45):

$$\mathbf{A^i} = \mathbb{I} + \alpha (\lambda^i)^{-\alpha-2} l_2 \begin{bmatrix} \dfrac{\tau_e}{\psi_e G_2} & \dfrac{\tau_e}{\psi_e E_2} \\ \dfrac{\sigma_e}{\delta_e G_2} & \dfrac{\sigma_e}{\delta_e E_2} \end{bmatrix} \begin{bmatrix} \dfrac{u^i}{u_c^2} g_T & 0 \\ 0 & \dfrac{w^i}{w_c^2} g_N \end{bmatrix} \tag{5.48}$$

A brief example on the rate of convergence of the proposed algorithm has been conduced in [82], considering a simple Mode I test and changing the ratio g_N/w_c, the convergence is reached in every case in 4 up to 6 iterations and the error at $(i+1)th$ iteration is the square of the error at ith iteration, implying quadratic convergence of the algorithm. An operative flow-chart of the procedure is presented in Tab. 5.2.

INPUT	from the main subroutine: gaps $\mathbf{g_T}$ and $\mathbf{g_N}$
INITIALIZE	(i=0) compute initial approximate values τ^0 and σ^0 using series expansion proposed in [82] compute w^0, u^0, λ^0, and D^0 as functions of τ^0 and σ^0
DO	Compute $\mathbf{\Delta t^{i+1}}$ from Eq. (5.47)(a) Compute $\mathbf{t^{i+1}}$ from Eq. (5.47)(b) Compute w^{i+1}, u^{i+1}, λ^{i+1}, and D^{i+1} Compute relative error $\frac{\lvert D^{i+1}-D^i\rvert}{D^i}$
WHILE	relative error > prescribed tolerance
RETURN	cohesive tractions and their derivatives w.r.t. g_N and g_T

Table 5.2: Iterative procedure for the computation of the cohesive tractions based on the series expansion and the Newton-Raphson method.

In addition to the cohesive tractions σ and τ, the computation of the interface stiffness matrix requires the evaluation of the tangent constitutive matrix $\mathbf{C}$ in Eq. (5.38). Once the cohesive tractions σ and τ are computed, they can be considered as known quantities in the l.h.s. of Eqs. (5.44). Hence, the derivatives of the tractions with respect to g_N and g_T are given by:

$$\frac{\partial \tau}{\partial g_T} = \frac{\tau_e}{\psi_e}\left(\frac{1-\lambda^\alpha}{\lambda^\alpha}\right) - \frac{\alpha \tau_e g_T}{\psi_e}\lambda^{-\alpha-2}\frac{u}{u_c^2} \tag{5.49a}$$

$$\frac{\partial \tau}{\partial g_N} = -\frac{\alpha \tau_e g_T}{\psi_e}\lambda^{-\alpha-2}\frac{w}{w_c^2} \tag{5.49b}$$

$$\frac{\partial \sigma}{\partial g_T} = -\frac{\alpha \sigma_e g_N}{\delta_e}\lambda^{-\alpha-2}\frac{u}{u_c^2} \tag{5.49c}$$

$$\frac{\partial \sigma}{\partial g_N} = \frac{\sigma_e}{\delta_e}\left(\frac{1-\lambda^\alpha}{\lambda^\alpha}\right) - \frac{\alpha \sigma_e g_N}{\delta_e}\lambda^{-\alpha-2}\frac{w}{w_c^2} \tag{5.49d}$$

The derivatives can be directly determined from the matrix $\mathbf{A}$ of the last converged step of the above Newton-Raphson method:

$$\mathbf{C} = -\mathbf{A}\begin{bmatrix} \frac{G_2}{l_2} & 0 \\ 0 & \frac{E_2}{l_2} \end{bmatrix} + \begin{bmatrix} \frac{G_2}{l_2} + \frac{\tau}{g_T} & 0 \\ 0 & \frac{E_2}{l_2} + \frac{\sigma}{g_N} \end{bmatrix} \tag{5.50}$$

In conclusion, the discussion about the implementation in the finite element method of the nonlocal CZM allows to make a comparison with respect to standard CZMs, underlining

the main difference. While standard CZMs express an explicit dependency between the cohesive tractions and the normal and tangential gaps at the interface, the nonlocal CZM leads to an implicit expression for σ and τ that is numerically resolved iteratively using the Newton-Raphson method. In order to further increase the convergence speed of the solution, can be adopted a series expansion to obtain initial estimates of the tractions used in the iterative procedure.

The proposed numerical scheme can be suitably used to investigate on polycrystalline materials, focusing on the new capabilities and advantages of the nonlocal CZM with respect to a standard one. More specifically, it has been shown that we obtain a distribution of interface fracture parameters in a straightforward way. This is the consequence of the distribution of interface thicknesses, which are related to the grain size as a result of the manufacturing process. Due to specific parameters required as input by the model in order to perform the calculation, where it is taken into consideration the specific thickness of each interface for the calculation of the fracture energy, instead of assuming an average value of energy equal for all the interfaces.Finally, has been also noticed that the same CZM model is able to well reproduce the grain-size effect on the tensile strength, so that can be investigate the different behaviour of different sample of the same material subjected to the same boundary conditions.

For the numerical simulation of transgranular and intergranular cracking in polycrystalline silicon, a 2D plane stress model is considered. The principle of virtual work reads:

$$\int_V (\nabla \delta \mathbf{u})^T \sigma dV - \int_S \delta \mathbf{g}^{\mathbf{T}} \mathbf{t} dS = \int_{\partial V} \delta \mathbf{u}^{\mathbf{t}} \mathbf{f} dS \tag{5.51}$$

where the first term on the left hand side is the classical virtual work of deformation of stresses and strains inside the bulk V and the right hand side is the virtual work of tractions acting on the boundaries of the cell ∂V for the displacements of their corresponding points of application. The second term on the left hand side is the contribution to the virtual work of the vector of the normal and tangential cohesive tractions $\mathbf{t} = (\sigma, \tau)^T$ for the corresponding relative opening and sliding displacements $\mathbf{g} = (g_N, g_T)^T$ at all the element boundaries S. The CZM is adopted to depict the nonlinear process of crack growth in silicon. According to this approach, tractions normal and tangential to crack faces are functions of the relative opening and sliding displacements of the crack faces themselves. Here, we consider the CZM formulation recently proposed in [14, 104], which is based on an analogy between contact mechanics and fracture mechanics and is also suitable for proper modelling the localized additional thermal resistance of cracks in case of coupled thermoelastic analyses. The cohesive tractions are linear increasing functions of the corresponding gaps up to a maximum value reached in correspondence of the dimensionless separation l_0/R, where R is the root-mean-square roughness of the heights of the crack profile at complete separation. The ratio between the peak cohesive traction and l_0 corresponds to the stiffness of the interface element during the linear branch of the constitutive law. Hence, the parameter l_0 physically corresponds to the maximum normal gap before reaching the softening in the cohesive zone formulation. Although for adhesive joints it can be related to the actual thickness and elastic properties of the adhesive, in the present study it is mostly a dummy parameter to modify the interface stiffness and avoid mesh-dependent results in the framework of the intrinsic CZM approach. It is therefore tuned by varying the mesh size in order to have the slope of the stress-strain curve

of silicon in the linear stage approximately equal to the Young modulus of silicon. After the linear branch, an exponential softening is assumed in the CZM formulation. The resulting expressions of the cohesive tractions, accounting for Mode Mixity, i.e., when both opening and sliding take place at the same time, are (see Fig. 5.5 for a graphical representation):

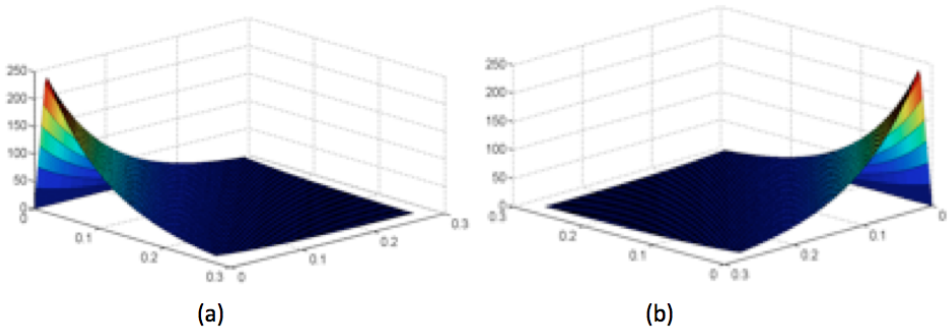

Figure 5.5: Cohesive constitutive laws accounting for Mode Mixity.

$$\sigma = \begin{cases} \sigma_{max} \exp\left(\frac{-l_0-|g_T|}{R}\right) \frac{g_N}{l_0} & \text{if} \quad 0 \le \frac{g_N}{R} \le \frac{l_0}{R} \\ \sigma_{max} \exp\left(\frac{-g_N-|g_T|}{R}\right) & \text{if} \quad \frac{l_0}{R} \le \frac{g_N}{R} \le \frac{g_{Nc}}{R} \\ 0 & \text{if} \quad \frac{g_N}{R} \ge \frac{g_{Nc}}{R} \end{cases} \tag{5.52}$$

$$\tau = \begin{cases} \tau_{max} \exp\left(\frac{-l_0-|g_N|}{R}\right) \frac{g_T}{l_0} & \text{if} \quad 0 \le \frac{g_T}{R} \le \frac{l_0}{R} \\ \tau_{max} \exp\left(\frac{-g_T-|g_N|}{R}\right) & \text{if} \quad \frac{l_0}{R} \le \frac{g_T}{R} \le \frac{g_{Tc}}{R} \\ 0 & \text{if} \quad \frac{g_T}{R} \ge \frac{g_{Tc}}{R} \end{cases} \tag{5.53}$$

The finite element approximation of the weak form in Eq. (5.51) is achieved by using linear triangular elements for the continuum and linear interface elements for the cohesive cracks. The matrix formulation, the consistent linearization of the nonlinear CZM for the use of the Newton-Raphson method, and for the numerical implementation in the finite element analysis programme FEAP is followed the same method explained before in this same Chapter, and wider in [16, 82, 105].

5.1.2 Model geometry using Gmsh software

The nonlocal CZM proposed in the previous section has been adopted by Infuso et al. [106] for the numerical study of the crack propagation inside a polycrystalline PV silicon cell. To correctly model the geometry of the involved structure, it is necessary to focus the attention on the particular shape of the material. In the following, a method to identify grains and grain boundaries is proposed by a novel image analysis formulation. Then finite element meshes are generated by using the open source software GMSH.Visual results of experimental test, in

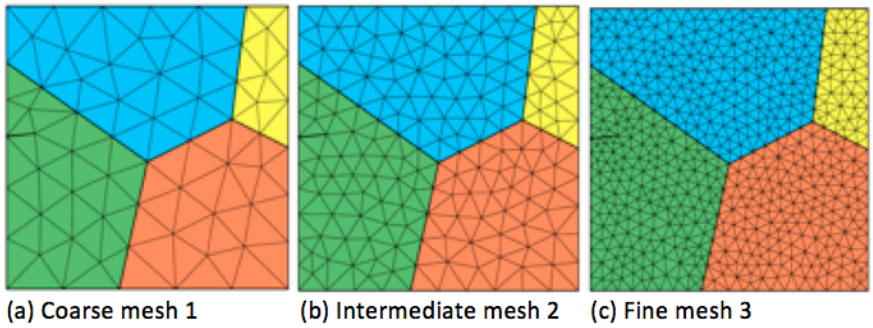

Figure 5.6: FE meshes with different element size used in the numerical tests. Note the initial crack inserted in the green grain.

which the Silicon PV module is subject to a cracking process, are achieved with a innovative image analysis technique, useful to process commercial solar cell pictures, identify grains and grain boundaries in polycrystalline silicon, and finally generate finite element meshes for the numerical simulation. Using a modified intrinsic cohesive zone model approach similar to the previous one to avoid mesh dependency, nonlinear finite element simulations show how grain boundaries and silicon bulk properties influence the crack pattern. Numerical results demonstrate a prevalence of transgranular over intergranular cracking for similar interface fracture properties of grains and grain boundaries, in general agreement with the experimental observation.
PV modules are composite laminates with very different layer thicknesses and silicon thin cells are usually embedded in an encapsulating polymer layer (EVA) covered by a much thicker tempered glass in traditional PV modules as in Fig. 5.7(a), while in semi-flexible PV panels symmetric glass-polymer-silicon-polymer-glass laminates are used, especially for covering areas on semi-transparent facades as in Fig. 5.7(b).

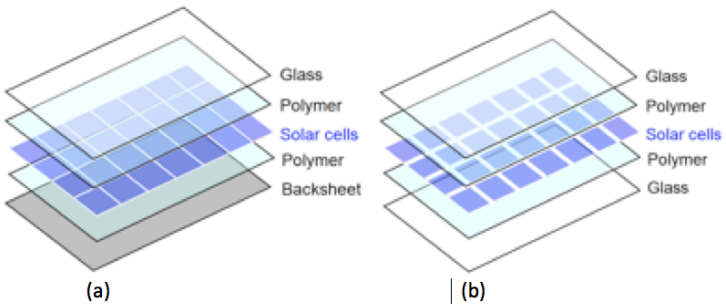

Figure 5.7: Two typical stacks of PV modules: (a) PV module for roofs or for solar fields; (b) PV module for semi-transparent roofs or facades.

As regards the crystalline structure of the silicon layer, the majority of solar cells available on the market are made of either monocrystalline or polycrystalline silicon. Solar cells are separated in their plane by a variable content of EVA, depending on the amount of shading requested. Two main semiconductors, called busbars, electrically connect the cells in series. Very thin aluminium conductors perpendicular to the busbars, called fingers, are also present to collect the electrons originated by the photovoltaic effect from the surface of the cells to the busbars (see Fig. 5.8).

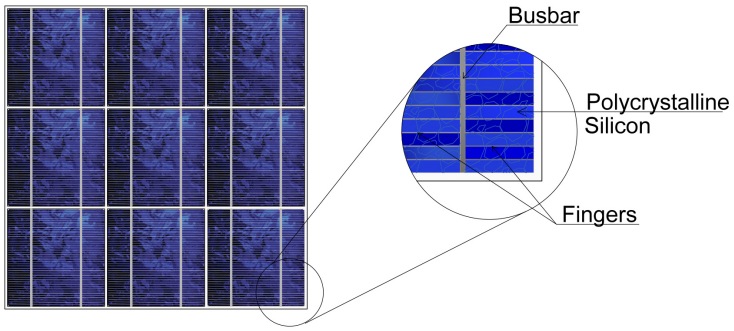

Figure 5.8: Sketch of a PV module and detail of busbars and fingers over the silicon cell.

The aim of the study is to prevent the generation of cracking inside the silicon layer, since there are several sources of damages: apart from the production defects for which involved cells are theoretically discarded during manufacturing, main sources of damage in silicon cells are transport, installation and use (in particular impacts, vibrations, snow loads and environmental ageing caused by temperature and relative humidity variations [107,108,109]). The occurrence of cracking is an important problem to be carefully controlled, since it can lead to large electrically disconnected areas, causing an urgent need to understand the origin of this phenomenon and find new technical solutions to improve the durability of PV modules.
To assess the effect of mechanical loads on cracking in solar cells, ad-hoc built mini-modules of 10 cells disposed along two rows (5 cells per row) have been subjected to 4-point bending in [110] (see Fig. 5.9(a)) for the layout of the test. The force-displacement curve obtained from this test is depicted in Fig. 5.9(b) and shows brittle failure as soon as cracking propagates. Microcrack patterns, impossible to be detected with a naked-eye inspection of the cells, were monitored by using the electroluminescence (EL) technique, see Fig. 5.10 [110]. The proposed images are related to the module span where the bending moment is constant. It is noticed that cracks develop along some preferential lines almost parallel to the direction of line loading. In case of horizontal busbars perpendicular to the line of loading, Fig. 5.10(a), a diffuse crack pattern is observed with the appearance of crack branching. For vertical busbars parallel to the line of loading, Fig. 5.10(b), single cracks propagate and lead to large electrically disconnected black areas. In reason of this, it is clear that the orientation of busbars and of the thin electric fingers with respect to the direction of application of loading has therefore

a role on the crack pattern at failure [110].
Both transgranular and intergranular cracks are clearly present during the damaging process and should have therefore to be considered in numerical models, although a qualitative visual inspection of Fig. 5.10 would suggest that transgranular cracking is more frequent than the intergranular one.
From the modelling point of view, a multi-physics and multi-scale computational model has been proposed [7], with the original idea to couple elastic, thermal and electric fields to achieve a predictive stage in the numerical simulations. To simulate fracture in solar cells of a commercial PV module, structural analysis has been performed by using the finite element method at the real scale and by considering the laminate as a multi-layered plate. The peculiarity of the model is to compute in-plane displacements at the boundaries of the cells are transferred to the micro-models of the individual cells, where the actual material microstructure is properly considered. In the preliminary analysis presented in [7], intergranular cracking was considered as the only possible source of damage. Further progress has been presented in [14, 104], where coupling between the elastic and the thermal fields has been accounted for by developing a specific thermo-elastic Cohesive Zone Model (CZM) able to consider all possible fracture mechanisms occurring inside the polygrain material.

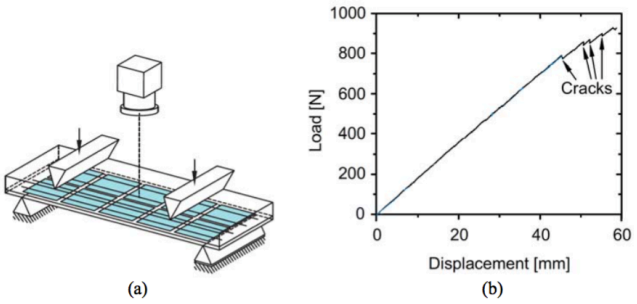

Figure 5.9: Setup of the experimental test on mini-modules carried out in [110] and obtained load-displacement curve (b)(adapted from [110]).

In the present study, transgranular cracking, i.e., cracking through the grains, is also considered in addition to the intergranular one, i.e., cracking along grain boundaries, and their competition is examined. To this aim, a novel image analysis procedure for the identification of grains and grain boundaries is proposed. Exploiting a modified intrinsic approach to cohesive crack propagation to reduce mesh dependency, a MATLAB pre-processor has been coded to automatically generate finite element (FE) meshes with cohesive interface elements inserted around all the FE edges. Different fracture parameters can be associated to the interface elements depending on their position (along the grain boundaries or inside the grains). Numerical examples are provided to show the applicability of this computational approach to polycrystalline silicon solar cells. Depending on the cohesive properties associated to the grain boundary and grain interior cracks, the computed crack patterns are compared and general trends are determined.

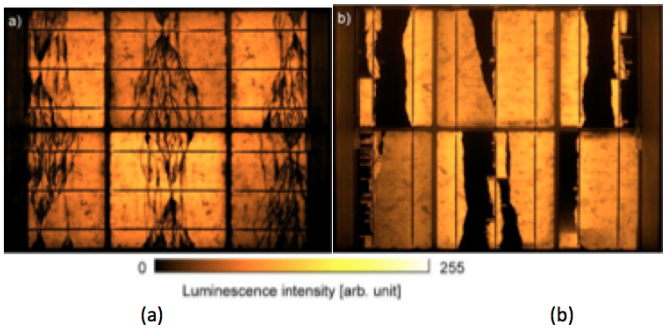

Figure 5.10: Crack patterns of mini-modules made of polycrystalline silicon tested according to the setup in Fig. 5.9. Line loading perpendicular to busbars (a); line loading parallel to busbars (b) (adapted from [110]).

The most common commercial PV modules are made either of mono- or polycrystalline silicon: this difference has a significative role on the electric performance of the cell, because grain boundaries are introducing additional resistances to the current flow not present in monocrystalline silicon. Two different images obtained with the electroluminescence (EL) technique taken in our laboratory are shown in Fig. 5.11, from which it is possible to notice the visual difference between a mono- and polycrystalline structure.

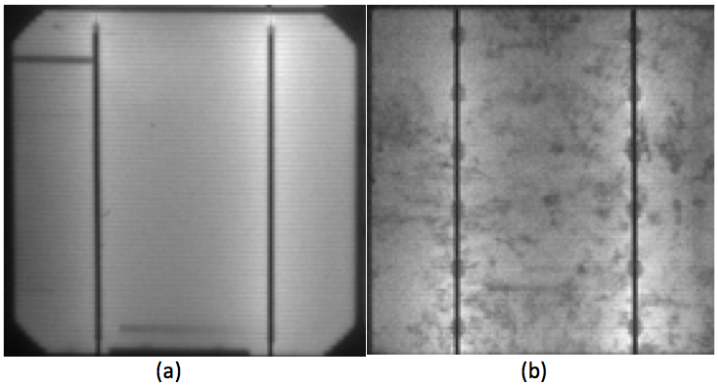

Figure 5.11: EL images of a mono (a) and a polycrystalline (b) solar cell. Grain boundaries lead to a nonuniform EL intensity due to local additional resistances.

The material microstructure plays also a role as far as the mechanical response is concerned. Different grain orientations may lead to different elastic parameters, as usually observed in polycrystals. Moreover, the role of grain boundaries on cracking is an aspect not

yet clarified in the literature related to Silicon PV. To investigate on this issue, the heterogeneity in the material microstructure has to be taken into account in numerical simulations and the proposed models have to be as close as possible to reality [98, 96]. When examining polycrystalline solar cells embedded in photovoltaic modules in daylight conditions, grain boundaries are nearly impossible to be distinguished due to a blue anti-reflective coating which covers the material microstructure (see Fig. 5.12(a)). Post-processing of EL images may partially help to recognize the grain microstructure by the non-uniform EL emission (see Fig. 5.12(b)), although the presence of thin electric conductors (fingers) on the cell surface makes grain boundary recognition a not trivial task. For quantitative image processing, good candidates are silicon cells without anti-reflective coating used to produce semi-transparent glass-polymer-silicon-polymer-glass modules for car sheds or facades, where fingers are replaced by a thin layer of conducting aluminium deposited over the whole cell. If illuminated by the sun on one side, the quasi-transparency allows material microstructure identification by taking a daylight photo from the opposite side.

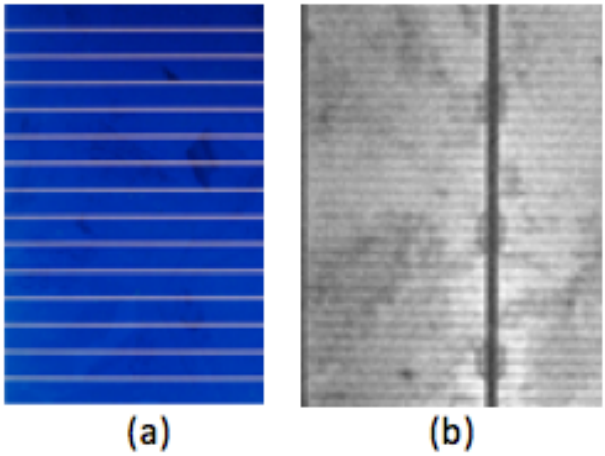

Figure 5.12: Grain boundary identification is a challenging task in polycrystalline cells: disturbance of the blue anti-reflective coating in daylight pictures (a); disturbance of fingers (thin horizontal dark lines) and busbars (thick black vertical line) in EL images.

The only remaining disturbance is given by the two vertical busbars (see Fig. 5.13). Grains appear of different colours and transparency due to their different orientation. The smallest grain is of a few millimetre size (the lateral size of the cell is about 10 cm). The complexity regards the grain geometry, since very often grains have a very elongated shape due to silicon wafer processing (see Fig. 5.13), which poses challenges for their identification and finite element meshing.

An innovative image analysis procedure is proposed here for grain boundary identification and the subsequent finite element mesh generation. The basic steps are illustrated in reference to Figs. 5.14 and 5.15. A high resolution colour image of a cell is the starting point

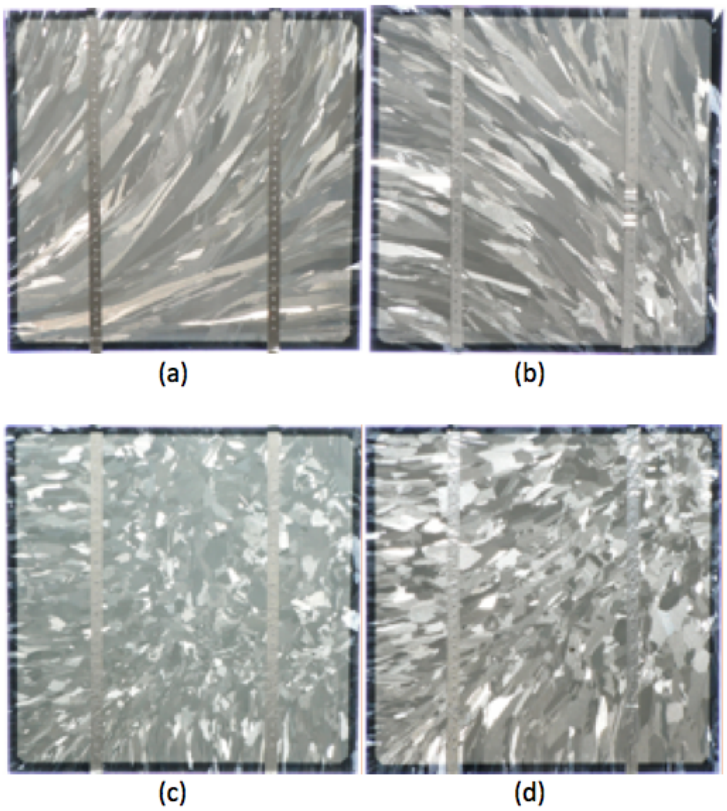

Figure 5.13: Daylight images of solar cells embedded in glass-polymer-silicon- polymer-glass photovoltaic modules.

(Fig. 5.14). The first step is to transform the master colour picture in a grey scale image in Fig. 5.15(a). This procedure filters the number of grains in the model by limiting the number of possible orientations to a maximum of 256 (each grain orientation corresponds to a grey intensity varying from 0 to 255). The resulting image is still very complex, with very elongated grains having similar grey levels nearly impossible to be distinguished. It is therefore recommended to further process Fig. 5.15(a) by transforming it in a black and white image (Fig. 5.15(b)). This procedure further filters grains close to each other and having very similar orientations. From this operation, however, a noise represented by small black dots is artificially introduced and it is a source of disturbance for the next stage of grain boundary identification. It is therefore useful to apply to Fig. 5.15(b) an averaging filter over 64 neighbouring points for each image pixel, with a weight of 1/64 for all the pixels. This leads to Fig. 5.15(c), where black dots are basically removed. Finally, the last step is to identify the grain boundaries. By treating the image as a 3D array with 0 or 1 integer values for each (x, y) pixel position, a point belonging to a grain boundary is identified by scanning the whole

image by horizontal cross-section lines and finding the pixels where there is a transition from 0 to 1 or vice versa (see Fig. 5.15(d)).

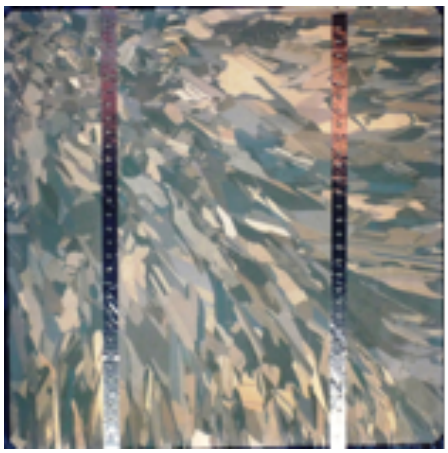

Figure 5.14: A colour image of a polycrystalline solar cell taken under daylight conditions.

With the help of Fig. 5.15(d), grain boundaries are further approximated by polylines as closed polygons whose topological properties (coordinate vertices and connectivity matrix of the edges) are stored in an array for the subsequent finite element mesh generation. The obtained polygons are shown in Fig. 5.16, superimposed to the original image.

The data structure of the various polygons is passed in input to the free software GMSH [111] for meshing the grains as if they were joined. This operation can be done with linear triangular or quadrilateral finite elements with a prescribed mesh density. The output of GMSH is then elaborated by a post-processing code developed in house and written in MATLAB. This programme automatically duplicates all the nodes of the finite elements and inserts interface elements all around them. The mechanical properties of the interface elements can be finally attributed depending on their position (inside the grains or along the grain boundaries). The final output is represented by a list of nodal coordinates and by the elements connectivity matrix in a format suitable for running a simulation with the finite element analysis programme FEAP [81]. Other formats used by commercial FE software like Abaqus or ANSYS can also be produced.

5.2 Implementation in FEAP: Application to a polycrystalline Silicon cell

In order to simulate crack growth in the material microstructure, an intrinsic approach is herein adopted. Triangular elements from the beginning of the simulation are surrounded by interface elements. As compared to an extrinsic approach, where interface elements are adaptively inserted in the model at each time step, the advantage is that remeshing operations

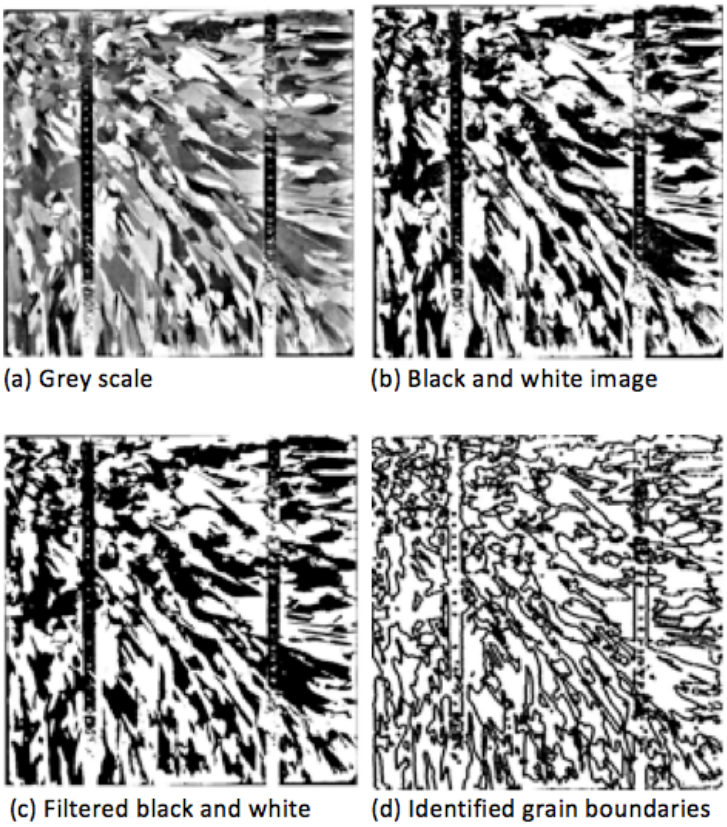

Figure 5.15: Some steps of image processing for grain boundary identification.

and nodes and elements renumbering is avoided [112]. On the other hand, the necessity of having an initial linear increasing branch in the CZM to capture the physical condition of vanishing stresses in the bulk in correspondence to vanishing strains introduces an artificial compliance related to the linear branch of the CZM that may be unrealistic. Another problem is the possible mesh dependency of the crack trajectory, which is constrained by the mesh discretization, and has to be ascertain with care by a suitable mesh dependency study.
The just mentioned issue of mesh dependency of the crack pattern is now investigated by considering three different mesh discretizations. To avoid the artificial increase of compliance induced by the intrinsic approach, a modified scheme is proposed where the initial stiffness of the CZM formulation is increased by refining the mesh by suitably reducing the parameter l_0 and keeping constant the fracture energy and the peak cohesive tractions, given by the products $\sigma_{\max} \exp(-l_0/R)$ and $\tau_{\max} \exp(-l_0/R)$, that should be treated as material properties. The optimal values of l_0 to be used in the simulations are chosen so that the initial slope of the obtained homogenized stress-strain curve is almost independent of the mesh size and equal

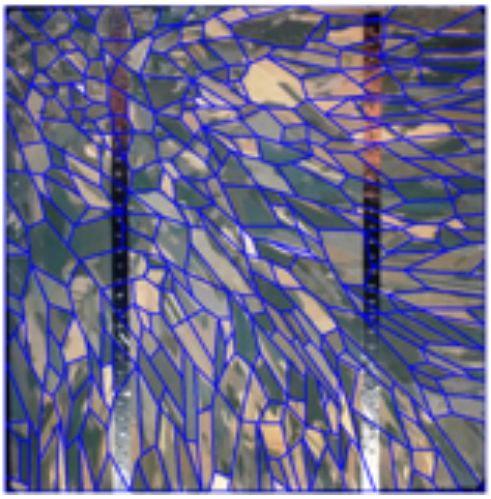

Figure 5.16: The real image of a polycrystalline silicon cell with its polygonal grain approximation superimposed.

to a value representative of the physical response of a polycrystalline material composing a solar cell, by keeping constant the tensile strength and the fracture energy of silicon.
It is remarkable to note that this rescaling of the initial compliance of the CZM by keeping constant the fracture energy is not possible with other CZM formulations like that by Tvergaard [92], because it is defined by a single nonlinear function of the gaps over the whole separation range. In order to prove the goodness of the proposed method it is applied to a sample model problem consisting of 4 grains (lateral size of about 1 cm) is analyzed under plane stress conditions with a typical thickness of solar cells equal to 0.166 mm. Three different FE mesh densities are considered,as it is possible to see in Fig. 5.6, where each coloured zone corresponds to a different grain, black thicker lines identify the border of the grains and thinner black lines draw finite elements for the numerical analysis.
An edge crack is placed on the left side with the aim to localize the deformation and simulate a pre-existent defect inside a grain. This microstructure is tested under vertical displacement control, imposed on the top side to simulate crack propagation in tension. The horizontal side on the bottom is restrained to displacements in the vertical direction, whereas the other sides are free. According to [113, 114, 115], the finest mesh size used in this study is expected to provide a reasonable approximation to the stress field. To investigate on the competition between transgranular and intergranular cracking by varying the fracture properties of the grain boundaries, a parametric study is performed. For the interface elements inside the grains, they are selected to represent the properties of bulk silicon: $\sigma_{\text{peak}} = \tau_{\text{peak}} = 1.5$ GPa (to which corresponds a tensile strength of silicon $\sigma_{\text{peak}} = 250$ Nmm/mm^2 for a cell with thickness of 0.166 mm), $g_{Nc} = g_{Tc} = 280$ m. The fracture energy, that for a cell with thickness of 0.166 mm results to be $G_F = 22$ N mm/mm, is higher than for a stand-alone polycrystalline silicon and takes into account the toughening effects exerted by the metallic fingers that act as fibres

keeping cracks closed and by the viscoelastic epoxy material encapsulating the silicon cell. The parameter R has been estimated equal to 88.2 μm in order to have the area below the Mode I CZM curve equal to the selected fracture energy [14]. The remaining parameter l_0 is tuned to avoid mesh dependency and obtain the same stress-strain curve in the elastic regime regardless of the mesh size: $l_0 = 18.0$ μm for the coarse mesh 1, $l_0 = 10.0$ μm for the intermediate mesh 2 and $l_0 = 5.2$ μm for the fine mesh 3. The CZM parameters of the interface elements along the grain boundaries are modified with respect to those of the bulk by considering $\sigma^{GB}_{peak}/\sigma^{grain}_{peak}$= 1.00, 0.75, 0.55, 0.40, that is, the peak peak grain boundary strength is progressively diminished as compared to the bulk strength. All the other fracture parameters are kept constant, so that the fracture energy scales according to the peak strength. Regarding the computational effort, the finest meshes require approximately 1h of computing time to determine the whole stress-strain curve until failure.

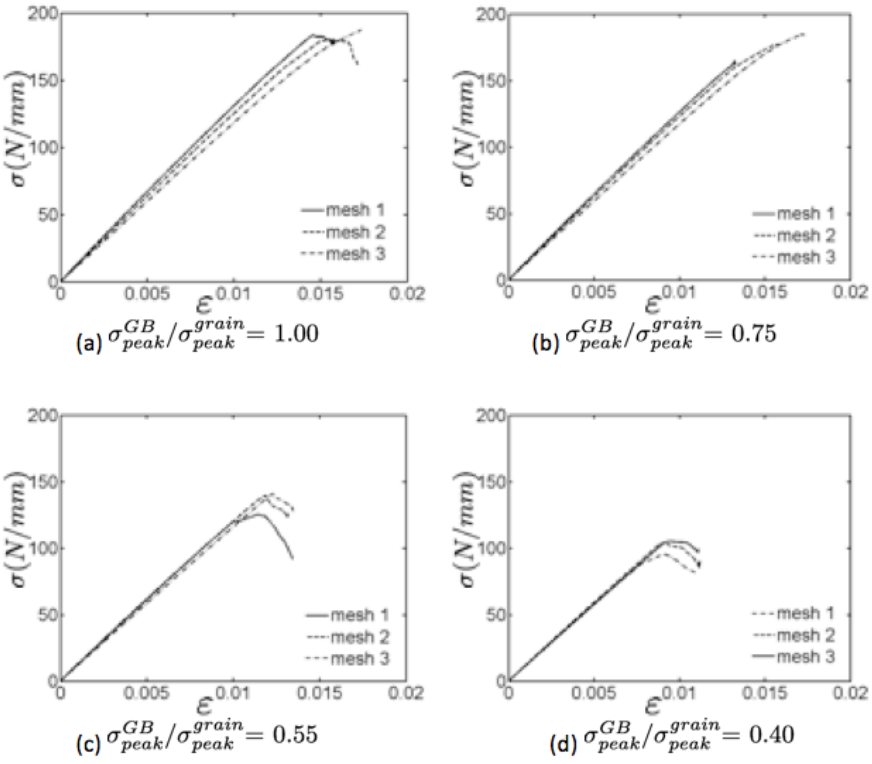

Figure 5.17: Homogenized mechanical response by varying the ratio between the peak cohesive tractions of the grain boundaries and of the grains, $\sigma^{GB}_{peak}/\sigma^{grain}_{peak}$. In each peak peak plot, results for meshes 1-3 in Fig. (5.16) are compared.

The computed average axial force per unit length, evaluated by summing up all the nodal reactions in the vertical direction on the top side and dividing the result by the side

length, are plotted vs. the imposed strain in Fig. 5.17. By reducing the ratio between the peak cohesive tractions of the elements belonging to the grain boundary and of those elements inside the grains, $\sigma^{GB}_{peak}/\sigma^{grain}_{peak}$, in the range from 1.00 to 0.40 (from Fig. 5.17(a) to (d)), grain boundaries become weaker and weaker and the microstructure is more and more prone to intergranular cracking. For each value of $\sigma^{GB}_{peak}/\sigma^{grain}_{peak}$, results obtained from different mesh sizes are almost the same in terms of maximum axial force per unit length. This proves that the procedure adopted to rescale the parameter l_0 of the CZM relation to provide a unique initial linear elastic regime in the homogenized curves is effective to obtain mesh-size independent results.
The examination of the contour plot of the vertical displacements at maximum load shows that, if all the interface elements have the same fracture properties regardless of their position (first line in Fig. 5.18(a)), then the initial stress-free defect propagates and transgranular cracking prevails over the intergranular one. Grain boundaries are highlighted by blue lines, whereas the crack path is shown with white lines. By reducing the cohesive peak tractions ratio $\sigma^{GB}_{peak}/\sigma^{grain}_{peak}$ to 0.75, the initial defect propagates inside the grain and then grain boundary decohesion takes place when the defect meets the first grain boundary (second line in Fig 5.18(b)).For $\sigma^{GB}_{peak}/\sigma^{grain}_{peak}$ =0.55,the initial defect does not propagate any longer and cracking is pure intergranular (third line in Fig. 5.18(c)). This kind of failure is even more evident for lower values, e.g., for $\sigma^{GB}_{peak}/\sigma^{grain}_{peak}$ = 0.40, for all the mesh sizes (fourth line in Fig. 5.18(d)).

A computational framework for the simulation of intergranular and transgranular cracking in polycrystalline silicon solar cells has been proposed in the present work. To this aim, a specific image analysis procedure and a MatLab pre-processor have been developed to generate FE meshes with embedded interface elements. To avoid mesh dependency, the intrinsic CZM approach has been modified by adapting the initial stiffness of the linear part of the CZM by changing the mesh size. Nonlinear finite element simulations on exemplary polycrystalline microstructures show a clear prevalence of transgranular cracking over intergranular fracture, unless very weak grain boundaries are present. These numerical results are consistent with the experimental observation in [7]. This pinpoints the necessity of simulating transgranular cracking in real solar cells. Clearly, the computational cost and convergence problems due to the very brittle nature of silicon are enhanced. Indeed, further research is envisaged for the development of suitable techniques computationally affordable to simulate transgranular cracking in polycrystalline solar cells on a larger scale. Moreover, the presence of fingers and busbars, here accounted for as a global toughening effect, could also be properly modelled as a discrete reinforcement. Identification of CZM parameters is also expected to be crucial for reproducing the experimental stress-displacement curves in closer detail.

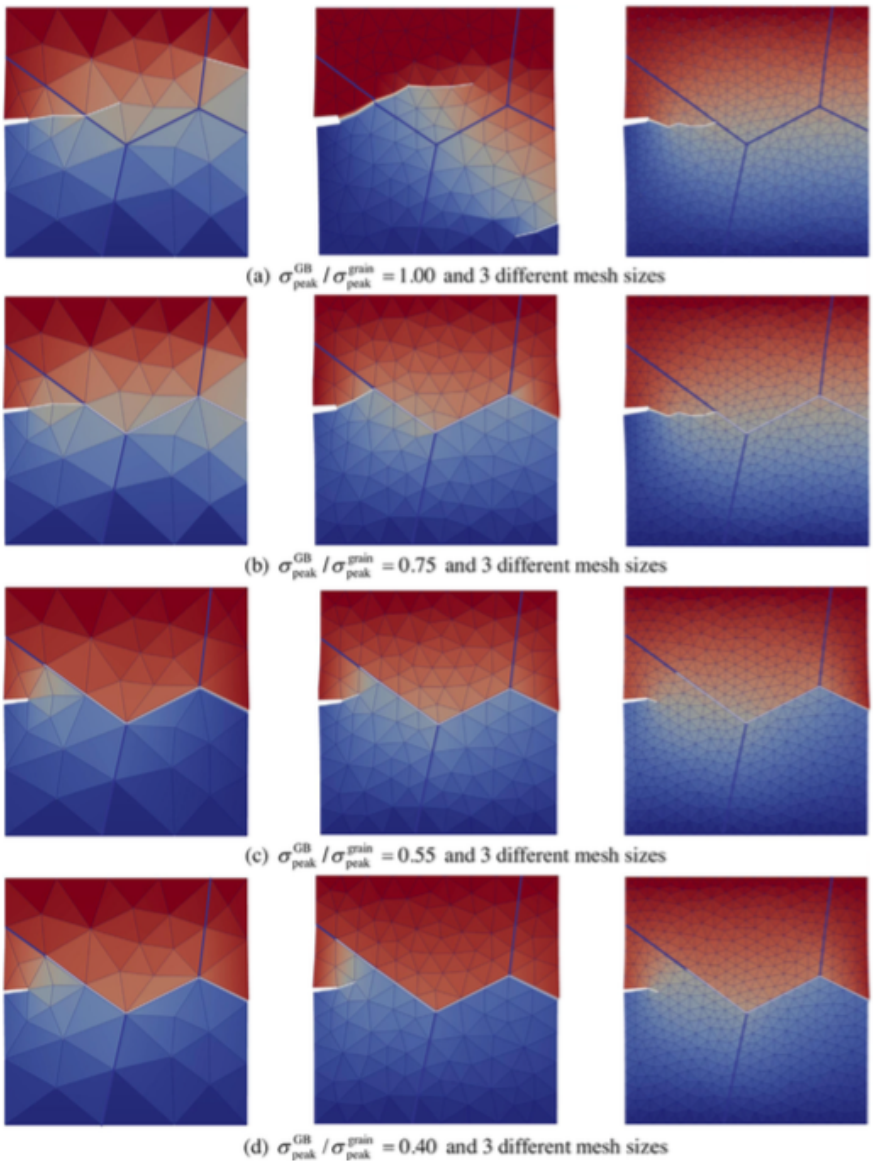

Figure 5.18: Contour plots of the vertical displacements at maximum load, for different mesh sizes (columns) and different ratios $\sigma^{GB}_{peak}/\sigma^{grain}_{peak}$ (rows from a to d).

Chapter 6

Macro-scale Models: real size tests and experiments

In this Chapter two experimental campaigns on commercial semi-flexible PV modules are presented, involving our research team and the technologies available at the laboratory of Materials and Structures of the Department of Structural, Geotechnical and Building Engineering of Politecnico di Torino.
In particular the first experimental campaign is related to bending tests conduced on the same typology of semi-flexible panels described in the previous Chapters, in order to understand their behaviour when variable cyclic stresses due to repeated bending actions are imposed. Experimental data have been analyzed to obtain a graphical representation of the performance decay due to fatigue degradation that involve the module. Another point under investigation, reason for which these tests are of particular importance, is the study of the capacity of the Silicon layer to regain its conductive electrical capacity again, although a fracture process with the presence of a crack causing interruptions in the continuity of the material is present. The idea of the research is to highlight the "self-healing" capacity of the material, that is the ability to return to a full or partial functionality of its inactive zones after the release of the bending. The electroluminescence (EL) technique, used to monitor crack growth is detailed in the Appendix B. Results obtained show that crack propagation in monocrystalline Silicon cells embedded in PV is a complex phenomenon. Even if Silicon has a very brittle nature, thanks to the mutual action of the encapsulating polymer and residual thermo-elastic stresses, cracked regions can recover the electric conductivity during mechanical unloading due to crack re-closure. This pinpoints the importance of reducing cyclic stresses caused by vibrations due to transportation and use, in order to limit the effect of cracking in Silicon cells.

The second experimental campaign is related to several tests conduced with the aid of a hail shooting machine located in the laboratory of Materials and Structures of the Department of Structural, Geotechnical and Building Engineering of Politecnico di Torino, in order to reproduce the effect of low-velocity impacts (i.e. hail or any body falling and hitting the surface during the factory production, transportation and assembly) on semi-flexible PV modules. Damage on the Silicon layer of the module is checked through an EL image analysis.

Interposing different materials between the PV module and a infinitely rigid substrate, the effect of various material stiffnesses are investigated in order to assess how they influence the crack pattern and the stress inside the Silicon layer. The numerical simulation of impact tests, conduced using the FEAP software, is conduced in relation to a simplified quasi-static and a dynamic approach. Results highlight the important role of the substrate stiffness on the extension of the electrically inactive area due to cracking in Silicon solar cells embedded in photovoltaic modules. Moreover, numerical evidences demonstrate the accuracy of the simplified quasi-static model with dynamics modeled by a single degree of freedom to capture the overall response of the whole system, while the more accurate solution of the dynamic contact problem is required for a realistic prediction of the stress distribution in the Silicon layer by accounting for stress wave propagation and reflection. A simple strength criterion based on the achievement of a nominal ultimate tensile strength is finally proposed and its application to the numerically computed stress distributions leads to a predicted extension of the crack pattern for the different substrate stiffness in very good agreement with experimental observation.

6.1 Bending tests on semi-flexible PV modules

Even if photovoltaic (PV) modules are supposed to have a lifetime longer than 20 years under the exposure to environmental conditions, ageing effects due to snow, wind gusts, hail and rapid temperature variations are responsible for further propagation of cracks [11], although it is nearly impossible to assess the individual contribution of each factor. Analysis and statistics of degradation mechanisms in Silicon modules observed in the field have reported various sources of failure of PV modules, namely: laminate internal electric circuit failure, glass breakage, junction box or cables failure, encapsulant decoloration or backsheet debonding, cell failures due to cracking. Among them, cell failure is considered to be responsible for 10% of the totally observed PV module failures, with an occurrence analogous to that of junction box or cables failure and to encapsulant decoloration or backsheet debonding [116]. Cracks on the millimetre or centimetre size are mostly invisible by naked eye but they can be localized recurring to the EL technique [117]. Cracks can lead to electrically inactive cell areas thus reducing the power output of the module and the fill factor, taking place via the following mechanisms, i.e: a linear decreasing of the short circuit current by increasing the inactive cell area and an increase in the series resistance of the cell due to cracking [108,118]. Potentially, if a crack crossing an Aluminium finger is sufficiently open, then the finger may fail and the electric flow to the busbar in case of normal operating condition, or from the busbar in case of forward bias condition as in the EL testing, would be interrupted. Therefore, portions of Si cells can be potentially deactivated by cracks and their impact on power-loss reasonably depends on their inclination and position with respect to the busbars determining dark non conductive zones, as can be seen in Figs. 6.1(a) and 6.1(b). For instance, a crack parallel to the busbar on the upper side of the cell could lead up to 25% of electrically inactive area (Fig. 6.1(b)) significantly reducing the electrical performance. Giving importance to the pure geometrical criterion, for which are no taken into consideration neither physical mechanisms such as thermo-mechanical deformation, nor the fact that the cells are embedded in the composite PV module, worst-case scenarios have been predicted by considering all the

experimentally detected [108] or numerically simulated [7] cracks as perfectly insulated lines.

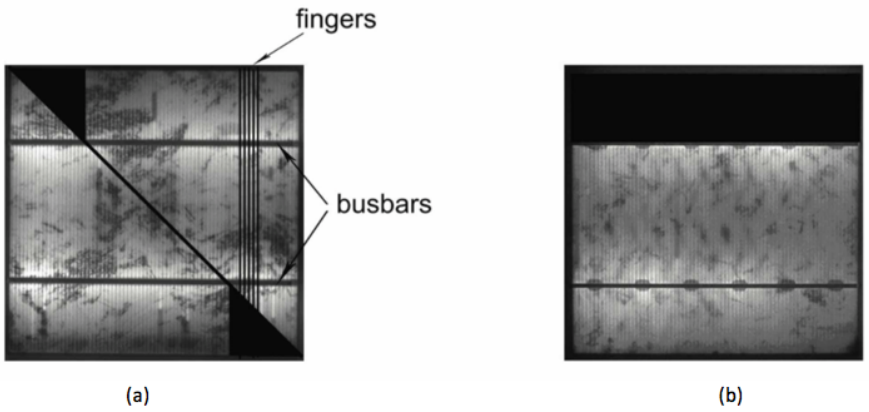

Figure 6.1: Geometrical criterion showing the expected amount of potentially inactive cell areas depending on the orientation of the crack with respect to the busbars: 6% of potentially inactive cell (a); 25% of potentially inactive cell (b).

In reality, it is reasonable to expect intermediate configurations where cracks may partially conduct depending on the relative crack opening displacement at crack faces. A complete modelling of the phenomenon should therefore consider the following steps:

- Simulation of crack nucleation and propagation according to a computational approach based on the cohesive zone model (CZM) [82, 105], where cohesive tractions opposing to the relative displacements of the crack faces are decreasing functions of opening and sliding,
- Analysis of thermal effects by augmenting the basic mechanical CZM to take into account the additional thermal resistance of cracks [14],
- Modelling of the electric response of the cell. For this last item, localized series resistances dependent on crack opening might be postulated in correspondence of cracks, in addition to the distributed series resistance.

A preliminary experimental observation supporting coupling effects induced by the thermo-mechanical field on the electric one due to cracking regards the highly oscillating electrical response in time of a PV string containing a cracked cell, depending on the cell temperature [13]. The electric model of solar cells developed so far do not consider this form of coupling induced by cracking. To achieve a predictive stage useful for power-loss predictions and durability assessment of PV systems exposed to environmental loads, series resistance values used as input of the circuit model should be related to the thermo-elastic stress state in the solar cell.

6.1.1 Description of bending test

In order to understand the effect of the mechanical deformation on the electric response, a bending test on a rectangular PV module has been performed in the laboratory by monitoring cracking at different deformation levels by EL imaging. A semi-flexible module made of 2 rows of 5 monocrystalline Si cells each is used (see Fig. 6.2(a)). The dimension of the cells is 156 x 156 mm. The partially symmetric arrangement of the layers through the thickness (0.265 mm of polyethylene terephthalate, 0.600 mm of epoxy-vinyl-acetate, 0.166 mm of Silicon, 0.400 mm of epoxy-vinyl-acetate and 0.345 mm of backsheet) and the different Young moduli of the materials leads to Si cells just above the neutral axis of the cross-section (see Fig. 6.2(c)). A certain flexibility is allowed thanks to the lack of the glass front-sheet, so that it can be used also for application where the shape of the underlying structure is curved. In order to induce a tensile stress state inside solar cells, the curvature imposed to the module is such that the convex side after bending corresponds to the PET side (front side in Fig. 6.2(c)).

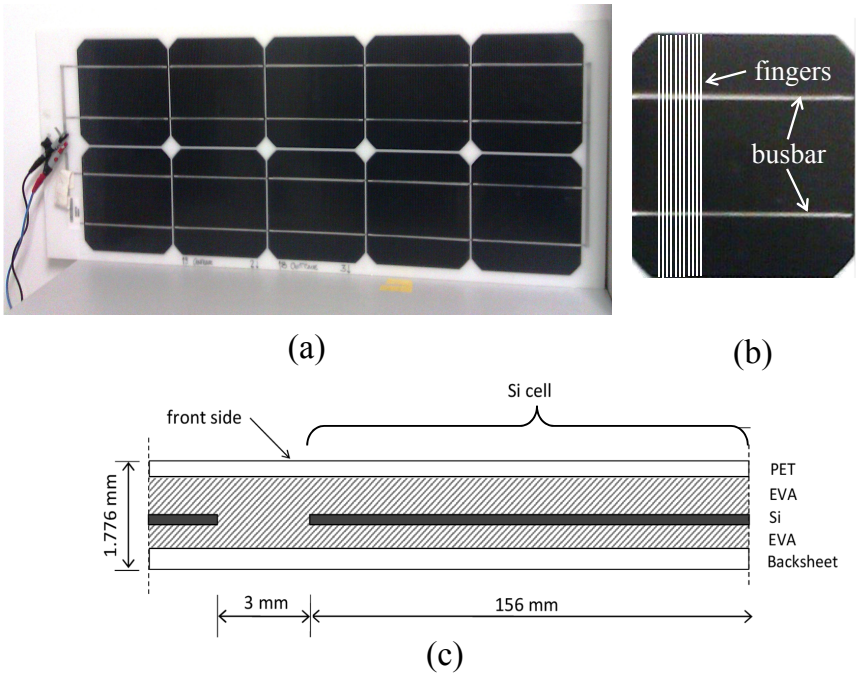

Figure 6.2: Semi-flexible PV module: (a) photo of one of the tested modules; (b) detail of a solar cell; (c) sketch of the cross-section of the PV module with the different layers.

In order to create pre-existing cracks on the module and then study their evolution depending on the imposed bending load, moderate impacts have been made with PMMA balls of 4 cm of diameter at a velocity of 6 m/s. In this way, cracks are introduced by an indentation effect. The EL images of four solar cells in the middle of the panel are shown in Fig. 6.3.

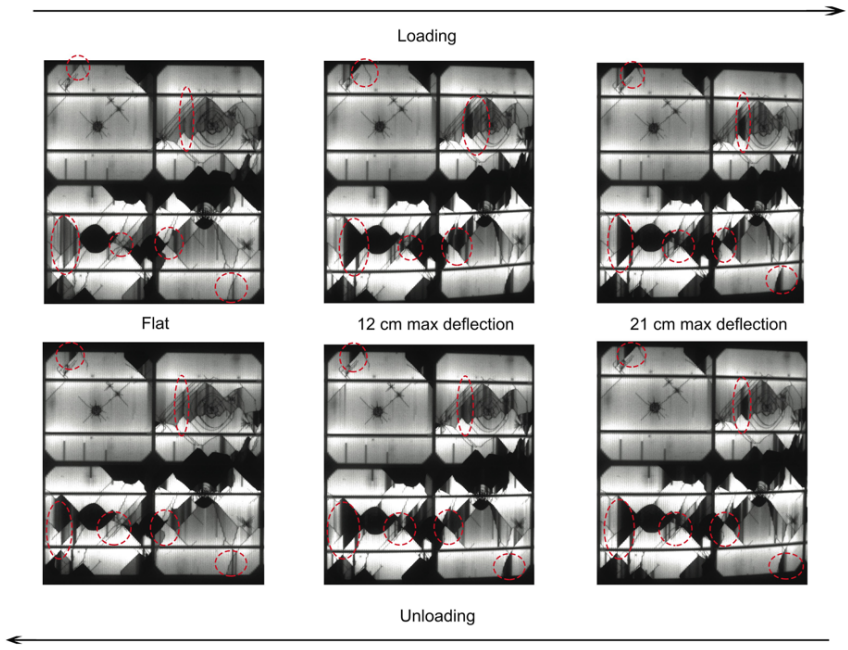

Figure 6.3: Evolution of EL signal during bending loading and unloading for different deflections.

Impact points of the PMMA sphere can be clearly distinguished by the circular dark spots from which diagonal cracks, influenced by the crystallographic planes of cubic face centred monocrystalline Silicon, depart. Since these patterns are completely invisible with naked eye, it is necessary for the determination to employ the EL technique. In some cases, large electrically insulated cell portions, appearing as dark areas, are visible. Other portions, circled in Fig. 6.3 with dashed lines, identify regions isolated by cracks but still partially conducting from the electrical point of view. This can be properly explained by the assumption that their crack opening is smaller than a critical value which should cause the complete electric insulation and by a compressive stress state inside the cells due to residual thermo-elastic stresses induced by cooling down the module from the lamination temperature at 150°C to the ambient temperature at 20°C.

The estimation of the residual stress and deformation scenario inside the PV module, a 2D plain strain finite element (FE) model of the layered composite in the plane of bending has been analyzed using the Finite Element Analysis Programme FEAP [81]. Taking advantage of the structural symmetry, just one half of the module has been analyzed by introducing symmetry boundary conditions on the symmetry line and considering the opposite edge of the module as simply supported in the direction orthogonal to the longitudinal axis. The parameters related to the thermal expansion coefficient of the plastic layers, EVA and

Silicon are respectively $\alpha = 5.04 \times 10^{-5}$, 2.70×10^{-4} and 2.49×10^{-6}, while the other elastic parameters are as in [3]. In consideration of the observed thermo-visco-elastic behaviour, a Young modulus of EVA equal to 1 MPa has been chosen, which is the lowest value in the considered range of temperatures according to experimental results [3]. Basically, due to a possible variation of the Young modulus of EVA from 1 to 10 MPa, an increase of about 10% in the compressive stresses inside Silicon may be introduced. The analysis conduced through the FE numerical procedure estimates the presence of a compressive stress field in the Si cells with variable values from 0 MPa at their borders up to 60 MPa in their centre as reported in the contour plot in Fig. 6.4). Moreover, the presence of this residual stress field is beneficial aspect for the material in the module since any initial crack or defect present in Silicon would be closed by compression.

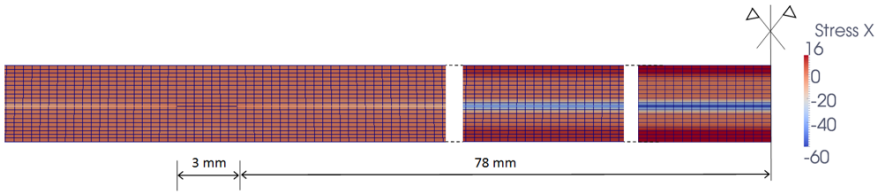

Figure 6.4: Contour plot of the horizontal stresses inside the PV laminate in the portion near the symmetry line.

By gradually increasing the mid-span bending deflection (following the images in the upper row in Fig. 6.3, loading direction from left to right), the process of crack opening begins and additional insulated dark areas appear, thus confirming that the electrical behaviour of cracks does depend on the elastic deformation. Very interesting is the reverse process related to the unloading stage (lower row in Fig. 6.3 instead unloading direction from right to left), where there is a partial reclosing of the cracks, up to come into contact and conduct again restoring the electrical flux. Hence, although globally the amount of accumulated damage is increased during the cycle due to repeated action of loading and unloading, since the final EL image is more dark than before, an electric recovery due to crack closure is reported. A second target of the experimental campaign is the monitoring of the evolution of degradation by increasing the amount of bending cycles (from zero to a maximum mid-span deflection of 21 cm per cycle). Comparative results at certain steps of the bending story are shown in Fig. 6.5(a), where EL images of a certain significant cell of the module recorded at the point of maximum deflection for 1, 50, 200, 250, 300, 350, 500 and 650 cycles are reported. The cyclic tests have been conducted in the standard ambient temperature (20°C) so that thermal properties of materials allow to consider not to be in a temperature range particularly critical. Regarding the EL measurement procedure, to minimize localized heating effects in the cells, that can eventually influence the tests, the total time of application of the external voltage was limited to 30 s (for further details read Appendix B). From the time of switching the power supplier on to its switching off, six EL images have been recorded to monitor this transient regime. During that, no crack propagation was observed, reason for which temperature effects

can be excluded and considered non influent. Brittle crack propagation due to over-loading has also to be excluded. In fact, the force-displacement curve of the panel tested under displacement control was linear elastic over the whole displacement range. This is in line with analogous previous experimental observations [110] regarding glass-laminated mini-modules tested under four-point bending. Moreover, unloading and reloading was taking place along the same curve. This is reasonable since the pre-existing crack pattern due to hail tests is slightly changing from cycle to cycle and it does not significantly affect the overall stiffness of the module. On the other hand, the effect of the crack pattern regards the electric response, as shown by comparing the EL images at different cycles.

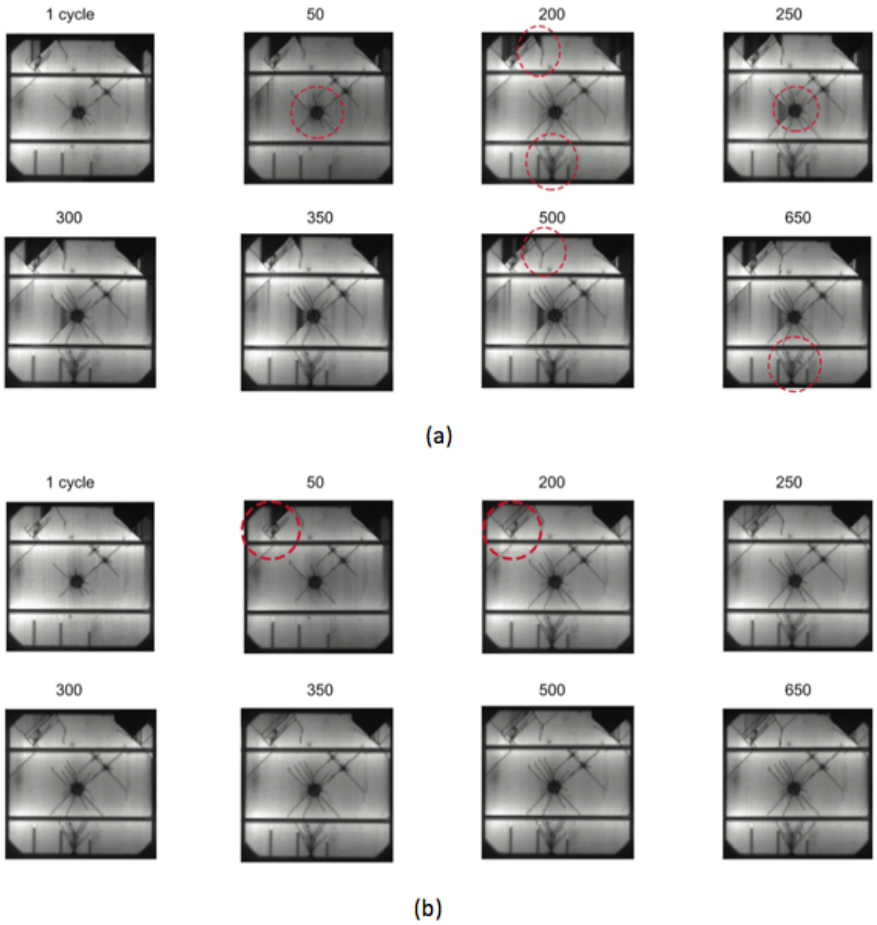

Figure 6.5: Fatigue degradation of the electric response and increasing crack pattern at different bending cycles. EL images are taken at the maximum deflection point of the module (δ = 21 cm) (a) and at the unloaded configuration (δ = 0 cm) (b).

During the first 50 cycles only a propagation of cracks around the dark central point of impact can be appreciable. Crack propagation takes place from 50 to 200 cycles, with the growth of new cracks from the lower border of the cell, originating from an edge crack. No crack propagation can be clearly detected from 200 to 250 cycles, although the EL intensity between diagonal cracks diminishes, thus implying a material degradation and leading to a reduction of electric conductivity across the cracks. This trend still goes on by increasing the number of cycles, with noticeable further crack propagation (cycle 300) and coalescence of two propagating cracks (cycle 350). At 500 cycles, there is the presence of a new crack, originated from an initial one on the upper side of the cell, as a result of a crack-branching mechanism. After the appearance of this new crack, the dark EL area just on the left of it becomes conductive again, with apparent contrast to what seems logical to expect. This can be explained as the effect of a well known phenomenon frequently observed in brittle materials, called strain localization, which corresponds to a stress relief in the surrounding cracks when a major crack propagates [82]. For this reason, with the appearance of a new crack requesting a great contribute of stress, the previous one in the surrounding is relaxed and it experiences a gradational reduction of its relative opening displacement.

6.1.2 Results and possible further developments

To prove the effect of the growth of a new fracture process on the opening of a preexisting cracks in case of a brittle material embedded in the laminate, a FE study based on nonlinear fracture mechanics is proposed. For more details about the CZM, see Chapter 5 and [14]. In the 2D approximation of the PV module shown in Fig. 6.6(a), one or two cohesive cracks (distant 0.9 cm from each other) are introduced in the Si cell placed near the symmetry line, as presented in the details in Figs. 6.6(b) and 6.6(c)). In the numerical simulations, the PV module is loaded by imposing a displacement to the middle cross-section up to $\delta_{\max} = 21$ cm as shown in Fig. 6.6(a). Residual thermo-elastic stresses are not considered here for the sake of simplicity and justified by the fact that if the stress relief takes place, then it would happen also in the presence of residual thermo-elastic stresses. A very low cohesive peak stress of $\sigma_{max} = 0.2$ MPa is considered to simulate a very low cohesion due to a severe state of damage. The contour plots of the horizontal stress field superimposed to the deformed meshes of the portion of the module where cracks are placed are shown in Figs. 6.6(b) and 6.6(c). Stresses are slightly reduced by the simultaneous presence of two cracks and the crack opening of the pre-existing crack reduces from 11 mm to 9 mm. Therefore, the effect of strain localization induced by the propagation of new cracks supports the hypothesis of unloading effects at pre-existing cracks that might come into contact, thus leading to a recovery of their electric conductivity.

The phenomenon of electric recovery due to crack closure already noticed in the case of the first cycle can be observed also after several cycles. For instance, comparing the EL data along a cross-section perpendicular to the busbars and passing through a crack in the loaded and unloaded configurations for 50 cycles (Figs. 6.5(a) and 6.5(b)), we obtain the diagram in Fig. 6.7. Values of EL close to unity correspond to very bright Si areas, whereas values close to zero are dark "electrically inactive" zones. As visually emphasized by the superimposed parabolic trend with a discontinuity of first type in correspondence of the crack ($x/l = 0.15$), a jump in the EL data takes place and it is higher for the configuration at maximum deflection

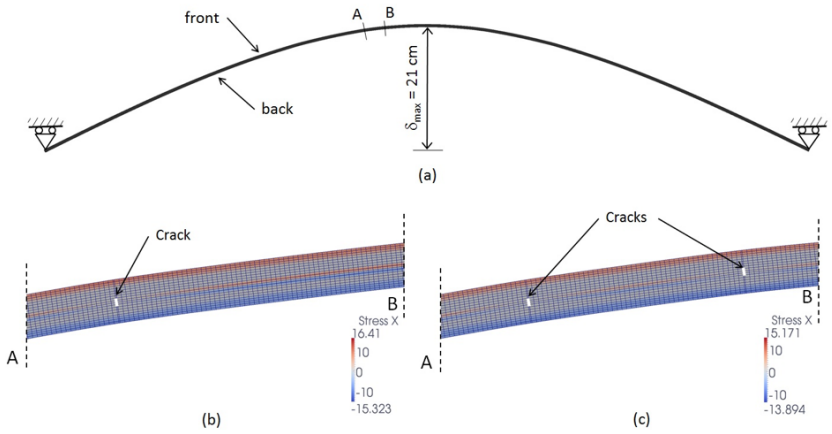

Figure 6.6: Structural scheme (a); contour plot of the horizontal stress field in case of one single crack (b); contour plot of the horizontal stress field in case of two cracks (c).

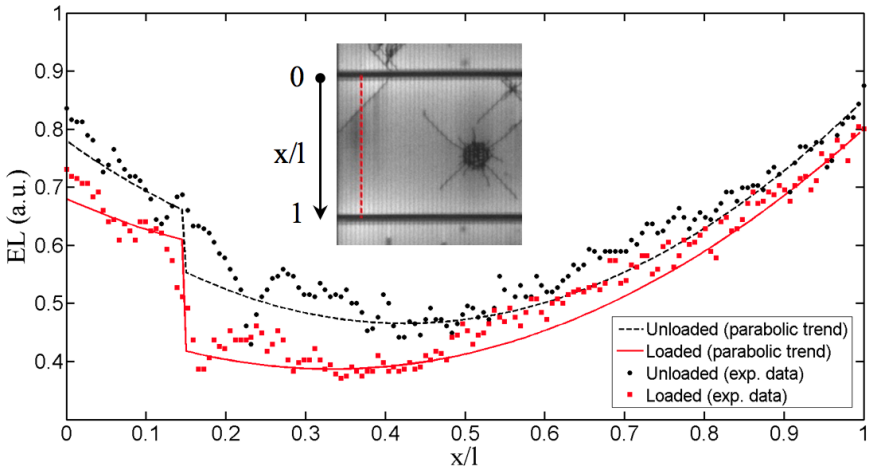

Figure 6.7: EL data along a cross-section passing through a crack for 50 cycles in the loaded and unloaded configurations.

where the crack opening is reasonably larger.
Finally, strain-localization can be evidenced again by comparing in Fig. 6.5(b) EL images for 50 and 200 cycles, see the circled areas. The propagation of a diagonal crack to the left relieves the deformation in the Si area, the diagonal crack on the right experiences a reduction in crack opening and the EL image of Silicon above becomes brighter. A quantitative anal-

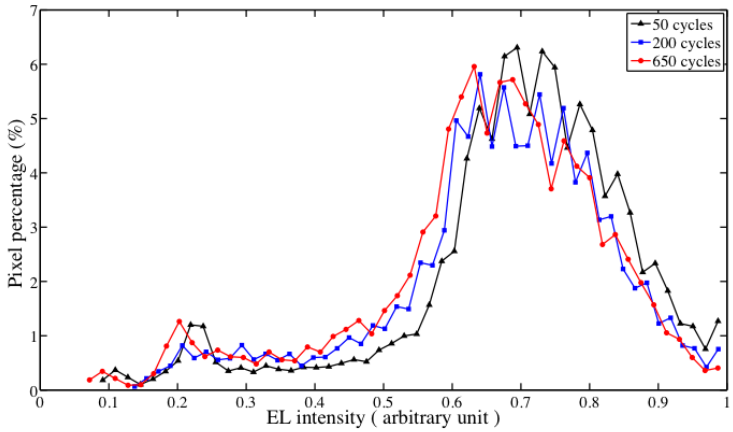

Figure 6.8: EL distributions for different number of bending cycles at maximum deflection. Note the shift of the distributions to the left by increasing the number of cycles, a trend consistent with the progression of fatigue degradation.

ysis of EL images at maximum deflection (Fig. 6.5(a)) shows that the statistical distribution of pixels having a given EL intensity is particularly skew-symmetric, with a long tail for EL intensities less than 0.5 (Fig. 6.8). Moreover, although the difference between EL images by increasing the number of cycles is apparently marginal, (i.e., only a few cracks propagate and some regions become darker), the EL distributions quantify the fatigue degradation trend. By increasing the number of cycles, in fact, the EL distribution shifts to the left. For high EL intensities, the pixel percentage is diminished by increasing the number of cycles. Exactly the opposite trend takes place in the low EL intensity range, (i.e. more pixels become darker). Basically, the results obtained from the present analysis demonstrate that due to the particular configuration of the modules, in which the Si cells are encapsultated into a ductile polymeric material, coupling between the electric response measured by EL images and the elastic deformation takes place due to cracking. Therefore, the worst case scenario in which all the detected cracks as perfectly insulated has to be considered with care, since more complex degradation phenomena occur in reality. In particular, the appearance of electrical recovery due to crack closure and residual thermo-elastic stresses, fatigue degradation, crack branching and crack coalescence, stress relief and recovery in the EL signal in case of strain localization induced by crack propagation of existing cracks or by new crack nucleation are all complex phenomena in their interpretation and moreover it is not trivia to establish in what way performance could be influenced by them. It has to be remarked that all of these phenomena are impossible in stand alone Si cells which are very brittle and display a different behaviour as compared to Silicon at the micro-scale, like that used for MEMS [119, 96, 97]. Therefore, modelling of Si solar cells behaviour by neglecting their embedding into a composite should be done with many caution in case of PV applications. The creation of mechanical defects and its effect on the solar cell performance is also relevant for thin film solar cells. An addi-

tional complexity as compared to MEMS is related due to the very different size-scales and thicknesses of the various layers which suggests the use of multi-scale computational strategies to model 3D geometries. The reported results have general implications for any kind of conductive material embedded into a ductile polymeric one, see, (e.g., graphene layers dispersed into a polymeric matrix [12]. In other words, the global behaviour cannot be predicted from the mechanical properties of the individual constituents, but it comes out as the result of the interaction of the components of the system, a feature typical of complex systems. The present results express a strong need of modelling thermo-electro-mechanical coupling effects in polycrystalline Si solar cells embedded in PV modules, requiring the development of multidisciplinary research involving electronics, materials science and computational mechanics. From the industrial and engineering point of views, the present results imply that the quasi-static application of very high distributed pressures as requested by qualification standards [120] is not enough if we are interested in evaluating the actual degradation rate and possibly infer about the lifetime of produced PV modules. In fact, other unexpected forms of damage, like fatigue degradation, are indeed possible due to the composite structure of the module and can be induced by very common sub-critical loads like vibrations due to transportation or wind gusts, phenomena not yet characterized so far.

6.2 Impact tests

The problem of low-velocity hail impacts on flexible photovoltaic modules is herein investigated from both the experimental and the modeling points of view. Results obtained from an experimental campaign conduced by the same research group, emphasizes the key-role of the substrate stiffness, conditioning the extension of the dark electrically inactive area due to cracking in Silicon layer of cells embedded in photovoltaic modules. On the other hand, an interpretation of the experimentally observed damaged area and crack patterns using the electroluminescence test is attempted, with the formulation of a simplified single-degree-of-freedom (SDOF) model and a rigorous but computationally more expensive finite element solution of the contact problem in dynamics. Results achieved express the accuracy of the simplified model to capture the overall response of the system, while the rigorous method is anyhow required for the most realistic prediction of the stress distribution in the Silicon layer by accounting for the presence of stress wave propagation and reflection inside the Silicon layer. A simple strength criterion based on the achievement of a nominal ultimate tensile strength is finally proposed, in order to be applied to the numerically computed stress distributions providing an estimation of an expected extension of the crack pattern for the different substrate stiffness in very good accordance with experimental observation.

6.2.1 Aim of the experimental campaign

A starting point for the analysis is given by the content of the applicable standards for the performance discipline assessment and rating of PV model in order to be approved. In the European zone, PV modules are usually designed in order to comply with the IEC 61215:2006 standards [5] (International Electrotechnical Commission), including also a regulatory part about hail impact tests required to be performed by firing a molded ice ball with a pneu-

matic launcher onto the PV module. The standard dimension of the ball is 25 mm diameter, and the imposed impact velocity is 23 m/s but however, it is possible to switch to different diameters and velocities for particular environments. The objective of the test is purely to verify the module capacity of withstanding the impact of hailstones and as a consequence, it provides merely a simple pass/fail assessment rather than providing a quantitative evaluation of the PV module response after impacts. More precisely, the following sequence of fires is requested to hit specific locations of the PV module considered more critical, recording by visual inspection any sign of damage and visual effects after each sequence:

1. A corner of the module window, not more than 50 mm from the frame (1 shot);
2. An edge of the module, not more than 12 mm from the frame (1 shot);
3. Over edges of cells, near an electrical joint (2 shots);
4. Over points of minimum spacing between cells (2 shots);
5. On the module window, not more than 12 mm from one of the points at which the module is fixed to the supporting structure (2 shots);
6. On the module window, at points farthest from the points selected above (2 shots);
7. Any points which may prove especially vulnerable to hail impact.

The requirements to pass the test is to have:

- No visible evidence of major visual defects;
- The measurable degradation of maximum output power should not exceed 5% of the value measured before the test;
- Insulation resistance should meet the same requirements as for the initial measurements.

Therefore, the accurate inspection of the crack pattern developed in the Silicon solar cells is not explicitly requested. At first look the evaluation of the power-loss could be considered as a good criterion to assess the immediate effect of impacts, because can be supposed that this measure and the electrically active portion of the cell are directly proportional. However, partially electrically conductive cracks that do not initially affect the electric response of the PV module may further degrade over time after a sequence of cyclic loading (thermal cycling and also vibrations as explained before), leading to substantial power-losses over time exceeding the threshold value requested by the criterion. The first documents found in the literature related to experimental tests simulating hail impacts were pioneeringly carried out in 1978 at the Jet Propulsion Laboratory of the California Institute of Technology [121]. In those tests different types of PV modules were under investigation, differing from each other mainly for the top layer material used: tempered glass, annealed glass, acrylic sheet and Silicone potting.

The impact tests were performed with a pneumatic gun, firing ice balls with different diameters, at different velocities. The control parameters for the validation of the results

were visual inspections and the determination of the electrical power-loss. The experiments established that no semi-flexible panels (those with a Silicone potting top layer) were capable of withstanding 1-inch diameter simulated hailstone impacting at a velocity of 23 m/s or higher, presenting in every case the occurrence of solar cell cracking. In any case, at that time there were not more advance technical instruments capable to analyse the experimental results by means of more sophisticate technologies, such as the electroluminescence (EL) technique, which is nowadays the most suitable type of control that allows to clearly identify the crack pattern and its effect on the electric response. In the present research, the effect of hail impacts on semi-flexible PV modules is investigated from a quantitative point of view in order to get a clear picture of the mechanical damage induced by impacts. The commercial semi-flexible PV modules that have been used for the experimental tests are of the same type of those used for the bending test presented in previous part. The impact of hailstone on PV modules was reproduced with low-velocity impact tests, performed by shooting a polyamide sphere with a pneumatic gun. During the impact tests, the PV modules were laid on substrates with different mechanical properties in order to reproduce several installation conditions that may be found in real applications and assess their role on damage, an aspect not yet investigated in the literature. The effective extent of damage created inside the solar cells after each impact of the sphere has been assessed by taking an EL image, which clearly shows crack patterns and electrically inactive portions of the solar cell as dimmer areas. A pneumatic gun, located into the laboratory cited in the introduction, built to perform low-velocity impact tests [122] (maximum allowed velocity of 20m/s) with a spherical ad-hoc projectile having a diameter of 40mm made of Polyamide was used (see Fig. 6.9). The pneumatic gun apparatus is composed by several parts, herein described in each its part with reference to Fig. 6.9:

1. An air compressor;
2. A tank for the storage of compressed air;
3. A vertical gun barrel. The spherical projectile is restrained at the top of it, with an electromagnetic jaw, manually unlocked by the operator;
4. A manual control tap to adjust the inlet air pressure;
5. A pressure gauge to read and check the air pressure stored in the storage tank;
6. A velocity gauge at the bottom end of the gun barrel to measure the output velocity of the projectile, that can be read on a computer screen linked with test machine;
7. A rigid mounting plane, over which the PV module is laid.

Before the beginning of the test, a preliminary set of shots was performed in order to derive a calibration curve relating the pressure of the stored air to the velocity of the projectile measured at the exit of the gun barrel and read on the external device linked to the hail machine. The obtained curve is shown in Fig. 6.10(a). In addition to that, the obtained preliminary series of shots was used to select the appropriate velocity of the projectile to be used in the tests. Originally, IEC standards [105] indicate to reproduce hailstone with molded ice balls, and provide the impact velocity to be used for the test as a function of the diameter of the sphere. However, there are two different inconvenient aspect in this approach:

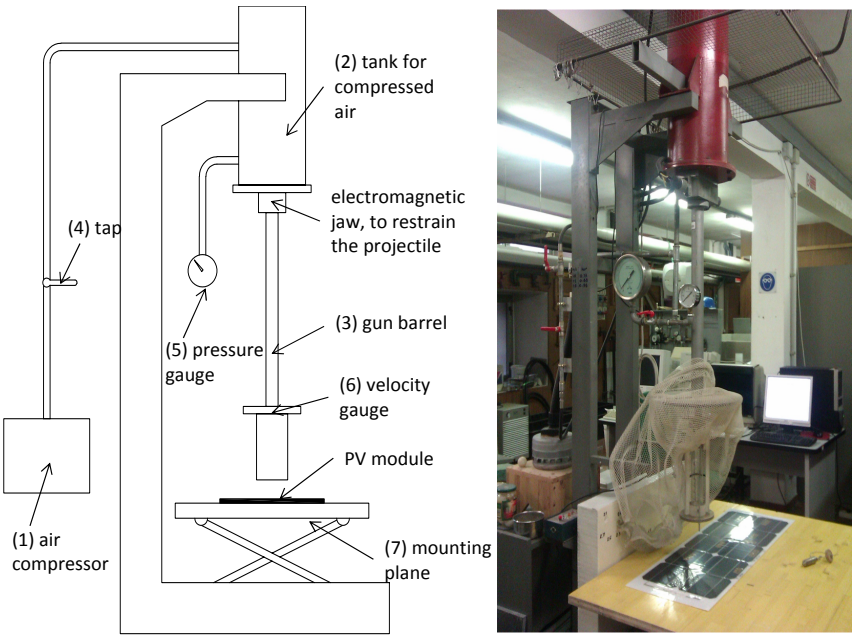

(a) (b)

Figure 6.9: Equipment for the impact test: (a) sketch; (b) picture of the pneumatic gun.

1. There must be the availability of a mold suitable for the creation of the spheres, as well as a freezer in which to properly solidify and retain the ice-balls.

2. Then, the procedure requires a careful examination of the ice balls before firing, to avoid defective ice balls and ice cracks influencing the repeatability of the test itself.

For research purposes, to assure repeatability and propose also a much simpler and reliable testing procedure, a polyamide sphere with a diameter of 40 mm was used instead of ice balls. In this case, the provisions of the IEC standards cannot be used, and the conversion of the velocity in order to have the same linear momentum as prescribed for the ice balls cannot be applied, due to the completely different characteristics of the two involved materials. In fact, ice and polyamide have also a completely different response during impacts and deriving energetic equilibrium. A mechanical linear elastic can be assumed for the polyamide sphere and brittle for ice that shatters into many pieces, contributing to energy dissipation. Hence, the selection of the best velocity of impact for the proposed tests was done in order to reproduce similar crack patterns and damage zones. The crack patterns due to different impact velocities with polyamide spheres are shown in Fig. 6.10(b). First set of impacts, with a velocity of 10 and 12 m/s show a fully indented solar cells with large dimmer areas representing electrically insulated regions making not easy the detection of induced damages

layout, whereas impacts with a velocity of 6 and 7 m/s produce a well identifiable crack pattern similar to the effects of IEC hail impacts. In particular, the velocity of 6m/s was selected as the most appropriate for the present setup.

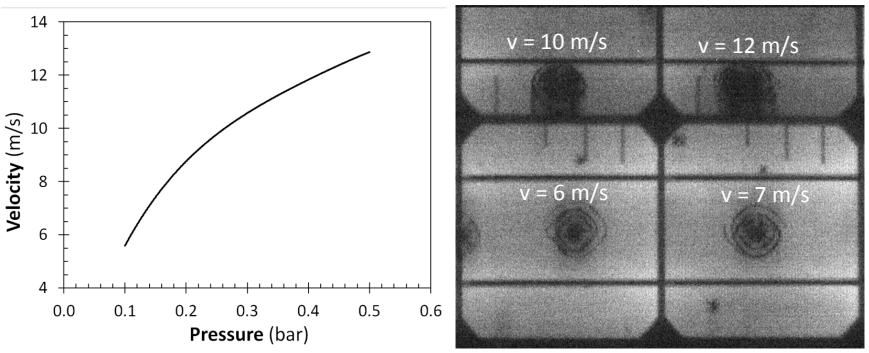

(a) (b)

Figure 6.10: (a) Calibration curve relating air pressure and output velocity of the projectile; (b) electrically damaged areas for different impact velocities.

During tests, as it can be seen in the picture shown in Fig. 6.9(b), the PV module lies horizontally on the mounting plane, perpendicular to the gun barrel, and as close as possible to the bottom end of the gun barrel in order to limit the effect of the gravity acceleration on the impact velocity, facilitate the reading of the correct speed of expulsion (and contact) of the sphere and guarantee the reproducibility of the imposed impact velocity. Impact tests subject to this study, were all performed by impacting each solar cell in its center to avoid spurious effects caused by busbars soldered on solar cells, as well as boundary effects. Preliminary tests also impacting the cells on their peripherals parts (between busbars and the edge of the cells) or directly on the busbars strips were conduced with the goal to visually verify if impacts in this points may cause more substantial damages on Silicon. Regarding the substrate interposed between the PV module and the rigid mounting plane, three cases were considered to simulate the conditions typical of different installation setups and analyze their effect on damage. The three substrates, listed from the stiffer to the softer, are:

- A wooden board;
- An alveolar polycarbonate (PC) layer interposed between the PV module and the wooden board;
- A polystirene (EPS) layer interposed between the PV module and the wooden board.

In the sequel, they will be referred to as *hard*, *medium* and *soft* substrate, respectively. Cracks and electrically inactive areas in Silicon solar cells are not usually visible with the

naked eye. However, they can be analyzed by means of the electroluminescence (EL) technique [123] which is a non-destructive method based on the evaluation of the level of luminescence emitted by Silicon when subjected to an imposed electric potential in forward bias condition. Electrically insulated zones or cracks can be identified by their low EL intensity, thus resulting in dimmer images. Specific parameters and regulations of the EL camera for the present tests can be found in the Appendix.
The EL images of the Si cells subjected to impact are shown in Fig. 6.11, for the three considered substrates whose sketch is shown above. For the Case A (hard substrate), damage remains mainly localized in a small area surrounding the impact point. Inside such a circular region, solar cells are heavily indented and their region is electrically inactive at all, whereas outside them damage appears in the form of few radial cracks, which in most cases do not compromise the proper usage condition of the cell. Two small black spots close to the impact point are due to the collateral bouncing effect of the sphere after the main impact. The radius r^* of the circular dimmer area is 7.5 mm. By reducing the stiffness of the substrate, moving to Case B, damage becomes less localized and it spreads over a wider region around the impact point. The crack pattern is characterized by both radial and circumferential cracks, the extension of the latter being larger than the former. The radius r^* of the circular area interested by the longer circumferential crack is 15.8 mm. Finally, by decreasing further the substrate stiffness, Case C, a crack pattern similar to that of the Case B is observed, although with even more extended circumferential cracks. In this case, in fact, r^* is equal to 31.0 mm. On the contrary, the lengths of the radial cracks are almost the same as in the previous case.

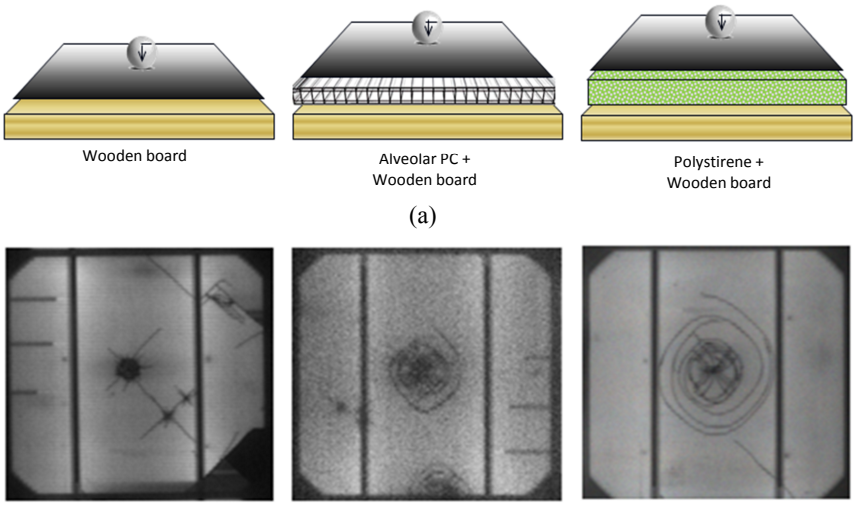

Figure 6.11: Experimental impact tests: (a) sketches of the three considered substrates; (b) EL images showing the resulting crack patterns and electrically inactive areas.

Besides the impact tests, indentation tests were carried out in order to quantify the stiffness of the substrates and assign them a specific parameter. Such a parameter is also fundamental for the identification of the variable parameters that have to be used in the numerical simulations, in order to correctly model the different behavior of the substrates. Hence, quasi-static indentation tests were carried out with a Zwick Allround electro-mechanical testing machine (maximum capacity of the load cell of 10 kN). The indenter had a cylindrical shape, with radius equal to 5 mm and length of 40 mm. The test has been performed in the MUSAM-Lab at the IMT School for Advanced Studies Lucca for each of the three materials used as substrate, namely wood, alveolar PC, and EPS (see Fig. 6.12). The force vs. indentation curves are shown in Fig. 6.13(a).

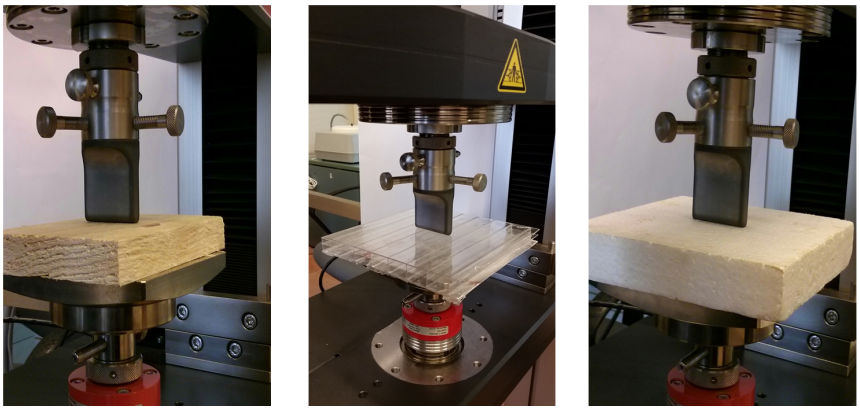

(a) (b) (c)

Figure 6.12: Pictures of the indentation tests on: (a) wooden board; (b) alveolar polycarbonate; (c) polystirene.

The contact stiffness k_{sph} of a sphere indenting a substrate can be deduced from the contact stiffness k_{cyl} of a cylinder from basic contact mechanics formulae valid for linear elastic media [124]. For a sphere, the force for indentation F_{sph} is function of the indentation depth u as:

$$F_{sph} = \frac{4}{3} E^* R_{sph}^{1/2} u^{3/2} \tag{6.1}$$

where where R_{sph} is the radius of the sphere and E^* is an equivalent elastic modulus function of the elastic properties of the materials in contact. Similarly, for a cylinder, the following relation holds:

$$F_{cyl} = \frac{\pi}{4} E^* L u \tag{6.2}$$

where L is the length of the cylinder. The area of contact in the two cases is also dependent

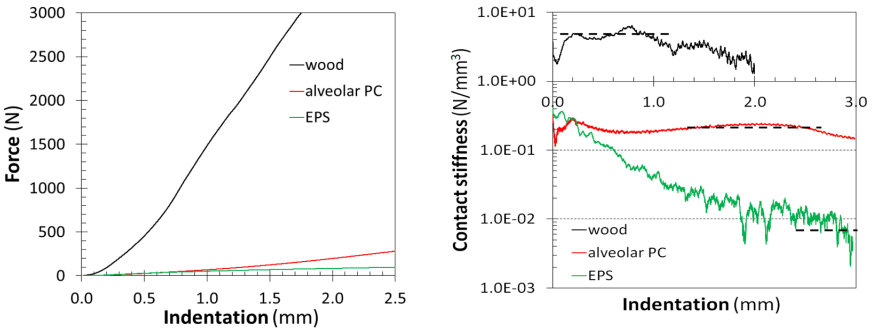

(a) (b)

Figure 6.13: Results of the experimental indentation tests: (a) force vs. indentation depth and (b) average indentation stiffness.

on the indentation depth:

$$a_{sph} = \pi R_{sph} u \tag{6.3a}$$

$$a_{cyl} = l\sqrt{2R_{cyl}u} \tag{6.3b}$$

The average contact pressure for the sphere can therefore be obtained from a combination between Eqs. (6.1) and (6.3)(a):

$$\overline{p}_{\text{sph}} = \frac{F_{\text{sph}}}{a_{\text{sph}}} = \frac{4}{3\pi} E^* \sqrt{\frac{u}{R_{\text{sph}}}} \tag{6.4}$$

and from Eqs. (6.2) and (6.3)(b) for the cylinder:

$$\overline{p}_{\text{cyl}} = \frac{F_{\text{cyl}}}{a_{\text{cyl}}} = \frac{\pi}{8} E^* \sqrt{\frac{u}{2R_{\text{cyl}}}} \tag{6.5}$$

The contact stiffness can be obtained as the derivative of the average pressure with respect to the indentation depth. For the sphere and the cylinder they read, respectively:

$$k_{\text{sph}} = \frac{\mathrm{d}\overline{p}_{\text{sph}}}{\mathrm{d}u} = \frac{4}{6\pi} \frac{E^*}{\sqrt{R_{\text{sph}} u}} \tag{6.6a}$$

$$k_{\text{cyl}} = \frac{\mathrm{d}\overline{p}_{\text{cyl}}}{\mathrm{d}u} = \frac{\pi}{8} \frac{E^*}{\sqrt{2R_{\text{cyl}} u}} \tag{6.6b}$$

Therefore, those relations allow the computation of the average stiffness due to the indentation of the half-plane by a sphere with radius R_{sph} from the average stiffness of a cylinder

with radius R_{cyl} in contact with the same half-plane:

$$k_{\text{sph}} = \frac{16\sqrt{2}}{3\pi^2}\sqrt{\frac{R_{\text{cyl}}}{R_{\text{sph}}}}\kappa_{\text{cyl}}. \tag{6.7}$$

The contact stiffness of the three substrates subject to the indentation of a sphere with radius of 20 mm is computed as a function of the indentation depth from the curves shown in Fig. 6.13(a) and applying in sequence the formulae in Eqs. (6.5), (6.6)(b), and (6.7). The derived curves are shown in Fig.. 6.13(b). The vertical axis is in logarithmic scale to emphasize the differences between the three cases. From the obtained curves, can be noticed that the contact stiffness depends on the indentation depth. As it will be shown in the next section, the maximum value of indentation reached during the tests and in the simulations differs from substrate to substrate and it increases by decreasing stiffness. Therefore, based on the actual indentation depth experienced in the experiments, the characteristic values to be used in input to the numerical simulations are marked by dashed lines in Fig.. 6.13(b). In particular, they are 0.0065 N/mm^3 for EPS, 0.2N/mm^3 for alveolar PC, and 5 N/mm^3 for wood. The ratio between the contact stiffness of the three cases with respect to EPS is $1 : 30 : 770$.

6.2.2 Computational models

Two different approaches having a different degree of approximation are herein proposed to model the sphere impacting on the PV module and calculate the induced stress field. The first approach is a simplified one, in which quasi-static nonlinear finite element (FE) contact simulations are performed to predict the load vs. indentation response of the system and the equation describing the nonlinear single-degree-of-freedom (SDOF) spring-mass model is used to generalize the solution to dynamics. The second approach is the most accurate as possible and it considers the solution of the dynamic problem by using a fully implicit FE solution scheme. In both cases, the finite element analysis program FEAP [81] is used for the solution of the equation set resulting from the weak form of the problem and the imposition of the initial and boundary conditions representative of the experimental tests. The real problem is approximated in the FE analysis by the axis-symmetric model shown in Fig. 6.14.

Linear quadrilateral finite elements are used to discretize the continuum. Linear elastic constitutive relations have been considered for all the materials composing the layers of the PV module and for the sphere, except for the epoxy material (EVA) encapsulating the solar cells. This is in fact a polymeric material with a pronounced thermo-viscoelastic behavior [125, 126]. Due to the testing conditions of dynamic loading and constant room temperature, these two complex mechanical aspects can be neglected, and a neo-Hookean constitutive relation has been adopted. The material parameters are listed in Tab. 6.1.

An implicit time integration scheme based on the Newmark method, and in particular the constant average acceleration scheme, is used to solve the contact problem between the impacting sphere and the module in dynamics. The contact problem is solved by using the node-to-segment contact strategy [127] to identify the finite elements in contact and the penalty method is adopted to impose the satisfaction of the unilateral contact constraint. In this regard, the penalty method was preferred over the method of Lagrange multipliers since it was possible to provide a physical meaning to the penalty stiffness to be used in the

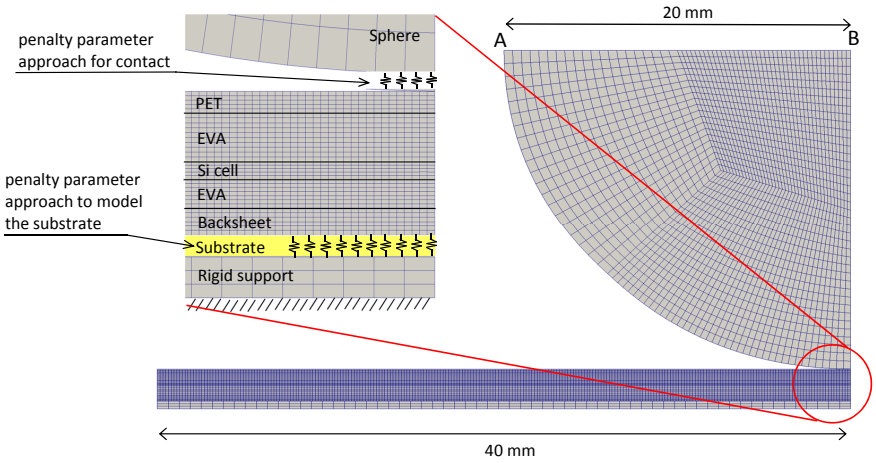

Figure 6.14: Sketch of the axis-symmetric model geometry for FE simulations.

	$E(\mathrm{N/m^2})$	ν	$\rho(\mathrm{kg/m^3})$
Back sheet	$2.8 \cdot 10^9$	0.30	1200
EVA	$1.0 \cdot 10^7$	0.30	1180
Silicon	$1.3 \cdot 10^{11}$	0.22	2330
PET	$2.5 \cdot 10^9$	0.30	1300
Polyamide (sphere)	$3.0 \cdot 10^9$	0.30	1200

Table 6.1: Material parameters used in the FE simulations.

simulations. Different values of the penalty parameter have been used along the contact interface between the PV module and the rigid mounting plane of the testing machine in order to simulate contact with substrates characterized by different indentation stiffness as in the experimental tests. Specifically, the penalty parameters used for the contact problem along this interface are taken proportional to the values of the contact stiffness experimentally evaluated, i.e., 1×10^6 N/m^3 for the soft substrate, 3×10^7 N/m^3 for the medium substrate, and 7.7×10^8 N/m^3 for the hard substrate. Therefore, the ratio $1 : 30 : 770$ was preserved as in the experimental tests. Regarding the interface between the sphere and the laminate, a very high penalty parameter is used to avoid as much as possible spurious interpenetration of the sphere and satisfy almost exactly the unilateral contact problem along that interface.

6.2.3 Single degree of freedom model

The problem of impact of a sphere on a PV module laid on a substrate can be approximated with a SDOF spring-mass model by following the methodology presented in [13] (see

Fig. 6.15(a)). In this case, the mass of the equivalent system is given by that of the sphere, since the mass of the portion of module interested by the impact is negligible. On the other hand, the stiffness of the equivalent spring has to take into account both the stiffness of the sphere and the contact stiffness. The governing equation for the SDOF system is:

$$M\ddot{u} + K(u)u = 0 \tag{6.8}$$

where $K(u)$ is the nonlinear stiffness of the spring, that can be determined from a quasi-static FE simulation of the sphere indenting the PV module. In particular, three different cases were examined, one for each substrate typology. Simulations were conducted under displacement control, i.e. the displacement of the boundary AB of the sphere (see Fig. 6.14) was increased step-by-step and the resulting force was computed as the sum of the reactions along the same boundary. The obtained quasi-static force vs. indentation depth curve is shown in Fig. 6.15(b) for the three substrates. Each curve was then approximated with a polynomial function of the 4th degree (the corresponding equations are also superimposed to Fig. 6.15(b)). The nonlinear stiffness entering Eq. (6.8) is therefore provided by the derivative of the polynomial functions fitting the force vs. indentation curves. Due to the nonlinear character of the problem, Eq. (6.8) was then solved with a step-by-step numerical integration method, assuming a constant acceleration within each time step, and imposing the initial conditions of indentation $u(t = 0) = 0$ and velocity $\dot{u}(t = 0) = 6\text{m/s}$.

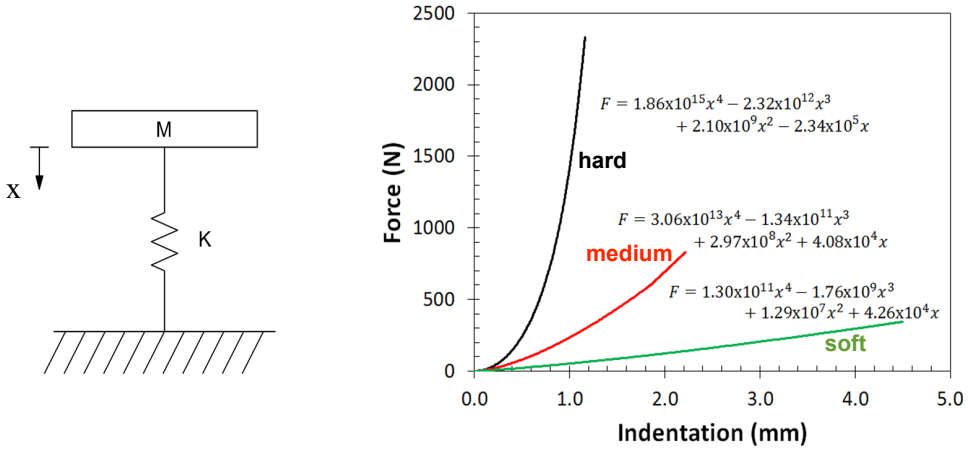

(a) (b)

Figure 6.15: (a)Sketch of the SDOF spring-mass model; (b)indentation force vs. indentation depth curves from quasi-static FE simulations, for the three considered substrates.

6.2.4 Dynamic model

The alternative approach used to simulate the impact tests is based on the FE method used to solve the dynamical problem with a fully implicit time stepping technique. The solution strategy adopted for this problem is a step-by-step implicit dynamics, using the Newmark constant average acceleration scheme for time integration. At each time step, the Newton-Raphson incremental iterative scheme is adopted to solve the nonlinear set of algebraic equations. The mass matrix of the finite elements was computed in lumped form and energy dissipation phenomena, for instance due to friction, were neglected. Due to the hardening behavior of the EVA material, and in order to avoid instabilities, the time step was changed during the simulation, starting from 1μs and decreasing it down to 0.1μs by approaching the maximum indentation depth. As discussed in the previous section, the present approach is the most accurate method as possible, and it will be shown it is more precise than the SDOF spring-mass model for the analysis of the stress field. On the other hand, it is computationally much more expensive, since it has to deal with dynamics, contact mechanics, and the material nonlinearity of EVA at the same time.

6.2.5 Effect of the substrate material stiffness

The predictions of the two numerical methods used to simulate the impact test are reported. Furthermore, they are compared with the experimental results in order to assess the possibility of using numerical simulations to predict the extension of the area subject to cracking caused by impacts. First, the analysis of the results is carried out in term of global response, i.e., by examining the relation between indentation depth and time. Then, a more detailed analysis is carried out by examining the stress field in the PV module, with particular focus on the layer containing the solar cells. The outcome of the numerical simulations, in terms of indentation depth vs. time and velocity vs. time, are shown in Fig. 6.16. The dashed lines refer to the solution obtained by a quasi-static FE simulation combined by the SDOF spring-mass model, whereas the solid lines refer to the FE prediction by solving the contact problem in dynamics. In both cases, the simulations are stopped at the maximum indentation. Clearly, the two approaches provided almost identical results. As expected, the maximum indentation and the duration of the impact do depend on the substrate hard- ness. In particular, a maximum indentation of 1.16 mm is reached after 0.26 ms for the hard substrate, 2.20 mm after 0.54 ms for the medium substrate, and 4.54 mm after 1.14 ms for the soft substrate. Correspondingly, the negative gradient of the velocity increases by increasing the substrate stiffness.

The stress field inside the PV module is herein examined in order to verify whether it is possible to correlate the stress distributions in the Silicon layer to the extension of the cracked area observed in the EL images. Considering the brittle behavior of Silicon, it is reasonable to assume that cracking takes place as soon as the radial stresses reach the ultimate tensile strength of the material. Hence, even by assuming linear elasticity for Silicon, it is reasonable to expect that all the portion of the solar cell where the radial stress overcomes the ultimate tensile strength of Silicon correlates with the extension of the electrically inactive zones. Moreover, the point where the circumferential stresses become lower than such a threshold could be used to identify the maximum length of the radial cracks observed in experiments. Due to the axis-symmetry of the model, the stress field is identified through

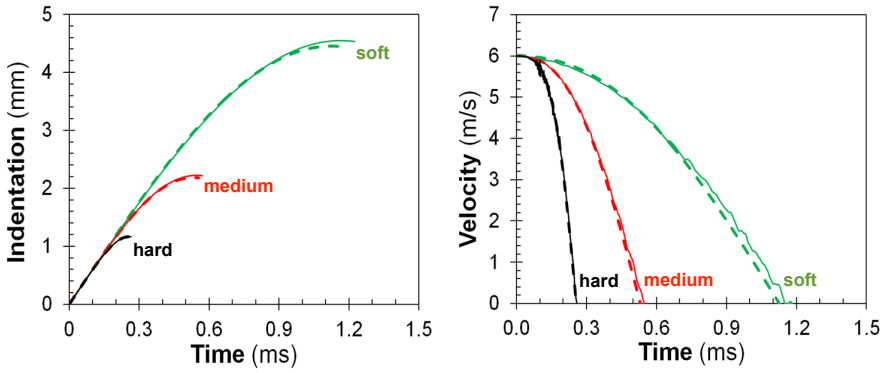

(a) (b)

Figure 6.16: Results of the numerical simulations for different substrate stiffnesses: (a) indentation depth vs. time; (b) velocity vs. time. The dashed lines refer to the SDOF spring-mass model whereas the solid lines to the FE solution in dynamics.

the radial stress, σ_r, and the circumferential stress, σ_θ . In the case of the SDOF spring-mass model approach, the stress field is quantified from a quasi-static simulation up to a deformation level corresponding to a maximum indentation depth predicted by the SDOF method. As an example, the contour plots of the radial stresses are shown in Fig. 6.17 for the three considered substrates. The highest stress level is located inside the solar cell, which has a Young modulus from 2 to 4 orders of magnitude higher than that of the other materials composing the PV stack. The indentation of the sphere in the module determines a localized flexural state in the impacted solar cell. Therefore, the maximum and minimum stresses are achieved on the lower and upper surfaces of the layers. From a qualitative comparison of the three contour plots, the region subjected to the highest stresses increases by decreasing the substrate stiffness, in qualitative agreement with the experimental evidences.

In order to quantitatively compare the three cases, the distributions of the radial and circumferential stresses along the radial coordinate at the bottom surface of the solar cell, i.e., the surface further from the side of impact, are shown in Figs. 6.18 and 6.19. In the SDOF spring-mass model, since there are no dynamic effects explicitly taken into account, the condition of maximum indentation corresponds to the achievement of the maximum radial stress in the module (see Fig. 6.18) and this simplifies the estimation of the extension of the cracked area of Silicon. On the other hand, the same procedure is not viable for the rigorous FE solution of the dynamic problem. The identification of the maximum and minimum stresses at the lower boundary of the solar cells is in fact complicated by the phenomenon of stress wave propagation which is not accounted for in the SDOF method. As a consequence of this, the peak stress in the various points along the lower boundary of the solar cells is reached at different time steps. Therefore, in this case, an envelope diagram of the stresses is required to assess the maximum extension of the solar cell layer experiencing a radial stress higher than the Silicon ultimate tensile strength. Hence, the diagram in Fig. 6.19 represents, for each

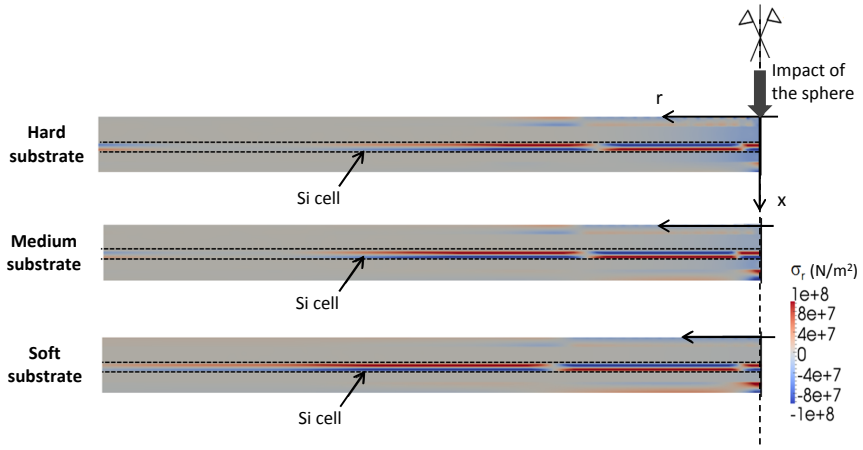

Figure 6.17: Contour plot of the radial stress in the PV module for the three considered substrates. These predictions are obtained based on the SDOF method.

material point, the maximum and the minimum radial stresses reached during the entire load history in the dynamic simulation. The radial and circumferential stress distributions shown in Fig. 6.18 for the SDOF method and the corresponding envelope diagrams obtained from FE dynamic simulations shown in Fig. 6.19 display common features. The maximum values of the radial and circumferential stresses take place within the area of contact between the ball and the PV module. The maximum radial stress σ_r is found in a point about 3 mm far from the symmetry line. Further from the impact area, the radial stresses change sign, and the minimum values take place at a distance from 6 to 12 mm from the symmetry line. After the minimum, the radial stresses tend to vanish at a distance sufficiently far from the point of impact. The circumferential stresses σ_θ also tend to zero far from the point of impact, but without changing sign.

The diagrams in Figs. 6.18 and 6.19 are now interpreted in relation to the EL images showing dimmer areas (see Fig. 6.11(b)) in order to assess the possibility of using these numerical predictions to identify the region of the solar cell that becomes electrically inactive. As mentioned before, the key idea is to define such a region as the area where the absolute value of the radial stresses σ_r overcome a threshold given by the ultimate tensile strength of Silicon. The use of the absolute value is justified by the fact that, on the upper layer of the solar cell, stresses are almost the same as those acting on the bottom surface in Figs. 6.18 and 6.19, but with opposite sign due to bending. To this purpose, the envelope diagrams obtained from dynamic FE simulations are considered first. Considering a threshold value of 60 MPa for σ_r (see the horizontal dashed lines in Fig. 6.19), the region potentially subjected to circumferential cracks are predicted to have an extension defined by a radius r^* of 10.5 mm for the hard substrate, 17.8mm for the medium one, and 31.3mm for the soft substrate. These values are in very good agreement with the experimentally observed extension of the crack patterns (see Fig. 6.11). The same threshold on the diagrams of the circumferential

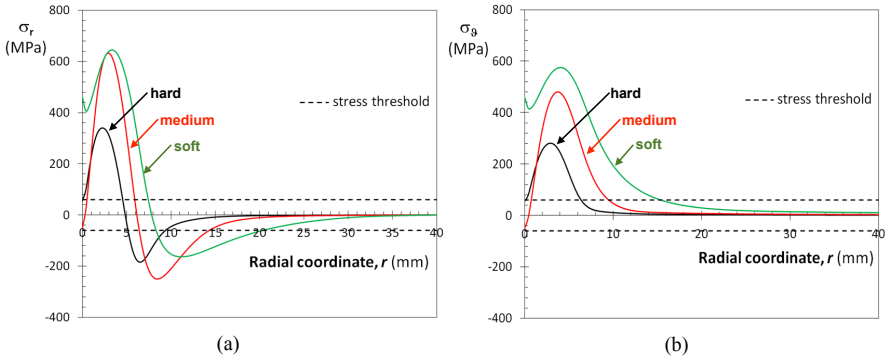

Figure 6.18: Stress distributions along the radial coordinate at the bottom surface of the Si cell predicted by the SDOF method: (a) radial stress; (b) circumferential stress.

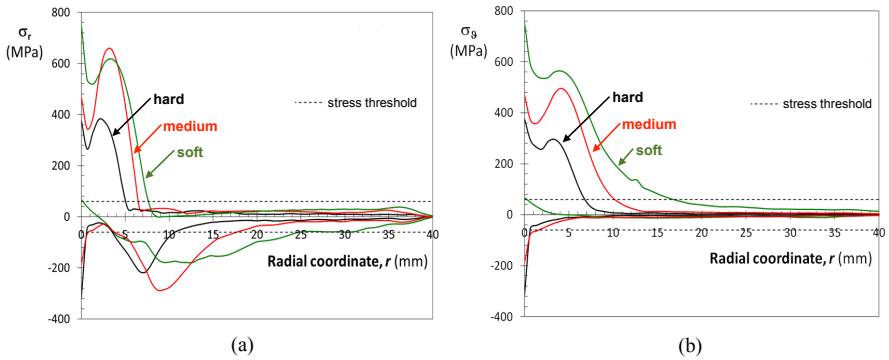

Figure 6.19: Envelopes of the stresses along the radial coordinate at the bottom surface of the Si cell predicted by dynamic FE simulations: (a) radial stress; (b) circumferential stress.

stress σ_θ identifies regions where radial cracks can develop with a radius of 6.8mm for the hard substrate, 10.2 mm for the medium one, and 16.5 mm for the soft substrate. Based on these results, the extension of the solar cell portion subjected to radial cracks is predicted to be smaller than that subjected to circumferential cracks, which is fully consistent with the experimental observation (see Fig. 6.11). The same analysis of the stress diagrams resulting from the SDOF method (see Fig. 6.18) does not lead to the same level of agreement with the experimental observation of the extension of the crack pattern. This is particularly evident for the radial stresses. In fact, for the same threshold of 60 MPa, SDOF predictions for r^* are 9.4mm for the hard substrate, 14.2mm for the medium one, and only 20.3 mm for the soft substrate. A direct comparison between experimental results and numerical predictions based on the two proposed mod- els for the extension of the cracked area, r^*, is provided in Fig. 6.20. Predictions by FE dynamics simulations are in excellent agreement with experimental results,

since they lie very close to the dashed line at 45°.

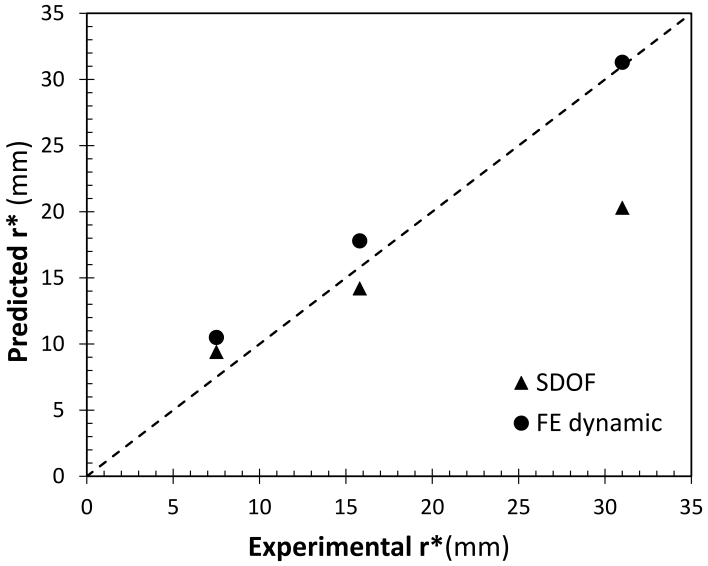

Figure 6.20: Comparison between experimental results and numerical predictions of the extension of the silicon area cracked by circumferential cracks, r^*.

It is worth noting that the tensile strength of intact mono-crystalline silicon is usually much higher than the threshold assumed in this analysis. However, solar cells used to produce PV modules are cut from a big cylindrical wafer and are subject to several industrial processes up to their final incapsulation in the EVA layers. All of these steps can induce impurities, micro-cracks and defects leading to stress concentrations and a much lower nominal tensile strength.

6.2.6 Possible technical improvements for yield increase

The impact of hailstone on semi-flexible PV modules has been studied from the experimental and the numerical points of view. With respect to [121], the use of the EL technique represents a significant step forward for the accurate detection and analysis of the crack pattern. The use of the EL technique for a quantitative analysis of electric damage and crack pattern, although not requested by international qualification standards, is highly recommended in the case of flexible PV modules that are much more vulnerable to hail impacts than the rigid ones. Moreover, the effect of the type of substrate was also found to be very important and should be considered in the design of PV installations for the assessment of potential safety risks connected to hot spots induced by cracking. As far as the numerical modeling is concerned, the proposed simplified approach based on quasi-static FE simulations and the application of

the SDOF model provides good results in terms of global response, i.e., indentation depth vs. time behavior. However, stresses predicted by this approach to be used to predict the extension of the crack pattern do not satisfactorily correlate with the experimentally observed dimmer areas in the EL images. On the other hand, fully implicit dynamic FE simulations accounting for phenomena including stress wave propagation and reflection provide stress diagrams that can be effectively used to assess the extension of cracking in solar cells due to impacts. In particular, the use of a nominal ultimate tensile strength of 60 MPa to identify the extension of the crack zones leads to predictions that compare very well with experimental observations. Therefore, the proposed method can be used in practical engineering applications to assess different laminate configurations both in terms of layers thickness and material composition, and in relation to different mounting substrates. As regards future perspectives, the analysis of the evolution of the crack patterns induced by impacts due to the exposure to cyclic thermal loads, performed by means of experimental tests inside a climate chamber, will be of high relevance for a complete evaluation of the actual durability of cracked PV modules. In fact, further propagation of cracks and an increase of their opening can lead to an increase of electrically inactive solar cell areas, with a consequent increase of power-loss [128]. In this regard, the crack pattern with partial electric insulation observed for the soft substrate (see Fig. 6.11(b)), difficult to be assessed from the inspection of current-voltage curves, could be quite dangerous in perspective, since it can lead to a very large electrically insulated area and a host spot after a series of cyclic thermal loading in the field.

Chapter 7

Conclusions and future developments

From the technical details in the Chapter 1 the fundamental role of the light (prevalently deriving from the sun irradiation) for the proper functioning of the PV Silicon modules is explained. Basically, the transformation of sunlight into electrical current can be possible only if the electric charges generated into the Silicon cells can reach the metallic strips (busbars) and be collected for the input in the general electrical system. Even though it is an oversimplification of how a Photovoltaic system works, the second essential aspect can be identified in the need to preserve the integrity of the Si cells inside the multilayer structure of the PV module.

PV modules can be classified in two main categories, mainly depending on the material with which is built the upper layer (front-layer) of the module: in traditional (rigid) Silicon Photovoltaic modules it is made of glass, giving in this way a certain resistance to the bending, while in semi-flexible modules it is used a thin layer of transparent plastic material, conferring the confirming the possibility of flexing also adapting to curved surfaces. On the other hand, while in the traditional PV modules the Si layer is protected against impact and external mechanical actions by the glass, in semi-flexible modules this role is less pronounced, exposing more the Si to mechanical damage.

This was the main topic of this thesis, i.e. the determination of the causes of damage that may affect the conservation of functional integrity of the modules causing a loss in the attended performance (declared by the producer), excluding those linked with the natural decay of performance due to ageing and degradation phenomena, i.e.:

- Climate variation with thermal excursion throughout the day;
- Seasonal changes;
- Acid rain or transport of debris from the wind, situations that can dull the front surface of the panel, thus compromising the transparency and limiting the absorbance of the sunlight;

- Other chemical and thermal phenomena that may be of interest, if not directly to the silicon cells or layers of the module, the other other parts of the system (i.e. busbars, electrical cables and terminals,...).

The mechanical damage of the module may take place in the following phases:

- During production, for contact with sharp parts of machinery or during the internal handling in the production plant, both during construction is in process concluded during storage;
- During transport, due to impacts and vibration transferred in the handling and shipment;
- During handling and positioning prior to assembly. Moreover, in the installation procedure for falling work tool because of the walkway on their surface;
- During the service status, for bodies impacting (i.e. hail) on the front-sheet and wind action causing repeated oscillations to the module.

The qualification standards currently available have been examined in order to understand what kind of evidence is required in order to classify the performance of the modules, and thus determine what could be the maximum damage during and at the end of the module lifetime. The criterion until today is only a judgment of approval, that has to be applied at the time of manufacturing and which should ensure the level of expected performance. From the findings obtained in the present thesis, there is not an explicit criterion for the study of damaging processes, and particularly an evidence obtained by a calculation model that can predict and prevent the cracking states of Silicon, that is the core of the solar panel. The criteria for the study of the fracture in these particular multiplayer elements are not yet defined, where thermal, electrical and mechanical actions interact creating a synergistic effect. As is for building and in general for mechanical design, a methodology for a proper calculation of involved stresses in order to prevent major damages is needed.
In this regards, an analysis was made of the most commonly applied methods of analysis of materials, in order to achieve the formulation of a suitable approach for the study of fracture mechanics for Silicon. Starting from continuum approaches to fracture presented in Chapter 2, a brief description of the linear elastic and nonlinear fracture mechanics has been presented. Formulation based on integrals, differential equations and fractals are possible, bringing out limitations that induce the user to deepen the research and turn its attention to different strategies. The application of methodologies based on continuum approaches are quite difficult for this kind of systems where materials with different mechanical behaviour are involved, further introducing problem at the interfaces due to interaction between the various material components. In the Chapter 3 a general introduction to numerical methods for a multi-scale analysis of fracture was presented, with a classification based on different scales at which they are applicable. Methods based on nano- and micro-scale presented in Chapter 4 are not suitable for their direct application to the study of the fracture as understood in the classical sense, as based on energy principles taking account of phenomena that occur locally in a restricted area between molecules, often requiring a too detailed and costly analysis.
Energy theories deriving form pure molecular dynamics can be applied if expressed within a

finite element approach. In this context, the material is discretized by a series of nodes joining together beam elements. The method takes into account deformation in the plane and out of it. The constitutive law can be characterized with specific behavior according to the type of materials in object, by also setting a distance cut-off in the σ-ε or σ-w relationships in order to take in account phenomena of breakage of the material. The very interesting character of the 4-nodes approach is the consideration of nonlocality effect in the cracking process, so that it includes the concept of *nonlocality index* proposed to take into account of the collaboration of surrounding elements in the process of crack opening. A future improvement of this approach is the completion of its implementation in a finite element analysis procedure software (FEAP) and its application for the study of cracking mechanisms.

The numerical study of the intergranular and transgranular propagation of the crack in Si polycrystalline materials has been conducted in Chapter 5 with the application of a Cohesive Zone Model, providing a particular formulation to take into account of the interface problem on the grain boundaries.

The modeling of the damage phenomena at the macroscale was carried out in Chapter 6 with the aid of laboratory tests carried out on semi-flexible panels. The first experimental campaign concerned a repeated bending to simulate fatigue on the module to study crack propagation and crack closure inside Si cells, noting an unexpected behaviour regarding the ability of the multilayer structure to trigger a "self-healing" process. In fact, although there is a cracking process in place while the module is bent, when the module is relaxed and returns to a planar shape the dark zones return to be bright, meaning that the electrical flow is able to pass through the crack and Si cell is again conductive. According to what has been observed experimentally, it may find useful to conduct further bending tests on panels having a different stratigraphy or whose intermediate layer is made of polycrystalline Si cells instead of monocrystalline Si. This may influence the capacity of the material to give rise to the crack reclosure process, since potentially every grain boundary constitutes a possible separation surface along which a crack path may develop. With respect to the second experimental campaign, relative to hail impact tests, appreciable results have been obtained relatively to the study of mechanisms of fracture and relatively to the extension of the areas in which the cells are no longer conductive. An appreciable estimation of the value of stress at which occurs the cracking of the Silicon has been achieved. The purely dynamic model can be further refined, and different substrates can be simulated in order to evaluate if it is preferable a stiff or a soft one, depending on what kind of crack pattern is considered less dangerous. For the study of the evolution of the fractures, due to temperature changes, it can be expected to condition the samples through the use of a climate chamber, according to the temperature variation diagram suggested for the characterization of typical photovoltaic panels. In this way, it is possible to experimentally know if damaged panels from impact phenomena can be further degraded by thermal effects.

For a more accurate reading of the results, it may be suggested to make use of a computerized image analysis, in which EL images of damages modules can be artificially subdivided (i.e. an orthogonal pattern of line) and each area (pixel) classified using a gray-scale as parameter, establishing if conductive or not. By the count of the dark pixels should be obtained the extension of the damaged area for each cell.

Ultimately, the issue relative to fracture in multi-layers materials subject to multi-fields actions remains still open. Several modelling steps have yet to be made to obtain an algorithm

that brings a correct design of the materials used. There are many practical problems to be faced, yield, light weight, low cost and ease of implementation and many others, but certainly the most important is here:

after thinking about an eco-friendly system for the generation of electricity, without exploiting not renewable hydrocarbon resources, or nuclear energy power, can we also provide a complete reuse of materials, which can fit into the culture of reuse?

Chapter 8

Appendix A
Development of the numerical model for FEAP implementation

From the derivative of the residual forces with respect to the coordinates

$$K_{ij}(\mathbf{x_k}) = \frac{\partial R_i}{\partial x_j}\Big|_{x_k} \tag{8.1}$$

we get the stiffness matrix **K**. It consists of parts of the residual forces at

node I

$$\begin{aligned}\frac{\partial \mathbf{R_I}}{\partial \mathbf{x_I}} = &+\mathbf{n_{IJ}} \otimes \frac{\partial F_{IJ}}{\partial \mathbf{x_I}} + F_{IJ}\frac{\partial \mathbf{n_{IJ}}}{\partial \mathbf{x_I}} - \mathbf{n_I} \otimes \frac{\partial F_{IJK}}{\partial \mathbf{x_I}} \\ &-F_{IJK}\frac{\partial \mathbf{n_I}}{\partial \mathbf{x_I}} + \mathbf{n_{IJK}} \otimes \frac{\partial F_{IJKL}}{\partial \mathbf{x_I}} + F_{IJKL}\frac{\partial \mathbf{n_{IJK}}}{\partial \mathbf{x_I}}\end{aligned} \tag{8.2}$$

$$\begin{aligned}\frac{\partial \mathbf{R_I}}{\partial \mathbf{x_J}} = &+\mathbf{n_{IJ}} \otimes \frac{\partial F_{IJ}}{\partial \mathbf{x_J}} + F_{IJ}\frac{\partial \mathbf{n_{IJ}}}{\partial \mathbf{x_J}} - \mathbf{n_I} \otimes \frac{\partial F_{IJK}}{\partial \mathbf{x_J}} \\ &-F_{IJK}\frac{\partial \mathbf{n_I}}{\partial \mathbf{x_J}} + \mathbf{n_{IJK}} \otimes \frac{\partial F_{IJKL}}{\partial \mathbf{x_J}} + F_{IJKL}\frac{\partial \mathbf{n_{IJK}}}{\partial \mathbf{x_J}}\end{aligned} \tag{8.3}$$

$$\begin{aligned}\frac{\partial \mathbf{R_I}}{\partial \mathbf{x_K}} = &+\mathbf{n_I} \otimes \frac{\partial F_{IJK}}{\partial \mathbf{x_K}} - F_{IJK}\frac{\partial \mathbf{n_I}}{\partial \mathbf{x_K}} + \mathbf{n_{IJK}} \otimes \frac{\partial F_{IJKL}}{\partial \mathbf{x_K}} \\ &+F_{IJKL}\frac{\partial \mathbf{n_{IJK}}}{\partial \mathbf{x_K}}\end{aligned} \tag{8.4}$$

$$\frac{\partial \mathbf{R_I}}{\partial \mathbf{x_L}} = +\mathbf{n_{IJK}} \otimes \frac{\partial F_{IJKL}}{\partial \mathbf{x_L}} \tag{8.5}$$

node J

$$\begin{aligned}\frac{\partial \mathbf{R_J}}{\partial \mathbf{x_I}} = &-\mathbf{n_{IJ}} \otimes \frac{\partial F_{IJ}}{\partial \mathbf{x_I}} - F_{IJ}\frac{\partial \mathbf{n_{IJ}}}{\partial \mathbf{x_I}} + \mathbf{n_I} \otimes \frac{\partial F_{IJK}}{\partial \mathbf{x_I}} \\ &+F_{IJK}\frac{\partial \mathbf{n_I}}{\partial \mathbf{x_I}} + \mathbf{n_K} \otimes \frac{\partial F_{IJK}}{\partial \mathbf{x_I}} + F_{IJKL}\frac{\partial \mathbf{n_K}}{\partial \mathbf{x_I}} \\ &-\frac{3}{2}\mathbf{n_{IJK}} \otimes \frac{\partial F_{IJKL}}{\partial \mathbf{x_I}} - \frac{3}{2}F_{IJKL}\frac{\partial \mathbf{n_{IJK}}}{\partial \mathbf{x_I}} - \frac{1}{2}\mathbf{n_{JKL}} \otimes \frac{\partial F_{IJKL}}{\partial \mathbf{x_I}}\end{aligned} \tag{8.6}$$

$$\begin{aligned}\frac{\partial \mathbf{R_J}}{\partial \mathbf{x_J}} = &-\mathbf{n_{IJ}} \otimes \frac{\partial F_{IJ}}{\partial \mathbf{x_J}} - F_{IJ}\frac{\partial \mathbf{n_{IJ}}}{\partial \mathbf{x_J}} + \mathbf{n_{JK}} \otimes \frac{\partial F_{JK}}{\partial \mathbf{x_J}} \\ &+F_{JK}\frac{\partial \mathbf{n_{JK}}}{\partial \mathbf{x_J}} + \mathbf{n_I} \otimes \frac{\partial F_{IJK}}{\partial \mathbf{x_J}} + F_{IJK}\frac{\partial \mathbf{n_I}}{\partial \mathbf{x_J}} \\ &+\mathbf{n_K} \otimes \frac{\partial F_{IJK}}{\partial \mathbf{x_J}} + F_{IJK}\frac{\partial \mathbf{n_K}}{\partial \mathbf{x_J}} - \mathbf{n_J} \otimes \frac{\partial F_{JKL}}{\partial \mathbf{x_J}} \\ &-F_{JKL}\frac{\partial \mathbf{n_J}}{\partial \mathbf{x_J}} - \frac{3}{2}\mathbf{n_{IJK}} \otimes \frac{\partial F_{IJKL}}{\partial \mathbf{x_J}} - \frac{3}{2}F_{IJKL}\frac{\partial \mathbf{n_{IJK}}}{\partial \mathbf{x_J}} \\ &-\frac{1}{2}\mathbf{n_{JKL}} \otimes \frac{\partial F_{IJKL}}{\partial \mathbf{x_J}} - \frac{1}{2}F_{IJKL}\frac{\partial \mathbf{n_{JKL}}}{\partial \mathbf{x_J}}\end{aligned} \tag{8.7}$$

$$\begin{aligned}\frac{\partial \mathbf{R_J}}{\partial \mathbf{x_K}} = &+\mathbf{n_K} \otimes \frac{\partial F_{JK}}{\partial \mathbf{x_K}} + F_{JK}\frac{\partial \mathbf{n_{JK}}}{\partial \mathbf{x_K}} + \mathbf{n_I} \otimes \frac{\partial F_{IJK}}{\partial \mathbf{x_K}} \\ &+F_{IJKL}\frac{\partial \mathbf{n_I}}{\partial \mathbf{x_K}} + \mathbf{n_K} \otimes \frac{\partial F_{IJK}}{\partial \mathbf{x_K}} + F_{IJKL}\frac{\partial \mathbf{n_K}}{\partial \mathbf{x_K}} \\ &-\mathbf{n_J} \otimes \frac{\partial F_{JKL}}{\partial \mathbf{x_K}} - F_{JKL}\frac{\partial \mathbf{n_J}}{\partial \mathbf{x_K}} - \frac{3}{2}\mathbf{n_{IJK}} \otimes \frac{\partial F_{IJKL}}{\partial \mathbf{x_K}} \\ &-\frac{3}{2}F_{IJKL}\frac{\partial \mathbf{n_I JK}}{\partial \mathbf{x_K}} - \frac{1}{2}\mathbf{n_{JKL}} \otimes \frac{\partial F_{IJKL}}{\partial \mathbf{x_K}} - \frac{1}{2}F_{IJKL}\frac{\partial \mathbf{n_{JKL}}}{\partial \mathbf{x_K}}\end{aligned} \tag{8.8}$$

$$\begin{aligned}\frac{\partial \mathbf{R_J}}{\partial \mathbf{x_L}} = &-\mathbf{n_J} \otimes \frac{\partial F_{JKL}}{\partial \mathbf{x_L}} - F_{JKL}\frac{\partial \mathbf{n_J}}{\partial \mathbf{x_L}} - \frac{3}{2}\mathbf{n_{IJK}} \otimes \frac{\partial F_{IJKL}}{\partial \mathbf{x_L}} \\ &-\frac{1}{2}\mathbf{n_{JKL}} \otimes \frac{\partial F_{IJKL}}{\partial \mathbf{x_L}} - \frac{1}{2}F_{IJKL}\frac{\partial \mathbf{n_{JKL}}}{\partial \mathbf{x_L}}\end{aligned} \tag{8.9}$$

node K

$$\begin{aligned}\frac{\partial \mathbf{R_K}}{\partial \mathbf{x_I}} = &-\mathbf{n_K} \otimes \frac{\partial F_{IJK}}{\partial \mathbf{x_I}} - F_{IJK}\frac{\partial \mathbf{n_K}}{\partial \mathbf{x_I}} + \frac{1}{2}\mathbf{n_{IJK}} \otimes \frac{\partial F_{IJKL}}{\partial \mathbf{x_I}} \\ &+\frac{1}{2}F_{IJKL}\frac{\partial \mathbf{n_{IJK}}}{\partial \mathbf{x_I}} + \frac{3}{2}\mathbf{n_{JKL}} \otimes \frac{\partial F_{IJKL}}{\partial \mathbf{x_I}}\end{aligned} \tag{8.10}$$

$$\begin{aligned}\frac{\partial \mathbf{R_K}}{\partial \mathbf{x_J}} &= -\mathbf{n_{JK}} \otimes \frac{\partial F_{JK}}{\partial \mathbf{x_J}} - F_{JK}\frac{\partial \mathbf{n_{JK}}}{\partial \mathbf{x_J}} - \mathbf{n_K} \otimes \frac{\partial F_{IJK}}{\partial \mathbf{x_J}} \\ &\quad -F_{IJK}\frac{\partial \mathbf{n_K}}{\partial \mathbf{x_J}} + \mathbf{n_J} \otimes \frac{\partial F_{JKL}}{\partial \mathbf{x_J}} + F_{JKL}\frac{\partial \mathbf{n_J}}{\partial \mathbf{x_J}} \\ &\quad +\mathbf{n_L} \otimes \frac{\partial F_{JKL}}{\partial \mathbf{x_J}} + F_{JKL}\frac{\partial \mathbf{n_L}}{\partial \mathbf{x_J}} + \frac{1}{2}\mathbf{n_{IJK}} \otimes \frac{\partial F_{IJKL}}{\partial \mathbf{x_J}} \\ &\quad +\frac{1}{2}F_{IJKL}\frac{\partial \mathbf{n_{IJK}}}{\partial \mathbf{x_J}} + \frac{3}{2}\mathbf{n_{JKL}} \otimes \frac{\partial F_{IJKL}}{\partial \mathbf{x_J}} + \frac{3}{2}F_{IJKL}\frac{\partial \mathbf{n_{JKL}}}{\partial \mathbf{x_J}}\end{aligned} \tag{8.11}$$

$$\begin{aligned}\frac{\partial \mathbf{R_K}}{\partial \mathbf{x_K}} &= -\mathbf{n_{JK}} \otimes \frac{\partial F_{JK}}{\partial \mathbf{x_K}} - F_{JK}\frac{\partial \mathbf{n_{JK}}}{\partial \mathbf{x_K}} + \mathbf{n_{KL}} \otimes \frac{\partial F_{KL}}{\partial \mathbf{x_K}} \\ &\quad +F_{KL}\frac{\partial \mathbf{n_{KL}}}{\partial \mathbf{x_K}} - \mathbf{n_K} \otimes \frac{\partial F_{IJK}}{\partial \mathbf{x_K}} - F_{IJK}\frac{\partial \mathbf{n_K}}{\partial \mathbf{x_K}} \\ &\quad +\mathbf{n_J} \otimes \frac{\partial F_{JKL}}{\partial \mathbf{x_K}} + F_{JKL}\frac{\partial \mathbf{n_J}}{\partial \mathbf{x_K}} + \mathbf{n_L} \otimes \frac{\partial F_{JKL}}{\partial \mathbf{x_K}} \\ &\quad +F_{JKL}\frac{\partial \mathbf{n_L}}{\partial \mathbf{x_K}} + \frac{1}{2}\mathbf{n_{IJK}} \otimes \frac{\partial F_{IJKL}}{\partial \mathbf{x_K}} + \frac{1}{2}F_{IJKL}\frac{\partial \mathbf{n_{IJK}}}{\partial \mathbf{x_K}} \\ &\quad +\frac{3}{2}\mathbf{n_{JKL}} \otimes \frac{\partial F_{IJKL}}{\partial \mathbf{x_K}} + \frac{3}{2}F_{IJKL}\frac{\partial \mathbf{n_{JKL}}}{\partial \mathbf{x_K}}\end{aligned} \tag{8.12}$$

$$\begin{aligned}\frac{\partial \mathbf{R_K}}{\partial \mathbf{x_L}} &= +\mathbf{n_{KL}} \otimes \frac{\partial F_{KL}}{\partial \mathbf{x_L}} + F_{KL}\frac{\partial \mathbf{n_{KL}}}{\partial \mathbf{x_L}} + \mathbf{n_J} \otimes \frac{\partial F_{JKL}}{\partial \mathbf{x_L}} \\ &\quad +F_{JKL}\frac{\partial \mathbf{n_J}}{\partial \mathbf{x_L}} + \mathbf{n_L} \otimes \frac{\partial F_{JKL}}{\partial \mathbf{x_L}} + F_{JKL}\frac{\partial \mathbf{n_L}}{\partial \mathbf{x_L}} \\ &\quad +\frac{1}{2}\mathbf{n_{IJK}} \otimes \frac{\partial F_{IJKL}}{\partial \mathbf{x_L}} + \frac{3}{2}F_{IJKL}\frac{\partial \mathbf{n_{JKL}}}{\partial \mathbf{x_L}} + \frac{3}{2}\mathbf{n_{JKL}} \otimes \frac{\partial F_{IJKL}}{\partial \mathbf{x_L}}\end{aligned} \tag{8.13}$$

node L

$$\frac{\partial \mathbf{R_L}}{\partial \mathbf{x_I}} = -\mathbf{n_{JKL}} \otimes \frac{\partial F_{IJKL}}{\partial \mathbf{x_I}} \tag{8.14}$$

$$\begin{aligned}\frac{\partial \mathbf{R_L}}{\partial \mathbf{x_J}} &= -\mathbf{n_L} \otimes \frac{\partial F_{JKL}}{\partial \mathbf{x_J}} - F_{JKL}\frac{\partial \mathbf{n_L}}{\partial \mathbf{x_J}} - \mathbf{n_{JKL}} \otimes \frac{\partial F_{IJKL}}{\partial \mathbf{x_J}} \\ &\quad -F_{IJKL}\frac{\partial \mathbf{n_J KL}}{\partial \mathbf{x_J}}\end{aligned} \tag{8.15}$$

$$\begin{aligned}\frac{\partial \mathbf{R_L}}{\partial \mathbf{x_K}} &= -\mathbf{n_{KL}} \otimes \frac{\partial F_{KL}}{\partial \mathbf{x_K}} - F_{KL}\frac{\partial \mathbf{n_{KL}}}{\partial \mathbf{x_K}} - \mathbf{n_L} \otimes \frac{\partial F_{JKL}}{\partial \mathbf{x_K}} \\ &\quad -F_{JKL}\frac{\partial \mathbf{n_L}}{\partial \mathbf{x_K}} - \mathbf{n_{JKL}} \otimes \frac{\partial F_{IJKL}}{\partial \mathbf{x_K}} - F_{IJKL}\frac{\partial \mathbf{n_{JKL}}}{\partial \mathbf{x_K}}\end{aligned} \tag{8.16}$$

$$\begin{aligned}\frac{\partial \mathbf{R_L}}{\partial \mathbf{x_L}} &= -\mathbf{n_{KL}} \otimes \frac{\partial F_{KL}}{\partial \mathbf{x_L}} - F_{KL}\frac{\partial \mathbf{n_{KL}}}{\partial \mathbf{x_L}} - \mathbf{n_L} \otimes \frac{\partial F_{JKL}}{\partial \mathbf{x_L}} \\ &\quad -F_{JKL}\frac{\partial \mathbf{n_L}}{\partial \mathbf{x_L}} - \mathbf{n_{JKL}} \otimes \frac{\partial F_{IJKL}}{\partial \mathbf{x_L}} - F_{IJKL}\frac{\partial \mathbf{n_{JKL}}}{\partial \mathbf{x_L}}\end{aligned} \tag{8.17}$$

The repeated application of the product and chain rule yields the derivative of the normal vectors

$$\frac{\partial \mathbf{n_{ij}}}{\partial \mathbf{x_i}} = -\frac{\partial \mathbf{n_{ij}}}{\partial \mathbf{x_j}} = \frac{\mathbf{n_{ij}} \otimes \mathbf{n_{ij}} - \underline{1}}{|\mathbf{x_j} - \mathbf{x_i}|} \quad \text{with i=I,J,K; j=J,K,L} \tag{8.18}$$

$$\frac{\partial \mathbf{n_{ij}}}{\partial \mathbf{x_k}} = \underline{0} \quad \text{with } k \neq i \text{ et } k \neq j \tag{8.19}$$

$$\frac{\partial \mathbf{n_i jk}}{\partial \mathbf{x_l}} = \frac{(\underline{1} - \mathbf{n_{ijk}} \otimes \mathbf{n_{ijk}})(\mathbf{n}_{ij} \times \frac{\partial \mathbf{n_{jk}}}{\partial \times_l} - \mathbf{n}_{jk} \times \frac{\partial \mathbf{n_{ij}}}{\partial \times_l})}{|\mathbf{n_{ij}} \times \mathbf{n_{jk}}|} \quad \text{with i=I,J; j=J,K; k=K,L; l= I,J,K,L} \tag{8.20}$$

and

$$\frac{\partial \mathbf{n_I}}{\partial \mathbf{x_i}} = \mathbf{n_{IJ}} \times \frac{\partial \mathbf{n_{IJK}}}{\partial \mathbf{x_i}} - \mathbf{n_{IJK}} \times \frac{\partial \mathbf{n_{IJ}}}{\partial \mathbf{x_i}} \quad \text{with i=I,J,K} \tag{8.21}$$

$$\frac{\partial \mathbf{n_J}}{\partial \mathbf{x_i}} = \mathbf{n_{JK}} \times \frac{\partial \mathbf{n_{JKL}}}{\partial \mathbf{x_i}} - \mathbf{n_{JKL}} \times \frac{\partial \mathbf{n_{JK}}}{\partial \mathbf{x_i}} \quad \text{with i=J,K,L} \tag{8.22}$$

$$\frac{\partial \mathbf{n_K}}{\partial \mathbf{x_i}} = \mathbf{n_{JK}} \times \frac{\partial \mathbf{n_{IJK}}}{\partial \mathbf{x_i}} - \mathbf{n_{IJK}} \times \frac{\partial \mathbf{n_{JK}}}{\partial \mathbf{x_i}} \quad \text{with i=I,J,K} \tag{8.23}$$

$$\frac{\partial \mathbf{n_L}}{\partial \mathbf{x_i}} = \mathbf{n_{KL}} \times \frac{\partial \mathbf{n_{JKL}}}{\partial \mathbf{x_i}} - \mathbf{n_{JKL}} \times \frac{\partial \mathbf{n_{KL}}}{\partial \mathbf{x_i}} \quad \text{with i=J,K,L} \tag{8.24}$$

After some manipulations, the derivatives of the forces (norms) are given as

$$\begin{aligned}\frac{\partial F_{ij}}{\partial \mathbf{x_i}} = -\frac{\partial F_{ij}}{\partial \mathbf{x_j}} = &-(2\alpha n)^2 \frac{D_e}{12}[exp(-2\alpha n(|x_j - x_i| - R - e)) \\ &-0.5exp(-\alpha n(|x_j - x_i| - R_e))]\mathbf{n_{ij}} \quad \text{with i=I,J,K; j=J,K,L}\end{aligned} \tag{8.25}$$

and

$$\frac{\partial F_{ijk}}{\partial \mathbf{x_l}} = \frac{C_{ijk}}{4}[\cos\Theta_j^0 \cos\Theta_{ijk} - \cos(2\Theta_{ijk})] - \frac{\partial \Theta_{ijk}}{\partial \mathbf{x_l}} \quad \text{with i=I,J; j=J,k; k=K,L; l= I,J,K,L} \tag{8.26}$$

with

$$\frac{\partial \Theta_{ijk}}{\partial \mathbf{x_l}} = -\frac{\mathbf{n_{ijk}}(\mathbf{n_{ij}} \times \frac{\partial \mathbf{n_{jk}}}{\partial \mathbf{x_l}} - \mathbf{n_{jk}} \times \frac{\partial \mathbf{n_{ij}}}{\partial \mathbf{x_l}})}{\sqrt{1 - |\mathbf{n_{ij}} \times \mathbf{n_{jk}}|^2}} \tag{8.27}$$

as well as

$$\frac{\partial F_{IJKL}}{\partial \mathbf{x_i}} = \frac{1}{\sqrt{3}R_e} \frac{V_{JK}}{4} \mathbf{n_{JK}^2} \cos[\mathbf{n_{JK}}(\varphi_{\mathbf{IJKL}} - \varphi_{\mathbf{JK}}^{\mathbf{0}})] \frac{\partial \varphi_{IJKL}}{\partial \mathbf{x_i}} \quad \text{with i=I,J,K,L} \tag{8.28}$$

with

$$\frac{\partial \varphi_{IJKL}}{\partial \mathbf{x_i}} = \begin{cases} +\dfrac{(\mathbf{n_{IJK}} \times \mathbf{n_{JKL}})\dfrac{\partial \mathbf{n_{JK}}}{\partial \mathbf{x_i}} + \mathbf{n_{JK}}(\mathbf{n_{IJK}} \times \dfrac{\partial \mathbf{n_{JKL}}}{\partial \mathbf{x_i}} - \mathbf{n_{JKL}} \times \dfrac{\partial \mathbf{n_{IJK}}}{\partial \mathbf{x_i}})}{\sqrt{1 - [(\mathbf{n_{IJK}} x \mathbf{n_{JKL}}) \cdot \mathbf{n_{JK}}]^2}} & \text{if } (\mathbf{n_{IJK}} \cdot \mathbf{n_{JKL}}) \geq 0 \\ -\dfrac{(\mathbf{n_{IJK}} \times \mathbf{n_{JKL}})\dfrac{\partial \mathbf{n_{JK}}}{\partial \mathbf{x_i}} + \mathbf{n_{JK}}(\mathbf{n_{IJK}} \times \dfrac{\partial \mathbf{n_{JKL}}}{\partial \mathbf{x_i}} - \mathbf{n_{JKL}} \times \dfrac{\partial \mathbf{n_{IJK}}}{\partial \mathbf{x_i}})}{\sqrt{1 - [(\mathbf{n_{IJK}} \times \mathbf{n_{JKL}}) \cdot \mathbf{n_{JK}}]^2}} & \text{if } (\mathbf{n_{IJK}} \cdot \mathbf{n_{JKL}}) < 0 \end{cases} \tag{8.29}$$

Chapter 9

Appendix B
Technical details related to the Electroluminescence image acquisition

Cracks and electrically inactive areas in Silicon solar cells are not usually visible with the naked eye. However, they can be analyzed by means of the electroluminescence (EL) technique which is a nondestructive method based on the evaluation of the level of luminescence emitted by Silicon when subjected to an imposed electric potential in forward bias condition. Electrically insulated zones or cracks can be identified by their low EL intensity, thus resulting in dimmer images.

9.1 Parameters for the EL technique application in the bending test

In the present tests, PV panels are supplied by a 10 A bias DC by the Genesys GENH60-12.5 (750W-1U, TDK Lambda) power supplier (see Fig. 9.1).

EL emission is detected by the cooled digital 12 bit CCD camera pco.1300 solar (see Fig. 9.2), with a resolution of 1392 x 1040 pixel and equipped by the Schneider Kreuznach XNP F1.4 lens with SWIR coating 800 - 1800 nm. In order to reach a meaningful level of detection it is essential to maintain a high signal to noise ratio, cutting off all possible sources of light.

Hence, tests are performed inside a darkroom shading all the possible sources of light to avoid reflection effects. By using nearly the maximum aperture of the camera (F1.8), the focus of the camera has been adjusted during the bending test to obtain perfect focus for all the various deflections of the module. An exposure time of 5 s has been used. A post-processing of the acquired EL images has been made by using the facilities of the software

Figure 9.1: The Genesys GENH60-12.5 power supplier

Figure 9.2: The CCD camera pco.1300 solar

CamWare. In particular, cut-off filters of 600 and 8200 nm have been used for all the images to make them comparable and remove very high and very low emission spectrum frequencies. In Fig. 9.3 is reported the complete set-up built into the laboratory for the acquisition of EL images.

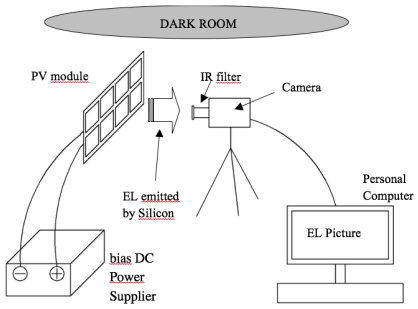

Figure 9.3: The CCD camera pco.1300 solar

9.2 Parameters for the EL technique application in hail impact tests for crack path individuation

In the present tests, a voltage of 0.7 V was applied to the PV panels by the Genesys GENH60-12.5 (750W-1U, TDK Lambda) power supplier. EL emission was detected by the cooled digital 12 bit CCD camera pco.1300 solar, with a resolution of 1392 $\times$ 1040 pixel and equipped by the Schneider Kreuznach XNP F1.4 lens with SWIR coating 800 - 1800 nm. Tests were performed inside a darkroom, shading all the possible sources of light to avoid reflection. Nearly the maximum aperture of the lens (F2) was selected, with an exposure time of 5s. Post-processing of the acquired EL images was made by using the facilities of the software CamWare. In particular, cut-off filters of 600 and 8200 nm were used for all the images to make them comparable and remove very high and very low emission in the EL signal spectrum.

Bibliography

[1] Green M.A. *Solar Cells, Operating Principles, Technology, and System Applications*. Prentice Hall Inc, Englewood Cliffs, New Jersey, 1982.

[2] Goetzberger A, Hebling C, and Schock H-W. Photovoltaic materials, history, status and outlook. *Materials Science and Engineering*, 40:1–46, 2003.

[3] Paggi M., Kajari-Schröder S., and Eitner U. Thermomechanical deformations in photovoltaic laminates. *Journal of Strain Analysis for Engineering Design*, 46:772–782, 2011.

[4] IEEE Standards Association. *IEEE Standards*. Internet site, www.iec.ch, 2016.

[5] IEEE Standards Association. *IEEE IEC 61215:2006 Crystalline Silicon Terrestrial Photovoltaic PV Modules-Design Qualification and Type Approval*. International Electrotechnical Commission, Geneva,Switzerland, 2006.

[6] Wohlgemuth J. *IEC 61215: What is it and isn't - Slideshow*. NREL Conference, Geneva,Switzerland, 2012.

[7] Paggi M., Corrado M., and Rodriguez MA. A multi-physics and multi-scale numerical approach to microcracking and power-loss in photovoltaic modules. *Composite Structures*, 95:630–638, 2013.

[8] Gow J.A. and Manning C.D. Development of a photovoltaic array model for use in power-electronics simulation studies. *IEEE Proc Electron Power Appl*, 146:193–200, 1999.

[9] Alonso-Garcia M.C. and Ruiz J.M. Analysis and modelling the reverse characteristic of photovoltaic cells. *Solar Energy Mater Solar Cells*, 90:1105–1120, 2006.

[10] Munoz M.A., Alonso-Garcia M.C., and et al. Early degradation of silicon pv modules and guaranty conditions. *Solar Energy*, 85:2264–2274, 2011.

[11] van Mölken JI UA, Safiei A, and et al. Impact of micro-cracks on the degradation of solar cell performance based on two-diode model parameters. *Energy Procedia*, 27:167–172, 2012.

[12] Shahil K. M. F. and thedin A.A. Graphene - multilayer graphene nanocomposites as highly efficient thermal interface materials. *Nano Lett.*, 12:861–867, 2012.

[13] Weinreich B., Schauer B., et al. *Validierung der Vermessung gebrochener Zellen im Feld mittels Leistungs PV-Thermographie*. Tagungsband 27. Symposium Photovoltaische Solarenergie 190-196, Bad Staffelstein, Germany, 2012.

[14] Paggi M. and Sapora A. A numerical modelling of microcracking in pv modules induced by thermo-mechanical loads. *Energy Procedia*, 38:506–515, 2013.

[15] Sapora A. and Paggi M. A coupled cohesive zone model for transient analysis of thermoelastic interface debonding. *Computational Mechanics*, 53:845–857, 2013.

[16] Paggi M. and Wriggers P. A nonlocal cohesive zone model for finite thickness interfaces part i: mathematical formulation and validation with molecular dynamics. *Computational Materials Science*, 50:1625–1633, 2011.

[17] Ozdemir I., Brekelmans W.A.M., and Geers M.G.D. A thermo-mechanical cohesive zone model. *Computational Mechanics*, 26:735–745, 2010.

[18] Hattiangadi A. and Siegmund T. A thermomechanical cohesive zone model for bridged delamination cracks. *Journal of the Mechanics and Physics of Solids*, 52:533–566, 2004.

[19] Barber JR. Proceedings of the royal society of london ser. a. *Journal of the Mechanics and Physics of Solids*, 459:53–66, 2003.

[20] Paggi M. and Barber JR. Contact conductance of rough surfaces composed of modified rmd patches. *International Journal of Heat and Mass Transfer*, 4:4464–4672, 2011.

[21] Greenwood J.A. and Williamson J.B.P. Contact of nominally flat surfaces. *Proceedings of the Royal Society of London Ser. A*, 295:300–319, 1966.

[22] Gdoutos E.E. *Fracture Mechanics: An Introduction*. Kluwer Academic, AA Dordrecht, Netherlands, 2005.

[23] Carpinteri A. Post-peak and post-bifurcation analysis of cohesive crack propagation. *Engineering Fracture Mechanics*, 32:265–278, 1989.

[24] Carpinteri A. Notch sensitivity in fracture testing of aggregative materials. *Engineering Fracture Mechanics*, 16:467–481, 1982.

[25] Carpinteri A. *Meccanica dei Materiali e della Frattura*. ed. Pitagora, Bologna, Italia, 1992.

[26] Dugdale D.S. Yielding of steel sheets containing slits. *J. Mech. Phys. Solids*, 8:100–108, 1960.

[27] Baremblatt G. I. The mathematical theory of equilibrium of cracks in brittle fracture. *Adv. Appl. Mech.*, 7:55–129, 1962.

[28] Hillerborg A., Modéer N., and Petersson P.E. Analysis of crack formation and crack growth in concrete by means of fracture mechanics in finite elements. *Cement Concrete Res*, 6:773–782, 1976.

[29] Bazant Z.P. and Planas J. *Fracture and Size Effects in Concrete and Other Quasi brittle Materials*. CRC Press LLC, Boca Raton, Florida, 1998.

[30] Carpinteri A., Cornetti P., Sapora A., Di Paola M., and Zingales M. Fractional calculus in solid mechanics: Local vs non-local approach. *Physica Scripta*, 136:014003–014010, 2009.

[31] Carpinteri A. Softening and snap-back instability in cohesive solids. *International Journal for Numerical Methods in Engineering*, 28:1521–1537, 1989.

[32] Li S., Zeng X., Ren B., and others. An atomistic-based interphase zone model for crystalline solids. *Computer Methods in Applied Mechanics and Engineering*, 29:87–109, 2012.

[33] Zeng X. and Li S. A multiscale cohesive zone model and simulations of fractures. *Computer Methods in Applied Mechanics and Engineering*, 199:547–556, 2010.

[34] Qian J. and Li S. Application of multiscale cohesive zone model to simulate fracture in polycrystalline solids. *Journal of Engineering Materials and Technology*, 133:1–37, 2011.

[35] Bazant Z.P. and Oh O.H. Crack band theory for fracture of concrete. *Materiaux et Constructions*, 16:155–177, 1983.

[36] Bazant Z.P. and Jirasek M. Nonlocal integral formulations of plasticity and damage: survey of progress. *Journal of Engineering Mechanics*, 128:1119–1149, 2002.

[37] Onufriev A. *The generalized Born model: its foundation and application and limitations*. Departments of Computer Science and Physics, Blacksburg, Virginia, USA, 2010.

[38] Parisi A., Caldarelli G., and Pietronero L. Roughness of fracture surfaces. *Europhysics Letters*, 52:304–310, 2000.

[39] Caldarelli G. and Vespignani A. Fixed scale transformation approach for born model of fractures. *Fractals*, 3:829–837, 1995.

[40] Sigalov G., Scheffel P., and Onufriev A. Incorporating variable dielectric environments into the generalized born model. *J Chem Phys*, 122:094511, 2005.

[41] Schlangen E. and van Mier J.G.M. Simple lattice model for numerical simulation of fracture of concrete materials and structures. *Materials and Structures*, 25:534–542, 1992.

[42] Hsu T.T.C. Mathematical analysis of shrinkage stresses in a model of hardened concrete. *Journal Proceedings*, 60:371–390, 1963.

[43] Liliu G. and van Mier J.G.M. 3d lattice type fracture model for concrete. *Eng Fract Mat*, 70:927–941, 2003.

[44] van Mier J.G.M. *Failure of concrete under uniaxial compression: an overview - Proceeding of FRAMCOS-3*. AEDIFICATIO Publishers", address = "Germany, 1998.

[45] Rots J.G., Invernizzi S., and Belletti B. *Fracture via a sequence of events: a saw-tooth softening model - Proceeding of FRAMCOS-6*. AEDIFICATIO Publishers", address = "Germany, 2007.

[46] Valavala P.K. and Odegard G.M. Modeling techniques for determination of mechanical properties of polymer nanocomposites. *Rev.Adv.Mater.Sci. Mechanics*, 9:33–34, 2005.

[47] Mori T. and Tanaka K. Average stress in matrix and average elastic energy of materials with misfitting inclusions. *Rev.Adv.Mater.Sci. Mechanics*, 21:571–574, 1973.

[48] Eshelby J.D. The determination of the elastic field of an ellipsoidal inclusion, and related problems. *Proceedings of the Royal Society of London A*, 241:376, 1957.

[49] Gates T.S., Odegard G.M., and others. Computational materials: Multi-scale modeling and simulation of nanostructured materials. *Composites Science and Technology*, 65:2416–2434, 2005.

[50] Paggi M. and Infuso A. Flaw-tolerance of nonlocal discrete systems and interpretation according to network theory. *Extended abstract and conference presentation*, 1:34–36, 2014.

[51] Phillips R. *Crystals, Defects and Microstructures: Modeling Across Scales*. Cambridge University Press, Cambridge, UK, 2001.

[52] Ortiz M., Cuitino A.M., Knap J., and Koslowski M. Mixed atomistic-continuum models of material behavior: the art of transcending atomistics and informing continua. *MRS Bullettin*, 26:216–221, 2001.

[53] Umeno Y., Kushima A., Kitamura T., and et others. Ab initio study of the surface properties and ideal strength of (100) silicon thin films. *Physical Reviews B*, 72:165431, 2005.

[54] Alder B.J. and Wainwright T.E. Phase transition for a hard sphere system. *J Chem Phys*, 27:1208–12011, 1957.

[55] Rahman A. Correlations in the motion of atoms in liquid argon. *J Chem Phys*, 136:405–411, 1964.

[56] Allen M.P. and Tildesley D.J. *Computer simulation of liquids*. Clarendon Press, Oxford, UK, 1989.

[57] Plimpton S.J. Fast parallel algorithms for short-range molecular dynamics. *J Comp Phys*, 117:1–19, 1995.

[58] Cornell W.D., Cieplak P., Bayly C.I., and et al. A second generation force field for the simulation of proteins, nucleic acids, and organic molecules. *J Am Chem Soc*, 117:5179–5197, 1995.

[59] MacKerell Jr. A. D., Bashford D., and et al. All-atom empirical potential for molecular modeling and dynamics studies of proteins. *J Phys Chem B*, 102:3586–3616, 1998.

[60] Brooks B.R., Bruccoleri R.E., Olafson B.D., and et al. Charmm: A program for macromolecular energy, minimization, and dynamics calculations. *Journal of Computational Chemistry*, 4:187–217, 1983.

[61] Mayo S.L., Olfason B.D., and Goddard III W. Dreiding: a generic force field for molecular simulations. *J. Phys. Chem.*, 94:8897–8909, 1990.

[62] Tersoff J. New empirical approach for the structure and energy of covalent systems. *Phys. Rev. B*, 37:6991, 1988.

[63] Tersoff J. Empirical interatomic potential for carbon, with applications to amorphous carbon. *Phys. Rev. Lett.*, 61:2879, 1988.

[64] Abell G. Empirical chemical pseudopotential theory of molecular and metallic bonding. *Phys. Rev. B*, 31:6184, 1985.

[65] Abell G. A second-generation reactive empirical bond order (rebo) potential energy expression for hydrocarbons. *J. Phys.: Condens. Matter*, 14:783–802, 2002.

[66] Stuart S.J., Tutein A.B., and Harrison J.A. A reactive potential for hydrocarbons with intermolecular interactions. *The Journal of chemical physics*, 112:6472–6486, 2000.

[67] Brenner D.W. Empirical potential for hydrocarbons for use in simulating the chemical vapor deposition of diamond films. *Phys. Rev. B*, 42:9458, 1990.

[68] Zheng Q.H., Yu A.B., and Lu G.Q. Multiscale modeling and simulation of polymer nanocomposites. *Progress In Polymer Science*, 33:191–269, 2008.

[69] Metropolis N., Rosenbluth A.W., et al. Equations of state calculation by fast computing machines. *J. Chem. Phys.*, 21:1087–1092, 1953.

[70] Aifantis and E.C. On the gradient approach - relation to eringen's nonlocal theory. *Int. J. Eng. Sci.*, 49:1367–1377, 2001.

[71] Peerlings R.H.J., de Borst R., et al. Gradient enhanced damage for quasi-brittle materials. *Int. J. Numer. Meth. Eng.*, 39:3391–3403, 1996.

[72] Bertoldi K., Bigoni D., and Drugan W.J. Structural interfaces in linear elasticity. part i: Nonlocality and gradient approximations. *J. Mech. Phys. Solids*, 55:1–34, 2007.

[73] Eringen A.C. and Kim B.S. Relation between non-local elasticity and lattice dynamics. *Crystal Lattice Defects*, 7:51–57, 1977.

[74] Di Paola M. and Zingales M. Long-range cohesive interactions of non-local continuum faced by fractional calculus. *Int. J. Solids Struct.*, 45:5642–5659, 2008.

[75] van Mier J.G.M., Schlangen E., and Vervuurt A. *Lattice type fracture models for concrete - Chapt. 10 in Continuum Models for Materials with Microstructure*. John Wiley & Sons, Chichester, UK, 1995.

[76] Onufriev A. Fixed scale transformation approach for born model of fractures. *Fractals*, 3:829–837, 1995.

[77] Tan H., Jiang L.Y., Huang Y., Liu B., and Hwang K.C. The effect of van der waals-based interface cohesive law on carbon nanotube-reinforced composite materials. *Compos. Sci. Technol.*, 67:2941–2946, 2007.

[78] Jiang L.Y., Huang Y., Jiang H., Ravichandran G., and et al. A cohesive law for carbon nanotube/polymer interfaces based on the van der waals force. *J. Mech. Phys. Solids*, 54:2436–2452, 2006.

[79] van Mier J.G.M. Multi-scale interaction potentials (f-r) for describing fracture of brittle disordered materials like cement and concrete. *Int. J. Fract.*, 143:41–78, 2007.

[80] Infuso A. and Paggi M. Flaw-tolerance of nonlocal discrete systems and interpretation according to network theory. *Fract. Struct. Integr.*, 29:302–312, 2014.

[81] Zienkiewicz O.C. and Taylor R.L. *The Finite Element Method 1-2, 6th edition*. Elsevier Oxford, Oxford, UK, 2005.

[82] Paggi M. and Wriggers P. A nonlocal cohesive zone model for finite thickness interfaces part ii: Fe implementation and application to polycrystalline materials. *Computational Materials Science*, 50:1634–1643, 2011.

[83] Nasdala L., Kempe A., and Rolfe R. The molecular dynamic finite element method (mdfem). *CMC*, 19:57–104, 2010.

[84] Odegard G.M., Gates T.S., Nicholson L.M., and Wise K.E. Equivalent-continuum modeling of nano-structured materials. *Composites Science and Technology*, 62:1869–1880, 2002.

[85] Nasdala L. and Ernst G. Development of a 4-node finite element for the computation of nano-structured materials. *Computational Materials Science*, 33:443–458, 2005.

[86] Mase G.E. *Theory and problems of continuum mechanics*. McGraw-Hill, New York, NY USA, 1970.

[87] Carpinteri A. Cusp catastrophe interpretation of fracture instability. *Journal of the Mechanics and Physics of Solids*, 37:567–582, 1989.

[88] Tvergaard V. and Hutchinson J.W. The relation between crack growth resistance and fracture process parameters in elastic-plastic solids. *Journal of the Mechanics and Physics of Solids*, 40:1377–1397, 1992.

[89] Bolzon G., Fedele R., and Maier G. Parameter identification of a cohesive crack model by kalman filter. *Computer Methods in Applied Mechanics and Engineering*, 191:2847–2871, 2002.

[90] Carpinteri A. and Colombo G. Numerical analysis of catastrophic softening behaviour (snap-back instability). *Computers & Structures*, 31:607–636, 1989.

[91] LI S., Thouless M.D., Waas A.M., Schroeder J.A., and Zavattieri P.D. Use of mode-i cohesive-zone models to describe the fracture of an adhesively-bonded polymer-matrix composite. *Composites Science and Technology*, 65:281–293, 2005.

[92] Tvergaard V. Effect of fibre debonding in a whisker-reinforced metal. *Materials Science and Engineering: A*, 107:23–40, 1990.

[93] Ortiz M. and Pandolfi A. Finite-deformation irreversible cohesive elements for three-dimensional crack-propagation analysis. *International Journal for Numerical Methods in Engineering*, 44:1267–1282, 1999.

[94] Zavattieri P.D., Raghuram P.V., and Espinosa H.D. A computational model of ceramic microstructures subjected to multi-axial dynamic loading. *Journal of the Mechanics and Physics of Solids*, 49:27–68, 2001.

[95] Benson D.J., Fu H.H., and Meyers M.A. On the effect of grain size on yield stress: extension into nanocrystalline domain. *Materials Science and Engineering A*, 319-321:854–861, 2001.

[96] Mariani S., Ghisi A., Corigliano A., and et al. Modeling impact-induced failure of polysilicon mems: A multi-scale approach. *Sensors*, 9:556–567, 2009.

[97] Mariani S., Martini R., Ghisi A., Corigliano A., and et al. Monte carlo simulation of micro-cracking in polysilicon mems exposed to shocks. *Int J Fract*, 167:83–101, 2011.

[98] Comi C., Mariani S., and Perego U. An extended fe strategy for transition from continuum damage to mode i cohesive crack propagation. *Int J Numer Anal Meth Geomech*, 00:1–6, 2002.

[99] Bfer G. An isoparametric joint/interface element for finite element analysis. *International Journal for Numerical Methods in Engineering*, 21:585–600, 2001.

[100] Point N. and Sacco E. Delamination of beams: an application to the dcb specimen. *International Journal of Fracture*, 79:225–247, 1996.

[101] Segurado J. and Llorca J. A new three-dimensional interface finite element to simulate fracture in composites. *International Journal of Solids and Structures*, 41:2977–2993, 2004.

[102] Leppin C. and Wriggers P. Numerical simulation of rapid crack propagation in viscoplastic materials. *Computers & Structures*, 61:1169–1175, 1996.

[103] Schellekens J.C.J. and de Borst R. On the numerical integration of interface elements. *International Journal for Numerical Methods in Engineering*, 36:43–66, 1993.

[104] Sapora A and Paggi M. A coupled cohesive zone model for transient analysis of thermoelastic interface debonding. *Comput Mech*, 38:506–515, 2013.

[105] Paggi M. and Wriggers P. Stiffness and strength of hierarchical polycrystalline materials with imperfect interfaces. *J Mech Phys Solids*, 60:557–572, 2012.

[106] Infuso A., Corrado M., and Paggi M. Image analysis of polycrystalline solar cells and modelling of intergranular and transgranular cracking. *Journal of the European Ceramic Society*, 34:2713–2722, 2014.

[107] Kajari-Schröder S., Kunze I., Eitner U., and Köntges M. Spatial and orientationtional distribution of cracks in crystalline photovoltaic modules generated by mechanical load tests. *Sol Energy Mater Sol Cells*, 95:3054–3059, 2011.

[108] Köntges M., Kunze I., Kajari-Schröder S., Breitenmoser X., and Bjrneklett B. The risk of power loss in crystalline silicon based photovoltaic modules due to microcracks. *Sol Energy Mater Sol Cells*, 95:1131–1137, 2011.

[109] Kajari-Schröder S., Kunze I., and Köntges M. Criticality of cracks in pv modules. *Energy Procedia*, 27:658–663, 2012.

[110] Sander M., Dietrich S., Pander M., Ebert M., and Bagdahn J. Systematic investigation of cracks in encapsulated solar cells after mechanical loading. *Sol Energy Mater Sol Cells*, 111:82–89, 2013.

[111] Geuzaine C. and Remacle J.-F. Gmsh: a three-dimensional finite element mesh generator with built-in pre- and post-processing facilities. *Int J Numer Meth*, 79:1309–1331, 2009.

[112] Kubair D.V. and Geubelle P.H. Comparative analysis of extrinsic and intrinsic cohesive models of dynamic fracture. *Int J Solids Struct*, 40:3853–3868, 2003.

[113] Kraft R.H. and Molinari J.F. A statistical investigation of the effects of grain boundary properties on transgranular fracture. *Acta Materialia*, 56:4739–4749, 2008.

[114] Espinosa H.D. and Zavattieri P.D. A grain level model for the study of failure initiation and evolution in polycrystalline brittle materials. part i: Theory and numerical implementation. *Mech Mater*, 35:333–364, 2003.

[115] Espinosa H.D. and Zavattieri P.D. A grain level model for the study of failure initiation and evolution in polycrystalline brittle materials. part ii: Numerical examples. *Mech Mater*, 35:365–394, 2003.

[116] De Graaff D., Lacerda R., and Campeau Z. Assessing the reliability and degradation of photovoltaic module performance parameters. *NREL 2011 Photovoltaic Module Reliability Workshop*, 1:1–2, 2011.

[117] Fuyuki T., Kondo H., Yamazaki T., and et al. Photographic surveying of minority carrier diffusion length in polycrystalline silicon solar cells by electroluminescence. *Appl. Phys. Lett.*, 86:1–3, 2005.

[118] Khatri R., Agarwal S., Saha I., Singh S. K., and Kumar B. Study on long term reliability of photo-voltaic modules and analysis of power degradation using accelerated aging tests and electroluminescence technique. *Energy Procedia*, 8:396–401, 2011.

[119] Mulhstein C.L., Stach E.A., and Ritchie R.O. A reaction-layer mechanism for the delayed failure of micron-scale polycrystalline silicon structural films subjected to high-cycle fatigue loading. *Acta Materialia*, 50:3579–3595, 2002.

[120] Meyer E.L. and van Dyk E.E. Assessing the reliability and degradation of photovoltaic module performance parameters. *IEEE Transactions on Reliability*, 53:83–92, 2004.

[121] Moore D., Wilson A., and Ross R. *Simulated hail impact testing of photovoltaic solar panels. Proc. 24th Annual Technical Meeting*. Institute of Environmental Sciences, Ft. Worth, Texas, 1978.

[122] Nelva R. and Morra L. L'effetto della grandine su cupole e lucernari. *Zenital*, 1:1–49, 2009.

[123] Paggi M., Berardone I., Infuso A., and Corrado M. Fatigue degradation and electric recovery in silicon solar cells embedded in photovoltaic modules. *Sci Rep*, 4:4506, 2014.

[124] Johnson K.L. *Contact Mechanics*. Cambridge University Press, Cambridge, UK, 1978.

[125] Paggi M. and Sapora A. An accurate thermoviscoelastic rheological model for ethylene vinyl acetate based on fractional calculus. *Int J Photoenergy*, 2015:ID–252740, 2015.

[126] Ojo S.O. and Sapora A. A thermo-visco-elastic shear-lag model for the prediction of residual stresses in photovoltaic modules after lamination. *Comp Struct*, 136:481–492, 2016.

[127] Abrate S. Modeling of impacts on composite structures. *Comp Struct*, 51:129–138, 2001.

[128] Lenarda P. and Paggi M. A geometrical multi-scale numerical method for coupled hygro-thermo-mechanical problems in photovoltaic laminates. *Comput Mech*, in press:–, 2016.